QUANTUM MULTICRITICALITY

by

GREGORY THOMAS OLIVER

A thesis submitted to
The University of Birmingham
for the degree of
DOCTOR OF PHILOSOPHY

School of Physics and Astronomy
The University of Birmingham

September 2016

Abstract

This thesis documents a theoretical investigation into quantum multicritical points (QMCPs), where a system near zero temperature is unstable towards two distinct ordered phases. We focus on quantum multicritical points in metallic systems, where the two ordered phases are both magnetic, but with different ordering wavevectors. This situation must be described by multiple dynamical exponents, which complicate the analysis.

By adapting Hertz-Millis theory, we build a model of a QMCP which we analyse using a renormalisation group approach. The regions of the phase diagram are identified, and the specific heat, thermal expansion and Grüneisen parameter are found in each region. The resistivity at finite temperatures above a QMCP is found by numerically solving the Boltzmann equation in the presence of disorder, and both ferro- and antiferromagnetic spin fluctuations. We believe our results explain the peculiar properties of the quantum critical compounds $NbFe_2$ and $Ta(Fe_{1-x}V_x)_2$, and we make predictions about properties of these systems which have not currently been measured.

We then investigate the related model of a metamagnetic quantum critical end-point and an antiferromagnetic quantum critical point in close proximity on the phase diagram. Using a self-consistently renormalised approach we identify the regions of the phase diagram, and the thermodynamic properties in each region. We highlight the experimentally measurable signatures of multicriticality in this model.

Acknowledgements

My biggest thanks must go to my supervisor, Andy Schofield. Without his continuous support over these four years this work would have been truly impossible. I'd also like to thank those with whom discussions have helped in some aspects of this thesis. Specifically, I'd like to thank Chris Hooley, Manuel Brando, Sven Friedemann, John Cleave, Rob Smith and Martin Long. I'd also like to thank the EPSRC and the University of Birmingham for funding this project.

I must also thank all those who have inhabited the fourth floor of Physics East during my time in East 416, for providing a truly unique environment to work in. Thanks to the staff for being so helpful, and thanks to the other students for never letting day-to-day life get remotely monotonous.

Thanks to my friends from outside of physics who, over the last four years, have helped to fill my spare time with silliness. So, thanks to the old circus lot, the lunch and board game crew, the rocksoc crew and the old metalsoc crew.

Finally, a massive thanks goes to my Mum, Dad, Grandad and sister. Without the support of my family I really would never have gotten this finished.

Contents

List of Figures

List of Tables

Chapter 1

INTRODUCTION

1.1 Thesis Overview

It is well known that in the proximity of second order phase transitions the physical properties of systems are controlled by fluctuations of an order parameter. For finite temperature phase transitions it is thermal fluctuations that dominate the physical properties in the vicinity of the transition, but the situation is drastically different for phase transitions without temperature. This is the basic idea of quantum phase transitions and quantum criticality.

Quantum phase transitions are phase transitions which occur in systems at zero temperature as some non-thermal control parameter is varied. For example, a magnet at zero temperature may lose its magnetic order as pressure is applied, at a so-called quantum critical point (QCP). While of course absolute zero is experimentally inaccessible, a quantum critical point in the phase diagram can actually influence physical properties of systems over some range of experimentally accessible temperatures. The question of how quantum critical points can influence physical properties of systems has been heavily researched both experimentally and theoretically in recent decades [1, 2]. The key feature that distinguishes quantum phase transitions from finite temperature (classical) phase transitions is that at zero temperature there can be no thermal fluctuations. The order parameter fluctuations at $T = 0$ are purely quantum mechanical in nature, and at finite temperatures above a quantum critical point the

interplay between quantum and thermal effects results in the unusual properties observed.

One scenario that is less well-understood than the basic idea of a phase transition at zero temperature is the idea of a zero temperature multicritical point, which is termed a quantum multicritical point (QMCP). The phrase multicritical point can be generically applied to any critical point requiring two or more parameters to tune to [3]. At certain types of multicritical points, for example bicritical and tetracritical points, several distinct ordered phases meet on the phase diagram. In this thesis we shall argue that the physics of a system at finite temperatures above such a quantum multicritical point is controlled by fluctuations of two or more distinct order parameters.

Recent experiments on $NbFe_2$ [4, 5, 6, 7], $Ta(Fe_{1-x}V_x)_2$ [8], $YbRh_2Si_2$ [9] and YbAgGe [10] have suggested that these compounds exhibit some form of quantum multicriticality. All of these compounds are metallic materials with magnetic instabilities, and appear to exhibit behaviours associated with both ferromagnetic and antiferromagnetic quantum criticality. For example the specific heat in $NbFe_2$ and $Ta(Fe_{1-x}V_x)_2$ exhibit a power law usually associated with ferromagnetic quantum criticality, but the resistivity obeys a power law usually associated with antiferromagnetic quantum criticality. Moreover, $Nb_{1-y}Fe_{2+y}$ has a quantum multicritical point in the phase diagram. $YbRh_2Si_2$ has been argued to have a multicritical nature, as the specific heat and Grüneisen parameter exhibit power laws associated with ferromagnetic quantum criticality, but the low temperature ordered phase is antiferromagnetic. YbAgGe has been argued to have a bicritical point in the phase diagram under the application of a magnetic field.

In this thesis we construct a model for quantum multicritical points in itinerant magnets, focusing on scenarios with two distinct magnetic order parameters with different ordering wavevectors; ferromagnetism and antiferromagnetism. Our model explains why the thermodynamic properties appear to be dominated by ferromagnetic quantities, and the resistivity dominated by antiferromagnetism. We are able to offer predictions about currently unmeasured quantities. We also develop a model of a metamagnetic quantum critical end-point

proximate to an antiferromagnetically ordered phase on the phase diagram.

The rest of the thesis is structured as follows. Motivated by the goal of constructing a model of a quantum multicritical point, in Chapter 1 we review the basic physical concepts and the techniques we employ in the remaining chapters. We briefly discuss the basics of phase transitions and the renormalisation group, and then discuss the physics of metallic systems and multicritical points. Chapter 2 is a second background chapter on quantum phase transitions, beginning with a general overview, and includes a detailed analysis of the Hertz-Millis theory of quantum phase transitions in itinerant magnets. Chapters 3, 4 and 5 are predominantly composed of original research. In Chapter 3 a model of a quantum multicritical point is constructed and analysed using the renormalisation group. Predictions are made for the specific heat, thermal expansion and Grüneisen parameter, and these are compared to experiments. In Chapter 4 transport properties are investigated near a quantum multicritical point, and the resistivity is calculated near such points. In Chapter 5 the model is extended to deal with magnetic fields, and the metamagnetic quantum critical end-point is investigated in the proximity of an antiferromagnetic quantum critical point. The thesis is summarised in Chapter 6, where we also discuss possible future avenues of research that stem from the work presented in this thesis.

1.2 Introduction

With the aim of developing a model for a quantum multicritical point, we now discuss the techniques we shall need in order to develop and analyse such a model. The model we present in Chapter 3 is an adaptation of the Hertz-Millis theory of quantum criticality in itinerant magnets, and Hertz-Millis theory can be analysed using the techniques which we discuss in this chapter. The main motivation of this chapter is to provide all the necessary background in order to analyse Hertz-Millis theory in Chapter 2, and our multicritical model in Chapter 3.

The rest of the chapter is structured as follows. In Section 1.3.1 we revise the basics of finite temperature phase transitions, and in Section 1.3.2 we discuss phenomenological theories of phase transitions. The Hertz-Millis model of Chapter 2 is a phenomenological model that shares many similarities with the Ginzburg-Landau model we discuss in this section. In Section 1.4 we revise the ideas behind the renormalisation group method, which is the tool we employ in Chapter 3 to analyse the quantum multicritical point. We then turn our attention to the literature on finite temperature multicritical points in Section 1.5. We end the chapter in Section 1.6 with a brief discussion on metallic systems, which are a necessary ingredient in the Hertz-Millis theory of Chapter 2.

1.3 Classical Phase Transitions

The subject of classical phase transitions and the renormalisation group is of course far too large to summarise in any amount of depth in this thesis, and there are many excellent textbooks which provide a much more thorough introduction to the subject [3, 11, 12, 13, 14, 15, 16]. In this section we go over the basic ideas which form the backbone of the thesis, emphasising the aspects which are crucial to the analysis in the later chapters.

Specifically we shall discuss the basics of phase transitions in Section 1.3.1, and phenomenological models phase transitions in Section 1.3.2. Section 1.4 is dedicated to the renormalisation group, detailing scaling analysis and momentum-shell renormalisation group.

The aim of this section is to highlight the ideas which are necessary for the analysis of the Hertz-Millis model of quantum critical points which we discuss in depth in Chapter 2, and later extend to a multicritical point in Chapter 3. Hertz-Millis theory is similar to the Ginzburg-Landau theory of phase transitions discussed in Section 1.3.2, but it is a model which we analyse above its upper critical dimension. The methods of scaling and momentum-shell renormalisation which we discuss in Section 1.4 enable the analysis of this model.

1.3.1 Phase Transitions

Phase transitions occur when a material changes its state in a discontinuous manner as some parameter is smoothly changed. These transitions occur in a wide variety of physical systems, even outside of the paradigm of condensed matter physics, but in this thesis we restrict our attention to magnetic phase transitions.

Phase transitions are commonly described in terms of an order parameter Φ, which is zero on one side of the transition and non-zero on the other. In the magnetic transitions considered in this thesis, the order parameter is some type of magnetisation, either uniform or staggered. This naturally forms a starting point for phenomenological theories of phase transitions, as we discuss in Section 1.3.2.

There are several types of phase transition. In first order phase transitions the order parameter Φ discontinuously jumps from a finite value below the transition to zero above it. In second order phase transitions, which are the subject of much of this thesis, the order parameter smoothly evolves from zero at the transition. In the vicinity of a second order phase transition in the phase diagram, the physical properties are dominated by fluctuations of the order parameter. It is this critical behaviour in the vicinity of second order phase transitions which we review in this chapter, as this behaviour is analogous to that near a quantum critical point at zero temperature.

Upon approaching second order phase transitions the correlation length diverges, and becomes infinite at the transition. The physics becomes dominated by fluctuations on the scale of the correlation length, which quickly becomes much larger than any microscopic scale in the system. The physical properties of systems near criticality therefore do not depend on the microscopic details such as the inter-atomic interactions, and only depend on general properties such as the spatial dimensionality and the symmetries of the system. This leads to the idea of universality, which is that physical properties of systems near phase transitions in materials with completely different microscopic properties exhibit the same critical behaviour, if they fall within the same universality class [12].

As a phase transition is approached by tuning some parameter t, which may for example be temperature, a number of physical properties exhibit power-law behaviour. The exponents are called the critical exponents, and the set of critical exponents in the vicinity of the phase transition define the universality class.

Because the microscopic properties are completely unimportant near the transition, and the only important length scale is the correlation length, the renormalisation group approach that we detail in Section 1.4 has naturally become a crucial tool for theoretically investigating physical properties near phase transitions. Before discussing this renormalisation group treatment, we discuss phenomenological theories for behaviour near a phase transition.

1.3.2 Phenomenological Theories

In this section we review phenomenological theories which describe the properties of materials in the vicinity of phase transitions, by describing them in terms of the order parameter Φ which is non-zero above the transition and zero below. We review the Landau theory, which is based on mean-field theory, and the Ginzburg-Landau theory which takes order parameter fluctuations into account. Our motivation for doing this is because the Hertz-Millis theory for quantum phase transitions is very similar to the Ginzburg-Landau theory we discuss here in many aspects.

The Landau theory of phase transitions is a mean-field model which assumes that the order parameter is a spatially uniform quantity. It is assumed that the free energy in the vicinity of the phase transition can be described by an analytic function of the order parameter. The free energy includes all powers of the order parameter that are allowed by symmetry. In many systems featuring second order magnetic phase transitions the relevant Landau free energy is

$$F(\Phi) = r\Phi^2 + u\Phi^4 + ..., \tag{1.3.1}$$

where the higher order terms are small close to the transition, and not necessary to include to

capture the relevant physics. When $u > 0$ the order parameter is zero for $r > 0$, and smoothly evolves from zero for $r < 0$. In finite temperature phase transitions r is the deviation from the critical temperature, $r = \frac{T - T_c}{T_c}$.

The mean-field critical exponents can be extracted from this model by calculating how physical properties change in the vicinity of the phase transition. The order parameter is found by minimising the free energy, by solving $\frac{\partial F}{\partial \Phi} = 0$. This tells us that $\Phi \sim (T_c - T)^{1/2}$ in the ordered phase, and by differentiating the free energy the specific heat can be found to be $C \sim T$ below the transition. However, the Landau model can say nothing about the disordered side of the transition.

It turns out that this mean field approximation is a poor approximation in dimensions below what is known as the upper critical dimension of the theory d_c^+, which for this model is equal to 4. Whether the mean-field approximation is suitable or not can be tested within the mean-field approximation. Taking into account the fact that the order parameter can fluctuate, the requirement for mean-field theory to be valid is that the fluctuations about the expectation value of Φ are small. This condition can be written as

$$\left\langle \left(\delta\Phi\left(\boldsymbol{x}\right)\right)^2 \right\rangle < \left\langle \Phi \right\rangle^2 , \tag{1.3.2}$$

which is known as the Ginzburg criterion. By calculating the average, using that the magnetic susceptibility in such systems is $\chi^{-1} = r + q^2$, it can be shown that this criterion is violated at temperatures sufficiently close to the transition in dimensions less than 4 [3]. The temperature it becomes violated at is known as the Ginzburg temperature.

A better model for analysing the phase transitions is the Ginzburg-Landau functional for the free energy, which takes into account that the order parameter can fluctuate in space. This is given by

$$F\left[\Phi\right] = \int d\boldsymbol{q} \left(r + q^2\right) \Phi^2\left(\boldsymbol{q}\right) + \int d\boldsymbol{x} \Phi^4\left(\boldsymbol{x}\right), \tag{1.3.3}$$

where $\Phi(\boldsymbol{q}) = \Phi(-\boldsymbol{q})$, and we have written the first term in reciprocal space and the second term in real space.

Physical properties of the Ginzburg-Landau model can be calculated from the partition function

$$\mathcal{Z} = \int \mathcal{D}\Phi(\boldsymbol{q}) \exp\left(-\beta F[\Phi]\right), \tag{1.3.4}$$

which is a functional integral over the field $\Phi(\boldsymbol{q})$. This quantity is, unfortunately, a rather difficult quantity to probe. If u were zero, the partition function would just be a Gaussian integral and the thermodynamic properties would follow from straight-forward calculations. Because this theory has a Φ^4 component, the partition function cannot be calculated exactly. This is a problem which is ubiquitous in theoretical physics, and plagues disciplines other than condensed matter physics, such as high-energy particle physics field theories [16].

The renormalisation group approach is one such technique which is useful in the analysis of models of this type.

1.4 Renormalisation Group

We now turn our attention to the renormalisation group technique, which enables further analysis of the Ginzburg-Landau functional described in the previous section. It also turns out to be a useful tool for investigating the physical properties of systems near quantum phase transitions, and in Chapter 2 we shall describe how it has been used to tackle the Hertz-Millis theory of quantum criticality. In Chapter 3 we use this method to analyse a quantum multicritical point. We therefore discuss it in some amount of detail in this section.

1.4.1 Basic Idea

The idea of the renormalisation group is that near a phase transition only the behaviour of the system on the scale of the correlation length is important, and the short-range, microscopic behaviour becomes negligible as the correlation length diverges.

The renormalisation group is a technique to generate an effective model which has the same physical properties as the original system. If a system is described by a set of parameters $\mathcal{K}$, the renormalisation group procedure involves systematically removing the short-range degrees of freedom from the system, to generate a new model described by a new set of parameters $\tilde{\mathcal{K}}$ [12].

There are many different techniques for eliminating the short-range degrees of freedom, including real-space techniques such as block spin renormalisation, or decimation, and techniques for working in reciprocal space such as momentum-shell renormalisation [3].

Regardless of the specific technique, the renormalisation group method allows us to calculate how the various parameters in the system change as we look at the system on longer and longer length scales. This enables us to identify irrelevant variables which tend to zero under the renormalisation group procedure, which can be used to justify using more simple models which depend on only a few relevant variables. Moreover, the renormalisation group method can be used to calculate the critical behaviour of systems. The renomalisation group procedures in general rely upon a rescaling of space by a factor b, which causes the parameters in the model to vary as some power of b. From these powers, called the renormalisation group eigenvalues, the critical behaviour of various physical properties can be calculated. This is illustrated in Section 1.4.2.

1.4.2 Scaling Analysis

We now illustrate how the renormalisation group can be used to determine the power-law behaviour of physical properties.

We consider a phase transition in a material at $t = 0 = \frac{T - T_c}{T_c}$, under the influence of an applied field h. Under the application of the renormalisation group procedure, we generally find that these variables scale as $t \to b^{1/\nu} t$ and $h \to b^{\lambda} h$ when space is rescaled by a factor b. For the original and the rescaled theories to be equivalent we must have that the free energy remains unchanged, which means that the free energy density obeys the homogeneity relation

$$f(t, h) = b^{-d} f\left(b^{1/\nu} t, b^{\lambda} h\right), \tag{1.4.1}$$

from which physical predictions can be made [12].

For example, setting $b = t^{-\nu}$ and differentiating twice with respect to temperature, we find that the specific heat when $h = 0$ is proportional to $t^{-\alpha}$, where $\alpha = d - 2\nu$. Similar relations can be found for the order parameter, $\langle \phi \rangle = \frac{\partial f}{\partial h} \sim t^{\nu(d-\lambda)}$, and the susceptibility $\chi = \frac{\partial^2 f}{\partial h^2} \sim t^{\nu(d-2\lambda)}$.

However, these scaling relations come with some caveats. Scaling relations involving the number of spatial dimensions d are called hyperscaling relations, and these are only expected to hold at or below the upper critical dimension of the theory. Above the upper critical dimension, so-called dangerously irrelevant variables may spoil these simple scaling relations. Below the upper critical dimension, while these hyperscaling relations are expected to hold, the system is not described by mean-field theory. The physics is controlled by an interacting theory, and the critical exponents must be found by applying the renormalisation group methods to a specific model [3].

We now turn our attention to how the scaling exponents can be found from a particular renormalisation group procedure. Specifically, we discuss the momentum-shell renormalisation group procedure.

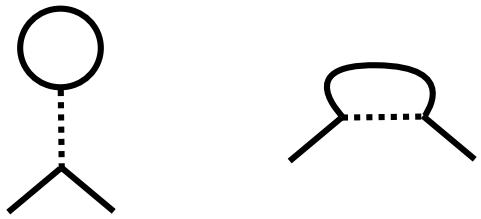

(a) (b)

Figure 1.1: Diagrams contributing to r. The dashed line represents the interaction u.

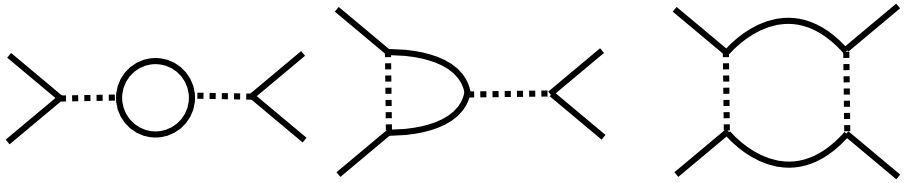

(a) (b) (c)

Figure 1.2: Diagrams contributing to u. The dashed line represents the interaction u.

1.4.3 Momentum-Shell Renormalisation Group

As alluded to in Section 1.4.1, there are various ways of implementing the renormalisation group. In this thesis the method we shall use is the momentum-shell RG procedure. This method is the standard method used to investigate the Hertz-Millis model which we discuss in Chapter 2, and in Chapter 3 we apply this technique to a model of a quantum multicritical point. Here we illustrate the key points involved by applying it to the Ginzburg-Landau functional, given by equation (1.3.3). The analysis here follows the analysis given by Chaikin and Lubensky [3].

The general idea is that we first impose a high-momentum cut-off Λ on the modes. This can be justified naturally as we are actually dealing with a discrete lattice of atoms so a cut-off on the order of the inverse lattice spacing is appropriate, or a cut-off can be justified as we only wish to deal with the long-wavelength behaviour near the phase transition. The precise value of the cut-off is unimportant, but its existence is necessary for the momentum-shell RG approach.

To begin the RG procedure, we decide that we are only interested in the long wavelength, low momentum behaviour, and declare modes with momenta near the cut-off unimportant. We define 'near' by meaning the modes with momenta satisfying $\Lambda/b < q < \Lambda$ where we take the scalar q to mean $|\boldsymbol{q}|$.

As a first approximation, in a procedure commonly called tree-level RG, we simply neglect the modes above the reduced cut-off and rescale momentum so that the cut-off in the rescaled variables is the original cut-off Λ. The other factors in the problem are rescaled such that the form of the free energy functional remains unchanged. The variables in the problem then become functions of the scaling variable b. Specifically we find $r(b) = b^2 r$ and $u(b) = b^{4-d}u$, where we immediately see how the upper critical dimension arises in this scheme. The coefficient of ϕ^4 flows to zero in dimensions above the upper-critical dimension of 4, and the system is described by an effective Gaussian theory.

Corrections to these RG equations can be found by considering the effect of the removed

modes on the low momentum modes via the quartic interaction term u. The effect of the low momentum modes interacting with the modes above the cut-off can be found systematically using the diagrammatic method of Feynman. To second order in u, the diagrams contributing to r are shown in Figure 1.1 and the diagrams contributing to u are shown in Figure 1.2. External legs represent modes below the cut-off, and internal lines represent modes above which are integrated over. The interaction u is represented as a dashed line so that the correct combinatoric prefactors of the diagrams can be calculated. In general ϕ is an n-component field, and the interaction u connects two pairs of fields which may be of different components. In the limit $b \to 1^+$ the one-loop integrals which renormalise r are simply given by $\frac{K_d}{r+\Lambda^2}$ and those which renormalise u are $\frac{K_d}{(r+\Lambda^2)^2}$, where K_d is the surface area of a d-dimensional sphere.

These diagrams lead to the RG equations [3]

$$\frac{dr}{d\ln b} = 2r(b) + 4(n+2)K_d u(b)\frac{1}{r(b)+\Lambda^2}, \tag{1.4.2a}$$

and

$$\frac{du}{d\ln b} = (4-d)\,u(b) - 4(n+8)K_d u^2(b)\frac{1}{(r(b)+\Lambda^2)^2}. \tag{1.4.2b}$$

Above the upper critical dimension, in the limit $b \to \infty$ the interaction term still flows to zero under RG, but the solution of equation (1.4.2a) is $b^2\tilde{r}$ where $\tilde{r}$ is the renormalised tuning parameter. The RG equations for the Hertz-Millis theory of quantum critical points we discuss in Chapter 2 look very similar to these equations.

While the solution of these equations above their upper critical dimension may be simple, analysis below the upper critical dimension is not so easy to perform. We now turn our attention to how the ϵ expansion technique can be used to investigate models below their upper critical dimension, with the foresight that we shall need similar analysis in Chapter 5, where we discuss metamagnetism and antiferromagnetism in the presence of a magnetic field.

1.4.4 The ϵ Expansion

While the Hertz-Millis theory for quantum critical points detailed in Chapter 2, and our model of a quantum multicritical point in Chapter 3, are models which are at or above their upper critical dimension in physically interesting situations, in Chapter 5 we shall present a model where this is not the case. For this reason we discuss the ϵ expansion, which can be used to investigate models below their upper critical dimension.

In dimensions lower than d_c^+ the Gaussian fixed point of the RG flow is unstable, and the physical properties of the system are controlled by some fixed point at finite u. It then seems that we should not be able to write the RG equations as a power series in the interaction terms u, as this is no longer a small quantity.

The ϵ expansion is a way of performing the loop expansion in terms of a small parameter, by letting the dimensionality of the system in the RG equations become a continuous variable, $d \to d_c^+ - \epsilon$ [17]. The idea of the ϵ expansion is that as ϵ grows from zero, the fixed point structure of model should smoothly evolve from the fixed point structure at the upper critical dimension, which is the single Gaussian fixed point. The location of these fixed points and the critical exponents associated with the fixed point can be found as a power series in ϵ.

Of course, extending this to the physically interesting cases of ϵ =1 or $\epsilon = 2$ may seem like a ridiculous thing to do. However, it turns out that at sufficiently high orders the predictions of the ϵ expansion are not dissimilar from physical observations. In addition, the ϵ expansion can be used to find which interactions lead to new fixed points, and characterise universality classes [12].

The one-loop RG equations, in equations (1.4.2), can be used to show that at order ϵ there is another fixed point given by

$$u^* = \frac{\epsilon}{4\,(n+8)\,K_d}, \tag{1.4.3a}$$

and

$$r^* = -\epsilon \left(\frac{n+2}{n+8} \right), \tag{1.4.3b}$$

in units where $\Lambda = 1$. This is known as the Heisenberg fixed point [3].

The RG equations can then be linearised around these fixed points, and it can be shown that δu is an eigenvector of the RG equations with eigenvalue $-\epsilon$, and hence the Heisenberg fixed point is stable. δr is an eigenvector of the RG equations with eigenvalue $2 - \epsilon \left(\frac{n+2}{n+8} \right)$, which gives the deviation from the mean-field correlation length exponent to order ϵ.

1.4.5 Discussion

In Chapter 2 we discuss Hertz-Millis theory for quantum phase transitions, which we subsequently adapt in Chapter 3 to the situation of a multicritical point. Hertz-Millis theory looks qualitatively like the Ginzburg-Landau theory of equation (1.3.3) but with an extra dimension associated with imaginary time. We shall find that in all physically relevant cases, the model we discuss is at or above its upper critical dimension, where mean-field theory is expected to hold.

However, in Hertz-Millis theory temperature enters the equations in a completely different manner to how it enters in the theories of finite temperature phase transitions. A consequence of this is that the one-loop integrals play a large role in shaping the phase diagram. Via the dangerously irrelevant interactions, the one-loop integrals end up affecting the temperature-dependence of the correlation length. The momentum-shell RG approach also captures logarithmic corrections to the expressions derived from scaling above the upper critical dimension.

This is the reason why a momentum-shell RG procedure is necessary even though we wish to analyse the model above its upper critical dimension.

1.5 Multicritical Points

As mentioned in the overview, in this thesis we are interested in quantum multicritical points where a system at zero temperature is simultaneously unstable towards two types of order. Before building a model of such points in Chapter 3, here we discuss finite temperature multicritical points.

A multicritical point is defined as a critical point which requires at least two non-ordering fields to be tuned in order to reach it [3]. Two types of multicritical point are schematically shown in the $g - T$ plane in Figure 1.3, where g represents a non-thermal tuning parameter which is required to tune to the multicritical point. Figure 1.3a shows a bicritical point where there is a first order transition between the two ordered phases below this point, and Figure 1.3b shows a tetracritical point where there is a region of coexistence of both types of order.

These multicritical points are of specific interest to us in this thesis as they have two distinct ordered phases. Near the multicritical point we expect the physical properties to be dominated by fluctuations of the two order parameters. We shall show in Chapter 3 that in a quantum critical version of these points, the dynamics of both types of order are important. This is an especially interesting scenario as it requires an analysis involving multiple dynamical exponents.

According to the definiton above, other types of multicritical points exist. Tricritical points are one such case, where a line of first order transitions changes into a line of second order transitions [3]. As this is characterised by a single order parameter, we do not consider such points in this thesis and restrict our attention to bicriticality and tetracriticality.

We now briefly discuss how the techniques of phase transitions and renormalisation can be applied to multicritical points. We begin by reviewing the scaling analysis, and then turn our attention to a phenomenological model. We summarise by reviewing the conclusions of a one-loop RG analysis. However we keep this section brief, as in Chapter 3 we shall find that much of the conclusions that are made about finite temperature points cannot be transferred to the quantum critical version.

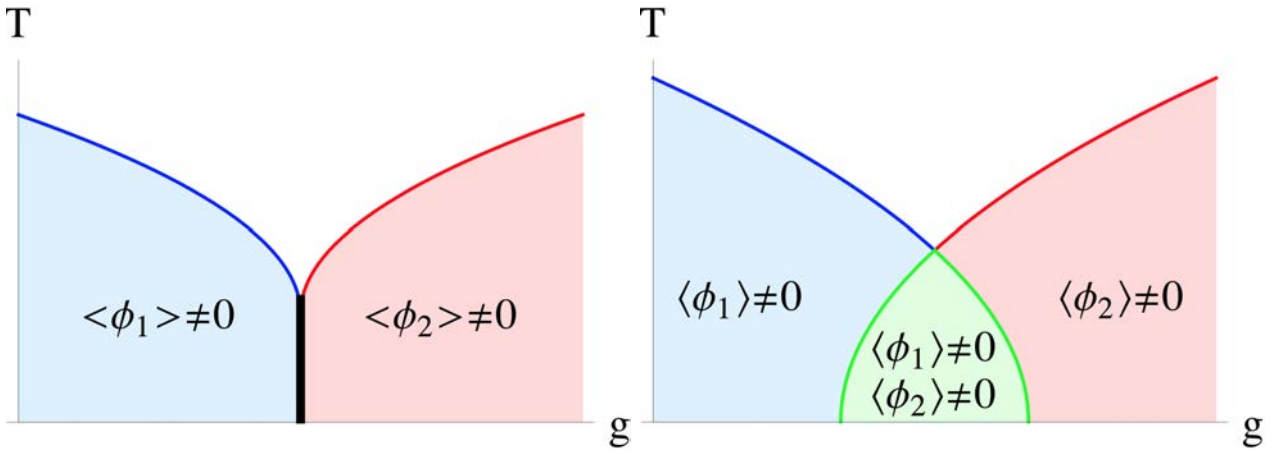

(a) Phase diagram with a bicritical point (b) Phase diagram with a tetracritical point

Figure 1.3: Finite temperature multicritical points

1.5.1 Scaling Analysis

We now discuss how the scaling analysis of Section 1.4.2 can be applied to a multicritical point, following the analysis of Chaikin and Lubensky [3].

In addition to temperature t, a non-thermal parameter g is required to tune to a multicritical point, which has a corresponding RG scaling eigenvalue λ_g. By adapting the scaling relation in equation (1.4.1), we find that

$$f(t, h, g) = b^{-d} f(b^{1/\nu} t, b^{\lambda} h, b^{\lambda_g} g). \tag{1.5.1}$$

This implies that the susceptibility obeys the relation

$$\chi(t, h, g) = b^{-(d+2\lambda)} f''(b^{1/\nu} t, b^{\lambda} h, b^{\lambda_g} g), \tag{1.5.2}$$

which can be rescaled to

$$\chi(t, h, g) = |t|^{-\gamma} X\left(\frac{h}{|t|^{\Delta}}, \frac{g}{|t|^{\phi}}\right), \tag{1.5.3}$$

where $\phi = \lambda_g \nu$ and X is a scaling function. At $h = 0$ the susceptibility diverges at the

boundaries of the ordered phases, which this scaling theory predicts obey the relation

$$t_c(g) \sim g^{1/\phi}. \tag{1.5.4}$$

We shall see in Section 3.2 that this analysis does not translate to the quantum multicritical point, as the boundaries of the ordered phases in that case are found from completely different methods.

Finding the value of the critical exponent ϕ requires a theory of the multicritical point, which we discuss in the next section. We now discuss a phenomenological theory that describes a multicritical point.

1.5.2 Phenomenological Theory

In order to build a phenomenological model of a quantum multicritical point, it is worth studying a phenomenological model of a classical multicritical point. A Landau theory can be used to describe finite temperature multicritical points between two ordered phases, characterised by $\langle\phi_1\rangle \neq 0$ and $\langle\phi_2\rangle \neq 0$ [3]. The appropriate Landau theory is

$$f(\phi_1, \phi_2) = (r-g)\,\phi_1^2 + (r+g)\,\phi_2^2 + u_1\phi_1^4 + u_2\phi_2^4 + u_{12}\phi_1^2\phi_2^2 \tag{1.5.5}$$

where in order for this to describe a classical multicritical point, r must be dependent on temperature as $r \sim T - T_c$, and g is a non-thermal tuning parameter. All the u terms are positive.

This model can be justified in a number of ways. It could simply just be written down based on general symmetry arguments, or it can be derived from a microscopic model of spins in an anisotropic environment interacting with an arbitrary interaction [18].

The possible phase diagrams of this model in the $r-g$ plane are shown in Figure 1.4. This model has a bicritical point at $r = g = 0$ if $4u_1u_2 < u_{12}^2$, and a tetracritical point if this inequality is reversed. There is a second order transition into the phase where $\langle\phi_1\rangle \neq 0$ at

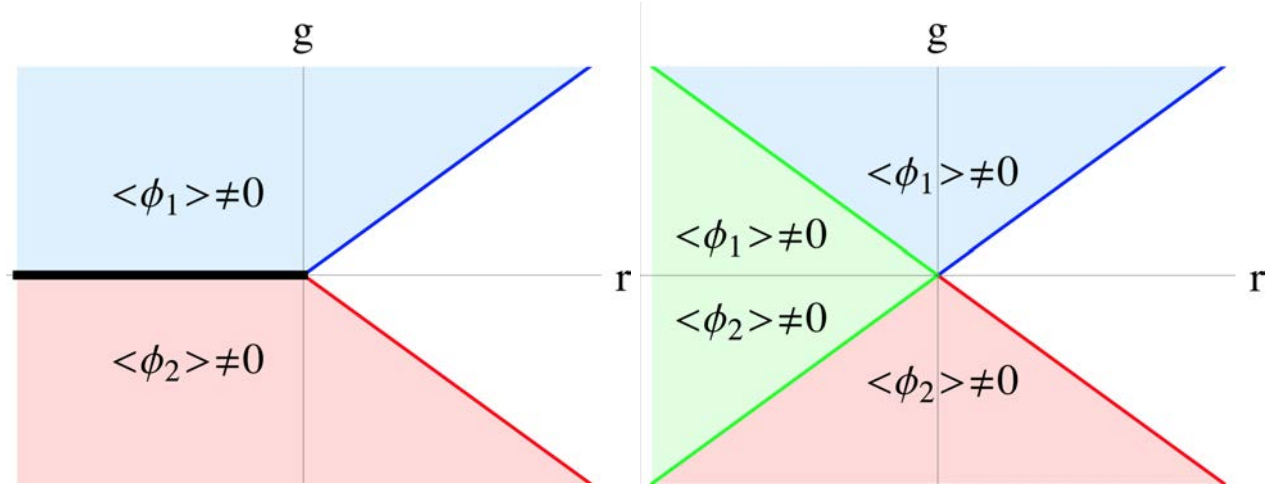

(a) Phase diagram with a bicritical point. Here, $u_{12}^2 > 4u_1u_2$.

(b) Phase diagram with a tetracritical point. Here, $u_{12}^2 < 4u_1u_2$.

Figure 1.4: Phase diagrams of equation (1.5.5) in the $r - g$ plane

$r = g$ when $g > 0$, and a second order transition into the phase where $\langle\phi_2\rangle \neq 0$ at $r = -g$ when $g < 0$. If $4u_1u_2 < u_{12}^2$ there is a first order transition between the two ordered phases along the line $g = 0$ when $r < 0$. If $4u_1u_2 > u_{12}^2$, when $r < 0$ there is a coexistence region where both $\langle\phi_1\rangle \neq 0$ and $\langle\phi_2\rangle \neq 0$, and all transitions on the phase diagram are second order.

When we come to discussing quantum phase transitions, we adapt Hertz-Millis theory which is known to only be valid on the disordered side of the phase transition. For this reason we do not offer an in-depth analysis of the evolution of the order parameters in the ordered phases.

A Ginzburg-Landau theory of such a multicritical point can be found by taking into account the spatial fluctuations of the order parameter, as

$$\begin{aligned} f(\phi_1, \phi_2) = &\int d\boldsymbol{q} \left(r - g + c_1 q^2\right) \phi_1^2(\boldsymbol{q}) + \int d\boldsymbol{q} \left(r + g + c_2 q^2\right) \phi_2^2(\boldsymbol{q}) \\ &+ \int d\boldsymbol{x} \left[u_1 \phi_1^4(\boldsymbol{x}) + u_2 \phi_2^4(\boldsymbol{x}) + u_{12} \phi_1^2(\boldsymbol{x}) \phi_2^2(\boldsymbol{x})\right], \end{aligned} \tag{1.5.6}$$

which we refer back to when deriving a model of quantum multicriticality.

We now discuss how this model has been analysed in the literature.

1.5.3 RG Analysis

In this section we discuss how the model of a multicritical point has been analysed using the renormalisation group in the literature. This will enable us to compare the results of the quantum multicritical model of Chapter 3 with the corresponding classical model. The Ginzburg-Landau theory of a multicritical point discussed in the previous section has been analysed under the renormalisation group analysis by Kosterlitz et al. [18]. In this section we summarise the results of their analysis, rather than focusing on the specific details of the calculation.

Just like in the Φ^4 theory of Section 1.3.2, the upper critical dimension of the model of a multicritical point is found to be 4. Above 4 dimensions the model flows to a stable, non-interacting fixed point.

Below the upper critical dimension, the model has a rather rich fixed-point structure. In $4-\epsilon$ dimensions 6 fixed points of the RG flow can be found, 4 with $u_{12}^* = 0$ and 2 with $u_{12}^* \neq 0$. The 4 fixed point with $u_{12}^* = 0$ can be analysed as two decoupled fixed points associated with ϕ_1 and ϕ_2 independently. They are classified as tetracritical points since $(u_{12}^*)^2 < 4u_1^* u_2^*$. They are all unstable with respect to perturbations of u_{12}, with the exception of one fixed point where the stability is dependent on the number of field components, but is unstable in physically relevant numbers of field components.

Of the two fixed points with $u_{12}^* \neq 0$, one can be associated with bicritical behaviour, and the other can be associated with tetracritical behaviour. Whether the bicritical or tetracritical interacting fixed point is stable depends on the number of field components. The renormalisation group eigenvalues around these fixed points can be used to find various critical exponents associated with classical multicriticality. For example the crossover exponent ϕ of equation (1.5.4) can be found to be greater than 1, and the susceptibility exponents can be found to order ϵ.

In summary, below the upper critical dimension there is a rich fixed point structure due to the three different interactions u_1, u_2 and u_{12}. However when we turn our attention to a

quantum multicritical point in Chapter 3, we analyse a model at or above its upper critical dimension and only flow to the non-interacting Gaussian fixed point. In contrast to classical multicriticality it is not the fixed point structure, but the dangerously irrelevant interactions which determine the physical effects of quantum multicriticality.

1.6 Metallic Systems

In this thesis we shall be investigating quantum phase transitions in itinerant magnetic systems, where we investigate magnetic phase transitions over a metallic background.

To deal with the metallic nature of the problem, we employ the standard Fermi liquid theory. The statement of Fermi liquid theory is roughly that despite all the complex interactions between electrons in a metal, the fundamental excitations can be treated as weakly interacting quasiparticles. This was original discussed by Landau [19], and has since become the standard approach to dealing with electrons in solids [20, 21].

If we consider a collection of electrons which do not interact with each other, the Pauli exclusion principle means that each will exist with a unique set of quantum numbers, and at zero temperature occupy all available energy states up to the Fermi energy. The basic idea behind Fermi liquid theory is that if we imagine 'adiabatically' turning on the interactions between the electrons, the fundamental excitations of the new system are no longer the bare electrons but instead fermionic quasiparticles which are assumed to smoothly evolve from the non-interacting states. The quantum numbers of these quasiparticle excitations are preserved, while the effective mass of the quasiparticles and their description in terms of the bare electrons can change quite dramatically. This means that the idea of a Fermi surface is preserved even in the presence of strong interactions.

This Fermi liquid approach can be used to find physical properties of systems. For example the temperature dependence of the specific heat of a Fermi liquid is linear, $C \sim T$, which can be shown for any system of particles obeying the Fermi distribution [21]. The resistivity of

a Fermi liquid at low temperatures can also be shown to obey $\rho(T) \sim \rho_0 + AT^2$ in $d = 3$ or $\rho(T) \sim \rho_0 + A \ln\left(\frac{1}{T}\right) T^2$ in $d = 2$ [1].

Since Fermi liquid theory has been found to hold for a wide range of metallic systems with a variety of different interaction strengths, situations where deviations from Fermi liquid behaviour are observed are of inherent interest [1]. Quantum phase transitions in metallic systems are one such situation where deviations from Fermi liquid behaviour are observed. We discuss these deviations in the next chapter.

Chapter 2

QUANTUM PHASE TRANSITIONS

As discussed in the previous chapter, the aim of this thesis is to investigate quantum multicritical points. In the previous chapter we reviewed the basics of phase transitions and the renormalisation group method, which can be used to analyse critical phenomena. We then reviewed the basics of bicritical and tetracritical points, and metallic systems. The previous chapter dealt exclusively with finite temperature behaviour, and we now turn our attention to zero temperature phase transitions. In addition to the techniques discussed in the previous chapter, an understanding of quantum phase transitions and the methods of analysing them is also required in order to build a model of a quantum multicritical point.

This chapter reviews the literature on aspects of quantum criticality which we require in subsequent chapters. We first discuss quantum phase transitions in general, before focusing on magnetic quantum phase transitions in metals. We discuss the scaling relations for the behaviour of systems near such a quantum critical point, and then discuss the Hertz-Millis model of quantum criticality. We discuss this in a significant amount of detail, as it is this model we adapt when building the model for a quantum multicritical point in Chapter 3. We offer an overview and a derivation of the Hertz-Millis model in Section 2.2, before presenting a renormalisation group analysis of it in Sections 2.3 and 2.4. We then discuss the problems with Hertz-Millis theory in Section 2.5. Following this we turn our attention to the literature on quantum critical points in the presence of multiple dynamical exponents in Section 2.6, as

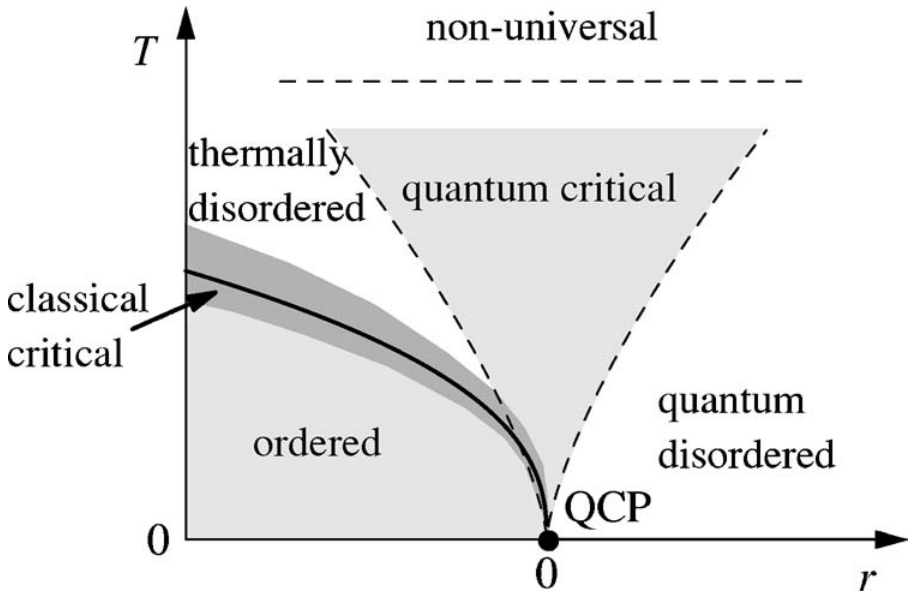

Figure 2.1: Schematic phase diagram of a material with a quantum critical point in the phase diagram, taken from Ref. [1]. The second order phase transition has been suppressed to zero under the application of a control parameter r.

we find it is necessary for the analysis of the quantum multicritical point in Chapter 3.

2.1 Basics of Quantum Criticality

2.1.1 General Quantum Criticality

As explored in the previous chapter, a lot of interesting physics can be observed in the vicinity of second order phase transitions in materials at finite temperatures, where the thermodynamic properties obey universal power-law behaviour dependent only on the symmetries of the system. Quantum critical systems are systems which are proximate to a second order phase transitions at zero temperature. They are also characterised by unconventional power-law properties in the vicinity of the phase transition, but the power laws are different from those associated with the corresponding finite-temperature transitions [1, 2]. One way of generating a quantum critical system is as follows. Suppose we have a material with a second order phase transition in it at a critical temperature T_c, and we choose to do something to

the system. We may, for example, consider physically squeezing the system and investigating its properties under pressure. In general we should expect the microscopic properties of the system, such as equilibrium inter-atomic spacing and magnetic interaction strengths between neighbouring atoms, to be different to the original properties of the system. This change of microscopic energy scales within the system in turn changes the critical temperature of the phase transition, which now becomes a function of pressure $T_c \rightarrow T_c(P)$. In many systems it is experimentally found that the transition temperature decreases under the application of pressure, and in some of these systems a pressure P^* can be experimentally reached such that the critical temperature of the transition is suppressed to absolute zero, $T_c\,(P^*) = 0$. This is shown in Figure 2.1.

While in the vicinity of finite temperature phase transitions the thermodynamic properties are dominated by thermal fluctuations of an order parameter, at zero temperature no thermal fluctuations are present. If we consider the system at zero temperature and tune through the critical pressure P^*, we go from an ordered phase to a disordered phase via a phase transition at absolute zero temperature. In this second order transition, it is quantum mechanical fluctuations of the order parameter which take the role of thermal fluctuations in finite temperature transitions and cause novel power laws to be observed in such systems.

One might argue that absolute zero temperature is never experimentally reachable, but just as the physics in the vicinity of a finite temperature phase transition is dominated by the order parameter fluctuations, the quantum critical point influences a wide region of the phase diagram. Effects of the quantum critical point can frequently be observed over a wide range of experimentally accessible temperatures. Above zero temperature, there is a whole quantum critical region where the physical properties are dominated by the interplay between quantum mechanical and thermal effects.

The argument presented above is not only valid for pressure, but any other possible tuning parameter. Another common parameter which is used is doping of the material with a particular element. Magnetic fields can also be used in some situations, but are known to lead to a

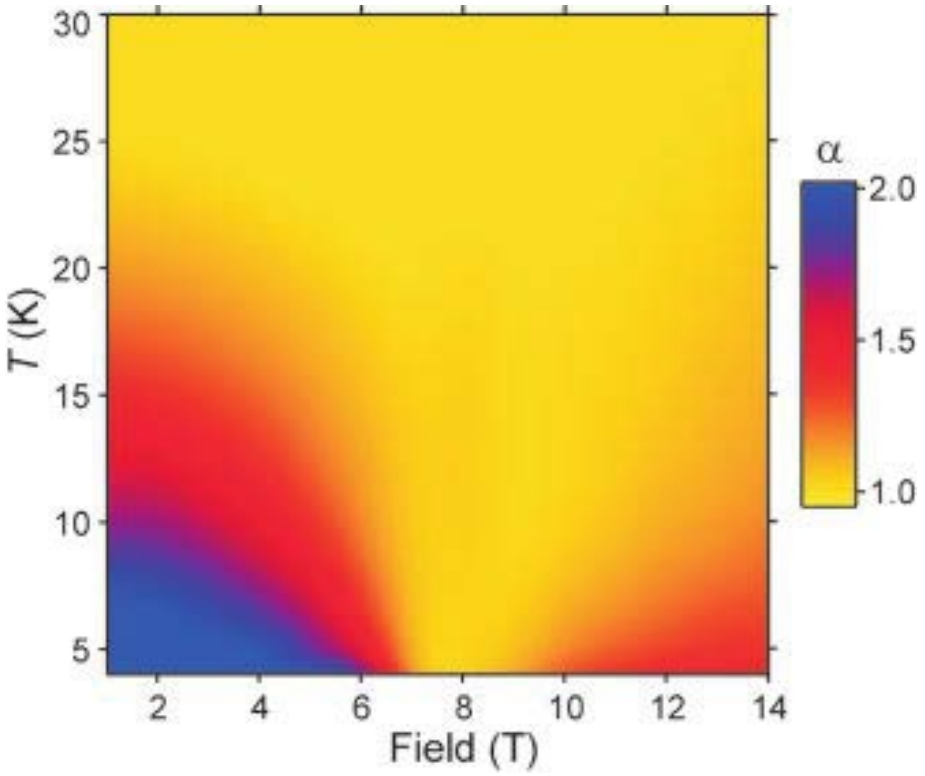

Figure 2.2: The effective resistivity exponent in $Sr_2Ru_3O_7$ calculated by fitting $\rho(T) = \rho_0 + AT^{\alpha}$), taken from Ref. [23]. $Sr_2Ru_3O_7$ has a metamagnetic quantum critical end-point tuned to by magnetic field, at $H = 7.8T$. An approximately linear resistivity is seen in the quantum critical region, and a T^2 resistivity in the Fermi liquid region outside of the 'V' shape.

variety of complications [22]. These complications will become important in Chapter 5 when we deal with metamagnetism, and we discuss these complications there. For the remainder of Chapter 2 and Chapter 3, unless explicitly stated, we do not consider magnetic fields as a tuning parameter for quantum criticality.

A typical experimental signature of a quantum critical point on the phase diagram is a 'V' shaped quantum critical region where the unusual critical exponents are observed. An example of a material where this is clearly seen is $Sr_2Ru_3O_7$, as shown in Figure 2.2. This can be understood by considering a characteristic energy scale in the system Δ, associated with the critical behaviour, which tends to zero at the quantum critical point. For example in second order phase transitions this may be the 'mass' of the order parameter fluctuations.

The origin of the 'V' shape is the crossover between the regimes $k_B T \lessgtr \Delta$. The quantum critical regime is the region within the 'V' shape, where $\Delta < k_B T$ [2]. The fluctuations have been made energetically cheap by the tuning parameter, and then become thermally excited in the quantum critical regime. These fluctuations lead to the observed unconventional power laws. The outside of the 'V' shape regime is commonly referred to as a 'quantum disordered' regime, and for the metallic systems considered in this thesis it is the Fermi liquid region.

A major difference between classical and quantum phase transitions is the role of the dynamical properties of the order parameter. When mathematically describing a quantum mechanical problem, a natural basis of states to work in is the set of eigenstates of the Hamiltonian. In the types of systems that exhibit quantum phase transitions however, the eigenstates of the Hamiltonian are not usually known. Moreover, often the underlying Hamiltonian of the system is not known. Instead we must use the only description we can, and discuss the physics near the transition in terms of an order parameter. In this thesis we shall be considering systems where the order parameter is a spatially dependent field ϕ, and the key quantity which allows us to calculate physical properties of systems is the partition function $\mathcal{Z}$, defined by

$$\mathcal{Z} = \mathrm{Tr} \exp\left(-\beta \hat{H}\right). \tag{2.1.1}$$

To represent the partition function in terms of the field ϕ, we must use Feynman's path integral formalism of quantum mechanics to write the partition function as

$$\mathcal{Z} = \int \mathcal{D}\phi\left(\boldsymbol{x}, \tau\right) \exp\left(-\beta S\left[\phi\right]\right), \tag{2.1.2}$$

where the action S is given by an integral over the Lagrangian

$$S = \int_0^\beta d\tau \int d\boldsymbol{x} \boldsymbol{\mathcal{L}}\left(\phi\right). \tag{2.1.3}$$

The integral over imaginary time τ arises due to the fact that the operator $\exp\left(-\beta \hat{H}\right)$ is the

same as the time-evolution operator in quantum mechanics, $\exp\left(-\frac{it}{\hbar}\hat{H}\right)$. The Lagrangian is dependent on τ in a non-trivial manner precisely because we are using a description in terms of states which are not eigenstates of the Hamiltonian.

We must now consider the order parameter as a function of both space and imaginary time - it is as if we have gained an extra dimension. The dependence of the action on imaginary time may not be the same as the spatial dependence of the action. This anisotropy can be characterised by the *dynamical exponent* z, which plays a crucial role in determining many physical properties of quantum critical systems [2, 1].

The importance of dynamical effects near a quantum phase transition also leads to another interpretation of the quantum critical regime observed at finite temperatures above the quantum critical point. The length of the imaginary time dimension L_τ is inversely proportional to temperature $L_\tau \sim 1/k_B T$, and so for any finite temperature it is not infinite. When tuning to a quantum critical point at $r = 0$ the correlation length diverges as $\xi \sim r^{-\nu}$, and correspondingly the correlation 'time' (the correlation length along the imaginary time dimension) diverges as $\xi_\tau \sim \xi^z$. At finite temperatures above such a quantum critical point it becomes meaningful to compare the correlation length along the imaginary time dimension ξ_τ to the length of this dimension. The quantum critical region is the region where $\xi_\tau > L_\tau$, and the fluctuations are completely correlated along the imaginary time dimension. The crossover to the so-called 'quantum disordered' regime is when $\xi_\tau \sim L_\tau$, or equivalently $T \sim r^{\nu z}$ [1].

In most examples of quantum phase transitions, the behaviour is characterised by a single dynamical exponent. The aim of this thesis is to analyse quantum multicritical points, which are examples of situations where multiple dynamical exponents are important at the phase transition. We examine other examples of situations featuring multiple dynamical exponents in Section 2.6.

2.1.2 Quantum Critical Points in Metals

In this thesis we shall be dealing exclusively with quantum critical points in metallic systems. These systems have been the subject of much experimental and theoretical research for several decades.

The main interest in quantum phase transitions in metals stems from the unusual power-law behaviour of physical properties observed in their vicinity. Commonly near quantum critical points, the usual Fermi-liquid power laws such as those mentioned in Section 1.6 are observed to be broken. As mentioned in that section, since Fermi-liquid behaviour is applicable to a wide range of metallic systems, cases where deviations from this are observed are inherently interesting.

The theoretical results of Hertz and Millis [24, 25, 26] motivated significant experimental study into quantum criticality, which led to the discovery of many interesting phenomena in the vicinity of quantum critical points. For example, in many systems around the quantum critical point superconductivity is observed [1]. It has been suggested that the superconductivity around such quantum critical points may be mediated by the quantum critical magnetic fluctuations [27]. The physics of some systems in the vicinity of the quantum phase transition seems to be controlled by other somewhat exotic behaviour, such as heavy fermion physics, the Kondo effect, or more exotic variants such as Kondo breakdown effects [1, 28]. Because of this, driving systems to their quantum critical points is often used as an experimental strategy for searching for new, interesting physics. In order to understand the systems exhibiting such behaviour, an understanding of the quantum criticality within them seems necessary.

We restrict our attention to the critical behaviour itself in materials where the quantum criticality is due to magnetic fluctuations. Despite predicting behaviour that deviates from Fermi liquid power laws, we shall consider systems where the Fermi surface is well defined and the assumptions behind Fermi liquid theory hold.

We now turn our attention to the theoretical aspects of quantum criticality in itinerant magnets. We first review the general scaling analysis that can be performed on quantum

critical points. Following that we discuss the Hertz-Millis model of quantum criticality, which is a model to specifically describe the suppression of a second order magnetic phase transition to zero temperature.

2.2 Theory of Quantum Criticality

We now review the literature on the theoretical understanding of quantum critical points in metallic systems. We discuss this in a significant amount of detail, as in Chapter 3 we shall adapt the models and methods described in this chapter to describe and analyse a quantum multicritical point. We begin by reviewing the literature on how simple scaling arguments can be applied to quantum critical points, as we shall find we can make some amount of progress by performing such an analysis on a quantum multicritical point. We then turn our attention to the Hertz-Millis theory of quantum phase transitions, an analysis of which forms the bulk of this chapter. This is because the model of a quantum multicritical point we introduce in Chapter 3 is a direct adaptation of Hertz-Millis theory, and we analyse that model in a similar manner.

2.2.1 Scaling analysis

In this section we review the literature on applying the RG scaling approach described in Section 1.4.2 to quantum criticality. We follow the analysis of Zhu et al. [29], and aspects of the review by Löhneysen et al. [1]. Suppose that upon approaching a quantum critical point, the free energy density $f(r, T)$ can be described by two parameters. r is the non-thermal tuning parameter which tunes to the QCP at $r = 0$, and T is the temperature. This is different to classical criticality as we have now separated the temperature T from the parameter which tunes to criticality, r. In addition, $f(r, T)$ is now a $d + 1$ dimensional density, as it depends on the additional imaginary time dimension. At all lengths except $T = 0$, this dimension has finite length ($L_{\mathcal{T}} \sim 1/T$).

At a finite temperature phase transition the correlation length diverges as the phase transition is approached by changing temperature. The correlation length divergence is because close to the phase transition, fluctuations of the order parameter get energetically cheaper and cheaper. Small fluctuations have a large effect on the surrounding medium. Thus the correlation length gets larger, and is infinite at the phase transition. At a quantum phase transition, the correlation length diverges as $\xi \sim |r|^{-\nu}$ as a definition of ν. We assume that in the imaginary time direction there is a single diverging timescale $\xi_\mathcal{T}$ which diverges as the correlation length diverges, as $\xi_\mathcal{T} \sim \xi^z$ which defines z.

We now consider analysing this situation using the renormalisation group, assuming that the energy is a function of r and T alone, $f(r, T)$. We rescale our spatial co-ordinates by b, so that we measure distances using $\tilde{x} = x/b$. This means the new correlation length is $\tilde{\xi} = b^{-1}\xi$ and so we find that $\tilde{r} = rb^{1/\nu}$. The correlation time has also changed, as $\tilde{\xi_\mathcal{T}} = b^{-z}\xi_\mathcal{T}$. This also defines how the temperature must scale, because the length of the imaginary time direction is proportional to $1/T$. Since lengths in the imaginary time direction scale as b^{-z}, T must scale as $\tilde{T} = Tb^z$. When we rescale the free energy density, dimensional analysis requires that it must rescale as

$$f(r, T) = b^{-(d+z)} f(rb^{1/\nu}, Tb^z), \tag{2.2.1}$$

as we have the three spatial dimensions, plus the imaginary time dimension in which distances scale as b^z instead of just b.

Several things can be obtained from this relation. By choosing $b = \xi$, $b = r^{-\nu}$ and $b = T^{-1/z}$ we can find three equivalent expressions for the free energy,

$$f(r, T) = \begin{cases} \xi^{-(d+z)} \phi_1 \left(\frac{\xi_\mathcal{T}}{L_\mathcal{T}} \right), \\ |r|^{\nu(d+z)} \phi_2 \left(\frac{T}{r^{\nu z}} \right), \\ T^{(d+z)/z} \phi_3 \left(\frac{r}{T^{1/\nu z}} \right), \end{cases} \tag{2.2.2}$$

where the ϕ functions are scaling functions. We immediately notice the crossover $T \sim r^{\nu z}$ in the argument of these scaling functions, which we have already argued separates the quantum critical ($T > r^{\nu z}$) and Fermi liquid ($T < r^{\nu z}$) regions of the phase diagram. The free energy written in these forms can be expanded in each regime to determine the dominant contribution to physical properties. We now use these forms of the free energy to discuss some physical properties which are commonly measured near quantum critical points. Specifically, we look at the specific heat, thermal expansion and Grüneisen parameter.

In the quantum critical regime we see that

$$f(0,T) \sim T^{(d+z)/z}\left(\phi_3(0) + \frac{r}{T^{1/\nu z}}\phi_3'(0)\right), \tag{2.2.3}$$

and in the Fermi liquid regime we see that

$$f(r,0) \sim |r|^{\nu(d+z)}\left(\phi_2(0) + A\left(\frac{T}{r^{\nu z}}\right)^2\right). \tag{2.2.4}$$

Derivatives of these expressions give the leading order behaviour of the specific heat and thermal expansion in each regime. The specific heat can be found from

$$C = T\frac{\partial^2 f}{\partial T^2}. \tag{2.2.5}$$

In the quantum critical regime this yields

$$C \sim T^{d/z}, \tag{2.2.6}$$

whereas in the Fermi liquid regime we see that

$$C \sim T r^{\nu(d-z)}. \tag{2.2.7}$$

In order to calculate the thermal expansion, we assume the parameter r depends on the

applied pressure p. We also assume that r changes linearly with pressure, so that $\frac{dr}{dp}$ is a constant. In this case the thermal expansion is

$$\alpha = \frac{\partial^2 f}{\partial r \partial T}. \tag{2.2.8}$$

In the quantum critical regime this gives

$$\alpha \sim T^{[d-(1/\nu)]/z}, \tag{2.2.9}$$

and in the Fermi-liquid regime we see that

$$\alpha \sim r^{\nu(d-z)-1}T. \tag{2.2.10}$$

A parameter which is commonly investigated near quantum critical points is the Grüneisen parameter, which is the ratio of these two quantities, $\Gamma = \frac{\alpha}{C}$. In the quantum critical regime, this diverges as

$$\Gamma \sim -T^{-1/\nu z}, \tag{2.2.11}$$

where the coefficient is not universal. In the Fermi liquid regime the divergence is

$$\Gamma = -\frac{G_r}{V_m}\frac{1}{r}, \tag{2.2.12}$$

where V_m is the molar volume, and G_r is a universal coefficient, given by $G_r = \nu(d-z)$.

Of interest in quantum critical points where the magnetic field tunes through the critical point is the magnetic analogue of the Grüneisen parameter, defined by $\Gamma_H = -\frac{(\partial M/\partial T)_H}{c_H}$, where M is the magnetisation and c_H is the specific heat at constant field. In the Fermi liquid regime

this parameter is given by

$$\Gamma_H \sim -\frac{1}{h}, \tag{2.2.13}$$

where h is the deviation of the magnetic field from its critical value, $h = H - H_c$.

The Grüneisen parameter, or its magnetic analogue, diverges at the quantum critical point and also changes sign at the transition. This means it is a useful parameter to measure, as it enables the location of the QCP to be found in situations where there are no symmetry broken phases [30].

Of course, the scaling relation in equation (2.2.1) comes with the same caveats as the scaling relation in Section 1.4.2. Specifically, it relies upon the absence of dangerously irrelevant operators and is only valid below the upper critical dimension. In physically interesting cases, the Hertz-Millis model is a model above its upper critical dimension. In Section 2.4.4 we discuss a more thorough calculation for the Hertz-Millis model, and find logarithmic corrections to these results.

2.2.2 Overview of Hertz-Millis Theory

We now turn our attention to the Hertz-Millis theory of quantum phase transitions, which we shall adapt in Chapter 3 to describe a quantum multicritical point. For this reason, we review the literature on this model in a fair amount of detail. In this section we describe the model, and present a derivation of it in Section 2.3.2 which we adapt in Chapter 3. In Sections 2.3 and 2.4 we discuss how physical properties can be obtained from this model.

The theoretical understanding of quantum phase transitions in metallic magnets was pioneered by Hertz in Ref. [26] and later revised by Millis in Refs. [24, 25]. This work builds off of a long history of theoretical research into spin-fluctuations in itinerant magnets, such as the paramagnon theory of Moriya [31]. The so-called Hertz-Millis theory formulates the problem in terms of spin-fluctuations which become soft at the quantum critical point. The theory can

be written as the action

$$S = \frac{1}{\beta} \sum_{\omega_n} \int \frac{d^d q}{(2\pi)^d} \left(\delta + q^2 + \frac{|\omega_n|}{\Gamma(q)} \right) \phi(\boldsymbol{q}, \omega_n) \phi(-\boldsymbol{q}, -\omega_n) + u \int d\boldsymbol{x} d\tau \phi^4(\boldsymbol{x}, \tau), \quad (2.2.14)$$

where δ is a non-thermal tuning parameter which tunes through the transition at $\delta = 0$, and temperature enters this action as the length of the imaginary time dimension. This looks like the Ginzburg-Landau functional for classical phase transitions, but with an extra imaginary time direction which is written as a sum over bosonic Matsubara frequencies, $\omega_n = 2\pi n/\beta$. Here $\phi(\boldsymbol{q}, \omega_n)$ is the order-parameter field which can describe either ferromagnetic or antiferromagnetic order. In the case of antiferromagnetic order, $\boldsymbol{q}$ is the deviation from the antiferromagnetic ordering wavevector $\boldsymbol{Q}$. This action is written as a power series in ϕ, and the coefficients of each term are written as power series' in both $\boldsymbol{q}$ and $|\omega_n|$. Only even powers of ϕ and $\boldsymbol{q}$ appear in the action due to symmetry. The situation is different for frequency however, where a term $|\omega_n| / \Gamma(q)$ appears in the quadratic part of the action. Higher order terms in the expansion do exist, but are not written down because Hertz-Millis theory assumes they are not relevant in a renormalisation group sense. We shall revisit this statement when discussing the problems with Hertz-Millis theory in Section 2.5.

The term $|\omega_n| / \Gamma(q)$ arises in the action because the spin-fluctuations are damped by the background of itinerant electrons, which Hertz-Millis theory assumes play no other role in the critical behaviour. The function $\Gamma(q)$ depends on whether we are considering ferromagnetic or antiferromagnetic quantum criticality. In the case of a ferromagnet, $\Gamma(q) \sim q$, leading to a dynamical exponent $z = 3$. For an antiferromagnet, $\Gamma(q)$ is a constant, leading to $z = 2$. For both ferromagnetic and antiferromagnetic quantum critical points we see that $\Gamma(q) \sim q^{z-2}$. In equation (2.2.14), space and temperature have been rescaled such that the coefficient of q^2 is unity, and so that $\Gamma(q) = q^{z-2}$.

The reason the damping takes this form may be qualitatively understood as follows. If we consider a ferromagnet, $\phi(q)$ describes a spin-wave with a wavelength proportional to $1/q$

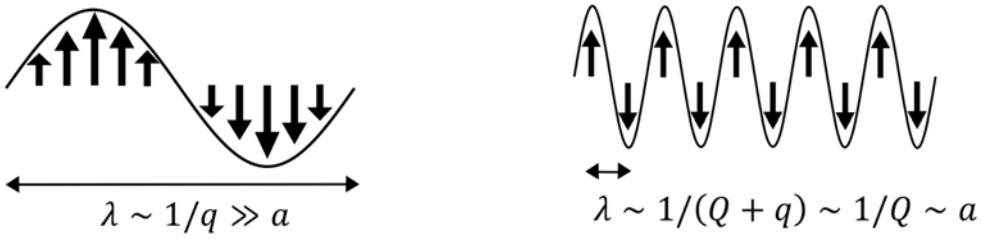

(a) A spin fluctuation near a ferromagnetic transition

(b) A spin fluctuation near an antiferromagnetic transition

Figure 2.3: Spin-fluctuations near ferromagnetic and antiferromagnetic transitions. λ is the wavelength of the fluctuation and a is the lattice spacing. The damping is explained in the main text.

as shown in Figure 2.3a. This can be damped by the background of electrons if an electron carries spin from a region of 'up' spins to a region of 'down' spins, which are separated by a distance proportional to the wavelength. If the electron travels ballistically at the Fermi velocity v_F, the time it takes to travel from a region of 'up' spins to a region of 'down' spins is proportional to $1/v_F q$. In the action the frequency is divided by the damping rate, leading to $|\omega|/q$. In an impure system the electrons would not travel ballistically, but diffuse due to repeated scattering from impurities. This means the time it takes to travel the same distance is proportional to $1/Dq^2$, which would lead to a dynamical exponent $z = 4$. For an antiferromagnet, $\phi(q)$ describes a spin-wave in the system with a wavelength $\boldsymbol{Q} + \boldsymbol{q}$, where $\boldsymbol{Q}$ is the antiferromagnetic ordering wave-vector. This is typically on the order of the inverse lattice spacing, as shown in Figure 2.3b. The distance an electron has to travel ballistically to get from a region of 'up' spins to a region of 'down' spins is proportional to $1/(\boldsymbol{Q} + \boldsymbol{q})$, which is approximately constant for $\boldsymbol{q}$ much smaller than $\boldsymbol{Q}$. Since the distance is constant, so is the scattering time and therefore the damping term is independent of $\boldsymbol{q}$.

The Hertz-Millis model of quantum critical points is only valid above the transition, in the disordered region of the phase diagram. This is because in an ordered phase the dynamics of order parameter fluctuations are different than above the transition [1].

The damping terms in the disordered phase are not just included because of the somewhat hand-wavy justification presented above. The Hertz-Millis action, including the damping

terms, can be derived from a microscopic model as we now show.

2.2.3 Derivation of the Hertz-Millis action

In this section we present a derivation of the Hertz-Millis action of equation (2.2.14). We include this derivation in this thesis because when we construct the model of a quantum multicritical point, we adapt the derivation of the Hertz-Millis action given in this section. Here we adapt the derivation given in Ref. [32].

The starting point is a system of electronic quasiparticles interacting with some arbitrary spin-spin interactions. We start with the Hamiltonian

$$H = \sum_{\mathbf{k}\sigma} c^{\dagger}_{\mathbf{k}\sigma} c_{\mathbf{k}\sigma} + \sum_{\mathbf{q}} J(\mathbf{q}) \mathbf{S}_{\mathbf{q}} . \mathbf{S}_{-\mathbf{q}}, \tag{2.2.15}$$

where $\mathbf{S}_{\mathbf{q}}$ is a spin-wave of momentum $\mathbf{q}$. This is given by

$$\vec{S}_q = \sum_{\mathbf{k}} \sum_{\alpha,\beta} c^{\dagger}_{\mathbf{k}+\mathbf{q},\alpha} \boldsymbol{\sigma}_{\alpha\beta} c_{\mathbf{k},\beta}, \tag{2.2.16}$$

where $\boldsymbol{\sigma}_{\alpha\beta}$ is the vector $\left(\sigma^x_{\alpha\beta}, \sigma^y_{\alpha\beta}, \sigma^z_{\alpha\beta}\right)$ where the σ^i are the Pauli matrices.

We tackle this Hamiltonian using the functional integral formulation of quantum field theory. We define fermionic fields by

$$c^{\dagger}_{\mathbf{k}\sigma} \to \bar{\psi}_{\mathbf{k},\sigma}(\tau) \qquad \text{and} \qquad c_{\mathbf{k}\sigma} \to \psi_{\mathbf{k},\sigma}(\tau),$$

where $\tau = it$ is imaginary time. The partition function for this system is

$$Z = \int \mathcal{D}\bar{\psi}\mathcal{D}\psi \exp\left[-S_0 - S_{\text{int}}\right]. \tag{2.2.17}$$

The non-interacting part of the action is given by

$$S_0 = \int_0^\beta d\tau \sum_{\mathbf{k}\mathbf{k}'} \sum_{\alpha,\beta} \bar{\psi}_{\mathbf{k}\alpha} \left[\mathcal{G}_0^{-1} \delta_{\alpha\beta} \delta(\mathbf{k} - \mathbf{k}') \right] \psi_{\mathbf{k}'\beta}, \tag{2.2.18}$$

where $\mathcal{G}_0$ is the free particle Green's function $\mathcal{G}_0 = (\partial_\tau + \epsilon_{\mathbf{k}} - \mu)^{-1}$. The interacting part of the action is given by

$$S_{\text{int}} = \int_0^\beta d\tau \sum_{\mathbf{q}} J_{\mathbf{q}} \mathbf{S}_{\mathbf{q}}(\tau) . \mathbf{S}_{-\mathbf{q}}(\tau), \tag{2.2.19}$$

where now

$$\mathbf{S}_{\mathbf{q}}(\tau) = \sum_{\mathbf{k}} \sum_{\alpha\beta} \bar{\psi}_{\mathbf{k}+\mathbf{q},\alpha}(\tau) \boldsymbol{\sigma}_{\alpha\beta} \psi_{\mathbf{k},\beta}(\tau). \tag{2.2.20}$$

The action is now quartic in the fermionic ψ field. In order to proceed we use the standard Hubbard-Statonovich transformation [11], and introduce a new bosonic vector field $\boldsymbol{\phi}_q(\tau)$ which couples to $\mathbf{S}_q$. This transformation ensures the action is now quadratic in the original ψ field, but includes an additional functional integral over the new $\boldsymbol{\phi}$ field. The mixed partition function is now

$$Z = \int \mathcal{D}\bar{\psi} \mathcal{D}\psi \mathcal{D}\boldsymbol{\phi} e^{-S\left(\bar{\psi},\psi,\boldsymbol{\phi}\right)}, \tag{2.2.21}$$

with

$$\begin{aligned} S\left(\bar{\psi},\psi,\boldsymbol{\phi}\right) = & \int_0^\beta d\tau \sum_{\mathbf{q}} \frac{1}{4J_{\mathbf{q}}} \boldsymbol{\phi}_{\mathbf{q}}(\tau) . \boldsymbol{\phi}_{-\mathbf{q}}(\tau) \\ & + \int_0^\beta d\tau \sum_{\mathbf{k}\mathbf{k}'} \sum_{\alpha\beta} \bar{\psi}_{\mathbf{k}\alpha}(\tau) \left[\mathcal{G}_0^{-1}(\mathbf{k}) \delta(\mathbf{k} - \mathbf{k}') \delta_{\alpha\beta} - i \boldsymbol{\sigma}_{\alpha\beta} . \boldsymbol{\phi}\left(\mathbf{k} - \mathbf{k}', \tau\right) \right] \psi_{\mathbf{k}'\beta}(\tau), \end{aligned} \tag{2.2.22}$$

where $\mathcal{G}_0$ is the free particle Green's function.

Since this action is quadratic in ψ, we may simply integrate out these fermionic fields to find the partition function exclusively in terms of the bosonic $\boldsymbol{\phi}$ fields. Using the properties of Gaussian integration, we find that

$$\mathcal{Z} = \int \mathcal{D}\boldsymbol{\phi} \exp\left[\mathrm{Tr} \ln\left(1 - i\mathcal{G}_0 V\right)\right]. \tag{2.2.23}$$

Using the notation $\zeta \equiv (\mathbf{k}, \omega_n)$ where ω_n is a Matsubara frequency

$$\mathcal{G}_0\left(\zeta, \zeta'; \alpha, \beta\right) = \mathcal{G}_0(\zeta)\delta(\zeta - \zeta')\delta_{\alpha\beta}, \tag{2.2.24}$$

and

$$V\left(\zeta, \zeta'; \alpha, \beta\right) \equiv \boldsymbol{\sigma}_{\alpha\beta}.\boldsymbol{\phi}\left(\zeta - \zeta'\right). \tag{2.2.25}$$

We proceed by performing an expansion of the logarithm in powers of $\boldsymbol{\phi}$. Only terms with even powers of $\boldsymbol{\phi}$ contribute, as the average of $\boldsymbol{\phi}$ is zero. This is because ϕ^z represents the difference between positions of the spin up and spin down Fermi surfaces in the z direction, and likewise for the other components [32]. Calculating the trace we find that second order term is

$$-\mathrm{Tr}\left(\mathcal{G}_0 V\right)^2 = 2\int d\zeta d\zeta' \mathcal{G}_0(\zeta')\mathcal{G}_0(\zeta' + \zeta)\boldsymbol{\phi}\left(\zeta\right).\boldsymbol{\phi}\left(-\zeta\right), \tag{2.2.26}$$

$$= -\int d\zeta \Pi\left(\zeta\right)\boldsymbol{\phi}\left(\zeta\right).\boldsymbol{\phi}\left(-\zeta\right). \tag{2.2.27}$$

Here, Π is the Lindhard function [11]. The spin labels α, β do not enter in the second order terms. We do not explicitly calculate the fourth order terms and assume that only the constant term is important, and that the momentum and frequency dependent corrections are irrelevant.

This leads to

$$S(\boldsymbol{\phi}) = \int d\zeta \left[\frac{1}{4J(\zeta)} + \Pi(\zeta)\right] \boldsymbol{\phi}(\zeta) . \boldsymbol{\phi}(-\zeta) + u \int d\mathbf{x} \sum_{\tau} \boldsymbol{\phi}^4(\mathbf{x}, \tau) + ... \tag{2.2.28}$$

We expand the function about $q = 0$ to investigate a ferromagnetic quantum critical point, or expand around $q = \boldsymbol{Q}$ to investigate the antiferromagnetic quantum critical point. Around $q = 0$ we find that

$$\begin{aligned} S(\boldsymbol{\phi}) =& \frac{1}{\beta} \sum_{\omega_n} \int \frac{d^d q}{(2\pi)^d} \left[r + \frac{q^2}{q_0^2} + \frac{|\omega_n|}{\Gamma q/q_0}\right] \boldsymbol{\phi}(q, \omega_n) . \boldsymbol{\phi}(-q, -\omega_n) \\ &+ u \int d\mathbf{x} d\tau \boldsymbol{\phi}^4(\mathbf{x}, \tau) + ... \end{aligned} \tag{2.2.29}$$

where here the q_0 is a constant on the order of k_F, and Γ is also a constant. r is the sum of the constant term in $1/J$ and the constant term in the Lindhard function. This is the parameter which can be tuned by adjusting the control parameter of the system. The quantum critical point occurs at $r = 0$.

Around an antiferromagnetic quantum critical point we expand around $q = \boldsymbol{Q}$, to find

$$\begin{aligned} S(\boldsymbol{\phi}) =& \frac{1}{\beta} \sum_{\omega_n} \int \frac{d^d q}{(2\pi)^d} \left[r + \frac{(\boldsymbol{q} + \boldsymbol{Q})^2}{q_0^2} + \frac{|\omega_n|}{\Gamma q/q_0}\right] \boldsymbol{\phi}(\boldsymbol{Q} + \boldsymbol{q}, \omega_n) . \boldsymbol{\phi}(-\boldsymbol{q} - \boldsymbol{Q}, -\omega_n) \\ &+ u \int d\mathbf{x} d\tau \boldsymbol{\phi}^4(\mathbf{x}, \tau) + ..., \end{aligned} \tag{2.2.30}$$

and we can shift the origin of $\boldsymbol{q}$ to write this as

$$\begin{aligned} S(\boldsymbol{\phi}) =& \frac{1}{\beta} \sum_{\omega_n} \int \frac{d^d q}{(2\pi)^d} \left[r + \frac{q^2}{q_0^2} + \frac{|\omega_n|}{\Gamma}\right] \boldsymbol{\phi}(q, \omega_n) . \boldsymbol{\phi}(-q, -\omega_n) \\ &+ u \int d\mathbf{x} d\tau \boldsymbol{\phi}^4(\mathbf{x}, \tau) + ... \end{aligned} \tag{2.2.31}$$

where we have used that to leading order $1/|\boldsymbol{Q} + \boldsymbol{q}|$ is a constant. This is the Hertz-Millis action for an antiferromagnetic quantum critical point.

In both cases we may rescale $q/q_0 \to q$ and $\omega_n/\Gamma \to \omega_n$ to arrive at

$$\begin{aligned} S(\boldsymbol{\phi}) =& \frac{1}{\beta}\sum_{\omega_n}\int \frac{d^d q}{(2\pi)^d}\left[r + q^2 + \frac{|\omega_n|}{q^{z-2}}\right]\boldsymbol{\phi}(q,\omega_n).\boldsymbol{\phi}(-q,-\omega_n) \\ &+ u\int d\mathbf{x}d\tau\boldsymbol{\phi}^4(\mathbf{x},\tau) + ... \end{aligned} \tag{2.2.32}$$

for $z = 2, 3$. In this thesis we shall use the notation $\Gamma(q) = q^{z-2}$.

This derivation of the Hertz-Millis action in equation (2.2.14) is adapted in Chapter 3 when we consider a quantum multicritical point.

2.3 Renormalisation Group Analysis of the Hertz-Millis Action

The renormalisation group approach can be applied to the Hertz-Millis action, and from such an analysis the distinct regions of the phase diagram can be identified. The power laws associated with the specific heat, thermal expansion and Grüneisen parameter can be found in each region. In the Chapter 3 we present a model of multicriticality which is based on Hertz-Millis theory. The calculation we perform there is an adaptation of the standard Hertz-Millis theory, and so we review the literature in some amount of detail.

In this section we summarise the results that can be obtained by performing a one-loop renormalisation group analysis on the Hertz-Millis action. For the most part we follow the analysis presented by Garst in Ref. [33], which has the same general approach as originally presented by Millis in Ref. [24], but solves the RG equations using better approximations.

In Section 2.3.1 we calculate the free energy using the linked cluster expansion, which will be the starting point for the RG analysis. The RG equations are derived from this in section 2.3.2. Following that, the RG equation for the interaction u is solved in Section 2.4.1, and we shall show that the physics is controlled by the non-interacting Gaussian fixed point in dimensions greater or equal to 2. The RG equations for the renormalised tuning parameters

are solved in Section 2.4.2, and from these solutions the regions of the phase diagram are identified in Section 2.4.3. In Section 2.4.4 the RG equation for the free energy is analysed and the thermodynamic properties are then found.

2.3.1 Linked Cluster Expansion

We now discuss the starting point of the renormalisation group analysis. The RG procedure outlined in Section 1.4 relies upon the existence of a high momentum cut-off which is systematically reduced. We therefore enforce a cut-off Λ on the momentum integrals. In the Hertz-Millis action, as well as a momentum cut-off a high frequency cut-off should also be enforced and systematically reduced.

As pointed out by Millis in Ref. [24], it is unclear how to mathematically smoothly reduce a cut-off on a discontinuous Matsubara sum. This complication can be avoided by calculating the free energy of the system, instead of performing renormalisation on the action directly. The idea is that in calculating the free energy, the Matsubara sums can be performed and the quantities can be written in terms of smooth integrals up to a cut-off.

This is possible as all Matsubara sums we need to do are functions of $|\omega_n|/q^{z-2}$. The modulus of ω_n appears in the Hertz-Millis action, as it is the low-frequency limit of the Lindhard function. In order to perform the Matsubara sums, we consider the full Lindhard function. The frequency-dependent part of this function is given by

$$\frac{i\omega_n}{\pi q^{z-2}} \ln\left[\frac{i\omega_n + q^{z-2}}{i\omega_n - q^{z-2}}\right] \sim \frac{|\omega_n|}{q^{z-2}}, \tag{2.3.1}$$

for $|\omega_n| \ll q^{z-2}$ [11].

The Matsubara sum can be performed using standard methods and converting it into a contour integral on the complex plane, but the analytic structure of the function $\frac{z}{X\pi}\ln\left[\frac{z+X}{z-X}\right]$ must be taken into consideration. This function has a branch cut on the real axis from $-X$ to X, so the Matsubara sum can be converted into a integral around this branch cut. This

naturally introduces the cut-off of q^{z-2} to the frequency integral. For ease of notation and consistency with the literature [33], we multiply q^{z-2} by a constant Ω. The result is that the cutoff of the momentum integral is Λ, whereas the cut-off on the frequency integral is $\Omega\Gamma(q)$, where $\Gamma(q) = q^{z-2}$. Of course the precise value of the cut-offs chosen in the calculation does not influence physical properties.

It turns out that the results of performing the renormalisation in this way are exactly the same as if we had not worried about this complication, and performed a diagrammatic expansion in terms of diagrams with external legs, similar to the analysis of Section 1.4.3. Such a calculation yields the same results as the method detailed here if the modes above the cut-off are integrated out correctly. We shall use this method in Chapter 5 where we consider a model of a metamagnetic quantum critical end-point interacting with an antiferromagnetic quantum critical point.

To derive the RG equations for the Hertz-Millis action, following the literature [26, 24, 33] we first calculate the free energy of the system using the linked cluster expansion [34], representing it as an infinite sum of diagrams in powers of the interaction term, u. Figures 2.4, 2.5 and 2.6 show the diagrams in this expansion to order u^2. The interaction u is drawn as a dotted line, as the field ϕ has n components, and u couples two pairs of modes. Each pair must have the same field component, but u can connect pairs with the same component, or different components.

We find that

$$F = F_G + un(n+2)I^2 - \frac{u^2}{2}\left[8n(n+2)^2 I^2 J + 8n(n+2)K\right], \tag{2.3.2}$$

where F_G is the Gaussian part of the free energy. This can be calculated as

$$F_G = \frac{n}{2}\frac{1}{\beta}\sum_{\omega_n}\int d\boldsymbol{q}\,\ln\left[\chi\left(q,\omega_n\right)\right], \tag{2.3.3}$$

$$= -\frac{n}{2}\int_0^{\Lambda}\frac{d^d q}{(2\pi)^d}\int_0^{\Omega\Gamma(q)}\frac{d\omega}{\pi}\coth\left(\frac{\omega}{2T}\right)\tan^{-1}\left(\frac{\omega/\Gamma\left(q\right)}{\delta+q^2}\right), \tag{2.3.4}$$

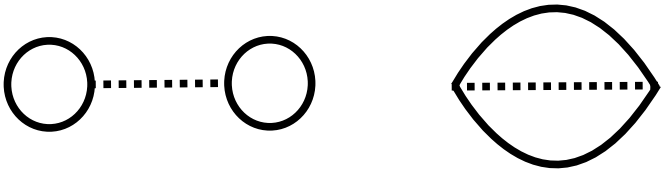

(a) (b)

Figure 2.4: Diagrams proportional to uI^2

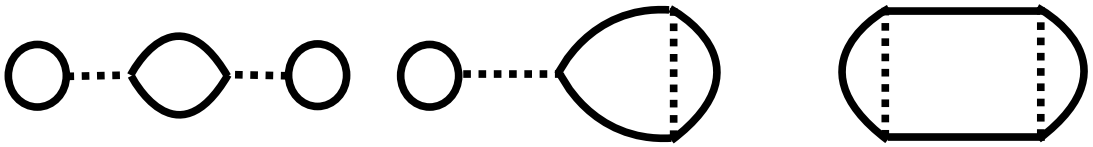

(a) (b) (c)

Figure 2.5: Diagrams proportional to u^2I^2J

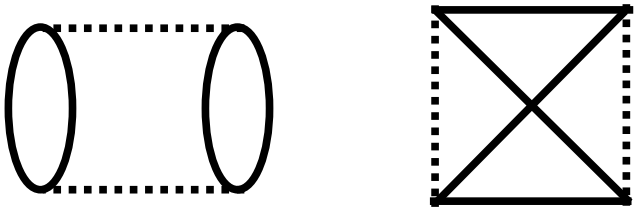

(a) (b)

Figure 2.6: Diagrams proportional to u^2K

where n is the number of field components [33]. Here

$$\chi^{-1}(q,\omega_n) = \delta + q^2 + \frac{|\omega_n|}{\Gamma(q)}. \tag{2.3.5}$$

The integrals I, J and K are the one-loop integrals

$$I = \frac{1}{\beta}\sum_n \int d\boldsymbol{q}\chi(\omega_n, q), \tag{2.3.6}$$

$$J = \frac{1}{\beta}\sum_n \int d\boldsymbol{q}\chi(\omega_n, q)\chi_0(-\omega_n, -q), \tag{2.3.7}$$

and

$$\begin{aligned} K = \frac{1}{\beta}\sum_{n_1,n_2,n_3,n_4} \int d\boldsymbol{q_1} d\boldsymbol{q_2} d\boldsymbol{q_3} d\boldsymbol{q_4} \chi(\omega_{n_1}, q_1)\chi(\omega_{n_2}, q_2) \\ \chi(\omega_{n_3}, q_3)\chi(\omega_{n_4}, q_4)\delta\left(\sum_{i=1}^4 \omega_{n_i}\right)\delta\left(\sum_{i=1}^4 \boldsymbol{q_i}\right). \end{aligned} \tag{2.3.8}$$

We have chosen to define J and K differently from the literature [24, 33], by a factor of -1.

The diagrams contributing to K are shown in Figure 2.6. As explained in Ref. [33], in the RG procedure that follows these diagrams end up renormalising the quartic interaction, u. The momentum-dependence of these integrals gives a momentum-dependent correction to u, which is irrelevant in the RG sense. The same momentum-independent renormalisation to u may be found by relaxing the constraints of the delta functions in equation (2.3.8) to only be between the momentum and frequency of two of the four modes. We may thus make the substitution $K = 6I^2J$ in the linked cluster expansion, where the corrections are irrelevant in the RG sense.

The linked cluster expansion can therefore be written as

$$F = F_G + un(n+2)I^2 - \frac{u^2}{2}\left[8n(n+2)(n+8)I^2J\right]. \tag{2.3.9}$$

Before we begin with renormalisation, we first perform the Matsubara sums to convert

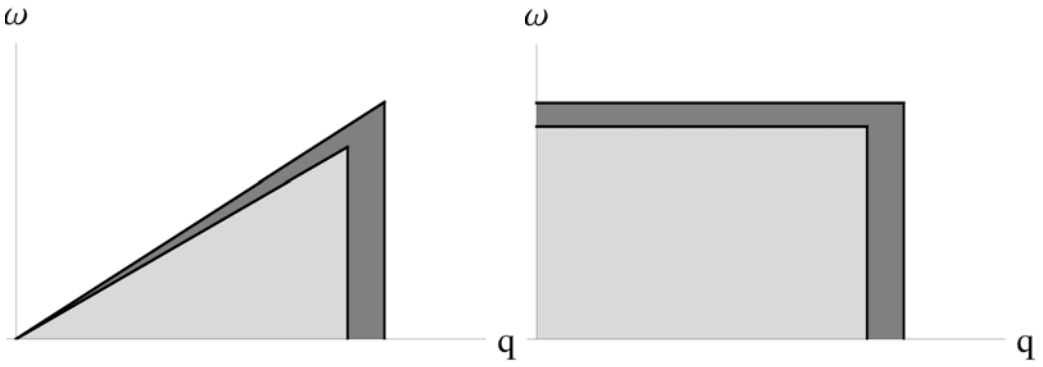

(a) Ferromagnet (b) Antiferromagnet

Figure 2.7: The reduction in cut-offs in the RG procedure for ferromagnetic and antiferromagnetic quantum critical points. The modes in the dark gray area are eliminated in each step of the RG procedure, leaving an effective model in terms of the modes in the light gray area.

these expressions into frequency integrals. We find that

$$I = \int_0^{\Lambda} \frac{d^d q}{(2\pi)^d} \int_0^{\Omega\Gamma(q)} \frac{d\omega}{\pi} \coth\left(\frac{\omega}{2T}\right) \frac{\omega/\Gamma(q)}{\left(\delta + q^2\right)^2 + \left(\omega/\Gamma\left(q\right)\right)^2} \tag{2.3.10}$$

and

$$J = \int_0^{\Lambda} \frac{d^d q}{(2\pi)^d} \int_0^{\Omega\Gamma(q)} \frac{d\omega}{\pi} \coth\left(\frac{\omega}{2T}\right) \frac{2\left(\delta + q^2\right)\omega/\Gamma\left(q\right)}{\left[\left(\delta + q^2\right)^2 + \left(\omega/\Gamma\left(q\right)\right)^2\right]^2}. \tag{2.3.11}$$

We are now in a position to derive the RG equations, which we do from equation (2.3.9).

2.3.2 Derivation of the Renormalisaion Group Equations

In this section we derive the RG equations, using the linked cluster expansion for the free energy in equation (2.3.9) as our starting point. We follow the same method as the literature [24, 33].

To derive the renormalisation group equations, we adopt a similar procedure as in Section 1.4.3 , and consider systematically integrating out high momentum modes, those with momentum between Λ/b and Λ, and considering the effective action for the low-momentum modes. The difference between the analysis of the classical model in Section 1.4.3 and the analysis

here is that when we rescale momentum we must also rescale frequency. In the integrals in equations (2.3.10) and (2.3.11), momentum is integrated up to a cut-off Λ and frequency is integrated up to a momentum-dependent cut-off $\Omega\Gamma(q)$. We must integrate out modes satisfying either $\Lambda/b \leq |\boldsymbol{q}| \leq \Lambda$ or $\Omega\Gamma(q)/b^2 \leq \omega \leq \Omega\Gamma(q)$. This is shown in Figure 2.7. Subsequently momentum is rescaled by a factor b and frequency by a factor b^z, and all other factors of b are absorbed into renormalised parameters.

The tree-level equations are derived by simply neglecting the modes above the reduced cut-off. We find that

$$T(b) = b^z T, \tag{2.3.12a}$$

$$\delta(b) = b^2 \delta, \tag{2.3.12b}$$

$$F_G(b) = b^{-(d+z)} F_G \tag{2.3.12c}$$

and

$$u(b) = b^{4-(d+z)} u. \tag{2.3.12d}$$

We use the notation that if a variable is written without explicit scale-dependence, we refer to its un-renormalised value, at $b = 1$. While this notation is not as clear as using a subscript, for example, we choose to do this to significantly simplify notation in Chapters 3, 4 and 5. From equation (2.3.12d) we see that in dimensions $d + z > 4$ the interaction term u is irrelevant, and scales to zero under renormalisation. The system can then be described by an effective Gaussian theory in terms of renormalised parameters. The free energy is then given simply by its Gaussian part in equation (2.3.4), and the thermodynamic properties of the system can be calculated as derivatives of this.

To calculate corrections to the tree-level equations, we let $F_G \to F_G^{<} + \frac{n}{2} f^{(0)} \ln b$, $I \to I^{<} + f^{(2)} \ln b$ and $J \to J^{<} + f^{(4)} \ln b$, where $I^{<}$ and $J^{<}$ are the integrals up the reduced cut-

offs, and the $f^{(0)}$, $f^{(2)}$ and $f^{(4)}$ functions are the integrals over the missing modes. There are two contributions, modes above the momentum cut-off and modes above the frequency cut-off. Explicitly

$$\begin{aligned} f^{(0)}(\delta,T) = -\frac{n}{2}\Lambda^{d-1}K_d \int_0^{\Omega\Gamma(\Lambda)} \frac{d\omega}{\pi} \coth\left(\frac{\omega}{2T}\right) \tan^{-1}\left(\frac{\omega/\Gamma(\Lambda)}{\delta+\Lambda^2}\right) \\ -\frac{n}{2}\int_0^{\Lambda} \frac{d^dq}{(2\pi)^d} \coth\left(\frac{\Omega q^{z-2}}{2T}\right) \tan^{-1}\left(\frac{\Omega}{\delta+q^2}\right), \end{aligned} \tag{2.3.13}$$

where K_d is the integral $\int \frac{d\Omega}{(2\pi)^d}$ over the surface of a d-dimensional sphere. We also find that

$$\begin{aligned} f^{(2)}(\delta,T) = \Lambda^{d-1}K_d \int_0^{\Omega\Gamma(\Lambda)} \frac{d\omega}{\pi} \coth\left(\frac{\omega}{2T}\right) \frac{\omega/\Gamma(\Lambda)}{(\delta+\Lambda^2)^2+(\omega/\Gamma(\Lambda))^2} \\ +\frac{1}{\pi}\int_0^{\Lambda} \frac{d^dq}{(2\pi)^d} \coth\left(\frac{\Omega q^{z-2}}{2T}\right) \frac{\Omega}{(\delta+q^2)^2+\Omega^2}, \end{aligned} \tag{2.3.14}$$

and

$$\begin{aligned} f^{(4)}(\delta,T) = \Lambda^{d-1}K_d \int_0^{\Omega\Gamma(\Lambda)} \frac{d\omega}{\pi} \coth\left(\frac{\omega}{2T}\right) \frac{2(\delta+\Lambda^2)\omega/\Gamma(\Lambda)}{\left[(\delta+\Lambda^2)^2+(\omega/\Gamma(\Lambda))^2\right]^2} \\ +\frac{2}{\pi}\int_0^{\Lambda} \frac{d^dq}{(2\pi)^d} \coth\left(\frac{\Omega q^{z-2}}{2T}\right) \frac{\Omega(\delta+q^2)}{\left[(\delta+q^2)^2+\Omega^2\right]^2}. \end{aligned} \tag{2.3.15}$$

We substitute this into the linked cluster expansion, equation (2.3.9), and neglect terms of order $(\ln b)^2$. We are then able to absorb some terms into the renormalisation of δ using the identity

$$I = \frac{2}{n}\frac{\partial F_G}{\partial \delta}, \tag{2.3.16}$$

and we absorb the other terms into a renormalisation of u. In the limit $b \to 1^+$ we find the RG equations

$$\frac{dF_G}{d\ln b} = (d+z)F_G - \frac{n}{2}f^{(0)}(\delta(b),T(b)), \tag{2.3.17a}$$

$$\frac{d\delta}{d\ln b} =2\delta(b) + 4(n+2)u(b)f^{(2)}\left(\delta(b), T(b)\right), \tag{2.3.17b}$$

and

$$\frac{du}{d\ln b} = \left[4-(d+z)\right]u(b) - 4(n+8)u^2(b)f^{(4)}\left(\delta(b), T(b)\right), \tag{2.3.17c}$$

where we have ignored terms of order u^2 in the equation for δ. These are the equations derived in Refs. [24, 33].

2.4 Solution of the Renormalisation Group Equations

We have now derived the RG equations, given in equations (2.3.17a), (2.3.17b) and (2.3.17c). The solution of these equations will allow us to find the regions of the phase diagram and the specific heat, thermal expansion and Grüneisen parameter in each region. These equations were first solved by Millis in Ref. [24], and were subsequently solved by Garst in Ref. [33] where more accurate approximations were made. We summarise the more accurate approach here.

We first solve equation (2.3.17c) in Section 2.4.1 to find the renormalised interaction, and hence the upper critical dimension of the theory. Then in Section 2.4.2 we solve equation (2.3.17b) for the renormalised tuning parameter, from which we are able to find the regions of the phase diagram which we present in Section 2.4.3. Finally in Section 2.4.4 we use equation (2.3.17a) to find the thermal expansion, specific heat, and Grüneisen parameter in each region of the phase diagram.

2.4.1 Interaction

We can solve equation (2.3.17c) to find the renormalised interaction term $u(b)$. In dimensions such that $d+z>4$, to leading order in u this parameter decays exponentially as $u(b) =$

$b^{4-(d+z)}u$, where we use that when u is written without explicit scale-dependence we mean the unrenormalised value $u \equiv u(b=1)$.

This is the case for both ferromagnetic and antiferromagnetic QCPs in $d=3$, and for a ferromagnetic QCP in $d=2$. The upper critical dimension of this theory is therefore $d_c^+ = 4-z$. The antiferromagnetic QCP in two spatial dimensions is the marginal case, where the model is at its upper critical dimension. In this case we adopt the assumption that $f^{(4)}(\delta, \mathcal{T})$ is a constant, $f^{(4)} \equiv f^{(4)}(0,0)$, and solve equation (2.3.17c) to show that

$$u(b) = \frac{1}{4(n+8)f^{(4)}} \frac{1}{\ln(gb)} \tag{2.4.1}$$

where $g = \exp\left[\frac{1}{4(n+8)f^{(4)}}\right]$. This still decays to zero, but much slower than the cases above the upper critical dimension.

The result of this is that since the interactions flow to zero in all cases of interest, the system can be described by an effective Gaussian model with a renormalised tuning parameter, which we obtain in Section 2.4.2 from the solution of equation (2.3.17b).

2.4.2 Tuning Parameter

In this section we solve equation (2.3.17b) to find the renormalised tuning parameter. Of physical interest here is the temperature-dependent correction to $\delta(b)$, which arises in the renormalisation group process from the dangerously irrelevant quartic interaction u. Even though this interaction term is irrelevant in the RG sense, it still ends up affecting some physical properties, such as the temperature-dependence of the correlation length. From the solution of this equation we calculate the correlation length, which for a Gaussian model is determined by the constant term in the inverse susceptibility.

The correlation length can be calculated from the renormalised tuning parameter, and from the correlation length the regions of the phase diagram can be found, as we demonstrate in

Section 2.4.3. The correlation length is given by

$$\xi^{-2} = \lim_{b\to\infty} \frac{\delta(b)}{b^2}, \tag{2.4.2}$$

where the division by b^2 converts the correlation length to the original unrenormalised units of length [33]. We find this technique works for $d + z > 4$, but in the marginal case we will use an adaptation of this to find the correlation length.

Adopting the notation of Garst [33], we define $\delta(b) = b^2 R(b)$, and integrate equation (2.3.17b) using an integrating factor to find that

$$R(b) = \delta + 4(n+2)\int_0^{\ln b} dx e^{-2x} u(e^x) f^{(2)}\left(e^{2x}R(e^x), T(e^x)\right), \tag{2.4.3}$$

which we write as $R(b) = \Delta(b) + R^{(T)}(b)$, where Δ is the zero-temperature part. Close to the transition the zero-temperature part is given by

$$\Delta(b) = \delta + 4(n+2)\int_0^{\ln b} dx e^{-2x} u(e^x) f^{(2)}\left(e^{2x}\Delta(e^x), 0\right). \tag{2.4.4}$$

The temperature-dependent part of the renormalised tuning parameter, $R^{(T)}$, is given by

$$R^{(T)}(b) = 4(n+2)\int_0^{\ln b} dx e^{-2x} u(e^x)\left[f^{(2)}\left(e^{2x}R(e^x), T(e^x)\right) - f^{(2)}\left(e^{2x}\Delta(e^x), 0\right)\right], \tag{2.4.5}$$

where we have ignored terms of order u^2 by subtracting $f^{(2)}\left(e^{2x}\Delta(e^x), 0\right)$ instead of $f^{(2)}\left(e^{2x}R(e^x), 0\right)$ in equation (2.4.5).

For $d + z > 4$, the term $\Delta(b)$ converges to the constant r in the limit $b \to \infty$, where

$$r = \delta \exp\left[\frac{4(n+2)f^{(4)}u}{4-d-z}\right] \tag{2.4.6}$$

and the QCP occurs at $r = 0$. In the marginal case of $d = z = 2$, Δ does not converge and

remains scale-dependent as

$$\Delta(b) \sim \frac{r}{[\ln(cb)]^{\frac{n+2}{n+8}}} \tag{2.4.7}$$

where c is a constant and r is proportional to δ. This scale-dependence of the zero-temperature part of the tuning parameter found by Garst [33] is missed in Millis' calculation [24], where less accurate approximations are made. Because of this, in $d = z = 2$ the correlation length is interpreted to be $\xi^{-2} = R(b^*)$ instead of the definition in equation (2.4.2), where b^* is defined by $\delta(b^*) = 1$.

We now turn out attention to the temperature-dependent part, $R^{(T)}(b)$. Above the upper critical dimension, the integral in equation (2.4.5) has different limits when $\lim_{b\to\infty} R(b) \lesseqgtr T^{2/z}$, which reduces to $r \lesseqgtr T^{2/z}$. The quantum critical regime is when $r < T^{2/z}$ and the Fermi liquid regime is when this inequality is reversed.

In the Fermi liquid regime $R^{(T)}$ has the usual T^2 Fermi liquid temperature dependence, whereas in the quantum critical regime the temperature dependence is more interesting. This integral has been analysed in the literature by Garst [33] in the limit $b \to \infty$, and the result depends on the dynamical exponent and number of spatial dimensions. The results have the same temperature dependence as originally discovered by Millis [24].

We summarise these results by looking at the correlation length in each regime. In the quantum critical regime ($r < T^{2/z}$) in $d = 3$, equation (2.4.5) can be shown to be

$$\xi^{-2} = r + 4(n+2)c_{d,z}^{(QC)} u T^{(d+z-2)/z}, \tag{2.4.8}$$

for $z = 2$ and $z = 3$. Here $c_{d,z}^{(QC)} = \frac{K_d}{z\cos\left(\frac{d-2}{2z}\pi\right)}\Gamma\left(1+\frac{d-2}{z}\right)\zeta\left(1+\frac{d-2}{z}\right)$, where $\Gamma(x)$ and $\zeta(x)$ are the gamma and zeta functions. The quantum critical regime is then further split into two regions, depending on whether the tuning parameter r or the temperature-dependent component dominate the correlation length.

In $d = 3$ in the Fermi liquid region ($r > T^{2/z}$), the correlation length is given by

$$\xi^{-2} = r + 4(n+2)c_{d,z}^{(FL)} u T^2 r^{(d-z-2)/2}, \tag{2.4.9}$$

which also turns out to hold in $d = 2$ when $z = 3$. In this equation $c_{d,z}^{(FL)} = \frac{\pi^2}{12} \frac{d-z}{\sin\left(\frac{d-z}{2}\pi\right)} K_d$.

For a ferromagnetic $z = 3$ QCP in $d = 2$, in the quantum critical regime ($r < T^{2/z}$), the correlation length is given by

$$\xi^{-2} = r + 2(n+2)K_2 u T \ln\left(\frac{1}{\xi^{-2} T^{-2/3}}\right), \tag{2.4.10}$$

which must be solved iteratively. We find that

$$\xi^{-2} = \begin{cases} r & \text{for } r > \frac{2}{3}(n+2)K_2 u T \ln\left(\frac{1}{T}\right), \\ \frac{2}{3}(n+2)K_2 u T \ln\left(\frac{1}{T}\right) & \text{for } r < \frac{2}{3}(n+2)K_2 u T \ln\left(\frac{1}{T}\right). \end{cases} \tag{2.4.11}$$

In the marginal case of $d = z = 2$, as explained above, the zero temperature component does not converge and the correlation length is evaluated at the scale b^* where $\delta(b^*) = 1$. Similarly, the crossover between the Fermi liquid and crossover regimes should be interpreted as $R(b^*) \sim T^{2/z}$, which leads to the definition of the quantum critical regime as $\frac{r}{\left[\ln\left(\frac{c}{r}\right)\right]^{\frac{n+2}{n+8}}} < T^{2/z}$ when $d = z = 2$.

In the limit $b \to \infty$ however, $R^{(T)}$ still converges and in the quantum critical regime is proportional to

$$R^{(T)} \sim uT \frac{\ln\left(\frac{T}{\xi^{-2}}\right)}{\ln\left(\frac{1}{\xi^{-2}}\right)}. \tag{2.4.12}$$

The correlation length is approximated using Δ evaluated at the scale b^*, but $R^{(T)}$ calculated

in the limit $b \to \infty$. This yields

$$\xi^{-2} \sim \begin{cases} \frac{\ln\left(\ln\left(\frac{1}{T}\right)\right)}{\ln\left(\frac{1}{T}\right)} & \text{for } \frac{\ln\left(\ln\left(\frac{1}{T}\right)\right)}{\ln\left(\frac{1}{T}\right)} > \frac{r}{\left(\ln\left(\frac{c}{r}\right)\right)^{\frac{n+2}{n+8}}}, \\ \frac{r}{\left(\ln\left(\frac{c}{r}\right)\right)^{\frac{n+2}{n+8}}} & \text{for } \frac{\ln\left(\ln\left(\frac{1}{T}\right)\right)}{\ln\left(\frac{1}{T}\right)} < \frac{r}{\left(\ln\left(\frac{c}{r}\right)\right)^{\frac{n+2}{n+8}}}. \end{cases} \tag{2.4.13}$$

In the Fermi-liquid regime the correlation length is given by

$$\xi^{-2} = \Delta + \frac{\pi^2}{6}\frac{n+2}{n+8}\frac{T^2}{\Delta \ln\left(\frac{c}{\Delta}\right)}, \tag{2.4.14}$$

where c is a constant, and $\Delta = r\left[\ln\frac{c}{r}\right]^{-\frac{n+2}{n+8}}$.

The reason for delving into such detail in this section is that when we construct a model of a quantum multicritical point in Section 3, we must solve equations very similar to these. We find that the integrals for the multicritical point can be written in terms of the integrals solved in this section.

We have now reviewed the literature on the solution of the RG equation for tuning parameter and the interactions. In the next section we demonstrate how these can be used to determine the phase diagram.

2.4.3 Phase Diagram

By solving the RG equation (2.3.17b) for the renormalised tuning parameter, we identified several crossovers in the disordered region of the phase diagram. Firstly, there is a quantum critical to Fermi liquid crossover, defined by $r \sim T^{2/z}$ if $d + z > 4$ and by $\frac{r}{\left[\ln\left(\frac{c}{r}\right)\right]^{\frac{n+2}{n+8}}} \sim T^{2/z}$ if $d + z = 4$. In Section 2.4.4 we shall find that the specific heat and thermal expansion have different values in each regime. The quantum critical region is then further divided into two regions depending on whether the correlation length is dominated by the tuning parameter r, or thermal effects.

Before turning our attention to thermodynamic quantities, we investigate the boundary

of the ordered phase on the phase diagram. In $d = 3$, long-range order is permitted, and at $T = 0$ there is an ordered phase for $r < 0$. At finite temperatures we would naively argue that the ordered phase is when the correlation length diverges, meaning the critical temperature of the transition would be

$$T_c^{(d+z-2)/z} = \frac{-r}{4(n+2)c_{d,z}^{(QC)}u}. \tag{2.4.15}$$

However, this argument is not quite correct [24]. When attempting to describe the transition into the ordered phase at finite temperatures, sufficiently close to the transition the system becomes correlated along the entirety of the imaginary-time axis. Therefore, only the $\omega_n = 0$ mode needs to be taken into account. This means that the system should be described by the corresponding classical model for the $\omega_n = 0$ mode. In this case, the effective quartic action is $v(b) = u(b)T(b)$. Since the corresponding classical theory is a model below its upper critical dimension $d_c^+ = 4$, sufficiently close to the transition mean field theory is not valid. Mean field theory breaks down when the Ginzburg criterion is violated at the Ginzburg temperature, as explained in Section 1.3.2.

The condition for the applicability of mean-field theory is that at the scale $\delta(b^*) = 1$, the effective quartic interaction for the $\omega_n = 0$ mode, $v(b^*)$, must be much less than 1 [33]. This translates to the condition $R^{(4-d)/2} \gg uT$, where $R = R(b^*)$. This leads to another crossover in the $r - T$ plane where the physics is not described by the Gaussian behaviour of Hertz-Millis theory. To find the Ginzburg temperature T_G we assume that $R(b^*)$ may be approximated as $R(\infty)$, and solve the equation

$$R^{(4-d)/2} = uT_G, \tag{2.4.16}$$

using the expression for R in the quantum critical regime. We note that R itself depends on

temperature in this region. In $d = 3$ the deviation from T_c is found to be

$$\frac{T_G - T_c}{T_c} = c_G u T_c^{1-1/z}, \tag{2.4.17}$$

where the constant of proportionality is $c_G = \frac{\frac{z^2}{1+z}\cos\left(\frac{\pi}{2z}\right)}{4(n+2)K_3\Gamma\left(1+\frac{1}{z}\right)\zeta\left(1+\frac{1}{z}\right)}$ [33].

In $d = 2$, the Mermin-Wagner theorem [35] tells us that no long-range order can exist, so there is no ordered phase on the phase diagram. Nevertheless, the Ginzburg criterion is still violated at some point, where the system cannot be described by Hertz-Millis theory and is characterised by non-Gaussian behaviour.

In $d = 2$, $z = 3$, the Ginzburg temperature is given by

$$r = uT_G \left[1 - 2(n+2)K_2 \ln\left(\frac{1}{uT_G^{1/3}}\right)\right], \tag{2.4.18}$$

and in the marginal case of $d = z = 2$, it is found to be [33]

$$r = -\frac{\pi}{n+8} T_G \left[\ln\left(\frac{c}{T_G}\right)\right]^{\frac{n+2}{n+8}-1} \left[(n+2)\ln\left(\ln\left(\frac{c}{T_G}\right)\right) - \pi\right], \tag{2.4.19}$$

which differs from Millis' original result [24] by a logarithmic factor, which can be traced back to the scale-dependence of $\Delta(b)$.

We have now described the regions in the phase diagram and the crossovers between them. Typical phase diagrams in both two and three dimensions are shown in Figure 2.8. We now find the physical properties in these regions of the phase diagram.

2.4.4 Thermodynamic Quantities

Since we have identified the various regions in the phase diagram in Section 2.4.3 and justified that the physics is described by an effective Gaussian model in Section 2.4.1, we now turn our attention to the thermodynamic quantities. Themodynamic quantities can be found by analysing the RG equation for the free energy, equation (2.3.17a). In the limit of large b, the

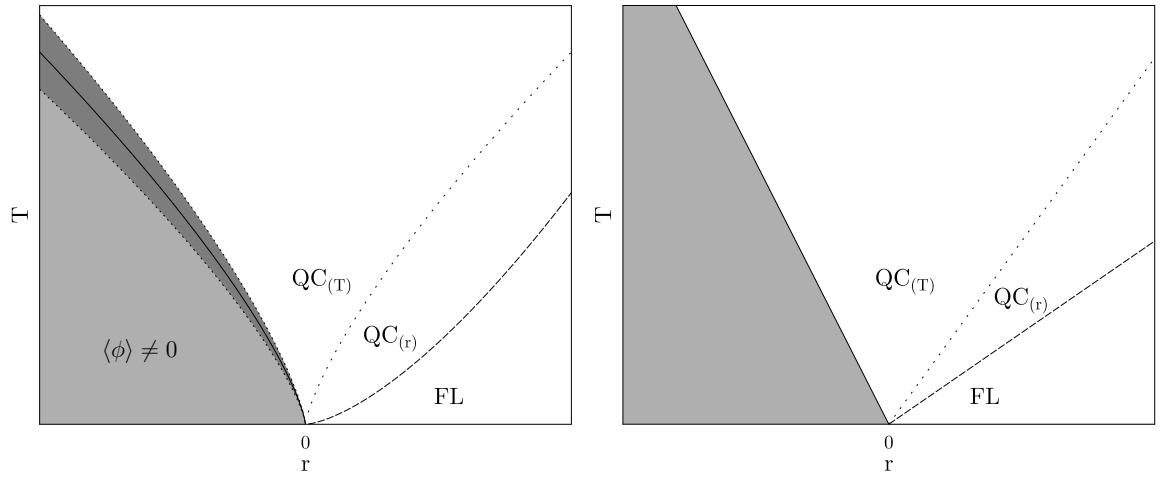

(a) $d = 3$ (b) $d = 2$

Figure 2.8: Phase diagrams in two and three spatial dimensions. The regions $\mathrm{QC}_{(T)}$ and $\mathrm{QC}_{(r)}$ are quantum critical regions where the correlation length is dominated by temperature and tuning parameter respectively. The region FL is the Fermi liquid region. In three dimensions the shaded area is the ordered phase, with the darker shaded region indicating where the Ginzburg criterion is violated. In two dimensions the shaded area is a disordered region not described by the Gaussian fixed-point of the RG flow. The crossovers between these regions are described in the main text.

free energy is given by

$$F = -\frac{n}{2}\int_0^\infty dx e^{-(d+z)x} f^{(0)}\left(R(e^x)e^{2x}, Te^{zx})\right), \tag{2.4.20}$$

and the specific heat and thermal expansion can be found as derivatives of this [33].

The specific heat can be calculated as $C = T\frac{\partial^2 F}{\partial T^2}$, leading to

$$C = T\frac{n}{2}\int_0^\infty dx e^{-(d+z)x}\frac{\partial^2}{\partial T^2} f^{(0)}\left(R(e^x)e^{2x}, Te^{zx})\right). \tag{2.4.21}$$

The thermal expansion α is the derivative of the free energy with respect to pressure and temperature, where we assume that only the parameter r depends on pressure, and the derivative $\frac{dr}{dp}$ is a constant. The functions $f^{(2)}$ and $f^{(0)}$ of equations (2.3.13) and (2.3.14) obey the relation $\frac{\partial}{\partial\delta} f^{(0)}(\delta, T) = f^{(2)}(\delta, T)$, which can be used to write the thermal expansion as

[33]

$$\alpha = \frac{n}{2}\int_0^\infty dx e^{(2-d-z)x}\frac{\partial R(e^x)}{\partial r}\frac{\partial}{\partial T}f^{(2)}\left(R(e^x), e^{2x}, Te^{zx}\right). \tag{2.4.22}$$

The results of these two calculations are again different in the quantum critical and Fermi liquid regimes, and depend on the number of spatial dimensions and the dynamical exponent. These integrals have been analysed in the literature, and the results are summarised in Table 2.1 which has been adapted from the literature [29]. Up to logarithmic corrections, these power laws agree with the results of scaling presented in Section 2.2.1. The coefficients of the power laws described in Table 2.1 have been calculated by Garst in Ref. [33], and we note that the thermal expansion is always proportional to

$$\alpha \sim \frac{\partial \xi^{-2}}{\partial p} \tag{2.4.23}$$

where p is the physical pressure. In the analysis presented here, this reduces to $\frac{\partial r}{\partial p}$ which we have assumed is an uninteresting constant. However, in Chapter 5 we examine a model where this coefficient is important and should not be neglected.

Another assumption made in Table 2.1 is that the correlation length $\xi^{-2} = r$ in the Fermi liquid regions. This is a fair assumption for the single quantum critical point considered here, as the temperature dependent correction is subleading, but in Sections 3.5 and 5.4.4 we shall need to replace r by ξ^{-2} to correctly describe the physical properties.

2.5 Problems with Hertz-Millis Theory

Despite the physical predictions of Hertz-Millis being observed in a large number of systems [1], there are problems with the Hertz-Millis theory which we briefly discuss here.

The assumption that we made in deriving the Hertz-Millis theory in Section 2.3.2 was that

	$d=3$ $z=3$	$d=3$ $z=2$	$d=2$ $z=3$	$d=2$ $z=2$
C_{QC}	$T\ln\left(\frac{1}{T}\right)$	$-T^{3/2}$	$T^{2/3}$	$T\ln\left(\frac{1}{T}\right)$
C_{FL}	$T\ln\left(\frac{1}{r}\right)$	$-Tr^{1/2}$	$Tr^{-1/2}$	$T\ln\left(\frac{1}{r}\right)$
α_{QC}	$T^{1/3}$	$T^{1/2}$	$\ln\left(\frac{1}{T}\right)$	$\ln\left(\ln\left(\frac{1}{T}\right)\right)$
α_{FL}	Tr^{-1}	$Tr^{-1/2}$	$Tr^{-3/2}$	Tr^{-1}
Γ_{QC}	$\frac{1}{T^{2/3}\ln\left(\frac{1}{T}\right)}$	$-T^{-1}$	$T^{-2/3}\ln\left(\frac{1}{T}\right)$	$\frac{\ln\left(\ln\left(\frac{1}{T}\right)\right)}{T\ln\left(\frac{1}{T}\right)}$
Γ_{FL}	$\frac{1}{r\ln\left(\frac{1}{r}\right)}$	$-r^{-1}$	r^{-1}	$\frac{1}{r\ln\left(\frac{1}{r}\right)}$

Table 2.1: Leading order contributions to the specific heat C, thermal expansion α and Grüneisen parameter Γ in the quantum critical (QC) and Fermi liquid (FL) regimes, from a quantum critical point in d dimensions with dynamical exponent z. This table is adapted from Ref. [29]. Note that the temperature-dependent component of the specific heat in $d=3$, $z=2$ is negative, but it is dominated by a temperature-independent positive constant.

we could completely integrate out the electronic degrees of freedom and describe the theory in terms of critical spin-fluctuations alone. However due to the Fermi surface, even at the quantum critical point there are zero-energy excitations (particle-hole pairs) which couple to the order parameter [2].

Mathematically, the problem resides in the step in the derivation where the electrons are integrated out and approximations are made about the Lindhard function. In a more careful analysis, it is found that higher order terms lead to non-analytic corrections to the Hertz-Millis action presented in equation (2.2.14). For example, in a clean three dimensional ferromagnet a term proportional to $q^2\ln\frac{1}{q}$ should enter the Gaussian part of the action [36], and in disordered systems a term proportional to $|q|$ arises [37]. In addition, the momentum dependence of the quartic interaction turns out to be $\ln\left(\frac{1}{q}\right)$ in clean systems and $1/q^3$ in disordered systems [1]. It is thought that these non-analytic corrections generically lead to the ferromagnetic transition in clean three dimensional systems becoming first order sufficiently close to where the QCP is expected to be [38].

A physical reason why these electronic modes complicate the situation is that they induce other timescales into the problem [1, 39]. For a ferromagnetic QCP, upon approaching the QCP the typical domain size is proportional to the correlation length of the order, ξ. As

explained in Section 2.2.1, the correlation length in the imaginary time direction is ξ^z with $z = 3$, which means that at $T = 0$ a typical timescale for order parameter fluctuations is ξ^3. However, an electron can travel ballistically through this region in a time proportional to ξ^1 in a clean system and ξ^2 in a disordered system. This additional timescale leads to a dangerously irrelevant variable missed by the usual Hertz-Millis approach [39].

In the case of a two dimensional antiferromagnet the assumption that the effective interaction terms are local, and that they may be expanded as a Taylor series in q, turns out to not be correct. When integrating out the fermionic degrees of freedom, the effective interactions gain strong non-local terms, which lead to an infinite number of marginal interactions [40]. It is then not sufficient just to consider the one marginal term considered in the analysis performed in this thesis.

Despite the shortcomings of the Hertz-Millis theory, it is believe that in three dimensions the physical predictions are broadly correct, with possible logarithmic corrections [1, 2]. However in two dimensions the problems are more severe [2].

For the rest of this thesis we shall work within the Hertz-Millis framework. In Chapter 3 we derive and solve a model of a quantum multicritical point using Hertz-Millis theory and sweep these complications under the carpet, until we discuss their relevance again in Section 3.6.2. In Chapter 5 we analyse another model for which these complications do not arise.

2.6 Multiple Dynamical Exponents

As explained in the introduction, the aim of this thesis is to investigate aspects of quantum multicritical points, where a material is susceptible towards both ferromagnetic and antiferromagnetic order. This is a situation where multiple dynamical exponents affect the RG flow. For this reason, in this section we review the literature on situations where a quantum critical point is described by multiple dynamical exponents. In Section 2.6.1 we review scaling analysis, and discuss its application to the physical case of a Pomeranchuk instability in Section

2.6.2.

2.6.1 Scaling Analysis

In this section, we review the literature on scaling analysis when a quantum phase transition is characterised by two dynamical exponents and a single tuning parameter. This scaling analysis builds from the analysis of Section 2.6.1, and in Chapter 3 we shall adapt this analysis to describe a quantum multicritical point.

We now consider a quantum critical point characterised by the dynamical exponents $z_>$ and $z_<$, and the tuning parameter, r. Here the two dynamical exponents are different, and $z_< < z_>$, and r is a non-thermal tuning parameter that tunes through the phase transition at $r = 0$ when $T = 0$. We follow the analysis presented in Ref. [41].

The free energy is assumed to split into the sum of two components, with different effective scaling dimensions $d + z_<$ and $d + z_>$, so that

$$F(r,T) = b_<^{-(d+z_<)} f_< \left(r b_<^{1/\nu}, \mathcal{T}_< b_<^{z_<}, \mathcal{T}_> b_<^{z_>} \right) + b_>^{-(d+z_>)} f_> \left(r b_>^{1/\nu}, \mathcal{T}_< b_>^{z_<}, \mathcal{T}_> b_>^{z_>} \right). \quad (2.6.1)$$

We have introduced two scaling parameters $b_>$ and $b_<$, which we may consider changing independently. Since the temperature scales according to the dynamical exponent, in the case of multiple dynamics there are two temperature scaling fields $\mathcal{T}_<$ and $\mathcal{T}_>$ which scale as indicated in the above equation. These are related to the actual temperature by $\mathcal{T}_< = \eta_< T$ and $\mathcal{T}_> = \eta_> T$, where $\eta_<$ and $\eta_>$ are known as kinetic coefficients. These appear in the model of a quantum multicritical point that we analyse in Chapter 3.

By choosing $b_< = b_> = |r|^{-\nu}$ this scaling relation can be used to show that

$$\begin{aligned} F(r,T) = |r|^{\nu(d+z_<)} f_< \left(\text{sign } r, \mathcal{T}_< |r|^{-\nu z_<}, \mathcal{T}_> |r|^{-\nu z_>} \right) \\ + |r|^{\nu(d+z_>)} f_> \left(\text{sign } r, \mathcal{T}_< |r|^{-\nu z_<}, \mathcal{T}_> |r|^{-\nu z_>} \right). \end{aligned} \quad (2.6.2)$$

At $T = 0$ we find that

$$F(r,T) = |r|^{\nu(d+z_<)} f_< \left(\text{sign } r, 0, 0\right), \tag{2.6.3}$$

which shows that at $T = 0$ upon approaching the QCP the term associated with the *lower* dynamical exponent dominates the free energy.

At finite temperatures, choosing $b_> = \mathcal{T}_>^{-1/z_>}$ and $b_< = \mathcal{T}_<^{-1/z_<}$, we find that

$$\begin{aligned} F(r,T) =& \mathcal{T}_<^{(d+z_<)/z_<} f_< \left(r\mathcal{T}_<^{-1/(\nu z_<)}, 1, \mathcal{T}_>\mathcal{T}_<^{-z_>/z_<}\right) \\ &+ \mathcal{T}_<^{(d+z_>)/z_>} f_> \left(r\mathcal{T}_>^{-1/(\nu z_>)}, \mathcal{T}_<\mathcal{T}_>^{-z_</z_>}, 1\right), \end{aligned} \tag{2.6.4}$$

which is unfortunately of limited use. Since the two scaling functions $f_<$ and $f_>$ in general depend on both temperature scaling fields, we cannot use these relations to investigate the physical properties as $r \to 0$ at finite temperature without knowing further information about the two scaling functions. A conclusion of Ref. [41] is that there are two possibilities for multiple dynamic scaling, coupled and decoupled. In the coupled case, the functions in equation (2.6.2) and (2.6.4) depend on all variables and these scaling functions cannot be simplified.

Decoupled multiple dynamic scaling is when the situation where the two scaling functions $f_<$ and $f_>$ *do not* depend on the other temperature field ($\mathcal{T}_>$ and $\mathcal{T}_<$ respectively). In this case, equations (2.6.2) and (2.6.4) become

$$\begin{aligned} F(r,T) =& |r|^{\nu(d+z_<)} f_< \left(\text{sign } r, \mathcal{T}_< |r|^{-\nu z_<}\right) \\ &+ |r|^{\nu(d+z_>)} f_> \left(\text{sign } r, \mathcal{T}_> |r|^{-\nu z_>}\right), \end{aligned} \tag{2.6.5}$$

and

$$\begin{aligned} F(r,T) =& \mathcal{T}_<^{(d+z_<)/z_<} f_< \left(r\mathcal{T}_<^{-1/(\nu z_<)}, \right) \\ &+ \mathcal{T}_<^{(d+z_>)/z_>} f_> \left(r\mathcal{T}_>^{-1/(\nu z_>)}\right). \end{aligned} \tag{2.6.6}$$

From the arguments of these functions we see there are two crossovers, $\mathcal{T}_< \sim r^{\nu z_<}$ and $\mathcal{T}_> \sim$

$r^{\nu z_>}$. We interpret these as the crossovers between the Fermi liquid and quantum critical regimes associated with each dynamical exponent.

We may use these scaling relations to find the specific heat and thermal expansion in each regime. In the quantum critical regime where $\mathcal{T}_< \gg r^{\nu z_<}$ and $\mathcal{T}_> \gg r^{\nu z_>}$, the specific heat and thermal expansion can be calculated from these equations as

$$C \sim c_> T^{d/z_>} + c_< T^{d/z_<}, \tag{2.6.7}$$

and

$$\alpha \sim a_> T^{[d-(1/\nu)]/z_>} + a_< T^{[d-(1/\nu)]/z_<}. \tag{2.6.8}$$

In these equations $c_>$, $c_<$, $a_>$ and $a_<$ are constants which the kinetic coefficients have been absorbed into. This shows that at low temperatures the mode with the greater dynamical exponent should dominate the specific heat, and the thermal expansion in dimensions $d > 1/\nu$.

In the Fermi liquid regime $\mathcal{T}_< \ll r^{\nu z_<}$ and $\mathcal{T}_> \ll r^{\nu z_>}$, the specific heat and thermal expansion are

$$C \sim c'_> |r|^{\nu(d-z_>)} T + c'_< |r|^{\nu(d-z_<)} T, \tag{2.6.9}$$

and

$$\alpha \sim a'_> |r|^{\nu(d-z_>)-1} T + a'_< |r|^{\nu(d-z_<)-1} T. \tag{2.6.10}$$

As $r \to 0$ the mode with the greater dynamical exponent dominates both the specific heat and the thermal expansion.

In the intermediate regime $\mathcal{T}_< < r^{\nu z_<}$ and $\mathcal{T}_> > r^{\nu z_>}$ the free energy is

$$\begin{aligned} F(r,T) =& \mathcal{T}_<^{(d+z_<)/z_<} f_< \left(r\mathcal{T}_<^{-1/(\nu z_<)}, \right) \\ &+ |r|^{\nu(d+z_>)} f_> \left(\text{sign } r, \mathcal{T}_> |r|^{-\nu z_>} \right). \end{aligned} \tag{2.6.11}$$

This leads to

$$C \sim c_> T^{d/z_>} + c'_< |r|^{\nu(d-z_<)} T, \tag{2.6.12}$$

and

$$\alpha \sim a_> T^{[d-(1/\nu)]/z_>} + a'_< |r|^{\nu(d-z_<)-1} T. \tag{2.6.13}$$

This analysis is adapted for a quantum multicritical point in Chapter 3, where we find it is described by a decoupled fixed point.

2.6.2 The Pomeranchuk Instability

This analysis has been applied to the Pomeranchuk instability in two dimensions, which is a situation where multiple dynamical exponents play a role in the quantum critical theory. The Pomeranchuk instability is an instability of the Fermi liquid to a symmetry-breaking deformation of the Fermi surface [42]. Two different polarisations of the order parameter have different dynamical exponents, characterised by $z = 3$ and $z = 2$ respectively. This scenario has been identified as exhibiting coupled multiple dynamic scaling [41, 43].

In two spatial dimensions, this has been investigated by Zacharias et al. [43] using the renormalisation group. In analysing this model using the renormalisation group, the authors developed a method of performing the renormalisation in the presence of multiple dynamical exponents. They show how it is possible to perform renormalisation by rescaling frequency by an arbitrary dynamical exponent z, which never needs to be specified in the RG analysis to

describe physical properties. The coefficients of the dynamic terms in the action, called the kinetic coefficients, are rescaled in the RG process. It is this technique which we shall adapt in Chapter 3 to enable a renormalisation group analysis of a quantum multicritical point. We explain it in more detail in Chapter 3 when we introduce the model of a quantum multicritical point.

In the case of a Pomeranchuk instability, it is found that the marginal $z = 2$ modes give logarithmic corrections to the correlation length. There are also two crossovers in the disordered region at $T \sim r^{3/2}$ and $T \sim r$, where r is the tuning parameter of the transition. The specific heat only changes at the crossover $T \sim r$, but the thermal expansion changes at both crossovers. The model was subsequently studied below its upper critical dimension by Meng et al. [41] who showed the model can be described by an interacting fixed point, and demonstrated the emergence of an effective dynamical exponent related to both $z = 2$ and $z = 3$.

In Chapter 3 we shall use similar techniques to those used to analyse the Pomeranchuk instability to investigate the quantum multicritical point, however there are some key differences. The main difference is that the Pomeranchuk instability is characterised by a single tuning parameter and a single correlation length, but two dynamical exponents. The model we present in Chapter 3 has two distinct order parameters, which means there are separate correlation lengths associated with each type of order. This means that in addition to two lengths in the imaginary time dimension, there are two physical lengths as well. Also of note is that the Pomeranchuk model is characterised by a single quartic interaction term, whereas the model of a quantum multicritical point in Chapter 3 requires 3 distinct quartic interactions.

These differences mean that while the method used to analyse the Pomeranchuk instability can be adapted to analyse a quantum multicritical point, the physics of the two systems turns out to be rather different.

2.7 Chapter Summary

In this chapter we have only scraped the surface of the vast literature on quantum criticality. The topic is so large and varied that we have only focussed on the aspects most relevant to the rest of this thesis, namely Hertz-Millis theory and situations with multiple dynamical exponents.

There are two specific aspects we have not mentioned in much detail at all here, as they are not necessary to follow the analysis of the quantum multicritical point in Chapter 3. Specifically, we have not touched upon transport properties near a quantum critical point. In Section 4.2, we review the literature which shows that transport properties can be found by considering electrons travelling through a quantum critical material scattering from spin-fluctuations and impurities. The resistivity depends upon the dynamical exponent of the transition, and is found to be proportional to $T^{5/3}$ in ferromagnetic systems, T^2 in clean antiferromagnets and $T^{3/2}$ in impure antiferromagnets. Another subject we have not touched upon is the possibility of other situations where quantum criticality can occur besides suppressing a second order phase transition to zero temperature. Quantum criticality can also be observed when the end-point of a line of first order transitions is suppressed to absolute zero. We review the literature on this topic in Chapter 5, where we analyse a metamagnetic quantum critical end-point interacting with an antiferromagnetic quantum critical point.

We have now reviewed the relevant literature on Hertz-Millis theory, and quantum criticality with multiple dynamical exponents. In Chapter 3 we use the techniques discussed here to derive and solve a model of a quantum multicritical point.

Chapter 3

QUANTUM MULTICRITICAL POINTS

3.1 Introduction

In the previous chapter we discussed quantum phase transitions in metallic systems. We showed that the phase diagram and physical properties are controlled by the dynamical properties of the order parameter, characterised by the dynamical exponent z. In this chapter, which is the first chapter primarily composed of original work, we build and solve a model of a quantum multicritical point. Specifically, we consider suppressing a bicritical or tetracritical point to zero temperature. Since bicritical and tetracritical points are points where two ordered phases and a disordered phase meet on the phase diagram, a quantum critical version of these points would be influenced by the dynamical properties of both order parameters.

An example of a quantum multicritical point that requires a description involving two different dynamical exponents is a multicritical point between a ferromagnetically ordered and an antiferromagnetically ordered phase, as these orders are described in Hertz-Millis theory by $z = 3$ and $z = 2$ respectively. We believe such multicritical points exist in nature, and we shall discuss the experimental evidence of multicriticality in Section 3.1.1.

Once we have highlighted the experimental relevance of quantum multicritical points, we begin building a quantum critical model for such a scenario. We first discuss generating the model in section 3.1.2. When then discuss general scaling arguments in Section 3.2, and derive

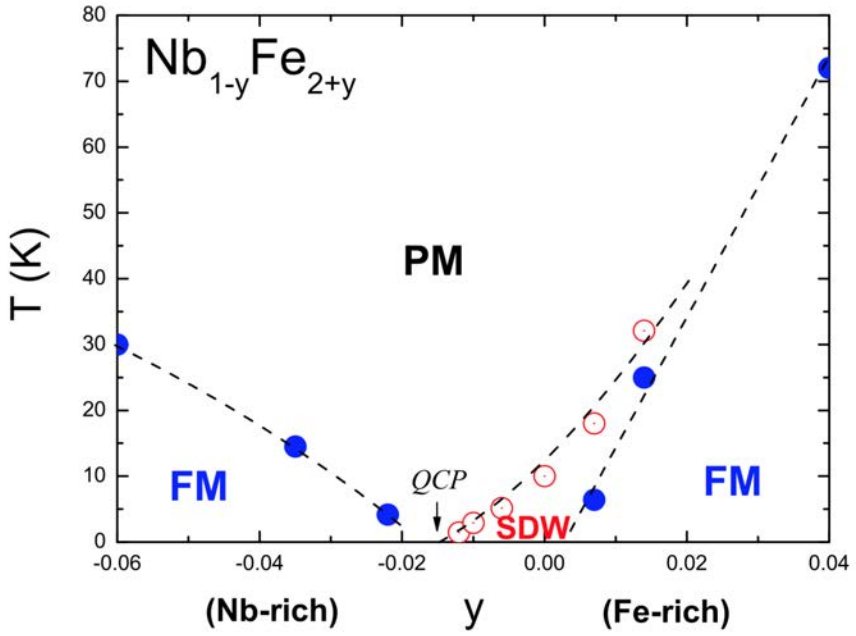

Figure 3.1: Phase diagram of $Nb_{1-y}Fe_{2+y}$, taken from Ref. [4]. At zero temperature this features two ferromagnetically ordered phases with an intermediate spin density wave state in between. The ferromagnetic and spin density state meet at a quantum multicritical point at $y \sim -0.015$.

and study a specific model of quantum multicriticality in Section 3.3. We adapt the methods of Chapter 2 to study the model using the renormalisation group, and find the phase diagram in Section 3.4 and the thermodynamic properties in Section 3.5. We then conclude this chapter by comparing our results to the experiments that are mentioned in Section 3.1.1.

3.1.1 Experimental Evidence of Quantum Multicriticality

Before developing a model of a quantum multicritical point, we summarise properties of several materials which have been argued to display aspects of quantum multicriticality.

$Nb_{1-y}Fe_{2+y}$ is a material that arguably features a quantum multicritical point in the phase diagram, which is shown in Figure 3.1. At zero temperature, near $y \sim -0.015$ a ferromagnetic state and a spin density wave state meet on the phase diagram [4, 5]. The specific heat in $NbFe_2$ varies as $C \sim T \ln\left(\frac{1}{T}\right)$ which is characteristic of a three dimensional ferromagnetic ($z = 3$) QCP, whereas the resistivity varies as $\rho \sim T^{3/2}$ which is characteristic of a three

dimensional antiferromagnetic ($z = 2$) QCP [6, 7]. This would suggest that fluctuations of both ferromagnetic and antiferromagnetic order contribute to the thermodynamic properties.

Another material with remarkably similar properties is $Ta(Fe_{1-x}V_x)_2$, which also features a competition between ferromagnetism and spin density wave order. The specific heat and resistivity of this material when $x = 0.016$ obey the same power-law behaviours as in $NbFe_2$ [8].

Both $NbFe_2$ and $Ta(Fe_{1-x}V_x)_2$ have been argued to have high susceptibilities at both zero momentum and a finite momentum Q associated with the spin density wave order [8, 7]. In Section 3.3 we develop a model of this situation, and we believe the results of this chapter can explain the specific heat measurements. In Chapter 4 we also explain how the observed resistivity power-laws are expected near such multicritical points.

There are other materials which have been argued to exhibit some form of multicriticality, that we do not believe are described by the model we present in this chapter.

Quantum multicriticality has also been related to the material $YbRh_2Si_2$, as the specific heat and Grüneisen parameter obey power laws usually associated with two dimensional ferromagnetism, yet at low temperatures the order is antiferromagnetic [9]. However, it is thought that this material is not explainable within the Hertz-Millis picture. Hall effect measurements suggest some kind of unconventional quantum criticality, related to Fermi surface reconstruction at the transition [28]. We do not consider such effects in this thesis, and therefore do not attempt to explain the properties of this material.

Quantum bicriticality has been argued to play a role in YbAgGe, which has a bicritical point at a temperature $T \approx 0.3K$ and a magnetic field field $\mu_0 H \approx 4.5T$ [10]. The low-field phase is antiferromagnetic, but the order in the high-field phase is to our knowledge currently identified. The suspicion is that this bicritical point is a spin-flop transition, which is a transition between two antiferromagnetically ordered states, where the axis of antiferromagnetism flips and the spins tilt towards the field. In this material it is the magnetic field which tunes through the bicritical point. In this chapter we construct a model which is only valid in the absence of

magnetic fields, to avoid complications that arise in that situation. In Chapter 5 we consider finite magnetic fields, and defer a discussion of this material until then.

The rest of this chapter details a study into quantum multicriticality between ferromagnetism and antiferromagnetism.

3.1.2 Generating Quantum Multicritical Points

Before modelling a quantum multicritical point, we begin by describing how we expect such points to be generated.

We consider a material with a finite temperature multicritical point in the $r-T$ plane, between two ordered phases associated with ferromagnetism ($\langle\phi_3\rangle \neq 0$) and antiferromagnetism ($\langle\phi_2\rangle \neq 0$). The subscripts 3 and 2 refer to the dynamical exponents that Hertz-Millis theory associates with each type of order. This scenario is shown in Figure 3.2. If we consider changing another non-thermal parameter, which we denote by g, the temperature this multicritical point occurs at could change. We may imagine that in some situations this multicritical point can be suppressed to absolute zero at a critical value $g = g^*$, which is the definition of a quantum multicritical point as shown in Figure 3.3a. We may imagine that increasing this parameter beyond g^* creates a phase diagram qualitatively similar to that shown in Figure 3.3b. This phase diagram looks like we have two quantum critical points in the phase diagram, which we expect will influence each other.

We now discuss discrepancies in notation between this chapter and Chapter 1. In Figure 1.3 we showed bicritical and tetracritical points in the $g-T$ plane. In Chapter 1, we used r to indicate the deviation from the critical temperature and g to describe the non-thermal tuning parameter. In Figure 3.2 we have the same phase diagram but in the $r-T$ plane. In this chapter, r describes the non-thermal control parameter which tunes through the multicritical point, and g is the parameter which tunes the multicritical point to zero temperature. Temperature enters our model of quantum multicriticality as the length of the imaginary time dimension. This discrepancy in notation is so that Chapter 1 is consistent with the literature

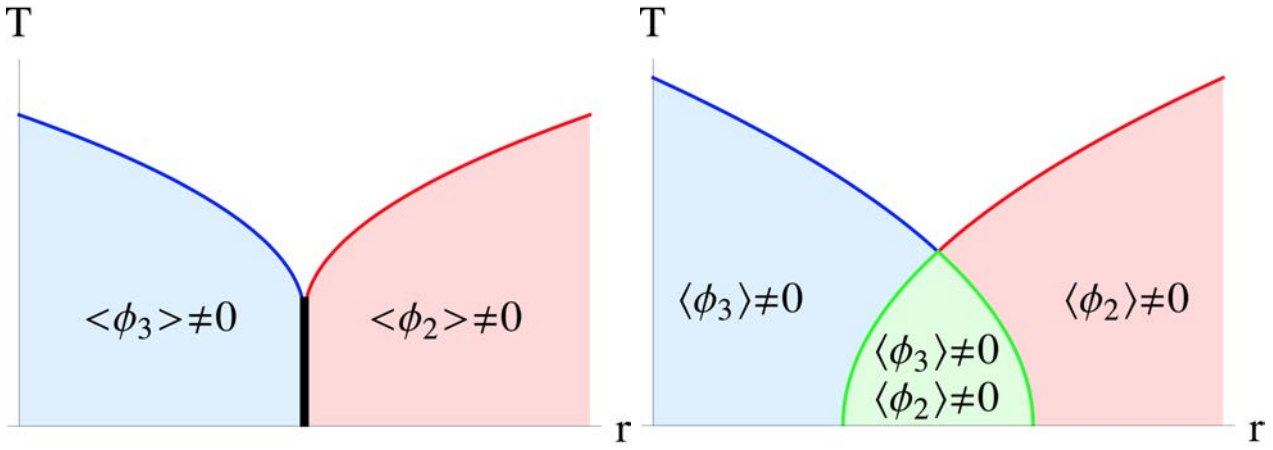

(a) Phase diagram with a bicritical point (b) Phase diagram with a tetracritical point

Figure 3.2: Finite temperature multicritical points

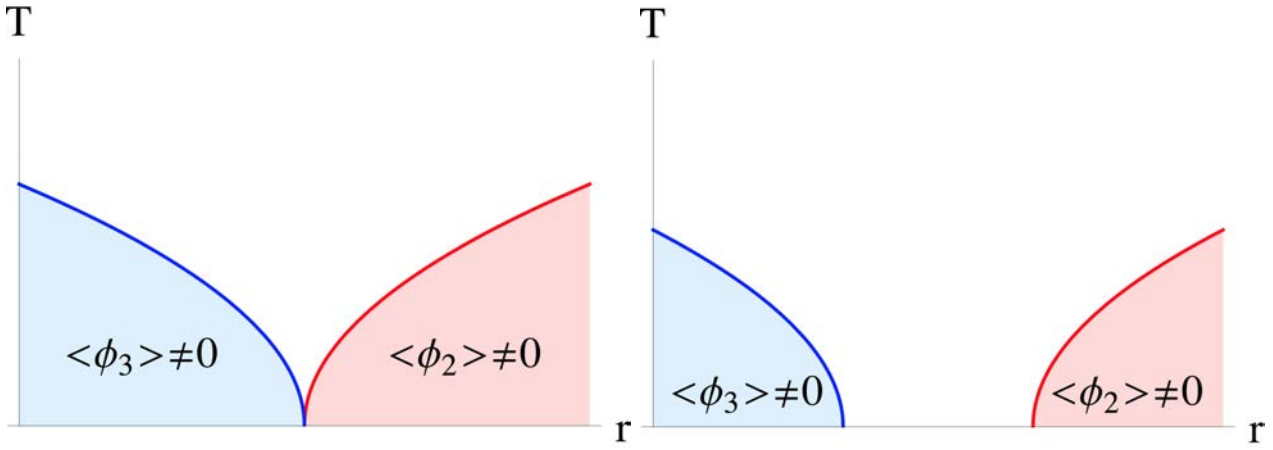

(a) Phase diagram with a quantum multicritical point (b) Phase diagram with two separated quantum critical points

Figure 3.3: Phase diagrams that can be obtained by adjusting another non-thermal tuning parameter to the phase diagrams in Figure 3.2

on classical multicritical points, and this chapter is consistent with the literature on quantum phase transitions.

In the rest of the chapter we shall be investigating phase diagrams of the type in Figure 3.3 where the two types of order are ferromagnetism and antiferromagnetism. We shall find the distinct regions in the disordered phase and the thermodynamic properties. In doing so, we find out exactly how the two QCPs in Figure 3.3b affect each other, and find that the results of our calculation are independent of whether we consider suppressing a bicritical or a tetracritical point to zero temperature.

3.2 Scaling Analysis for a Quantum Multicritical Point

We now begin the analysis of a quantum multicritical point. Before we write down a specific model, we first perform general scaling analysis for a quantum multicritical point. We adapt the arguments of Sections 2.6.1 and 1.5.1.

We begin by generalising equation (2.6.1) for a quantum multicritical point between two different types of order, each associated with a different dynamical exponent, $z_<$ and $z_>$. To tune to a quantum multicritical point we require two non-thermal tuning parameters $r_<$ and $r_>$, which tune to the quantum multicritical point at $r_> = r_< = 0$. There are now two correlation lengths in real space, corresponding to the fluctuations of each order parameter. These lead to two correlation lengths in the imaginary time dimension. In addition, there are two temperature scaling fields $\mathcal{T}_<$ and $\mathcal{T}_>$ as in Section 2.6.1. The free energy splits into the sum of the parts associated with each dynamical exponent, as

$$\begin{aligned} F\left(r_<, r_>, T\right) = b_>^{-(d+z_>)} f_> \left(r_< b_>^{1/\nu_<}, r_> b_>^{1/\nu_>}, \mathcal{T}_< b_>^{z_<}, \mathcal{T}_> b_>^{z_>}\right) \\ + b_<^{-(d+z_<)} f_< \left(r_< b_<^{1/\nu_<}, r_> b_<^{1/\nu_>}, \mathcal{T}_< b_<^{z_<}, \mathcal{T}_> b_<^{z_>}\right). \end{aligned} \tag{3.2.1}$$

For generality we have allowed the correlation length exponents $\nu_<$ and $\nu_>$ to be different for the two types of order. We use the notation that $z_> > z_<$, and the exponent $\nu_>$ is associated

with the order with the dynamical exponent $z_>$.

Because this energy depends on so many variables, it becomes difficult to analyse without knowing the scaling functions themselves. This model is even more complicated than the free energy in Section 2.6.1, and we are unable to make physical predictions about coupled multiple dynamic scaling.

We can make physical predictions in the special case of decoupled multiple dynamic scaling, where $f_>$ becomes independent of $\mathcal{T}_<$ and $r_<$, and vice-versa. We find that up to logarithmic corrections, this method correctly predicts the leading order physical properties and regions of the phase diagram. However, it does not capture the effects of multicriticality which we find in the full Hertz-Millis model of a quantum multicritical point. Specifically, it does not predict the boundaries of the ordered phases or the temperature-dependence of the correlation length.

The free energy in the case of decoupled multiple dynamic scaling is

$$F\left(r_<, r_>, T\right) = b_>^{-(d+z_>)} f_>\left(r_> b_>^{1/\nu_>}, \mathcal{T}_> b_>^{z_>}\right) + b_<^{-(d+z_<)} f_<\left(r_< b_<^{1/\nu_<}, \mathcal{T}_< b_<^{z_<}\right), \tag{3.2.2}$$

which is the sum of the free energies in two completely independent quantum critical points, of the type analysed in Section 2.2.1. In this case, the specific heat and thermal expansion are just the sum of the specific heat and thermal expansions for two independent quantum critical points.

The free energy above implies that there are now four possible regions of the phase diagram in the disordered phases, separated by the two crossovers $\mathcal{T}_< \sim r_<^{\nu_< z_<}$ and $\mathcal{T}_> \sim r_>^{\nu_> z_>}$. This is in contrast to the model in Section 2.2.1 where there were only three regions in the disordered phase.

The crossovers $\mathcal{T}_i \sim r_i^{\nu_i z_i}$ are interpreted as the crossovers when the modes associated with z_i change from the quantum critical region to becoming Fermi liquid-like. We label the regions of the phase diagram (a) through (d), and discuss the physical properties in each region.

In region (a), defined by $\mathcal{T}_> \gg r_>^{\nu_> z_>}$ and $\mathcal{T}_< \gg r_<^{\nu_< z_<}$, both types of mode are quantum

critical. The specific heat and thermal expansion are given by

$$C \sim c_> T^{d/z_>} + c_< T^{d/z_<}, \tag{3.2.3}$$

and

$$\alpha \sim a_> T^{[d-(1/\nu_>)]/z_>} + a_< T^{[d-(1/\nu_<)]/z_<} \tag{3.2.4}$$

where the $a_>$ and $a_<$ constants are not necessarily of the same sign, as the derivatives $\frac{dr_\leq}{dp}$ and $\frac{dr_>}{dp}$ may independently be positive or negative. These constants also contain the kinetic coefficients, in the same way as in Section 2.6.1. The specific heat is dominated by the higher dynamical exponent, whereas the thermal expansion depends on both $\nu_>$ and $\nu_<$ as well as the dynamical exponents. In situations where $\nu_> = \nu_<$, the higher dynamical exponent also dominates the thermal expansion.

In the remaining three regions of the phase diagram, there are two components contributing towards both the thermal expansion and specific heat, and neither contribution can be argued to vanish.

In region (b), defined by $\mathcal{T}_> \gg r_>^{\nu_> z_>}$ and $\mathcal{T}_< \ll r_<^{\nu_< z_<}$, the modes associated with $z_>$ are quantum critical and the modes associated with $z_<$ are Fermi liquid-like. The specific heat and thermal expansion are given by

$$C \sim c_> T^{d/z_>} + c'_< \left|r_<\right|^{\nu_<(d-z_<)} T, \tag{3.2.5}$$

and

$$\alpha \sim a_> T^{[d-(1/\nu_>)]/z_>} + a'_< \left|r_<\right|^{\nu_<(d-z_<)} T. \tag{3.2.6}$$

In region (c), defined by $\mathcal{T}_> \ll r_>^{\nu_> z_>}$ and $\mathcal{T}_< \gg r_<^{\nu_< z_<}$, the modes associated with $z_>$ are

Fermi liquid-like and the modes associated with $z_<$ are quantum critical. The specific heat and thermal expansion are given by

$$C \sim c'_> \left|r_>\right|^{\nu_>(d-z_>)} T + c_< T^{d/z_<}, \tag{3.2.7}$$

and

$$\alpha \sim a'_> \left|r_>\right|^{\nu_>(d-z_>)} T + a_< T^{[d-(1/\nu_<)]/z_<}. \tag{3.2.8}$$

In region (d), defined by $\mathcal{T}_> \ll r_>^{\nu_> z_>}$ and $\mathcal{T}_< \ll r_<^{\nu_< z_<}$, both types of mode are Fermi-liquid like. The specific heat and thermal expansion are given by

$$C \sim c'_> \left|r_>\right|^{\nu_>(d-z_>)} T + c'_< \left|r_<\right|^{\nu_<(d-z_<)} T, \tag{3.2.9}$$

and

$$\alpha \sim a'_> \left|r_>\right|^{\nu_>(d-z_>)} T + a'_< \left|r_<\right|^{\nu_<(d-z_<)} T. \tag{3.2.10}$$

We again note that these equations only hold if the modes decouple. When we reviewed the scaling analysis of classical multicriticality in Section 1.5.1, we were able to identify a crossover exponent which characterised the boundaries of the ordered phases. This is not possible to find for a quantum multicritical point via scaling, as in Hertz-Millis theory it is the temperature-dependence of the renormalised tuning parameter which governs the ordered phase boundary. As explored in Chapter 2, this is given by the dangerously irrelevant interactions.

The aim of the rest of this chapter is to use a specific model and perform a more thorough renormalisation group treatment in order to find the phase diagrams, and to determine whether these equations hold. As in the case of a single quantum critical point, we shall find that they do give the leading order contributions to specific heat and thermal expansion in each regime,

up to logarithmic corrections. However, the dangerously irrelevant interactions shape the phase diagram and give the renormalised tuning parameters their temperature-dependence.

3.3 Hertz-Millis Model of Multicriticality

To proceed further than the scaling arguments presented in Section 3.2, we now build a Hertz-Millis description of the quantum multicritical point discussed in Section 3.1.2. In Section 3.3.1 we derive the model by adapting the derivation of Hertz-Millis presented in Section 2.2.3 for a material unstable towards both ferro- and antiferromagnetic ordering. In order to analyse the regions of the phase diagrams and calculate thermodynamic properties we analyse the model using a renormalisation group procedure that is closely linked to the procedure used to analyse the Hertz-Millis model in Chapter 2.

3.3.1 Deriving the Model

In this section we derive the model that will be used for the rest of the chapter. By adapting the derivation of Section 2.2.3, we generate a model which describes a quantum multicritical point between a ferromagnetically ordered phase and an antiferromagnetically ordered phase.

We first assume that an action describing the physics in the vicinity of this multicritical point can be written in terms of spin-fluctuations alone, and that the electronic degrees of freedom can be safely integrated out. The starting point of the derivation is then the same Hamiltonian given by equation (2.2.15), but where the interaction term $J(q)$ is different. We follow the same steps as in Section 2.2.3, until we arrive at equation (2.2.28). We have

$$S\left(\boldsymbol{\phi}\right)=\int d\zeta\chi^{-1}\left(\zeta\right)\boldsymbol{\phi}\left(\zeta\right).\boldsymbol{\phi}\left(-\zeta\right)+u\int d\mathbf{x}d\tau\boldsymbol{\phi}^{4}\left(\mathbf{x},\tau\right), \tag{3.3.1}$$

with $\chi(\zeta)=\frac{1}{4J(\zeta)}+\Pi(\zeta)$, where $J(\zeta)$ is the spin-wave interaction and $\Pi(\zeta)$ is the Lindhard function. As before, $J(\zeta)$ is a complicated function that depends upon many microscopic

parameters. For a system unstable towards ordering at wave-vector $\boldsymbol{Q}$ (which may be zero) when a parameter δ is tuned to zero, the assumption made in the previous chapter is that the susceptibility can be expanded around this point as $\delta + \frac{1}{q_0^2}\left(\boldsymbol{q} - \boldsymbol{Q}\right)^2$, plus some damping terms which depend on whether $\boldsymbol{Q}$ is zero or non-zero. Such an expansion is only valid below certain frequency and momentum scales, and in Section 2.2 we enforced cut-offs on momentum and frequency integrals.

To derive an effective model for a material unstable to both ferro-and antiferromagnetic order, we assume that the susceptibility χ diverges in two distinct places, around $q = 0$ when $\delta_3 = 0$, and around $q = \boldsymbol{Q}$ when $\delta_2 = 0$. The subscripts 2 and 3 refer to the dynamical exponents that the spin-fluctuations around these points are damped by, according to Hertz-Millis theory.

We expand the inverse susceptibility χ^{-1} around these two points, letting

$$\chi^{-1}\left(q, i\omega_n\right) = \begin{cases} \chi_3^{-1}\left(q, i\omega_n\right) & \text{near } q = 0, \\ \chi_2^{-1}\left(q, i\omega_n\right) & \text{near } q = \boldsymbol{Q}. \end{cases} \tag{3.3.2}$$

The inverse susceptibilities are given by

$$\chi_3^{-1}\left(q, i\omega_n\right) = \delta_3 + c_3^2 q^2 + \eta_3 \frac{1}{c_3 q} \frac{|\omega_n|}{\Gamma_3} \text{ for } |c_3 q| < \Lambda_3, \tag{3.3.3}$$

and

$$\chi_2^{-1}\left(q, i\omega_n\right) = \delta_2 + c_2^2 q^2 + \eta_2 \frac{|\omega_n|}{\Gamma_2} \text{ for } |c_2 q| < \Lambda_2 \tag{3.3.4}$$

where, as an argument of χ_2^{-1}, $\boldsymbol{q}$ is the deviation from the ordering wave-vector $\boldsymbol{Q}$. We have explicitly written the coefficients of the dynamical terms as η_3 and η_2, which are known as the kinetic coefficients. By comparison with the literature described in Section 2.6.2, we expect that these must be allowed to rescale in order to perform renormalisation in the presence of

multiple dynamical exponents. Λ_2 and Λ_3 are the momentum cut-offs which we impose in our renormalisation group scheme. As in Chapter 2 our strategy will be to calculate the free energy using the linked cluster expansion and performing the Matsubara sums. There we shall find cut-offs in the continuous integrals. The cut-offs are

$$\eta_3 \frac{|\omega|}{c_3 q} < \Omega_3, \tag{3.3.5}$$

and

$$\eta_2 \frac{|\omega|}{\Gamma_2} < \Omega_2. \tag{3.3.6}$$

The momentum cut-offs give a concrete definition of momenta 'near' each ordering wavevector. This approximation for the inverse susceptibility is only possible if $\boldsymbol{Q}$ is sufficiently large, so that there is a clear separation between the two types of modes. The requirement is that

$$|\boldsymbol{Q}| - \frac{\Lambda_3}{c_3} > \frac{\Lambda_2}{c_2}. \tag{3.3.7}$$

This condition means that we do not consider long-wavelength spin density wave order.

Being careful about keeping track of coefficients, we find that if we rescale space and temperature such that $c_3 q \to q$ and $\frac{\omega}{\Gamma_3} \to \omega$, the Gaussian part of the action can be written as

$$S_G\left[\phi_3, \phi_2\right] = \frac{1}{\beta V}\left(\frac{\Gamma_3}{c_3^d}\right) \sum_{\omega_n, \boldsymbol{q}} \left(\chi_3^{-1} \phi_3^2 + \chi_2^{-1} \phi_2^2\right), \tag{3.3.8}$$

where

$$\chi_3^{-1}\left(q, i\omega_n\right) = \delta_3 + q^2 + \eta_3 \frac{|\omega_n|}{q} \text{ for } |q| < \Lambda_3, \tag{3.3.9}$$

and

$$\chi_2^{-1}(q, i\omega_n) = \delta_2 + q^2 + \eta_2 |\omega_n| \text{ for } |q| < \Lambda_2. \tag{3.3.10}$$

The ϕ_2 field has been rescaled by $\phi_2 \to \frac{c_3}{c_2}\phi_2$. We have also rescaled δ_2, and let $\eta_2 = \left(\frac{c_3}{c_2}\right)^2$, while $\eta_3 = 1$. We have let $\frac{c_3}{c_2}\Lambda_2 \to \Lambda_2$, but let Λ_3 stay unchanged. The cut-offs on the frequency integral that are derived when performing the Matsubara sum in these rescaled variables are

$$|\omega| < \Omega_3 \frac{|q|}{\eta_3}, \tag{3.3.11}$$

and

$$|\omega| < \Omega_2 \frac{1}{\eta_2}, \tag{3.3.12}$$

where we have rescaled $\Omega_2 \frac{\Gamma_2}{\Gamma_3} \to \Omega_2$.

We may now continue the expansion of the action in powers of the two fields, and write down the full action as

$$\begin{aligned} S[\phi_2, \phi_3] =& \frac{1}{\beta}\sum_{\omega_n}\int d\boldsymbol{q}\chi_3^{-1}(\boldsymbol{q}, \omega_n)\phi_3^2(\boldsymbol{q}, \omega_n) + \frac{1}{\beta}\sum_{\omega_n}\int d\boldsymbol{q}\chi_2^{-1}(\boldsymbol{q}, \omega_n)\phi_2^2(\boldsymbol{q}, \omega_n) \\ &+ \int d\boldsymbol{x}d\tau \left[u_3\phi_3^4(\boldsymbol{x}, \tau) + u_2\phi_2^4(\boldsymbol{x}, \tau) + u_{32}\phi_3^2(\boldsymbol{x}, \tau)\phi_2^2(\boldsymbol{x}, \tau)\right], \end{aligned} \tag{3.3.13}$$

where the quartic terms u_3, u_2 and and u_{32} are all different, and all positive.

We first note that this action looks like the action for two quantum critical points associated with ϕ_3 and ϕ_2 modes, but with an additional mode-mode coupling term proportional to u_{32}. Interpreting this model as describing two interacting quantum critical points turns out to be a useful way to think about the results of the renormalisation group analysis that is performed in the remainder of this chapter. It is also useful to realise that this model has a multicritical point in the zero-temperature plane, which may be either bicritical or tetracritical depending on the relations between the coefficients of the quartic parts in the action.

We also note that this model 'looks like' a quantum critical version of the free energy for a multicritical point described in Section 1.5.2. This is exactly what we would have written down if we had just tried to make a quantum critical version of the free energy in equation (1.5.6) by allowing the fields to vary in imaginary-time, and including the damping rates as prescribed by Hertz and Millis.

If we take into account the vectorial nature of the two order parameters, the quartic coupling written in equation (3.3.13) is $(\boldsymbol{\phi_3}.\boldsymbol{\phi_3})(\boldsymbol{\phi_2}.\boldsymbol{\phi_2})$. Another possible way these two vectors could interact is by a term proportional to $(\boldsymbol{\phi_3}.\boldsymbol{\phi_2})^2$. This term makes physical sense at it represents a suppression of antiferromagnetism in the same plane as any ferromagnetic order. However, neglecting such a term does not change, to leading order, any of the thermodynamic quantities we calculate. It does change some prefactors in the equations for the correlation lengths, but does not change the important temperature-dependence.

We now analyse this action using a similar RG procedure to the one applied in Section 2.3. This analysis enables us to find the regions of the phase diagram and the thermodynamic properties in each region. We first calculate the free energy using a linked cluster expansion in Section 3.3.2 which serves as the starting point of our RG scheme. In Section 3.3.3 we describe how we then reduce the cut-offs and derive the RG equations. The equations we derive are then solved in Section 3.4.

3.3.2 Free Energy Expansion

As in Chapter 2, a convenient starting point for the derivation of the RG equations is the free energy. To find the free energy we adapt the methods of Section 2.3.1 and perform a linked cluster expansion.

The first step is again to perform a linked cluster expansion for the free energy, which we calculate to quadratic order in the interaction terms. All the diagrams which contribute to

this expansion are shown in Appendix A. The diagrammatic sum leads to

$$\begin{aligned} F =& \tilde{F}_3^{(G)} + \tilde{F}_2^{(G)} + n_3(n_3+2)u_3\tilde{I_3}^2 + n_2(n_2+2)u_2\tilde{I_2}^2 + 2n_3n_2u_{32}\tilde{I_3}\tilde{I_2} \\ & - 4n_3(n_3+2)(n_3+8)u_3^2\tilde{I_3}^2\tilde{J_3} - 4n_2(n_2+2)(n_2+8)u_2^2\tilde{I_2}^2\tilde{J_2} \\ & - 4n_3n_2(n_3+2)u_{32}^2\tilde{I_3}^2\tilde{J_2} - 4n_3n_2(n_2+2)u_{32}^2\tilde{I_2}^2\tilde{J_3} \\ & - 8n_3n_2(n_3+2)u_3u_{32}\tilde{I_3}\tilde{I_2}\tilde{J_3} - 8n_3n_2(n_2+2)u_2u_{32}\tilde{I_3}\tilde{I_2}\tilde{J_2} - 8n_3n_2u_{32}^2\tilde{I_3}\tilde{I_2}\tilde{J_{32}}. \end{aligned} \tag{3.3.14}$$

Here, $\tilde{F}_i^{(G)}$ is the Gaussian part of the free energy associated with the ϕ_i modes, and is given by

$$\tilde{F}_i^{(G)} = \frac{n_i}{2}\frac{1}{\beta}\sum_{\omega_n}\int d\boldsymbol{q}\ln\left[\chi_i\left(q,\omega_n\right)\right]. \tag{3.3.15}$$

We have written this expansion in terms of the Matsubara sums

$$\tilde{I}_i = \frac{1}{\beta}\sum_n \int d\boldsymbol{q}\chi_i\left(\omega_n, q\right), \tag{3.3.16}$$

and

$$\tilde{J}_i = \frac{1}{\beta}\sum_n \int d\boldsymbol{q}\chi_i\left(\omega_n, q\right)\chi_i\left(-\omega_n, -q\right), \tag{3.3.17}$$

where $i = 2, 3$.

In deriving equation (3.3.14), we have adapted the analysis of Section 2.3.1 to deal with the term $\tilde{K_{ij}}$ given by

$$\begin{aligned} \tilde{K_{ij}} = \frac{1}{\beta^4}\sum_{n_1,n_2,n_3,n_4}\int & d\boldsymbol{q_1}d\boldsymbol{q_2}d\boldsymbol{q_3}d\boldsymbol{q_4}\chi_i\left(\omega_{n_1}, q_1\right)\chi_i\left(\omega_{n_2}, q_2\right) \\ & \chi_j\left(\omega_{n_3}, q_3\right)\chi_j\left(\omega_{n_4}, q_4\right)\delta\left(\sum_{i=l}^{4}\omega_{n_l}\right)\delta\left(\sum_{l=1}^{4}\boldsymbol{q}_l\right), \end{aligned} \tag{3.3.18}$$

where $i, j = 2, 3$. This arises from the diagrams in Figure A.3. Following the same arguments

as in Section 2.3.1, $\tilde{K_{33}}$ and $\tilde{K_{22}}$ can be reduced to $6\tilde{I_i}^2\tilde{J}_i$ by relaxing the δ function constraint to only enforce momentum and frequency conservation between two of the four possibilities. The corrections to this are irrelevant in the RG sense. The term $\tilde{K_{32}}$ needs more careful consideration, however.

Defining $\zeta \equiv (q, \omega_n)$, the δ functions in equation (3.3.18) can be written together as $\delta(\zeta_1 + \zeta_2 + \zeta_3 + \zeta_4)$. When we instead relax this constant to be $\delta(\zeta_1 + \zeta_2)$, we have $\tilde{K_{32}} \to \tilde{I_3}^2\tilde{J}_2$, and when this constant is $\delta(\zeta_3 + \zeta_4)$ we find $\tilde{K_{32}} \to \tilde{I_2}^2\tilde{J}_3$. For the other four options of choosing two of the four ζs as the argument for the δ function, one ζ will be an argument of χ_3 and the other will be an argument of χ_2. This leads to a term $\tilde{K_{32}} \to 4\tilde{I}_3\tilde{I}_2\tilde{J}_{32}$, where

$$\tilde{J_{32}} = \frac{1}{\beta}\sum_n \int d\boldsymbol{q}\chi_3(\omega_n, q)\,\chi_2(-\omega_n, -q)\,, \tag{3.3.19}$$

and we recall that $\chi_2(q, \omega_n)$ describes a spin-fluctuation at momentum $\boldsymbol{Q} + \boldsymbol{q}$. We shall find that the only way this term enters in the one-loop RG scheme is by a renormalisation to u_{32}, proportional to u_{32}^2.

We now perform the Matsubara sums in order to rewrite the linked cluster expansion in a form which is a convenient starting point for renormalisation. The Matsubara sums can be performed as in Section 2.3.1 to arrive at

$$\tilde{I}_i = \int_0^{\Lambda_i} \frac{d^d q}{(2\pi)^d} \int_0^{\Omega\Gamma(q)/\eta_i} \frac{d\omega}{\pi} \coth\left(\frac{\omega}{2T}\right) \frac{\eta_i\omega/\Gamma(q)}{(\delta_i + q^2)^2 + (\eta_i\omega/\Gamma_i(q))^2}, \tag{3.3.20}$$

and

$$\tilde{J}_i = \int_0^{\Lambda_i} \frac{d^d q}{(2\pi)^d} \int_0^{\Omega\Gamma(q)/\eta_i} \frac{d\omega}{\pi} \coth\left(\frac{\omega}{2T}\right) \frac{2(\delta_i + q^2)\,\eta_i\omega/\Gamma_i(q)}{\left[(\delta_i + q^2)^2 + (\eta_i\omega/\Gamma_i(q))^2\right]^2}, \tag{3.3.21}$$

for $i = 3, 2$. By rescaling ω we see that we can write these in terms of the same function that

arise in the standard Hertz-Millis model in Section 2.3.1, as

$$\tilde{I}_i\left(\delta_i, T\right) = \frac{1}{\eta_i} I_i\left(\delta_i, \mathcal{T}_i\right), \tag{3.3.22}$$

and

$$\tilde{J}_i\left(\delta_i, T\right) = \frac{1}{\eta_i} J_i\left(\delta_i, \mathcal{T}_i\right) \tag{3.3.23}$$

where I_i and J_i are the functions in equations (2.3.10) and (2.3.11) for the dynamical exponent z_i, and $\mathcal{T}_i$ is shorthand for $\eta_i T$. These are integrated up to the cut-offs Λ_i and $\Omega_i \Gamma_i(q)$.

The Gaussian part of the free energy may also be calculated in the same way as in Section 2.3.1. Performing the Matsubara sums and rescaling the frequency integrals we find that

$$\tilde{F}_i^{(G)}\left(\delta_i, T\right) = \frac{1}{\eta_i} F_G\left(\delta_i, \mathcal{T}_i\right), \tag{3.3.24}$$

where $F_G\left(\delta_i, \mathcal{T}_i\right)$ is the function given in equation (2.3.4) for dynamical exponent z_i, with the appropriate cut-offs as discussed above.

The $\tilde{J_{32}}$ term is a little different, however. Performing the Matsubara sum, we find that

$$\begin{aligned} \tilde{J_{32}} = \int_0^{\Lambda_<} \frac{d^d q}{(2\pi)^d} \int_0^{\Omega_<(q)} \frac{d\omega}{\pi} \Bigg(& \coth\left(\frac{\omega}{2T}\right) \\ & \frac{\left(\delta_3 + q^2\right)\eta_2 \omega + \left(\delta_2 + q^2\right)\eta_3 \omega / q}{\left[\left(\delta_3 + q^2\right)^2 + \left(\eta_3 \omega / q\right)^2\right]\left[\left(r_2 + q^2\right)^2 + \left(\eta_2 \omega\right)^2\right]} \Bigg), \end{aligned} \tag{3.3.25}$$

where $\Lambda_< = \min\left[\Lambda_2, \Lambda_3\right]$ and $\Omega_<\left(q\right) = \min\left[\Omega_2/\eta_2, \Omega_3 q/\eta_3\right]$. We have assumed that for $\omega > \Omega_<$, the integrand may be considered sufficiently small such that its contribution to $\tilde{J_{32}}$ is negligible. For the purpose of deriving the RG equations, we rescale the frequency integral to write

$\tilde{J_{32}} = J_{32}/\eta_3$, where

$$J_{32} = \int_0^{\Lambda_<} \frac{d^d q}{(2\pi)^d} \int_0^{\eta_3 \Omega_<(q)} \frac{d\omega}{\pi} \Bigg(\coth\left(\frac{\omega}{2\mathcal{T}_3}\right) \frac{(\delta_3 + q^2)\,\omega\,(\eta_2/\eta_3) + (\delta_2 + q^2)\,\omega/q}{\left[(\delta_3 + q^2)^2 + (\omega/q)^2\right]\left[(r_2 + q^2)^2 + (\omega\eta_2/\eta_3)^2\right]} \Bigg). \tag{3.3.26}$$

We then rewrite the linked cluster expansion as

$$\begin{aligned} F =& \frac{1}{\eta_3} F_3^{(G)} + \frac{1}{\eta_2} F_2^{(G)} + n_3(n_3+2)\frac{u_3}{\eta_3^2} I_3^2 + n_2(n_2+2)\frac{u_2}{\eta_2^2} I_2^2 + 2n_3 n_2 \frac{u_{32}}{\eta_3 \eta_2} I_3 I_2 \\ & - 4n_3(n_3+2)(n_3+8)\frac{u_3^2}{\eta_3^3} I_3^2 J_3 - 4n_2(n_2+2)(n_2+8)\frac{u_2^2}{\eta_2^3} I_2^2 J_2 \\ & - 4n_3 n_2(n_3+2)\frac{u_{32}^2}{\eta_3^2 \eta_2} I_3^2 J_2 - 4n_3 n_2(n_2+2)\frac{u_{32}^2}{\eta_3 \eta_2^2} I_2^2 J_3 \\ & - 8n_3 n_2(n_3+2)\frac{u_3 u_{32}}{\eta_3^2 \eta_2} I_3 I_2 J_3 - 8n_3 n_2(n_2+2)\frac{u_2 u_{32}}{\eta_3 \eta_2^2} I_3 I_2 J_2 - 8n_3 n_2 \frac{u_{32}^2}{\eta_3^2 \eta_2} I_3 I_2 J_{32}, \end{aligned} \tag{3.3.27}$$

from which we derive the RG equations.

3.3.3 The RG Equations

Now that we have found the free energy using the linked cluster expansion, we are able to adapt the methods of Section 2.3.2 to derive the RG equations. However the extension is not straight forward as we now have two dynamical exponents. This means it is not obvious how imaginary time should be rescaled as space is rescaled.

While the scaling analysis of Section 3.2 was performed using two independent scaling variables $b_<$ and $b_>$, we find that the only way to derive the one-loop RG equations is to use a single scaling variable b.

To derive the RG equations in the presence of multiple dynamical exponents, when rescaling space by a factor b, we take inspiration from the literature [41, 43] and rescale imaginary time by b^z, where z is an arbitrary, artificial dynamical exponent. The value of z we choose to rescale by does not end up affecting our calculations of any physical properties of the system.

We never need to specify a value for it in our calculations, and so shall leave it undefined. The kinetic coefficients η_2 and η_3 depend on z, and at tree-level RG we find that they obey

$$\eta_i(b) = b^{z_i - z}\eta_i, \tag{3.3.28}$$

where $z_2 = 2$ and $z_3 = 3$. This does not change when we look at the one-loop RG equations. From scaling arguments alone, we also find that temperature scales as $T(b) = b^z T$, however only the combinations $\mathcal{T}_i = \eta_i T$ enter the other RG equations. These combinations scale as $\mathcal{T}_i = b^{z_i}\mathcal{T}_i$. We find that the RG equations can be written in terms of the variables

$$\tilde{u_i} = \frac{u_i}{\eta_i}, \tag{3.3.29}$$

and

$$\tilde{w_i} = \frac{u_{32}}{\eta_i}, \tag{3.3.30}$$

for $i = 3, 2$. The quantities $\tilde{w_3}$ and $\tilde{w_2}$ are of course related, as $\tilde{w_3} = \tilde{w_2}\,(\eta_3/\eta_2)$, but we find it convenient to write them separately.

To derive the one-loop RG equations, we adapt the analysis of Section 2.3.2. We simultaneously reduce the momentum cut-offs on the I_i and J_i integrals by a factor b and the frequency cut-offs by a factor of b^2, and use that $I_i \to I_i^< + f_i^{(2)} \ln b$, $J_i \to J_i^< + f_i^{(4)} \ln b$ and $J_{32} \to J_{32}^< + f_{32}^{(4)} \ln b$. Here the superscript $<$ means only evaluated below the new cut-off. The $f_i^{(2)}\,(\delta_i, \mathcal{T}_i)$ and $f_i^{(4)}\,(\delta_i, \mathcal{T}_i)$ functions are the same as the functions that appear in the Hertz-Millis action, and are defined in equations (2.3.14) and (2.3.15). The only new term is $f_{32}^{(4)}\,(\delta_3(b), \delta_2(b), \mathcal{T}_3(b))$ which warrants further discussion. This term arises from reducing the cut-offs in the J_{32} term of equation (3.3.26). As noted before, the cut-offs are just the lower of the two cut-offs associated with each mode. For low values of q, the lower of the two cut-offs on frequency will be $\Omega_3 q/\eta_3$, but if $\frac{\eta_3}{\eta_2}\frac{\Omega_2}{\Omega_3} < \Lambda_<$, then at some q the lower of the two frequency

cut-offs will be Ω_2/η_2. However, because $\eta_3(b)/\eta_2(b)$ is proportional to $b^{z_3-z_2} = b$, then at some point in renormalisation, $\Omega_3\Lambda_</\eta_3$ will be less than Ω_2/η_2. Then, the frequency cut-off is $\Omega_3 q/\eta_3$ for all values of q. This is shown in Figure 3.4. To simplify analysis we then neglect all terms in J_{32} proportional to $\eta_2(b)/\eta_3(b)$ as they scale quickly to zero under renormalisation, and find that

$$J_{32} \approx \int_0^{\Lambda_<} \frac{d^d q}{(2\pi)^d} \int_0^{\Omega_3 q} \frac{d\omega}{\pi} \frac{1}{\delta_2 + q^2} \coth\left(\frac{\omega}{2\mathcal{T}_3}\right) \frac{\omega/q}{\left(\delta_3 + q^2\right)^2 + \left(\omega/q\right)^2}. \tag{3.3.31}$$

This means that

$$\begin{aligned} f_{32}^{(4)}\left(\delta_3(b), \delta_2(b), \mathcal{T}_3(b)\right) =& \frac{1}{\delta_2 + \Lambda_<^2} \Lambda_<^{d-1} K_d \int_0^{\Omega_3\Lambda_<} \frac{d\omega}{\pi} \coth\left(\frac{\omega}{2\mathcal{T}_3}\right) \frac{\omega/\Lambda_<}{\left(\delta_3 + \Lambda_<^2\right)^2 + \left(\omega/\Lambda_<\right)^2} \\ &+ \frac{1}{\pi} \int^{\Lambda_<} \frac{d^d q}{(2\pi)^d} \coth\left(\frac{\Omega_3 q}{2\mathcal{T}_3}\right) \frac{1}{\delta_2 + q^2} \frac{\Omega_3}{\left(\delta_3 + q^2\right)^2 + \left(\Omega_3\right)^2}. \end{aligned} \tag{3.3.32}$$

After making these substitutions in the linked cluster expansion and only keeping terms linear in $\ln b$, we follow the same steps as in Section 2.3.2 to derive the RG equations. Using that

$$I_i = \frac{2}{n_i} \frac{\partial F_i^{(G)}}{\partial \delta_i}, \tag{3.3.33}$$

we find that some terms can be absorbed into a rescaling of δ_3 and δ_2. We only consider corrections to the tuning parameter which are linear in the interactions. We absorb other terms into a rescaling of quartic interactions $\tilde{u_i}$ and $\tilde{w_i}$. We find that the one-loop RG equations are

$$\frac{d\delta_i}{d\ln b} = 2\delta_i(b) + 4(n_i+2)\tilde{u_i}(b) f_i^{(2)}\left(\delta_i(b), \mathcal{T}_i(b)\right) + 4n_j \tilde{w_j}(b) f_j^{(2)}\left(\delta_j(b), \mathcal{T}_j(b)\right), \tag{3.3.34a}$$

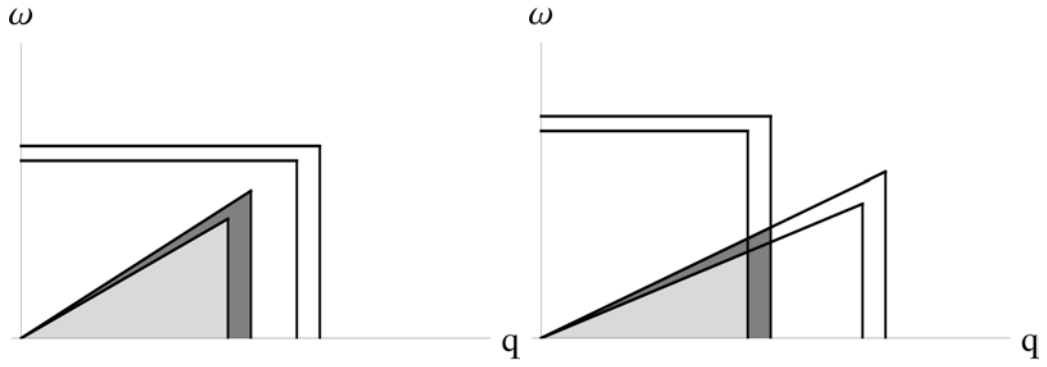

(a) $\Lambda_3 < \Lambda_2$ and $\frac{\Omega_3\Lambda_3}{\eta_3} < \frac{\Omega_2}{\eta_2}$

(b) $\Lambda_3 > \Lambda_2$ and $\frac{\Omega_3\Lambda_2}{\eta_3} < \frac{\Omega_2}{\eta_2}$

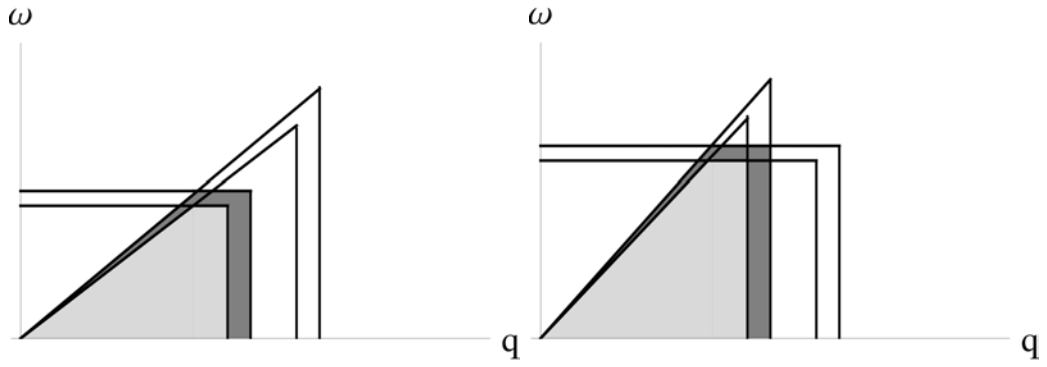

(c) $\Lambda_3 > \Lambda_2$ and $\frac{\Omega_3\Lambda_3}{\eta_3} > \frac{\Omega_2}{\eta_2}$

(d) $\Lambda_3 < \Lambda_2$ and $\frac{\Omega_3\Lambda_3}{\eta_3} > \frac{\Omega_2}{\eta_2}$

Figure 3.4: The cut-offs being simultaneously reduced. This affects the term $\tilde{J}_{32}$ in the RG equations. The two momentum cut-offs are Λ_3 and Λ_2, and the frequency cut-offs are $\Omega_3 q/\eta_3$ and Ω_2/η_2. At the beginning of the RG procedure any four of these options may be realised with the cut-offs chosen. As explained in the main text, after some amount of RG flow this figured in rescaled variables will look like either (a) or (b). This means that the appropriate frequency cut-off is $\Omega_3\Lambda_</\eta_3$.

$$\frac{d\tilde{u}_i}{d\ln b} = [4-(d+z_i)]\,\tilde{u}_i(b) - 4(n_i+8)\tilde{u_i}^2(b) f_i^{(4)}(\delta_i(b),\mathcal{T}_i(b)) - 4n_j\tilde{w}_i(b)\tilde{w}_j(b) f_j^{(4)}(\delta_j(b),\mathcal{T}_j(b)), \tag{3.3.34b}$$

and

$$\frac{d\tilde{w}_i}{d\ln b} = [4-(d+z_i)]\,\tilde{w}_i(b) - \sum_{p=3,2} 4\,(n_p+2)\,\tilde{u_p}(b)\tilde{w}_i(b) f_p^{(4)}(\delta_p(b),\mathcal{T}_p(b)) - 4\tilde{w}_3(b)\tilde{w}_j(b) f_{32}^{(4)}\left(\delta_3(b),\delta_2(b),\mathcal{T}_3(b)\right), \tag{3.3.34c}$$

where $i = 3, 2$ and $j = 2$ if $i = 3$, and $j = 3$ if $i = 2$.

The Gaussian part of the free energy, $F_G = \frac{F_3^{(G)}}{\eta_3} + \frac{F_2^{(G)}}{\eta_2}$, can be found from the equation

$$\frac{dF_G}{d\ln b} = (d+z)\,F_G - \sum_{i=3,2} \frac{1}{\eta_i(b)} f_i^{(0)}\left(\delta_i(b),\mathcal{T}_i(b)\right), \tag{3.3.35}$$

where $f_i^{(0)}\left(\delta_i,\mathcal{T}_i\right)$ is the same as the $f^{(0)}\left(\delta,T\right)$ function in the Hertz-Millis case for dynamical exponent z_i in equation (2.3.13).

We have now written the RG equations in terms of the same functions present in the Hertz-Millis RG equations, which allows us to solve them by referring back to the solution presented in Chapter 2.

3.4 Solving the RG Equations

We have derived the RG equations which we now solve in order to identify the regions of the phase diagram and calculate the specific heat, thermal expansion and Grüneisen parameter in each regime. As in Chapter 2, we use the notation that if a parameter is written without explicit scale-dependence then we are referring to its bare, unrenormalised value.

We first solve the equations for the renormalised interactions in Section 3.4.1 to show that in the case of $d \geq 2$ the system is described by an effective Gaussian model.

We then analyse the three dimensional case, by finding the renomalised tuning parameters

and phase diagram in Sections 3.4.2, 3.4.3 and 3.4.4. We then repeat the process for the more complicated two dimensional case in Sections 3.4.5, 3.4.6 and 3.4.7. In Section 3.5 we analyse the free energy and find the thermal expansion, specific heat, and Grüneisen parameter in each region of the phase diagram.

3.4.1 Interactions

We now solve the equations for the interaction terms $\tilde{w}_i$ and $\tilde{u}_i$, in both $d = 2$ and $d = 3$. In $d = 3$ the equations are simple to solve. We may neglect the one-loop corrections and find that $\tilde{u_3}(b) = b^{-2}\tilde{u_3}$ and $\tilde{w_3}(b) = b^{-2}\tilde{w_3}$, and that $\tilde{u_2}(b) = b^{-1}\tilde{u_2}$ and $\tilde{w_2}(b) = b^{-1}\tilde{w_2}$.

In $d = 2$ the analysis is a bit more involved. Since at tree level the terms $\tilde{u_3}$ and $\tilde{w_3}$ flow to zero, we assume that we do not need to consider the one-loop corrections and find that $\tilde{u_3}(b) = b^{-1}\tilde{u_3}$ and $\tilde{w_3}(b) = b^{-1}\tilde{w_3}$. The equations for $\tilde{u_2}$ and $\tilde{w_2}$ are a bit more complicated. The RG equations are

$$\frac{d\tilde{u_2}}{d\ln b} = -4(n_2+8)\tilde{u_2}^2(b) f_2^{(4)}(\delta_2(b), \mathcal{T}_2(b)) - 4n_3\tilde{w_3}(b)\tilde{w_3}(b) f_3^{(4)}(\delta_3(b), \mathcal{T}_3(b)), \tag{3.4.1}$$

and

$$\begin{aligned}\frac{d\tilde{w_2}}{d\ln b} = &- \sum_{p=3,2} 4\,(n_p+2)\,\tilde{u_p}(b)\tilde{w_2}(b) f_p^{(4)}(\delta_p(b), \mathcal{T}_p(b)) \\ &- 4\tilde{w_3}^2(b) f_{32}^{(4)}\left(\delta_3(b), \delta_2(b), \mathcal{T}_3(b)\right).\end{aligned} \tag{3.4.2}$$

We choose to write these as

$$\frac{d\tilde{u_2}}{dx} = -\alpha_1\tilde{u_2}^2(e^x) - \alpha_2 e^{-x}\tilde{w_2}^2(e^x), \tag{3.4.3}$$

and

$$\frac{d\tilde{w_2}}{dx} = -a_1\tilde{u_2}(e^x)\tilde{w_2}(e^x) - a_2 e^{-x}\tilde{u_3}\tilde{w_2}(e^x) - a_3 e^{-2x}\tilde{w_2}^2(e^x), \tag{3.4.4}$$

where we have used that $\tilde{w_3}(b) = b^{-1}\tilde{w_2}(b)$ and $\tilde{u_3}(b) = b^{-1}\tilde{u_3}$. We have also assumed that throughout the RG process the $f_i^{(4)}\left(\delta_i(b), \mathcal{T}_i(b)\right)$ functions may be approximated as the constants $f_i^{(4)}\left(0,0\right)$, which is the same approximation as made in Section 2.4.1. Similarly, we assume that the function $f_{32}^{(4)}\left(\delta_3, \delta_2, \mathcal{T}_3\right)$ can be approximated as $f_{32}^{(4)}\left(0,0,0\right)$.

Since all the interactions are positive, both $\tilde{w_2}(e^x)$ and $\tilde{u_2}(e^x)$ are decreasing functions of x. To make progress in these equations, we assume that after some amount of scaling $\alpha_2 e^{-x}\tilde{w_2}^2(e^x) \ll \alpha_1\tilde{u_2}^2(e^x)$ for $x > x_u$. Then equation (3.3.34b) for $\tilde{u_2}$ becomes

$$\frac{d\tilde{u_2}}{dx} = -\alpha_1\tilde{u_2}^2(e^x), \tag{3.4.5}$$

which leads to

$$\tilde{u_2}(e^x) = \frac{1}{\frac{1}{\tilde{u_2}(e^{x_u})} + \alpha_1(x - x_u)}, \tag{3.4.6}$$

for $x > x_u$. This can be written as

$$\tilde{u_2}(b) = \frac{1}{\alpha_1}\frac{1}{\ln\left(gb\right)}, \tag{3.4.7}$$

for $b > e^{x_u}$, where $g = \exp\left[\frac{1}{\alpha_1\tilde{u_2}(e^{x_u})} - x_u\right]$.

If for $x > x_w$ we assume that $\left(a_2 e^{-x}\tilde{u_3}\tilde{w_2}(e^x) + a_3 e^{-2x}\tilde{w_2}^2(e^x)\right) \ll a_1\tilde{u_2}(e^x)\tilde{w_2}(e^x)$, then equation (3.3.34c) for $\tilde{w_2}$ becomes

$$\frac{d\ln\tilde{w_2}}{dx} = -a_1\tilde{u_2}(e^x). \tag{3.4.8}$$

This is solved by

$$\tilde{w_2}(e^x) = \tilde{w_2}(e^{x_w})\exp\left[-a_1\int_{x_w}^{x} dx\tilde{u_2}(e^x)\right], \tag{3.4.9}$$

which for $x > \max[x_w, x_u]$ is proportional to

$$\tilde{w_2}(b) = \tilde{w_2}^* \left[\ln(gb)\right]^{-(n_2+2)/(n_2+8)}. \tag{3.4.10}$$

The exponent $(n_2+2)/(n_2+8)$ is the ratio a_1/α_1, and $\tilde{w_2}^*$ is some constant which depends on x_u and x_w.

We do not know the values of g or $\tilde{w_2}^*$ analytically, however we have found the behaviour of $\tilde{w_2}(b)$ and $\tilde{u_2}(b)$ at large b. The behaviour of $\tilde{u_2}$ is the same as the behaviour of u in the case of an antiferromagnetic quantum critical point in two dimensions, but this slow decay of $\tilde{w_2}$ is new, and unique to the multicritical case.

Note that since $\tilde{w_3}(b) = b^{-1}\tilde{w_2}(b)$, at large value of b we find that

$$\tilde{w_3}(b) = \tilde{w_2}^* b^{-1} \left[\ln(gb)\right]^{-(n_2+2)/(n_2+8)}. \tag{3.4.11}$$

We then note that since the interactions $\tilde{w_3}(b)$ and $\tilde{w_2}(b)$ have a logarithmic decay, the one-loop corrections may actually be important in the solution of $\tilde{u_3}(b)$. Taking the one-loop corrections arising from u_{32} into account, we find that at large values of b the interaction $\tilde{u_3}(b)$ scales as

$$\tilde{u_3}(b) = b^{-1}\left(u_3^* - \frac{c}{4-n_2}\left[\ln(gb)\right]^{(4-n_2)/(n_2+8)}\right) \tag{3.4.12}$$

if $n_2 \neq 4$, where u_3^* and c are constants. In the case of $n_2 = 4$, $\tilde{u_3}(b)$ scales as

$$\tilde{u_3}(b) = b^{-1}\left[u_3^* - \tilde{c}\ln(\ln(gb))\right] \tag{3.4.13}$$

where $\tilde{c}$ is a constant. Note that equations (3.4.5) and (3.4.8) are still valid for sufficiently large b, even when we include these logarithmic terms. This means that due to the marginal nature of the antiferromagnetic modes, all interactions have some logarithmic decay in two dimensions.

Nevertheless, the effective interaction terms decay to zero in both two and three dimensions, so the quantum multicritical point can be described by an effective Gaussian model. We now turn our attention to equation (3.3.34a) to find the renormalised tuning parameters and identify regions of the phase diagram.

3.4.2 Tuning Parameters in $d = 3$

In this section we solve equation (3.3.34a) to find the renormalised tuning parameters in three dimensions. This enables us to calculate the correlation lengths and identify the regions of the phase diagram. In the model of quantum multicriticality we consider here, there is a correlation length associated with ferromagnetic order ξ_3, and a correlation length associated with the antiferromagnetic order ξ_2. We calculate these lengths in this section.

We first analyse the situation in three dimensions, where the model is above its upper critical dimension. The calculation in two dimensions is presented in Section 3.4.5, where complications arise due to the marginal nature of the antiferromagnetic modes.

In three dimensions we may adapt the methods presented in Section 2.4.2. Solving equation (3.3.34a) using an integrating factor we find

$$\begin{aligned} R_2(b) = \delta_2 + 4(n_2+2)\int_0^{\ln b} dx e^{-2x}\tilde{u_2}(e^x) f_2^{(2)}\left(\delta_2(e^x), \mathcal{T}_2 e^{2x}\right) \\ + 4n_3\int_0^{\ln b} dx e^{-2x}\tilde{w_3}(e^x) f_3^{(2)}\left(\delta_3(e^x), \mathcal{T}_3 e^{3x}\right), \end{aligned} \tag{3.4.14}$$

and

$$\begin{aligned} R_3(b) = \delta_3 + 4(n_3+2)\int_0^{\ln b} dx e^{-2x}\tilde{u_3}(e^x) f_3^{(2)}\left(\delta_3(e^x), \mathcal{T}_3 e^{3x}\right) \\ + 4n_2\int_0^{\ln b} dx e^{-2x}\tilde{w_2}(e^x) f_2^{(2)}\left(\delta_2(e^x), \mathcal{T}_2 e^{2x}\right), \end{aligned} \tag{3.4.15}$$

where $R_i(b) \equiv b^{-2}\delta_i(b)$. We follow the arguments of Section 2.4.2 and split $R_i(b)$ into a zero-temperature component and temperature-dependent contributions arising from each mode.

We use the notation that

$$R_i(b) = \Delta_i(b) + R_{i,3}^{(T)}(b) + R_{i,2}^{(T)}(b), \tag{3.4.16}$$

where $R_{i,j}^{(T)}(b)$ is the temperature-dependent contribution to $R_i(b)$ arising from interactions with ϕ_j modes.

Here the zero temperature components are given by

$$\begin{aligned}\Delta_i(b) = \delta_i + 4(n_i+2)\int_0^{\ln b} dx e^{-2x}\tilde{u}_i(e^x) f_i^{(2)}\left(\Delta_i(e^x)e^{2x}, 0\right) \\ + 4n_j \int_0^{\ln b} dx e^{-2x}\tilde{w}_j(e^x) f_j^{(2)}\left(\Delta_j(e^x)e^{2x}, 0\right).\end{aligned} \tag{3.4.17}$$

The temperature dependent components are given by

$$R_{i,i}^{(T)}(b) = 4(n_i+2)\int_0^{\ln b} dx e^{-2x}\tilde{u}_i(e^x)\left[f_i^{(2)}\left(R_i(e^x)e^{2x}, \mathcal{T}_i e^{z_i x}\right) - f_i^{(2)}\left(R_i(e^x)e^{2x}, 0\right)\right], \tag{3.4.18}$$

and

$$R_{i,j}^{(T)}(b) = 4n_j\int_0^{\ln b} dx e^{-2x}\tilde{w}_j(e^x)\left[f_j^{(2)}\left(R_j(e^x)e^{2x}, \mathcal{T}_j e^{z_j x}\right) - f_j^{(2)}\left(R_j(e^x)e^{2x}, 0\right)\right]. \tag{3.4.19}$$

Just as in Section 2.4.2, by subtracting $f_i^{(2)}(R_i, 0)$ instead of $f_i^{(2)}(\Delta_i, 0)$ in these equations we are neglecting corrections of quadratic order in the interactions.

The zero-temperature component can be calculated by adapting the methods that lead to equation (2.4.4). The right hand side of equation (3.4.17) is expanded for small values of Δ, using that $f^{(2)}(y, 0) \approx f^{(2)}(0, 0) - y f^{(4)}(0, 0)$. In the limit $b \to \infty$ we find that

$$\Delta_i(b \to \infty) \equiv r_i = \delta_i\left[1 - \tilde{u}_i\frac{4(n_i+2)f_i^{(4)}(0,0)}{d+z_i-4}\right] - \delta_j\tilde{w}_j\frac{4n_j f_j^{(4)}(0,0)}{d+z_j-4}. \tag{3.4.20}$$

When calculating the temperature-dependent contributions we note that the integrals

$R^{(T)}_{3,k}(b)$ and $R^{(T)}_{2,k}$ are the same but with different coefficients, where $k = 2, 3$. We define

$$R^{(T)}_{3,3}(b) = 4(n_3 + 2)\tilde{u_3}L_3(b), \tag{3.4.21}$$

$$R^{(T)}_{3,2}(b) = 4n_2\tilde{w}_2L_2(b), \tag{3.4.22}$$

$$R^{(T)}_{2,2}(b) = 4(n_2 + 2)\tilde{u_2}L_2(b), \tag{3.4.23}$$

and

$$R^{(T)}_{2,3}(b) = 4n_3\tilde{w}_3L_3(b). \tag{3.4.24}$$

The integrals are

$$L_i(b) = \int_0^{\ln b} dx e^{-(1+z_i)} \left[f_i^{(2)} \left(R_i(e^x)e^{2x}, \mathcal{T}_i e^{z_i x} \right) - f_i^{(2)} \left(R_i(e^x)e^{2x}, 0 \right) \right], \tag{3.4.25}$$

for $i = 3, 2$, which have been investigated in Section 2.4.2. They have been shown to be

$$\lim_{b\to\infty} L_i(b) = \begin{cases} c^{(QC)}_{d,z_i} \mathcal{T}_i^{(d+z_i-2)/z_i} & \text{if } r_i \ll \mathcal{T}_i^{2/z_i}. \\ c^{(FL)}_{d,z_i} \mathcal{T}_i^2 r^{(d-z_i-2)/2} & \text{if } r_i \gg \mathcal{T}_i^{2/z_i}. \end{cases} \tag{3.4.26}$$

As in Chapter 2, the correlation lengths are calculated as $\xi_i^{-2} = \lim_{b\to\infty} R_i(b)$. These have different expansions in four regions of the phase diagram, separated by the two crossovers $r_3 \sim \mathcal{T}_3^{2/3}$ and $r_2 \sim \mathcal{T}_2$. These are the same crossovers predicted by the scaling analysis in Section 3.2. We use the same notation as in that section, and denote the four regions (a) through (d). We now list the correlation lengths in these regions.

Region (a): $r_3 < \mathcal{T}_3^{2/3}$ and $r_2 < \mathcal{T}_2$

In this region, both types of order are quantum critical. The correlation lengths are given by

$$\xi_3^{-2} = r_3 + \tilde{u_3}\frac{n_3+2}{3^{1/2}\pi^2}\Gamma\left(\frac{4}{3}\right)\zeta\left(\frac{4}{3}\right)\mathcal{T}_3^{4/3}, \text{ and} \tag{3.4.27}$$

$$\xi_2^{-2} = r_2 + \tilde{w_3}\frac{n_3}{3^{1/2}\pi^2}\Gamma\left(\frac{4}{3}\right)\zeta\left(\frac{4}{3}\right)\mathcal{T}_3^{4/3}. \tag{3.4.28}$$

The $\mathcal{T}_2^{3/2}$ terms from the ϕ_2 modes are sub-leading, and not written here. This region should be split into four regions depending on whether each correlation length is dominated by the temperature-independent or temperature-dependent parts. The antiferromagnetic correlation length acquires the temperature-dependence usually associated with ferromagnetism in this regime, due to interactions with quantum critical ϕ_3 modes.

Region (b): $r_3 < \mathcal{T}_3^{2/3}$ and $r_2 > \mathcal{T}_2$

In this region, only the ferromagnetic modes are quantum critical, but the antiferromagnetic correlation length is affected by interactions with these modes. The correlation lengths are given by

$$\xi_3^{-2} = r_3 + \tilde{u_3}\frac{n_3+2}{3^{1/2}\pi^2}\Gamma\left(\frac{4}{3}\right)\zeta\left(\frac{4}{3}\right)\mathcal{T}_3^{4/3}, \text{ and} \tag{3.4.29}$$

$$\xi_2^{-2} = r_2 + \tilde{w_3}\frac{n_3}{3^{1/2}\pi^2}\Gamma\left(\frac{4}{3}\right)\zeta\left(\frac{4}{3}\right)\mathcal{T}_3^{4/3}. \tag{3.4.30}$$

The $\mathcal{T}_2^2$ terms from the ϕ_2 modes are sub-leading, and not written here. This region should be split into two regions depending on whether the ferromagnetic correlation length is dominated by r_3 or $\mathcal{T}_3^{4/3}$. The antiferromagnetic correlation length is always dominated by r_2 in this region, but the temperature-dependent term has the exponent usually associated with ferromagnetism.

Region (c): $r_3 > \mathcal{T}_3^{2/3}$ and $r_2 < \mathcal{T}_2$

In this region, only the antiferromagnetic modes are quantum critical, but the ferromagnetic

correlation length is affected by interactions with these modes. The correlation lengths are given by

$$\xi_3^{-2} = r_3 + \tilde{w}_2 \frac{n_2}{(2\pi)^{1/2}\pi} \zeta\left(\frac{3}{2}\right) \mathcal{T}_2^{3/2}, \text{ and} \tag{3.4.31}$$

$$\xi_2^{-2} = r_2 + \tilde{u}_2 \frac{n_2+2}{(2\pi)^{1/2}\pi} \zeta\left(\frac{3}{2}\right) \mathcal{T}_2^{3/2}. \tag{3.4.32}$$

The $\mathcal{T}_3^2$ terms from the ϕ_3 modes are sub-leading, and not written here. This region should be split into two regions depending on whether the antiferromagnetic correlation length is dominated by r_2 or $\mathcal{T}_2^{3/2}$. The ferromagnetic correlation length is always dominated by r_3 in this region, but the temperature-dependent term has the exponent usually associated with antiferromagnetism.

Region (d): $r_3 > \mathcal{T}_3^{2/3}$ and $r_2 > \mathcal{T}_2$

This is a Fermi liquid region, where the correlation lengths are given by

$$\xi_3^{-2} = r_3 + \frac{2(n_3+2)}{3\pi} \tilde{u_3} \mathcal{T}_3^2 r_3^{-1} + \frac{n_2}{6} \tilde{w}_2 \mathcal{T}_2^2 r_2^{-1/2}, \text{ and} \tag{3.4.33}$$

$$\xi_2^{-2} = r_2 + \frac{(n_2+2)}{6} \tilde{u_2} \mathcal{T}_2^2 r_2^{-1/2} + \frac{2n_3}{3\pi} \tilde{w}_3 \mathcal{T}_3^2 r_3^{-1}. \tag{3.4.34}$$

$$\tag{3.4.35}$$

3.4.3 Ginzburg Criterion in $d = 3$

There are two phase transitions in the phase diagram of a material described by our model, into the ferromagnetic and antiferromagnetic phases. We may estimate the boundaries of the ordered phases as the temperature where the correlation lengths diverge. For the ferromagnetic phase, this is the line where

$$T_3^{(c)} = \frac{1}{\eta_3} \left[\frac{-r_3}{\tilde{u_3} \frac{n_3+2}{3^{1/2}\pi^2} \Gamma\left(\frac{4}{3}\right) \zeta\left(\frac{4}{3}\right)} \right]^{3/4}, \tag{3.4.36}$$

which does not depend on whether the antiferromagnetic modes are quantum critical or Fermi liquid-like.

Adapting the arguments of Section 2.4.2, the Hertz-Millis action is only applicable when the classical interaction term v can be treated perturbatively, which is not the case close to the transition into the ferromagnetic ordered phase. The Ginzburg criterion gives the region around this estimated ordered-phase boundary where the Gaussian fixed point of the RG flow no longer describes the physics of the system. In this model the effective classical coupling for the $\omega_n = 0$ mode for ϕ_3 is $v_3 = u_3 T$. This can be written as $v_3 = \frac{u_3}{\eta_3}\eta_3 T$ which is $v_3 = \tilde{u_3}\mathcal{T}_3$. The Ginzburg temperature $T_3^{(G)}$ can then be found from

$$\frac{T_3^{(G)} - T_3^{(c)}}{T_3^{(c)}} \approx \frac{\tilde{u_3} 3^{1/2}\pi^2 \left(\mathcal{T}_3^{(c)}\right)^{2/3}}{(n_3+2)\Gamma\left(\frac{4}{3}\right)\zeta\left(\frac{4}{3}\right)}. \tag{3.4.37}$$

The boundary of the antiferromagnetically ordered phase can be estimated as the line at which the correlation length diverges, which has different forms depending on whether the ferromagnetic modes are quantum critical or Fermi-liquid like. The critical temperature is given by

$$T_2^{(c)} = \begin{cases} \frac{1}{\eta_3}\left[\frac{-r_2 3^{1/2}\pi^2}{\tilde{w_3} n_3 \Gamma\left(\frac{4}{3}\right)\zeta\left(\frac{4}{3}\right)}\right]^{3/4} & \text{in region (a),} \\ \frac{1}{\eta_2}\left[-\frac{r_2 \pi (2\pi)^{1/2}}{\tilde{u_2}(n_2+2)\zeta\left(\frac{3}{2}\right)}\right]^{2/3} & \text{in region (c).} \end{cases} \tag{3.4.38}$$

The Ginzburg temperature upon approaching the antiferromagnetic phase can be also be found, by considering the effective classical coupling for the $\omega_n = 0$ mode for ϕ_2. This is $v_2 = u_2 T$, which is $v_2 = \tilde{u_2}\mathcal{T}_2$. This Ginzburg temperature is

$$\frac{T_2^{(G)} - T_2^{(c)}}{T_2^{(c)}} = \begin{cases} \left(\frac{\eta_2}{\eta_3}\right)^2 \frac{\tilde{u_2}^2 3^{1/2}\pi^2 \left(\mathcal{T}_3^{(c)}\right)^{2/3}}{\tilde{w_3} n_3 \Gamma\left(\frac{4}{3}\right)\zeta\left(\frac{4}{3}\right)} & \text{in region (a),} \\ \frac{\tilde{u_2}(2\pi)^{1/2}\pi \left(\mathcal{T}_2^{(c)}\right)^{1/2}}{(n_2+2)\zeta\left(\frac{3}{2}\right)} & \text{in region (c).} \end{cases} \tag{3.4.39}$$

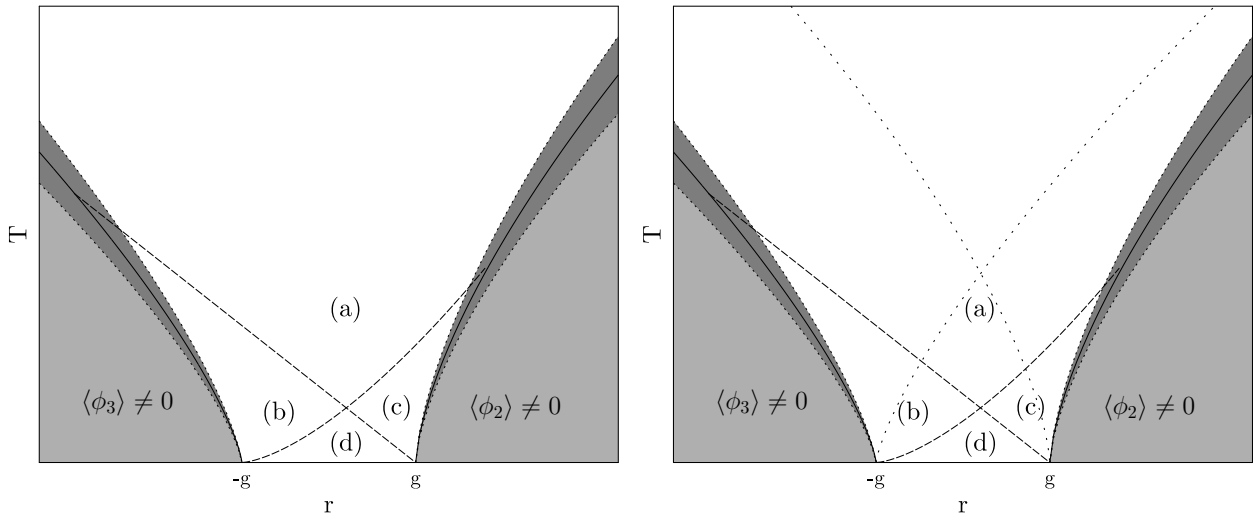

(a) Regions where thermodynamic properties are different

(b) Regions where the dominant contributions to the correlation lengths are different

Figure 3.5: Phase diagram of a quantum multicritical point in $d = 3$, with $r_3 = g + r$ and $r_2 = g - r$. Figure 3.5a shows the main regions of the phase diagram where the thermodynamic properties are different. Figure 3.5b further subdivides regions (a), (b) and (c) into sub-regions where the dominant contributions to the correlation lengths are different. The regions and their crossovers are explained in the main text.

This again depends on whether the ferromagnetic modes are quantum critical or Fermi-liquid like.

3.4.4 Phase Diagram in $d = 3$

Now that we have found the correlation lengths and the boundaries where the Ginzburg criterion is violated, we can find the possible phase diagrams. These are shown in Figure 3.5. These are derived by setting $r_3 = g + r$ and $r_2 = g - r$. At fixed $g \geq 0$, at zero temperature there is quantum phase transition from a ferromagnetically ordered region to a disordered region at $r = -g$, and a quantum phase transition from the disordered region into an antiferromagnetically ordered region at $r = g$. These two phase transitions coalesce to a quantum multicritical point at $g = 0$.

While the phase diagram may just look qualitatively like two quantum critical points separated by a distance $2g$, interactions with quantum critical ferromagnetic modes cause the

antiferromagnetic correlation length to acquire the temperature-dependence usually associated with ferromagnetic correlations. This in turn changes the temperature-dependence of the boundary of the ordered phase, which is protional to $T_2^{(c)} \sim (r-g)^{2/3}$ in region (c) of the phase diagram, and $T_2^{(c)} \sim (r-g)^{3/4}$ in region (a). The power law in region (a) is usually associated with the ferromagnetic phase boundary. The Ginzburg temperature upon approaching the antiferromagnetic phase is also different in regions (a) and (c). This change of power law is a consequence of multicriticality.

In Section 3.5 we shall investigate the thermodynamic quantities in each region of the phase diagram. First, we repeat this analysis in two dimensions to find the possible phase diagrams in two dimensions.

3.4.5 Tuning Parameters in $d = 2$

We now turn our attention to the two dimensional model. Due to the presence of antiferromagnetic $z = 2$ modes, this model is marginal and the problems that arise for the $d = z = 2$ Hertz-Millis theory arise in this case as well.

Due to the marginal nature of the theory, adapting the calculation of Section 2.4.2 is more difficult in two dimensions than in three dimensions. In order to proceed we choose to instead adapt Millis' original solution [24] for the two dimensional case. This involves making less accurate approximations for the correlation lengths. As mentioned in Chapter 2, Millis' original calculation misses the scale-dependence of the zero temperature part of the tuning parameter in the marginal case. This leads to difference in the Ginzburg criterion, of a logarithmic prefactor.

Millis' original solution also finds less accurate prefactors for the temperature-dependent contribution to the renormalised tuning parameter. However, in two dimensions we have already made approximations involving unknown coefficients for the interactions $\tilde{u}_2$ and $\tilde{w}_2$ in equations (3.4.7) and (3.4.10). For this reason we do not worry about the precise coefficients of the temperature-dependent part of the correlation lengths in two dimensions.

In two dimensions, integrating the differential equations for the tuning parameters yields

$$\begin{aligned} R_2(b) = \delta_2 + 4(n_2+2)\int_0^{\ln b} dx e^{-2x}\tilde{u_2}(e^x) f_2^{(2)}\left(e^{2x}R_2(e^x), \mathcal{T}_2 e^{z_2 x}\right) \\ + 4n_3\int_0^{\ln b} dx e^{-2x}\tilde{w_3}(e^x) f_3^{(2)}\left(e^{2x}R_3(e^x), \mathcal{T}_3 e^{2_3 x}\right), \end{aligned} \tag{3.4.40}$$

and

$$\begin{aligned} R_3(b) = \delta_3 + 4(n_3+2)\int_0^{\ln b} dx e^{-2x}\tilde{u_3}(e^x) f_3^{(2)}\left(e^{2x}R_3(e^x), \mathcal{T}_3 e^{z_3 x}\right) \\ + 4n_2\int_0^{\ln b} dx e^{-2x}\tilde{w_2}(e^x) f_2^{(2)}\left(e^{2x}R_2(e^x), \mathcal{T}_2 e^{z_2 x}\right), \end{aligned} \tag{3.4.41}$$

where $R_i(b) = \delta_i(b)/b^2$. We let

$$R_2(b) = \delta_2 + 4(n_2+2)\tilde{u_2}L_2^{(d=2)} + 4n_3\tilde{w_3}L_3^{(d=2)}, \text{ and} \tag{3.4.42}$$

$$R_3(b) = \delta_3 + 4(n_3+2)\tilde{u_3}\tilde{L}_3^{(d=2)} + 4n_2\tilde{w_2}\tilde{L}_2^{(d=2)}, \tag{3.4.43}$$

as definitions of $L_3^{(d=2)}$, $L_2^{(d=2)}$, $\tilde{L}_3^{(d=2)}$ and $\tilde{L}_2^{(d=2)}$.

We investigate these functions in the limit that $b \to \infty$. To do this, we adapt Millis' method [24] and define special values of b. We define b_i^* by $\delta_i(b_i^*) = 1$, and b_i^T by $\mathcal{T}_i(b_i^T) = 1$. The Fermi liquid region is defined by $b_i^* < b_i^T$ which means that at the scale where $\delta_i = 1$ the effective temperature is small. The quantum critical region is when this inequality is reversed. At tree level this is equal to the $r_i \sim \mathcal{T}_i^{2/z_i}$ crossover, usually seen at QCP.

Millis' approximation for dealing with these integrals is to assume that the function $f^{(2)}\left(\delta(b), \mathcal{T}(b)\right)$ is independent of $\delta(b)$, for $\delta(b) \leq 1$. Scaling stops when $\delta(b) = 1$, and the physical properties are investigated at this scale. For the region of scaling where $\mathcal{T}(b) < 1$, the function $f^{(2)}\left(0, \mathcal{T}(b)\right)$ is approximated by a Taylor series. In the region of scaling where $\mathcal{T}(b) > 1$, which only occurs in the quantum critical regime, the approximation is that $f^{(2)}\left(0, \mathcal{T}(b)\right) \sim c\mathcal{T}(b)$, where c is a constant. We now adapt this to our multicritical model.

We first note that when taking the limit $b \to \infty$, we may replace upper limit of the integrals

by $\ln b_i^*$. This is because for $\delta_i(b) \gg 1$, the integrands in the L integrals are

$$f_i^{(2)}\left(\delta_i(b), \mathcal{T}_i(b)\right) - f_i^{(2)}\left(\delta_i(b), 0\right) \sim \frac{1}{\delta_i^2(b)}. \tag{3.4.44}$$

These quickly decays to zero, so the dominant contribution to the L integrals come from $b < b_i^*$.

We investigate these equations using equations (3.4.7) and (3.4.10) for $\tilde{u_2}(b)$ and $\tilde{w_2}(b)$, but assume that the critical behaviour can be captured from the assumption that $\tilde{w_3}(b) = b^{-1}\tilde{w_3}$ and $\tilde{u_3}(b) = b^{-1}\tilde{u_3}$. In Section 3.4.1 we discussed logarithmic corrections to these interactions. This assumption may lead to logarithmic corrections to the correlation lengths we calculate.

Under this assumption, the integrals $\tilde{L_3}^{(d=2)}$ and $L_3^{(d=2)}$ are equal. The integral $L_3^{(d=2)}$ has been tackled by Millis [24], using the approximation that $f^{(2)}(\delta_3, \mathcal{T}_3) \sim f^{(2)}(0,0)$ from $b = 0$ to $b = b_3^T$, and $f^{(2)}(\delta_3, \mathcal{T}_3) \sim \mathcal{T}_3$ from b_3^T to b_3^*. The result is that

$$L_3^{(d=2)} = \begin{cases} c_{3F} & \text{in the Fermi liquid region,} \\ c_{3Q}\mathcal{T}_3 + c'_{3Q}\mathcal{T}_3 \ln\left(b_3^*\mathcal{T}_3^{1/3}\right) & \text{in the quantum critical region,} \end{cases} \tag{3.4.45}$$

where c_{3F}, c_{3Q} and c'_{3Q} are constants.

The integral $L_2^{(d=2)}$ reduces to an integral tackled by Millis for $b > b_u$ defined in Section 3.4.1. As long as $b_u \ll b_2^T$, we may use Millis' approximation for this integral. This condition is that the approximation $u_2(e^x) \sim 1/\ln b$ becomes valid while the renormalised temperature Tb^z is still less than 1. Using Millis' approximation

$$L_2^{(d=2)} = \begin{cases} c_{2F} & \text{in the Fermi liquid region,} \\ \frac{\mathcal{T}_2}{\ln\left(c_u\mathcal{T}_2^{-1/2}\right)}\left[c_{2Q} + c'_{2Q}\ln\left(b_2^*\mathcal{T}_2^{1/2}\right)\right] & \text{in the quantum critical region,} \end{cases} \tag{3.4.46}$$

where c_{2F}, c_u, c_{2Q} and c'_{2Q} are constants.

The integral $\tilde{L}_2^{(d=2)}$ again can only be tackled for $b > b_w$, where above b_w, $\tilde{w_2} \sim [\ln b]^{-(n_2+2)/(n_2+8)}$. In order to analyse this integral we must assume that $b_w \ll b_2^T$. In this case, it is straight

forward to adapt the method of Millis [24] and find that

$$\tilde{L}_2^{(d=2)} = \begin{cases} \tilde{c}_{2F} & \text{in the Fermi liquid region,} \\ \frac{\mathcal{T}_2}{\left[\ln\left(c_w \mathcal{T}_2^{-1/2}\right)\right]^{\frac{(n_2+2)}{(n_2+8)}}} \left[\tilde{c}_{2Q} + \tilde{c}'_{2Q} \ln\left(b_2^* \mathcal{T}_2^{1/2}\right)\right] & \text{in the quantum critical region,} \end{cases} \tag{3.4.47}$$

where $\tilde{c}_{2F}$, c_w, $\tilde{c}_{2Q}$ and $\tilde{c}'_{2Q}$ are constants.

The correlation lengths are defined as $\xi_i^{-2} = \lim_{b\to\infty} R_i(b)$, which we now investigate in each of the regions of the phase diagram.

As in three dimensions, the ferromagnetic modes may be quantum critical or Fermi-liquid like, independently of the ϕ_2 modes. The requirement for the quantum critical region is $r_3 \ll \mathcal{T}_3^{2/3}$. When the ϕ_3 modes are in the quantum critical region, the correlation length to leading order turns out to be independent of the antiferromagnetic modes. It is given by

$$\xi_3^{-2} \sim \begin{cases} \frac{2}{3}(n_3+2)\tilde{u_3}c'_{3Q}\mathcal{T}_3 \ln\left(\frac{1}{\mathcal{T}_3}\right) & \text{if } r_3 \ll \frac{2}{3}(n_3+2)\tilde{u_3}c'_{3Q}\mathcal{T}_3 \ln\left(\frac{1}{\mathcal{T}_3}\right), \\ r_3 & \text{if } r_3 \gg \frac{2}{3}(n_3+2)\tilde{u_3}c'_{3Q}\mathcal{T}_3 \ln\left(\frac{1}{\mathcal{T}_3}\right). \end{cases} \tag{3.4.48}$$

If the ϕ_3 modes are in this quantum critical region, then the antiferromagnetic correlation length acquires some temperature-dependent correction from interactions with ferromagnetic modes. This is the leading order temperature-dependent correction to the antiferromagnetic correlation length, so

$$\xi_2^{-2} \sim \begin{cases} r_2 + \frac{2}{3}n_2\tilde{w_3}c'_{3Q}\mathcal{T}_3 \ln\left(\frac{1}{\mathcal{T}_3}\right) & \text{if } r_3 \ll \frac{2}{3}(n_3+2)\tilde{u_3}c'_{3Q}\mathcal{T}_3 \ln\left(\frac{1}{\mathcal{T}_3}\right), \\ r_2 + \frac{2}{3}n_2\tilde{w_3}c'_{3Q}\mathcal{T}_3 \ln\left(\frac{1}{r_3}\right) & \text{if } r_3 \gg \frac{2}{3}(n_3+2)\tilde{u_3}c'_{3Q}\mathcal{T}_3 \ln\left(\frac{1}{\mathcal{T}_3}\right). \end{cases} \tag{3.4.49}$$

The condition for thermodynamic properties to display behaviour associated with the quantum critical regime for a single antiferromagnetic quantum critical point is that $R(b)T^{-1} \ll 1$, as explained in Section 2.4. The analogous condition in the multicritical case is that $R_2(b)\mathcal{T}_2^{-1} \ll 1$.

Due to the strong temperature-dependent renormalisation from interactions with the ferromagnetic modes, we see that in the limit $b \to \infty$ this is not obeyed in the limit $T \to 0$.

At finite temperatures the antiferromagnetic modes can be quantum critical, as long as $\frac{2}{3} n_2 \tilde{w}_3 c'_{3Q} \ln\left(\frac{1}{\mathcal{T}_3}\right) \ll 1$. Since this is not obeyed in the limit $T \to 0$, we conclude that there is no region in the $d = 2$ phase diagram where both order parameters are quantum critical. To enable comparison with the $d = 3$ case, we label the whole region $r_3 < \mathcal{T}_3^{2/3}$ as region (b).

When the ferromagnetic modes are Fermi liquid-like, the antiferromagnetic correlation length is not dominated by interactions with ferromagnetic modes. In region (c) of the phase diagram defined by $r_2 < \mathcal{T}_2$ and $r_3 > \mathcal{T}^{2/3}$, the ferromagnetic modes are Fermi liquid-like and the antiferromagnetic modes are quantum critical. In this region,

$$\xi_2^{-2} = c'_{2Q} \tilde{u}_2 \frac{\mathcal{T}_2 \ln\left[\ln\left(\frac{1}{\mathcal{T}_2}\right)\right]}{\ln\left(\frac{1}{\mathcal{T}_2}\right)}, \text{ and} \tag{3.4.50}$$

$$\xi_3^{-2} = r_3 + \tilde{c}'_{2Q} \frac{\mathcal{T}_2 \ln\left[\ln\left(\frac{1}{\mathcal{T}_2}\right)\right]}{\left[\ln\left(\frac{1}{\mathcal{T}_2}\right)\right]^{\frac{(n_2+2),}{(n_2+8)}}} \tag{3.4.51}$$

if $r_2 < c'_{2Q} \tilde{u}_2 \frac{\mathcal{T}_2 \ln\left[\ln\left(\frac{1}{\mathcal{T}_2}\right)\right]}{\ln\left(\frac{1}{\mathcal{T}_2}\right)}$. If this inequality is reversed,

$$\xi_2^{-2} = r_2, \text{ and} \tag{3.4.52}$$

$$\xi_3^{-2} = r_3 + \frac{\tilde{c}'_{2Q}}{2} \frac{\mathcal{T}_2 \ln\left(\frac{\mathcal{T}_2}{r_2}\right)}{\left[\ln\left(\frac{1}{\mathcal{T}_2}\right)\right]^{\frac{(n_2+2)}{(n_2+8)}}}. \tag{3.4.53}$$

In this region of the phase diagram the ferromagnetic correlation length is always dominated by r_3, but acquires a new temperature-dependence from interactions with the antiferromagnetic modes.

In region (d) of the phase diagram, defined by $r_2 > \mathcal{T}_2$ and $r_3 > \mathcal{T}_3^{2/3}$, the usual Fermi-liquid behaviour is observed. Here $\xi_3^{-2} = r_3$ and $\xi_2^{-2} = r_2$, both with corrections proportional to T^2.

3.4.6 Ginzburg Criterion in $d = 2$

We now use these results to investigate the boundaries of the regions where mean-field theory fails and the Ginzburg criterion is violated. For the ferromagnetic quantum critical point, we may use the same calculation as $d = 3$ and investigate $R_i(b)$ in the limit $b \to \infty$. We find the Ginzburg criterion for the ferromagnetic modes is violated when

$$\tilde{u_3}\mathcal{T}_3^{(G)} = r + \frac{2}{3}(n_3+2)\tilde{u_3}c'_{3Q}\mathcal{T}_3^{(G)} \ln\left(\frac{1}{\mathcal{T}_3^{(G)}}\right). \tag{3.4.54}$$

To calculate the Ginzburg criterion upon approaching the antiferromagnetic phase, we need to choose a scale b to evaluate the expression $\tilde{u_2}(b)\mathcal{T}_2(b) = R_2(b)$ at, because $\tilde{u_2}(b)$ decays logarithmically. We choose to evaluate it at b_2^*, so that $\delta_2(b_2^*) = 1$. The condition for the Ginzburg criterion becomes $\tilde{u_2}\mathcal{T}_2 = (\ln b_2^*)\, R_2(b_2^*)$. If the ferromagnetic modes are quantum critical, this is

$$\tilde{u_2}\mathcal{T}_2^{(G)} = \ln\left(\frac{1}{\mathcal{T}_2^{(G)}}\right)\left[r_2 + \frac{2}{3}2c'_{3Q}\tilde{w_3}\mathcal{T}_2^{(G)} \ln\left(\frac{1}{\mathcal{T}_2^{(G)}}\right)\right]. \tag{3.4.55}$$

If the ferromagnetic modes are Fermi liquid-like, this is instead

$$\tilde{u_2}\mathcal{T}_2^{(G)} = \ln\left(\frac{1}{\mathcal{T}_2^{(G)}}\right)\left[r_2 + c'_{2Q}\tilde{u_2}\mathcal{T}_2^{(G)} \frac{\ln\left(\ln\left(\frac{1}{\mathcal{T}_2^{(G)}}\right)\right)}{\ln\left(\frac{1}{\mathcal{T}_2^{(G)}}\right)}\right]. \tag{3.4.56}$$

3.4.7 Phase Diagram in $d = 2$

We are now in a position to construct the phase diagram in $d = 2$, using the solutions of the renormalised tuning parameter equation and the Ginzburg criterion in Sections 3.4.5 and 3.4.6. The phase diagram is plotted in Figure 3.6 in the $r - T$ plane, where $r_3 = g + r$ and $r_2 = g - r$ and $g > 0$. This has a ferromagnetic QCP at $r = -g$ and an antiferromagnetic QCP at $r = g$. The two QCPs coalesce to a quantum multicritical point at $r = 0$ when $g = 0$.

As in the three dimensional case, the phase diagram looks like two quantum critical points

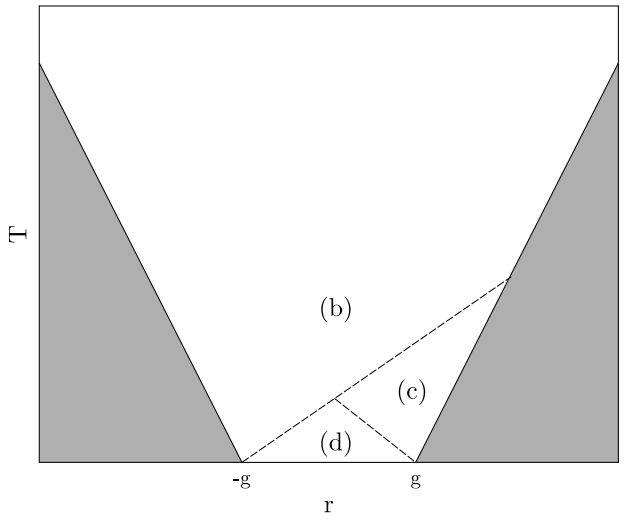

(a) Crossovers between the Fermi liquid-like and quantum critical regimes associated with each order parameter

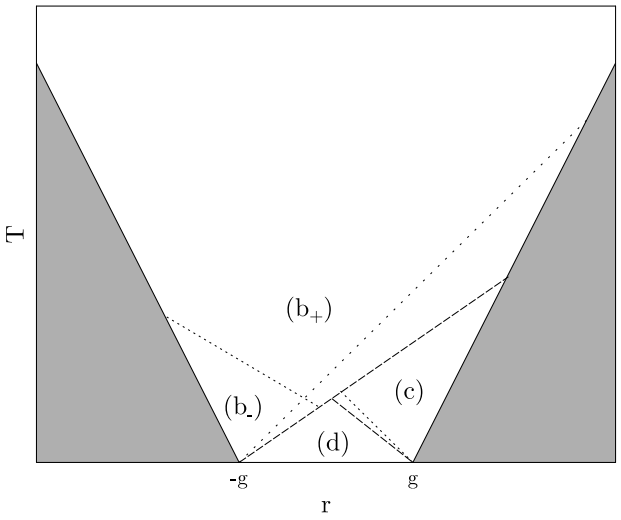

(b) Crossovers between regions where the contributions to the correlation lengths are different

Figure 3.6: Phase diagram of a quantum multicritical point in $d = 2$, with $r_3 = g + r$ and $r_2 = g - r$. The regions and their crossovers are explained in the main text.

separated by a distance $2g$. This picture is complicated by the result that when the ferromagnetic modes are in the quantum critical regime, the antiferromagnetic modes acquire a strong temperature-dependent renormalisation. This pushes them out of the quantum critical regime, meaning we do not simultaneously have quantum critical ferromagnetic and antiferromagnetic modes. We split region (b) in the phase diagram into (b_+), where the antiferromagnetic correlation length is dominated by temperature, and (b_-), where it is dominated by the antiferromagnetic tuning parameter r_2.

In region (b_-) the antiferromagnetic correlation length acquires the temperature-dependence usually associated with the ferromagnetic correlation length. This in turn changes the power law of the line on the phase diagram where the Ginzburg criterion is violated upon approaching the antiferromagnetic QCP.

3.5 Thermodynamic Quantities

Now that the regions of the phase diagram have been identified in Sections 3.4.4 and 3.4.7, we calculate the thermodynamic properties near a quantum multicritical point. The specific heat, thermal expansion, and Grüneisen parameter can be found by analysing equation (3.3.35) for the free energy. Solving this equation yields

$$F = -\sum_{i=3,2} \frac{n_i}{2} \int_0^\infty dx e^{-(d+z_i)x} f_i^{(0)} \left(R_i(e^x) e^{2x}, \mathcal{T}_i e^{z_i x} \right), \tag{3.5.1}$$

which is simply the sum of the free energies associated with the two types of fluctuation, weighted by the kinetic coefficients,

$$F = \frac{1}{\eta_3} F_3 + \frac{1}{\eta_2} F_2. \tag{3.5.2}$$

Here, F_i is the free energy associated with the corresponding $z = z_i$ Hertz-Millis quantum critical point, given by equation (2.4.20). The kinetic coefficients are taken at their bare values, $\eta_3 = 1$ and $\eta_2 = \left(\frac{c_3}{c_2}\right)^2$, where c_3 and c_2 are defined in equation (3.3.4).

The only difference between the free energy here and the sum of the two free energies in Chapter 2 is that the temperature-dependence of the correlation lengths has changed. We find that this does not affect the leading order temperature-dependence of the thermal expansion or the specific heat in any region of the phase diagram.

We may then differentiate the free energy for the specific heat and find that $C = \eta_3 C_3 + \eta_2 C_2$ where C_2 and C_3 are the specific heats for a Hertz-Millis QCP defined in equation (2.4.21). In calculating the thermal expansion, we must know how the two tuning parameters r_2 and r_3 depend on pressure. We assume that both of these parameters depend linearly on the applied pressure p, so that $\frac{dr_2}{dp} = a_2$ and $\frac{dr_3}{dp} = a_3$ are both constants, which are not necessarily of the same sign. Again, using the results of Section 2.4.4, we may write the thermal expansion as the sum of the thermal expansion associated with each type of mode, as $\alpha = \alpha_3 + \alpha_2$ where

α_2 and α_3 are the thermal expansions for a Hertz-Millis QCP defined in equation (2.4.4). The thermal expansion in this equation includes the term $\frac{\partial \xi_i^{-2}}{\partial p}$, and so each contribution to the thermal expansion in the multicritical case should be multiplied by a_2 or a_3.

Using the results of Section 2.4.4 we find the specific heat and thermal expansion in each region the phase diagram, and list them in three dimensions in Table 3.1 and in two dimensions in Table 3.2.

In three dimensions, in region (a) the specific heat is dominated by the $T \ln\left(\frac{1}{T}\right)$ term from the ferromagnetic modes, and the $T^{3/2}$ contribution from the antiferromagnetic modes is subleading. The ferromagnetic contribution to the thermal expansion is also dominated by the ferromagnetic $T^{1/3}$ term over the antiferromagnetic $T^{1/2}$ term. In the remaining 3 regions of the phase diagram, neither the ferromagnetic nor the antiferromagnetic contributions to the thermal expansion and specific heat can be argued to vanish throughout the whole of the region. The Grüneisen parameter is the ratio $\Gamma = \alpha/C$. In region (a) of the phase diagram this is equal to $\Gamma = a_3 \left(T^{2/3} \ln\left(\frac{1}{T}\right)\right)^{-1}$ which is the same as for a ferromagnetic quantum critical point. In the other three regions, this ratio cannot be reduced to a simple power law.

In two dimensions, in region (b_+) the specific heat is dominated by the $T^{2/3}$ term from the ferromagnetic modes. The subleading contribution from the antiferromagnetic modes is $T \ln\left(\frac{1}{\xi_2^{-2}}\right)$, which is $T \ln\left(\frac{1}{T}\right)$. The thermal expansion is also dominated by the ferromagnetic contribution $a_3 \ln\left(\frac{1}{T}\right)$. The subleading antiferromagnetic contribution is $\frac{T}{\xi_2^2}$ which is $\frac{1}{\ln\left(\frac{1}{T}\right)}$. In the other regions of the phase diagram neither the ferromagnetic contribution nor the antiferromagnetic contribution to either the thermal expansion or specific heat can be argued to vanish for the whole of the region. In region (b_+) the Grüneisen parameter is proportional to $T^{-2/3} \ln\left(\frac{1}{T}\right)$ which is the same for a ferromagnetic QCP in $d = 2$ in the quantum critical region. In the other regions of the phase diagram the Grüneisen parameter cannot be written as a simple power law.

	C	α
(a)	$T\ln\left(\frac{1}{T}\right)$	$a_3 T^{1/3}$
(b)	$T\ln\left(\frac{1}{T}\right) - Tr_2^{1/2}$	$a_3 T^{1/3} + a_2 T r_2^{-1/2}$
(c)	$T\ln\left(\frac{1}{r_3}\right) - T^{3/2}$	$a_3 T r_3^{-1} + a_2 T^{1/2}$
(d)	$T\ln\left(\frac{1}{r_3}\right) - Tr_2^{1/2}$	$a_3 T r_3^{-1} + a_2 T r_2^{-1/2}$

Table 3.1: Specific heat and thermal expansion in the regions of the phase diagram in $d = 3$. The regions of the phase diagram are explained in the main text.

	C	α
(b_+)	$T^{2/3}$	$a_3 \ln\left(\frac{1}{T}\right)$
(b_-)	$T^{2/3}$	$a_3 \ln\left(\frac{1}{T}\right) + a_2 \frac{T}{r_2}$
(c)	$Tr_3^{-1/2} + T\ln\left(\frac{1}{T}\right)$	$a_3 T r_3^{-3/2} + a_2 \ln\left(\ln\left(\frac{1}{T}\right)\right)$
(d)	$Tr_3^{-1/2} + T\ln\left(\frac{1}{r_2}\right)$	$a_3 T r_3^{-3/2} + a_2 T r_2^{-1}$

Table 3.2: Specific heat and thermal expansion in the regions of the phase diagram in $d = 2$. The regions of the phase diagram are explained in the main text.

3.6 Conclusions

3.6.1 Summary of Results

By adapting Hertz-Millis theory, in Section 3.3 we constructed a Hertz-Millis model of a quantum multicritical point in terms of spin-fluctuations alone. We have restricted our analysis to metallic systems so that the spin-fluctuations are damped according to Hertz-Millis theory, and only consider materials which have competing ferromagnetism and antiferromagnetism. We have only analysed the model in two and three spatial dimensions. We used a one-loop RG procedure, which enabled us to find the regions of the phase diagram and the correlation lengths in Section 3.4, and the specific heat, thermal expansion and Grüneisen parameter in Section 3.5.

We find it helpful to think about results in terms of two quantum critical points interacting with each other, which can be brought together to form the multicritical point. Since the quartic interaction terms are irrelevant in the RG sense, we find that there is no difference between a quantum bicritical point and a tetracritical point, defined by $4u_2u_3 > u_{32}^2$ and

$4u_2u_3 < u_{32}^2$ respectively. Our main conclusion is that ferromagnetism dominates.

In the region of the phase diagram where both types of order would be expect to be quantum critical (region (a) in Figure 3.5 in three dimensions and region (b_+) in Figure 3.6 in two dimensions), ferromagnetism dominates. The specific heat, thermal expansion and Grüneisen parameter are all dominated by the contribution from the ferromagnetic modes, and the observed power laws are those associated with a ferromagnetic quantum critical point. Interactions with quantum critical ferromagnetic modes also cause the antiferromagnetic correlation length to acquire the temperature-dependence usually associated with ferromagnetic correlations. In three dimensions this changes the boundary of the antiferromagnetically ordered phase in a way that suppresses antiferromagnetic order. In two dimensions it changes the boundary where the Ginzburg criterion is violated upon approaching the antiferromagnetic QCP. The strong temperature-dependent renormalisation to the antiferromagnetic tuning parameter pushes the antiferromagnetic modes out of the quantum critical regime in region (b_+) of the phase diagram, which affects subleading contributions to thermodynamic properties.

3.6.2 Link to Experiments and Outlook

We now look back to the experiments discussed in Section 3.6.2 and compare our results to them. In Section 3.5 we found that in the presence of quantum critical fluctuations of both ferromagnetism and antiferromagnetism, ferromagnetism dominates thermodynamic properties. These results are consistent with the experimental data on $NbFe_2$ and $Ta(Fe_{1-x}V_x)_2$ where the specific heat obeys $C \sim T \ln\left(\frac{1}{T}\right)$ usually associated with three dimensional ferromagnetism. To our knowledge no thermal expansion measurements have been performed on these materials, but we would expect to see the thermal expansion vary as $\alpha \sim T^{1/3}$ and a Grüneisen parameter obeying $\Gamma \sim 1/\left(T^{2/3} \ln\left(\frac{1}{T}\right)\right)$, as would be expected of a ferromagnet in three dimensions.

Another prediction of this theory is the shape of the boundaries on the phase diagram, which are predicted in Sections 3.4.4 and 3.4.7. While the phase diagrams of both $NbFe_2$ and

$Ta(Fe_{1-x}V_x)_2$ are known [4, 8], for both materials there are not enough data points on the boundary of the antiferromagnetic phase to determine the power law and test the prediction of the theory.

The theory we have developed appears to be consistent with experimental data on $NbFe_2$ and $Ta(Fe_{1-x}V_x)_2$, but questions still remain. In the analysis presented here ferromagnetism seems to dominate everything, so the experimental evidence that resistivity in $NbFe_2$ and $Ta(Fe_{1-x}V_x)_2$ is dominated by antiferromagnetism is somewhat of a surprise. In Chapter 4 we solve the Boltzmann transport equation to find the resistivity of the model described in this chapter and show that the power-law usually associated with the antiferromagnetic QCP does dominate. We are able to explain why this is the case, and why this power law is actually stabilised in the presence of ferromagnetic fluctuations.

The results we have derived rely upon the antiferromagnetic ordering wavevector $\boldsymbol{Q}$ being sufficiently large. There has been some discussion in the literature as to whether the antiferromagnetic wavevector in $Nb_{1-y}Fe_{2+y}$ is always finite or whether it smoothly evolves from zero with doping [7]. In Chapter 4 we show that the observed $T^{3/2}$ power law relies upon the presence of strong scattering at a finite $\boldsymbol{Q}$.

Another issue that we wish to address is the problems with the model itself. As explained in Section 2.5, Hertz-Millis theory is hindered by the fact that integrating out the electronic modes to construct an effective theory in terms of spin-fluctuations alone is not a safe thing to do, as non-analytic terms arise in the effective action when a more careful analysis is done. Despite this, Hertz-Millis theory correctly predicts power laws in many systems [1]. Since the model we derive in equation (3.3.13) also ignores these non-analytic terms, it is also plagued by the same illnesses. We must then question to what extent we trust the predictions of this model.

For the same reason that no true ferromagnetic QCPs exist, we would expect that a true quantum multicritical point between ferro- and antiferromagnetism could never exist. At some low temperature the ferromagnetic QCP would be driven first order by the non-analytic terms

which should exist in the model if the electrons are integrated out more carefully, as in Section 2.5. However, above a typical energy scale induced by these non-analyticities we would expect the thermodynamic properties of the material to be dominated by quantum critical fluctuations of both ferromagnetic and antiferromagnetic order. Above this energy scale, we expect our predictions to hold.

Even though the experimental links suggest our model is to be trusted, in Chapter 5 we analyse a quantum multicritical model where the non-analytic terms do not arise. Specifically, we analyse a metamagnetic quantum critical end-point described by the dynamical exponent $z = 3$ interacting with a $z = 2$ antiferromagnetic QCP. Metamagnetic transitions occur at finite magnetic fields, and these fields wipe out the non-analyticities associated with the ferromagnetic QCP. However, the magnetic field adds its own complications so we devote all of Chapter 5 to an analysis of this model.

Chapter 4

TRANSPORT NEAR A QUANTUM MULTICRITICAL POINT

In the previous chapter we demonstrated that at a quantum multicritical point, ferromagnetism seems to dominate the thermodynamic quantities. Our prediction that the ferromagnetic contribution dominates the specific heat agrees with experiments on $NbFe_2$, $Ta(Fe_{1-x}V_x)_2$ and $YbRh_2Si_2$. In $YbRh_2Si_2$ our prediction that the Grüneisen parameter is dominated by the ferromagnetic term is also seen.

One quantity which cannot be obtained directly from the renormalisation group approach of the previous chapter is the resistivity, as it is not a simple derivative of the free energy. In both $NbFe_2$ and $Ta(Fe_{1-x}V_x)_2$ this is seen to obey a $\rho = \rho_0 + cT^{3/2}$ power law, which would usually be associated with antiferromagnetic quantum criticality in a disordered system.

The resistivity near quantum critical points is well-understood. In a material near a ferromagnetic quantum critical point the resistivity obeys a $T^{5/3}$ power law [44]. Near an antiferromagnetic quantum critical point, in perfectly clean systems a T^2 resistivity is expected whereas in disordered systems a $T^{3/2}$ power law is expected at low temperatures. However, in these disordered systems there is a large crossover region with an almost-linear power law [45].

If one were to naively suppose that the ferromagnetic scattering process provides a $T^{5/3}$ contribution to the resistivity and the antiferromagnetic scattering process provides a $T^{3/2}$

power law, then we could conclude that the antiferromagnetism would dominate, as is experimentally observed. We shall show in this chapter that this justification is flawed. We perform numerical calculations to investigate the resistivity near a quantum multicritical point in three dimensions. We shall show that the ferromagnetic fluctuations actually stabilise the $T^{3/2}$ power law, and even in clean systems we expect this power law to hold.

We first discuss the methods involved in calculating the resistivity, and how they have been applied to quantum criticality. Section 4.1 is a background section where we review the Boltzmann equation, and how it can be used to find the resistivity. In Section 4.2 we review the literature documenting the application of the Boltzmann equation to the ferromagnetic and antiferromagnetic quantum critical points. We also write the equations in a form which we find convenient to numerically study in subsequent sections. In Section 4.3 we discuss original research on how the Boltzmann equation can be used to find the resistivity near a quantum multicritical point. We discuss the results in Section 4.3.2 and conclude by referring back to the experimental data in Section 4.5.

4.1 The Boltzmann Equation

4.1.1 Origin of the Boltzmann Equation

In this section we discuss the Boltzmann equation, which we use in this chapter to find transport properties near a quantum multicritical point. We begin by discussing the origin of the transport equation, before discussing how it can be used to find the resistivity. The Boltzmann equation gives the change in quasiparticle distribution under applied electric fields. In this section we follow the arguments of Ziman [46], but restrict our arguments to spatially homogeneous systems in the absence of temperature gradients or spatially varying chemical potentials.

Under application of an electric field to a material, the electronic quasiparticles accelerate along the direction of the field. They continue accelerating until they are scattered into a

different state, where the scattering mechanism can be disorder, phonons, or in this case spin-fluctuations. Once scattered to a new state, they begin their acceleration process again. The current can be described in terms of an average drift velocity of the electrons, which does not change over time.

Instead of considering the individual electronic quasiparticles, it is more convenient to consider the quasiparticle distribution function $f_{\boldsymbol{k}}$ which is the number of electronic quasiparticles with momentum $\boldsymbol{k}$. The goal is to find a steady-state solution in the presence of external fields and scattering processes.

In the presence of external fields, the rate of change of the quasiparticles' wavevectors is given by

$$\frac{d\boldsymbol{k}}{dt} = \frac{e}{\hbar}\left(\boldsymbol{E} + \frac{1}{c}\boldsymbol{v}_{\boldsymbol{k}} \wedge \boldsymbol{H}\right), \tag{4.1.1}$$

and so in a small time interval t, the wavevector $\boldsymbol{k}$ of a particle changes to $\boldsymbol{k} + \dot{\boldsymbol{k}}t$. This means that $f_{\boldsymbol{k}}(t) = f_{\boldsymbol{k}-\dot{\boldsymbol{k}}t}(0)$, leading to

$$\left.\frac{\partial f_{\boldsymbol{k}}}{\partial t}\right|_{\text{fields}} = -\dot{\boldsymbol{k}}.\frac{\partial f_{\boldsymbol{k}}}{\partial \boldsymbol{k}} = -\frac{e}{\hbar}\left(\boldsymbol{E} + \frac{1}{c}\boldsymbol{v}_{\boldsymbol{k}} \wedge \boldsymbol{H}\right)\boldsymbol{\nabla}_{\boldsymbol{k}} f_{\boldsymbol{k}}, \tag{4.1.2}$$

where $\nabla_{\boldsymbol{k}} \equiv \frac{\partial}{\partial \boldsymbol{k}}$.

The scattering processes are characterised by the quantity $\mathcal{P}_{\boldsymbol{k'k}} d\boldsymbol{k'}$ which is the probability of scattering from the state $\boldsymbol{k}$ to a state in the vicinity of $\boldsymbol{k'}$. We can write this in terms of the *intrinsic probability* $\mathcal{L}_{\boldsymbol{k'k}}$ which is the probability of the transition if $\boldsymbol{k}$ is full and $\boldsymbol{k'}$ is empty, as

$$\mathcal{P}_{\boldsymbol{k'k}} d\boldsymbol{k'} = f_{\boldsymbol{k}}\left(1 - f_{\boldsymbol{k'}}\right)\mathcal{L}_{\boldsymbol{k'k}}, \tag{4.1.3}$$

which enables us to write the scattering rate as

$$\left.\frac{df_{\boldsymbol{k}}}{dt}\right|_{\text{scatt}} = \int d\boldsymbol{k'} \left[f_{\boldsymbol{k'}} \left(1 - f_{\boldsymbol{k}}\right) \mathcal{L}^{\boldsymbol{k}}_{\boldsymbol{k'}} - f_{\boldsymbol{k}} \left(1 - f_{\boldsymbol{k'}}\right) \mathcal{L}^{\boldsymbol{k'}}_{\boldsymbol{k}} \right]. \tag{4.1.4}$$

The Boltzmann transport equation is the statement that in the steady state, the quasiparticle distribution does not change in time,

$$\left.\frac{df_{\boldsymbol{k}}}{dt}\right|_{\text{fields}} + \left.\frac{df_{\boldsymbol{k}}}{dt}\right|_{\text{scatt}} = 0, \tag{4.1.5}$$

for all $\boldsymbol{k}$. For small external fields we may linearise the Boltzmann equation around the equilibrium particle distribution $f^0_{\boldsymbol{k}}$. Defining $g_{\boldsymbol{k}} = f_{\boldsymbol{k}} - f^0_{\boldsymbol{k}}$, we find that the linearised Boltzmann equation can be written as

$$e\frac{\partial f^0_{\boldsymbol{k}}}{\partial \epsilon_{\boldsymbol{k}}} \boldsymbol{v}_{\boldsymbol{k}} . \boldsymbol{E} = \left.\frac{df_{\boldsymbol{k}}}{dt}\right|_{\text{scatt}} - \frac{e}{\hbar c} \left(\boldsymbol{v}_{\boldsymbol{k}} \wedge \boldsymbol{H}\right) . \frac{\partial g_{\boldsymbol{k}}}{\partial \boldsymbol{k}}, \tag{4.1.6}$$

where we have used that $\boldsymbol{v}_{\boldsymbol{k}} = \frac{1}{\hbar}\frac{\partial \epsilon_k}{\partial \boldsymbol{k}}$.

It is more convenient to make the transformation $g_{\boldsymbol{k}} = -\Phi_{\boldsymbol{k}} \frac{\partial f^0_{\boldsymbol{k}}}{\partial \epsilon_{\boldsymbol{k}}}$ so that

$$f_{\boldsymbol{k}} = f^0_{\boldsymbol{k}} + \Phi_{\boldsymbol{k}} \frac{f^0_{\boldsymbol{k}} \left(1 - f^0_{\boldsymbol{k}}\right)}{k_B T}. \tag{4.1.7}$$

$\Phi_{\boldsymbol{k}}$ can be interpreted as the average extra energy the quasiparticles in state $\boldsymbol{k}$ have, but our main reason for using this variable is that the resistivity can be calculated from the shape of $\Phi_{\boldsymbol{k}}$ alone, and does not depend on the overall magnitude.

In terms of $\Phi_{\boldsymbol{k}}$ the linearised Boltzmann equation is

$$e\frac{\partial f^0_{\boldsymbol{k}}}{\partial \epsilon_{\boldsymbol{k}}} \boldsymbol{v}_{\boldsymbol{k}} . \boldsymbol{E} = \frac{1}{k_B T} \int d\boldsymbol{k'} \mathcal{P}^0_{\boldsymbol{k'k}} \left[\Phi_{\boldsymbol{k'}} - \Phi_{\boldsymbol{k}}\right] + \frac{e}{\hbar c} \left(\boldsymbol{v}_{\boldsymbol{k}} \wedge \boldsymbol{H}\right) . \frac{\partial}{\partial \boldsymbol{k}} \left[\Phi_{\boldsymbol{k}} \frac{\partial f^0_{\boldsymbol{k}}}{\partial \epsilon_{\boldsymbol{k}}}\right]. \tag{4.1.8}$$

In writing this we have used the principle of microscopic reversibility, which is that

$$\mathcal{L}^{\boldsymbol{k}}_{\boldsymbol{k'}} f^0_{\boldsymbol{k'}} \left(1 - f^0_{\boldsymbol{k}}\right) = \mathcal{L}^{\boldsymbol{k'}}_{\boldsymbol{k}} f^0_{\boldsymbol{k}} \left(1 - f^0_{\boldsymbol{k'}}\right) = \mathcal{P}^0_{\boldsymbol{k'k}}, \tag{4.1.9}$$

where the 0 superscript on $\mathcal{P}$ means in equilibrium in the absence of external fields, as it includes the relevant occupation factors.

In this chapter we are only interested in the resistivity of materials under zero external magnetic field. In this case the Boltzmann equation becomes

$$e f^0_{\boldsymbol{k}} \left(1 - f^0_{\boldsymbol{k}}\right) \boldsymbol{v_k}.\boldsymbol{E} = \int d\boldsymbol{k'} \mathcal{P}^0_{\boldsymbol{k'k}} \left[\Phi_{\boldsymbol{k}} - \Phi_{\boldsymbol{k'}}\right]. \tag{4.1.10}$$

In this equation all quantities are known except the function $\Phi_{\boldsymbol{k}}$, which is found by solving this equation. It is this equation which we shall study where the scattering probabilities $\mathcal{P}^0_{\boldsymbol{k'k}}$ come from the scattering from quantum critical spin-fluctuations.

4.1.2 Resistivity from the Boltzmann Equation

We now describe two methods of calculating the resistivity from the function $\Phi_{\boldsymbol{k}}$ given in the Boltzmann equation, by again following the arguments of Ziman [46].

Once the Boltzmann equation has been solved for $\Phi_{\boldsymbol{k}}$, the resistivity can be directly calculated from the quasiparticle distribution as the net current is given by

$$\boldsymbol{J} = \sigma \boldsymbol{E} = e \int d\boldsymbol{k} \boldsymbol{v_k} f_{\boldsymbol{k}} = \frac{e}{k_B T} \int d\boldsymbol{k} \boldsymbol{v_k} f^0_{\boldsymbol{k}} \left(1 - f^0_{\boldsymbol{k}}\right) \Phi_{\boldsymbol{k}}. \tag{4.1.11}$$

In the case where $\boldsymbol{J}$ is parallel to $\boldsymbol{E}$ and σ is a scalar, using $\rho = 1/\sigma$ we find

$$\rho = \frac{E}{\frac{e}{k_B T} \int d\boldsymbol{k} \boldsymbol{v_k}.\hat{\boldsymbol{n}} f^0_{\boldsymbol{k}} \left(1 - f^0_{\boldsymbol{k}}\right) \Phi_{\boldsymbol{k}}}, \tag{4.1.12}$$

where $\hat{\boldsymbol{n}}$ is a unit vector in the direction of the electric field and $E = |\boldsymbol{E}|$. In general, the

resultant current may depend heavily on the orientation of the electric field, and may not necessarily be parallel to the applied electric field. This leads to the conductivity and resistivity being tensors. However, in this thesis we shall only consider Fermi surfaces such that the resultant current is parallel to the applied field, which means the off-diagonal elements of the conductivity and resistivity tensors will be zero.

From this equation it may look like the magnitude of $\Phi_{\boldsymbol{k}}$ at all points is needed to find the resistivity. However, it turns out only the shape of $\Phi_{\boldsymbol{k}}$ is needed to find the resistivity. This can be shown by multiplying equation (4.1.10) by $\Phi_{\boldsymbol{k}}$ and performing an integral over $\boldsymbol{k}$. Using that $\mathcal{P}^0_{\boldsymbol{k}\boldsymbol{k'}} = \mathcal{P}^0_{\boldsymbol{k'}\boldsymbol{k}}$ we see that the right hand side becomes

$$\int d\boldsymbol{k} d\boldsymbol{k'} \mathcal{P}^0_{\boldsymbol{k}\boldsymbol{k'}} \left(\Phi_{\boldsymbol{k}} - \Phi_{\boldsymbol{k'}}\right) \Phi_{\boldsymbol{k}} = \frac{1}{2} \int d\boldsymbol{k} d\boldsymbol{k'} \mathcal{P}^0_{\boldsymbol{k}\boldsymbol{k'}} \left(\Phi_{\boldsymbol{k}} - \Phi_{\boldsymbol{k'}}\right)^2, \tag{4.1.13}$$

and then the resultant equation can be rearranged for $|\boldsymbol{E}|$ and substituted into the equation for the resistivity to yield

$$\rho = \frac{\frac{k_B T}{2} \int d\boldsymbol{k} d\boldsymbol{k'} \mathcal{P}^0_{\boldsymbol{k}\boldsymbol{k'}} \left(\Phi_{\boldsymbol{k}} - \Phi_{\boldsymbol{k'}}\right)^2}{\left(e \int d\boldsymbol{k} \boldsymbol{v}_{\boldsymbol{k}} . \hat{\boldsymbol{n}} f^0_{\boldsymbol{k}} \left(1 - f^0_{\boldsymbol{k}}\right) \Phi_{\boldsymbol{k}}\right)^2}. \tag{4.1.14}$$

This is clearly independent of the overall magnitude of the $\Phi_{\boldsymbol{k}}$, which makes physical sense as a larger overall Φ will produce a larger current, whereas the resistivity should not depend on the size of the current, providing it is still small enough such that the linearised Boltzmann equation still holds.

In fact, $\Phi_{\boldsymbol{k}}$ can be found directly by considering the resistivity as a functional of $\Phi_{\boldsymbol{k}}$. The actual form the quasiparticle distribution takes is the one which minimises the resistivity. We shall now show this to be the case, again following the arguments of Ziman [46]. The Boltzmann equation is an equation of the form $X = \hat{P}\Phi$, where X is a known function, $\hat{P}$ is a known scattering operator, and Φ is the unknown function we wish to find. If we define an

inner product

$$\langle \Phi, \Psi \rangle \equiv \int d\boldsymbol{k} \Phi_{\boldsymbol{k}} \Psi_{\boldsymbol{k}}, \tag{4.1.15}$$

then we see that since $\mathcal{P}^0_{\boldsymbol{k}\boldsymbol{k}'} = \mathcal{P}^0_{\boldsymbol{k}'\boldsymbol{k}}$, the operator $\hat{P}$ is self-adjoint with respect to this inner product, meaning $\left\langle \Phi, \hat{P}\Psi \right\rangle = \left\langle \Psi, \hat{P}\Phi \right\rangle$. We also note that since $\mathcal{P}$ represents the probability of scattering, no elements can be negative. This means that $\left\langle \Phi, \hat{P}\Phi \right\rangle \geq 0$ for any function Φ.

If we take the inner product of the Boltzmann equation with Φ, we find $\left\langle \Phi, \hat{P}\Phi \right\rangle = \langle \Phi, X \rangle$. We consider another function Ψ that satisfies this relation $\left\langle \Psi, \hat{P}\Psi \right\rangle = \langle \Psi, X \rangle$, but does not satisfy the Boltzmann equation, $\hat{P}\Psi \neq X$. We must have that

$$0 \leq \left\langle (\Phi - \Psi), \hat{P}(\Phi - \Psi) \right\rangle, \tag{4.1.16}$$

which after expanding out can be shown to be equal to

$$0 \leq \left\langle \Phi, \hat{P}\Phi \right\rangle - \left\langle \Psi, \hat{P}\Psi \right\rangle, \tag{4.1.17}$$

where we have used that $\left\langle \Psi, \hat{P}\Phi \right\rangle = \langle \Psi, X \rangle = \left\langle \Psi, \hat{P}\Psi \right\rangle$.

This is the statement that the function which satisfies the Boltzmann equation is the function which maximises $\left\langle \Phi, \hat{P}\Phi \right\rangle$ subject to the constraint that $\left\langle \Phi, \hat{P}\Phi \right\rangle = \langle \Phi, X \rangle$. If we rescale $\Phi \to c\Phi$ and choose c so that this constraint is obeyed, we find $c = \frac{\langle \Phi, X \rangle}{\left\langle \Phi, \hat{P}\Phi \right\rangle}$ and so the function which maximises $c^2 \left\langle \Phi, \hat{P}\Phi \right\rangle$ is the function which maximises $\frac{|\langle \Phi, X \rangle|^2}{\left\langle \Phi, \hat{P}\Phi \right\rangle}$. This is, the function which satisfies the Boltzmann equation is the function that minimises

$$\frac{\left\langle \Phi, \hat{P}\Phi \right\rangle}{|\langle \Phi, X \rangle|^2} \tag{4.1.18}$$

which by comparing with equation (4.1.14) we see is proportional to the resistivity.

In this chapter, we shall be finding the function $\Phi_{\boldsymbol{k}}$ using analytic and numeric techniques.

We shall use both the Boltzmann equation in the form of equation (4.1.10), and the resistivity functional of equation (4.1.14) to find the quasiparticle distribution and calculate the resistivity. Since we have now found the starting point, we move on to finding the resistivity due to various scattering mechanisms.

4.2 The Three Individual Scattering Mechanisms

In this section we shall review the literature on the three individual scattering mechanisms that are present near the quantum multicritical point we wish to consider - impurities, ferromagnetic spin-fluctuations, and antiferromagnetic spin-fluctuations. All three scattering mechanisms are important at a quantum multicritical point, and we expect to recover the power laws associated with each type of scattering mechanism independently in certain limits. We first review impurity scattering in Section 4.2.1, then ferromagnetic scattering in Section 4.2.2, and antiferromagnetic scattering in Section 4.2.3. We do this such that in Section 4.3 we are able to analyse the resistivity near a quantum multicritical point.

4.2.1 Impurity Scattering

Scattering from impurities alone is the most simple scattering mechanism we shall review the literature on. It is also the only situation we shall discuss where the Boltzmann equation can be solved exactly [46, 47]. In this section we review the standard techniques in some amount of detail.

In this case, the scattering matrix is

$$\mathcal{P}^0_{\boldsymbol{k}'\boldsymbol{k}} = f^0_{\boldsymbol{k}'}\left(1 - f^0_{\boldsymbol{k}}\right) g^2_{\text{imp}} \delta\left(\epsilon_{\boldsymbol{k}} - \epsilon_{\boldsymbol{k}'}\right), \tag{4.2.1}$$

where the delta function ensures no energy is lost to the impurities during the scattering

process - the scattering is elastic. The Boltzmann equation in this situation becomes

$$ef^0_{\boldsymbol{k}}\boldsymbol{v}_{\boldsymbol{k}}.\boldsymbol{E} = g^2_{\text{imp}} \int d\boldsymbol{k'} f^0_{\boldsymbol{k'}} \delta\left(\epsilon_{\boldsymbol{k}} - \epsilon_{\boldsymbol{k'}}\right) \left[\Phi_{\boldsymbol{k}} - \Phi_{\boldsymbol{k'}}\right]. \tag{4.2.2}$$

To proceed we convert the integral on the right hand side into an integral over an equal-energy surface. The integral is of the form

$$\int d\boldsymbol{k} \delta\left(\epsilon_{\boldsymbol{k}} - \epsilon\right), \tag{4.2.3}$$

where ϵ is just a constant. Since $\frac{\partial \epsilon_{\boldsymbol{k}}}{\partial \boldsymbol{k}} = \hbar \boldsymbol{v}_{\boldsymbol{k}}$, the velocity $\boldsymbol{v}_{\boldsymbol{k}}$ must be perpendicular to the equal energy surface. We then integrate over the component perpendicular to the equal energy surface and find that

$$\int d\boldsymbol{k} \delta\left(\epsilon_{\boldsymbol{k}} - \epsilon\right) = \oint \frac{d\boldsymbol{k}}{\hbar v_{\boldsymbol{k}}}, \tag{4.2.4}$$

where the integral is now over all points on the surface, and $v_{\boldsymbol{k}}$ is the magnitude of the velocity at point $\boldsymbol{k}$.

Applied to equation (4.2.2), we find that

$$e\boldsymbol{v}_{\boldsymbol{k}}.\boldsymbol{E} = g^2_{\text{imp}} \oint \frac{d\boldsymbol{k'}}{\hbar v_{\boldsymbol{k'}}} \left[\Phi_{\boldsymbol{k}} - \Phi_{\boldsymbol{k'}}\right], \tag{4.2.5}$$

where the $\boldsymbol{k'}$ integral is a over a surface in reciprocal space where $\epsilon_{\boldsymbol{k'}} = \epsilon_{\boldsymbol{k}}$.

To proceed, we consider a spherical Fermi surface which has the free electron dispersion $\epsilon_{\boldsymbol{k}} = \frac{\hbar^2 k^2}{2m}$, then $\boldsymbol{E}.\boldsymbol{v}_{\boldsymbol{k}} = E v_k \cos\theta$, where θ is the angle from the axis of the electric field. We use the notation v_k to mean $|\boldsymbol{v}_{\boldsymbol{k}}|$ as the magnitude of the velocity only depends on the modulus of $\boldsymbol{k}$ with this dispersion relation. Switching to polar co-ordinates and using that

$k^2 = v_k^2 m^2/\hbar^2$ we find

$$\frac{e\hbar^3 E}{m^2 g_{\text{imp}}^2}\cos\theta = \int \frac{d\theta' d\phi'}{(2\pi)^3}\sin\theta'\left[\Phi\left(\theta,\phi\right) - \Phi\left(\theta',\phi'\right)\right]. \tag{4.2.6}$$

Since the left hand side of the equation does not depend on ϕ, we conclude that Φ is a function of θ only. It turns out that this equation is solved by $\Phi\left(\theta\right) = \alpha\cos\theta$, with

$$\alpha = \frac{2\pi^2 e\hbar^3 E}{m^2 g_{\text{imp}}^2}. \tag{4.2.7}$$

The resistivity can now be calculated from equation (4.1.12). If we substitute in $\Phi_{\boldsymbol{k}} = \alpha\cos\theta$, and switch to polar co-ordinates, we find that

$$\rho = \frac{k_B T E}{e\alpha}\left(\int d\boldsymbol{k} v_k f_k^0\left(1 - f_k^0\right)\cos^2\theta\right)^{-1}. \tag{4.2.8}$$

The function $f_{\boldsymbol{k}}^0\left(1 - f_{\boldsymbol{k}}^0\right)$ is sharply peaked at the Fermi surface, with an area of $k_B T$ underneath. Using this, we can perform the integral with respect to ϵ and simply evaluate k at the Fermi surface, where $k = k_F$. Then, we find that

$$\rho = \frac{E}{e\alpha}\left(\int \frac{d\theta}{(2\pi)^2}\frac{k_F^2}{\hbar}\sin\theta\cos^2\theta\right)^{-1}, \tag{4.2.9}$$

and so

$$\rho = \frac{3g_{\text{imp}}^2}{e^2 v_F^2}. \tag{4.2.10}$$

This shows that impurity scattering from impurities is *independent* of temperature. As mentioned in Section 1.6, the resistivity of a Fermi liquid is proportional to T^2, which comes from electron-electron scattering and is not captured in this equation.

We have shown that in the case of impurity scattering, the quasiparticle distribution takes

the form $\Phi(\theta) \sim \cos\theta$. Using that

$$f_{\boldsymbol{k}}(\epsilon) = f^0_{\boldsymbol{k}}(\epsilon) - \frac{\partial f^0_{\boldsymbol{k}}}{\partial \epsilon}\Phi_{\boldsymbol{k}}, \tag{4.2.11}$$

and that $\Phi(\theta) \sim \boldsymbol{v_k}.\boldsymbol{E}$, we find that

$$f_{\boldsymbol{k}}(\epsilon) \sim f^0_{\boldsymbol{k}}(\epsilon - \Phi). \tag{4.2.12}$$

In the case of $\Phi = c\boldsymbol{v_k}.\boldsymbol{E}e$,

$$f_{\boldsymbol{k}}(\epsilon) \sim f^0_{\boldsymbol{k}}(\epsilon - c\boldsymbol{v_k}.\boldsymbol{E}e), \tag{4.2.13}$$

which is physically interpreted as a *shifting* of the Fermi surface in reciprocal space along the direction of the electric field.

It is interesting to note that it can be analytically shown that $\Phi_{\boldsymbol{k}}$ takes the same form when the scattering mechanism is elastic and depends only upon the relative angle between the final and initial states. In that case, the analysis proceeds as above but with g^2_{imp} replaced by $\mathcal{M}(\chi)$, where χ is the angle between $\boldsymbol{k}$ and $\boldsymbol{k'}$. This leads to $\Phi(\theta) = \alpha\cos\theta$ with

$$\alpha = \frac{(2\pi)^2 eE\hbar^3}{m^2}\left(\int_0^\pi d\chi\,[1-\cos\chi]\sin\chi\mathcal{M}(\chi)\right)^{-1}. \tag{4.2.14}$$

We have demonstrated that the form of the quasiparticle distribution when only disorder is present is $\Phi(\theta) \sim \cos\theta$, which is interpreted as a shifting of the Fermi surface. The resistivity is a temperature-independent constant, but as we know from Section 1.6 that the electron-electron scattering processes lead to a resistivity proportional to T^2.

4.2.2 Ferromagnetic Spin-Fluctuations

We now review the literature on scattering from ferromagnetic spin fluctuations. This situation is slightly different from the impurity scattering case as the collisions are inelastic. This system can still be analysed using standard techniques, using the same methods that can be used to analyse scattering from phonons [46]. We follow that analysis here, adapted to ferromagnetic spin fluctuations.

To begin we need to consider the function analogous to $\Phi_{\boldsymbol{k}}$ but for spin-fluctuations, which we denote $\Psi_{\boldsymbol{q}}$. Then we need to consider the two processes of absorbing and emitting spin-fluctuations separately, and may write down that

$$\dot{f}_{\boldsymbol{k}}\big|_{\text{scatt}} = \frac{1}{k_B T}\int d\boldsymbol{k'}\left(\Phi_{\boldsymbol{k}} + \Psi_{\boldsymbol{q}} - \Phi_{\boldsymbol{k'}}\right)\mathcal{P}^{\boldsymbol{k'}}_{\boldsymbol{k},\boldsymbol{q}} + \frac{1}{k_B T}\int d\boldsymbol{k'}\left(\Phi_{\boldsymbol{k}} - \Psi_{\boldsymbol{q}} - \Phi_{\boldsymbol{k'}}\right)\mathcal{P}^{\boldsymbol{k'},\boldsymbol{q}}_{\boldsymbol{k}}, \quad (4.2.15)$$

where the first term is absorption of a spin-fluctuation, and the second is emission. If we then assume that the spin-fluctuations stay in equilibrium under the application of an electric field, then $\Psi_{\boldsymbol{q}} = 0$ and the spin-fluctuation distribution is given by the Bose distribution $n^0_{\boldsymbol{q}}(\omega)$. In this case the scattering is

$$\dot{f}_{\boldsymbol{k}}\big|_{\text{scatt}} = \frac{1}{k_B T}\int d\boldsymbol{k'}\left(\Phi_{\boldsymbol{k}} - \Phi_{\boldsymbol{k'}}\right)\mathcal{P}_{\boldsymbol{k}\boldsymbol{k'}}, \quad (4.2.16)$$

with

$$\mathcal{P}_{\boldsymbol{k},\boldsymbol{k'}} = \frac{2g_F^2}{\Gamma_3}\int_0^\infty d\omega \int d\boldsymbol{q}\delta\left(\boldsymbol{k}+\boldsymbol{q}-\boldsymbol{k'}\right)\delta\left(\epsilon_{\boldsymbol{k}}+\omega-\epsilon_{\boldsymbol{k'}}\right)n^0(\omega)\,f^0_{\boldsymbol{k}}\left(1-f^0_{\boldsymbol{k'}}\right)\Im\chi_3(\boldsymbol{q},\omega) \quad (4.2.17)$$

Here, $\chi_3(\boldsymbol{q},\omega)$ is the ferromagnetic spin susceptibility given by

$$\chi_3^{-1}(\boldsymbol{q},\omega) = r_3(T) + c_3^2 q^2 - \frac{i\omega}{\Gamma_3 c_3 q}, \quad (4.2.18)$$

for $\omega < \Gamma_3 c_3 q$, and zero otherwise [44]. Note that we do not include the η_3 coefficient of

Chapter 3, which is only necessary when performing a renormalisation group analysis. We have assumed that we may treat the spin-fluctuations using an effective Gaussian theory, so the tuning parameter $r_3(T)$ is the renormalised tuning parameter of Chapter 3, and it has acquired some temperature-dependence due to interactions. It is given by $r_3 + a_3 T^{3/2}$.

The resistivity can then be calculated from equation (4.1.14), which Mathon [44] has shown analytically to lead to a $T^{5/3}$ resistivity, under the approximation that $\Phi_{\boldsymbol{k}} \sim \cos\theta$.

We now deviate from following the literature. We evaluate the integrals in a different order to the analysis in Mathon [44]. Our aim is not to calculate the resistivity, but to instead write the resistivity in a form which is convenient to numerically investigate in Section 4.3.

The integral over $\boldsymbol{q}$ (within $\mathcal{P}^0_{\boldsymbol{k}\boldsymbol{k}'}$) can be performed by replacing $\boldsymbol{q}$ by $\boldsymbol{k}'-\boldsymbol{k}$ everywhere due to the delta function. It is more convenient to write the remaining two momentum integrals as integrals over energy, and integrals of momenta over equal energy surfaces. Then we can simply perform the ϵ' integral using the delta function to arrive at

$$\frac{2g_F^2}{\Gamma_3}\oint d\boldsymbol{k}\oint d\boldsymbol{k}'\int \frac{d\epsilon d\omega}{v_{\boldsymbol{k}}v_{\boldsymbol{k}'}}\left(\Phi_{\boldsymbol{k}}-\Phi_{\boldsymbol{k}'}\right)^2 n^0(\omega)\, f^0(\epsilon_{\boldsymbol{k}})\left(1-f^0(\epsilon_{\boldsymbol{k}'}+\omega)\right)\Im\chi_{\boldsymbol{k}'-\boldsymbol{k}}(\omega)\,. \quad (4.2.19)$$

The next step is to perform the integral over ϵ. Since the energy scales associated with magnetic fluctuations are much less than the Fermi energy, we may use the approximation $\omega \ll \epsilon_F$ to find that $f(\epsilon)(1-f(\epsilon+\omega)) \sim f(\epsilon)(1-f(\epsilon))$. This function is sharply peaked at the Fermi surface. We subsequently take $\boldsymbol{k}$ and $\boldsymbol{k}'$ to be points on the Fermi surface, and perform the ϵ integral using that

$$\int d\epsilon_{\boldsymbol{k}} f^0_\epsilon\left(1-f^0_{\epsilon+\omega}\right) = \omega\left(n^0(\omega)+1\right), \quad (4.2.20)$$

to arrive at

$$\int d\boldsymbol{k}d\boldsymbol{k}'\mathcal{P}^0_{\boldsymbol{k}\boldsymbol{k}'}\left(\Phi_{\boldsymbol{k}}-\Phi_{\boldsymbol{k}'}\right)^2 = \frac{2g_F^2}{\Gamma_3}\oint\frac{d\boldsymbol{k}}{\hbar v_{\boldsymbol{k}}}\oint\frac{d\boldsymbol{k}'}{\hbar v_{\boldsymbol{k}'}}\int d\omega\left(\Phi_{\boldsymbol{k}}-\Phi_{\boldsymbol{k}'}\right)^2\omega n^0(\omega)\left(n^0(\omega)+1\right)\Im\chi_{\boldsymbol{k}'-\boldsymbol{k}}(\omega)\,. \quad (4.2.21)$$

We next perform the integral over the modulus of the $\boldsymbol{k}$ on the denominator of equation (4.1.14) in the same way as in the impurity scattering case, as

$$e\int d\boldsymbol{k}\boldsymbol{v}_{\boldsymbol{k}}.\hat{\boldsymbol{n}}f^0_{\boldsymbol{k}}\left(1-f^0_{\boldsymbol{k}}\right)\Phi_{\boldsymbol{k}}=ek_BT\oint\frac{d\boldsymbol{k}}{\hbar v_{\boldsymbol{k}}}\boldsymbol{v}_{\boldsymbol{k}}.\hat{\boldsymbol{n}}\Phi_{\boldsymbol{k}}. \tag{4.2.22}$$

We may now write the resistivity as

$$\rho=\frac{1}{2e^2}\frac{\oint\frac{d\boldsymbol{k}}{v_{\boldsymbol{k}}}\oint\frac{d\boldsymbol{k'}}{v_{\boldsymbol{k'}}}F_3\left(\boldsymbol{k},\boldsymbol{k'}\right)\left(\Phi_{\boldsymbol{k}}-\Phi_{\boldsymbol{k'}}\right)^2}{\left(\oint\frac{d\boldsymbol{k}}{v_{\boldsymbol{k}}}\boldsymbol{v}_{\boldsymbol{k}}.\hat{\boldsymbol{n}}\Phi_{\boldsymbol{k}}\right)^2}, \tag{4.2.23}$$

where

$$F_3\left(\boldsymbol{k},\boldsymbol{k'}\right)=\frac{2g_F^2}{k_BT\Gamma_3}\int_0^{c_3q\Gamma_3}d\omega\frac{\omega^2n^0\left(\omega\right)\left(n^0(\omega)+1\right)/c_3q\Gamma_3}{\left(r_3(T)+c_3^2q^2\right)^2+\left(\left|\omega\right|/\Gamma_3c_3q\right)^2}, \tag{4.2.24}$$

with $\boldsymbol{q}=\boldsymbol{k'}-\boldsymbol{k}$.

Since $\boldsymbol{k'}$ and $\boldsymbol{k}$ are both points on the Fermi surface, and the scattering only depends on the distance $|\boldsymbol{q}|$ between them (or equivalently the angle between the two points), the trial function $\Phi_{\boldsymbol{k}}\sim\cos\theta$ used by Mathon must be correct.

We shall find that the antiferromagnetic spin-fluctuations can be written in a similar form, which allows us to combine the two in Section 4.3.

4.2.3 Antiferromagnetic Spin-Fluctuations

We now discuss the literature relating to scattering near an antiferromagnetic quantum critical point. We review the results of the numerical studies performed in the literature, before following the literature and writing the resistivity in a form which we find easiest to adapt in the next section.

In contrast to the other two scattering mechanisms discussed, scattering from antiferromagnetic spin-fluctuations does not exclusively depend on the angle between the two vectors on the Fermi surface. This is because the antiferromagnetic fluctuations are strongest around the

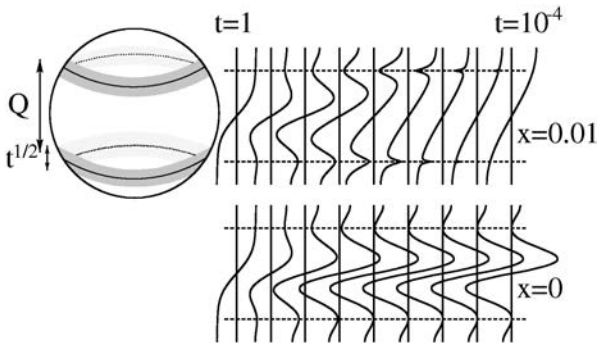

Figure 4.1: Hot lines on the Fermi surface near an antiferromagnetic quantum critical point, and the deviation from the equilibrium quasiparticle distribution. Here t is temperature, and x is the ratio $g_{\rm imp}^2/2g_A^2$. The quasiparticle distribution $\Phi(\theta)$ is shown as a function of the azimuthal angle. The top graphs show this for a dirty system, and the bottom curves show this for a clean system. Taken from Ref. [45].

ordering wavevector $\boldsymbol{Q}$, and there is large scattering between lines on the surface connected by this wavevector. Consequently, near antiferromagnetic quantum criticality the quasiparticle distribution does not necessarily take the $\Phi_{\boldsymbol{k}} \sim \cos\theta$ form of the previous sections.

The conclusion of the literature (see Ref. [45]) is that there are *hot lines* on the Fermi surface which are connected by the ordering wavevector $\boldsymbol{Q}$ where scattering is strongest, as illustrated in Figure 4.1. In clean systems, in order to minimise the resistivity, the quasiparticle distribution equilibrates between the two hot lines, and $\Phi_{\boldsymbol{k}}$ becomes zero around them, which leads to a T^2 resistivity. The situation in dirty metals with antiferromagnetic spin-fluctuations is rather different, however. At low enough temperatures the scattering from disorder is much larger than the spin-fluctuations, and the resistivity is minimised by $\Phi_{\boldsymbol{k}} \sim \cos\theta$. When the quasiparticle distribution takes this form in the presence of antiferromagnetic spin-fluctuations, a novel $\rho \sim T^{3/2}$ power law is observed. At higher temperatures, however, the spin-fluctuations become the dominant scattering mechanism and the hot lines are avoided. Rosch [45] has shown that this crossover leads to an almost linear power law. The results of numerical calculations by Rosch [45] of the effective resistivity exponent are shown in Figure 4.2.

In this thesis, we shall use the most simple model of antiferromagnetic spin-fluctuations,

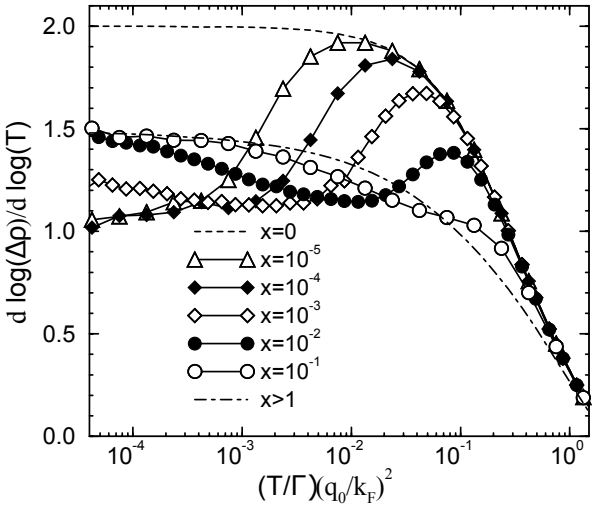

Figure 4.2: Numerical results of the effective resistivity exponent near an antiferromagnetic quantum critical point, where x is the ratio $g_{\rm imp}^2/2g_A^2$. An effective exponent of 2 is found in the cleanest systems, while 3/2 is observed at low temperatures in dirty systems. There is a large crossover region where the exponent is approximately 1 in dirty systems. Taken from Ref. [45].

where we have a spherical Fermi surface, and the antiferromagnetic ordering wavevector is parallel to the electric field. The magnetotransport of various different models has been investigated in the literature and the results were found to be qualitatively independent of the specific model [48].

We now follow the literature [49, 45, 48] and follow steps enabling us to write the scattering from antiferromagnetic spin-fluctuations in a similar form to equation (4.2.23). We begin the derivation in generic terms and note when we are using a specific model.

The derivation of the resistivity functional follows the same steps as the ferromagnetic spin-fluctuation case. We use that

$$\chi_2^{-2}\left(\boldsymbol{q},\omega\right) = r_2(T) + c_2 q^2 - \frac{i\omega}{\Gamma_2}, \tag{4.2.25}$$

where $r_2(T)$ is the renormalised tuning parameter, given by $r_2(T) = r_2 + a_2 T^{3/2}$ as shown in

the previous chapter. We find that

$$\rho = \frac{1}{2e^2} \frac{\oint \frac{d\boldsymbol{k}}{v_{\boldsymbol{k}}} \oint \frac{d\boldsymbol{k'}}{v_{\boldsymbol{k'}}} F_2\left(\boldsymbol{k}, \boldsymbol{k'}\right) \left(\Phi_{\boldsymbol{k}} - \Phi_{\boldsymbol{k'}}\right)^2}{\left(\oint \frac{d\boldsymbol{k}}{v_{\boldsymbol{k}}} \boldsymbol{v}_{\boldsymbol{k}} . \hat{\boldsymbol{n}} \Phi_{\boldsymbol{k}}\right)^2}, \tag{4.2.26}$$

where

$$F_2\left(\boldsymbol{k}, \boldsymbol{k'}\right) = \frac{2g_A^2}{\Gamma_2 k_B T} \int_0^{\Gamma_2} d\omega \frac{\omega^2 n^0\left(\omega\right)\left(n^0(\omega)+1\right)/\Gamma_2}{\left(r_2(T) + c_2^2\left(\boldsymbol{q} \pm \boldsymbol{Q}\right)^2\right)^2 + \left(\left|\omega\right|/\Gamma_2\right)^2}, \tag{4.2.27}$$

where $\boldsymbol{q} = \boldsymbol{k'} - \boldsymbol{k}$. We see that the scattering is largest when two points on the Fermi surface are separated by $\boldsymbol{Q}$.

In order to proceed we follow the analysis of Hlubina and Rice [49] and approximate the ω integral analytically. If we change variables to $w = \omega/\Gamma_2 k_B T$, we find

$$F_2 = 2g_A^2 \int_0^{1/\mathcal{T}_2} dw \frac{e^w}{\left(e^w - 1\right)^2} \frac{w}{y_2^2 + w^2}, \tag{4.2.28}$$

where $\mathcal{T}_2 = k_B T/\Gamma_2$ and $y_2 = \left(r_2(T) + c_2^2\left(\boldsymbol{q} \pm \boldsymbol{Q}\right)^2\right)/\mathcal{T}_2$. Since we wish to analyse this at low temperatures, and since the integral is not very sensitive to the upper cut-off, we change the upper limit of this integral to ∞.

Hlubina and Rice [49] investigated this integral in the two limits $y_2 \to \pm\infty$ and stitched together the answers to give an analytic function which has the same behaviour in these limits. First, we consider the case $y_2 \to \infty$. At low w, y_2 dominates the denominator of the integrand, and at large w ($w > y_2$), the integrand is suppressed by a factor $\sim e^{-w}$ and contributes a negligible amount to the integral. In this limit we approximate

$$F_2 \sim 2g_A^2 \frac{1}{y_2^2} \int_0^{\infty} dw \frac{w^2 e^w}{\left(e^w - 1\right)^2} = g_A^2 \frac{\pi^2}{3y_2^2}. \tag{4.2.29}$$

In the limit $y_2 \to 0$, the integral is dominated by low w, so we can expand $\frac{e^w}{(e^w-1)^2} \sim \frac{1}{w^2}$, and

find that

$$F_2 \sim 2g_A^2 \int_0^\infty dw \frac{1}{w^2 + y_2^2} = g_A^2 \frac{\pi}{2y_2}. \tag{4.2.30}$$

We can approximate the actual integral by a function which has the same leading order expansions in both limits. This is

$$F_2(y_2) \sim 2g_A^2 \frac{\pi^2}{y_2(3y_2 + 2\pi)}, \tag{4.2.31}$$

and so

$$F_2(R_2, T) \sim 2g_A^2 \frac{\pi^2 \mathcal{T}_2^2}{R_2(3R_2 + 2\pi\mathcal{T}_2)}, \tag{4.2.32}$$

where $R_2 = r_2(T) + c_2^2(\boldsymbol{q} \pm \boldsymbol{Q})^2$.

At this point we deviate from the literature, and progress further analytically for our specific model of a spherical Fermi surface with an electric field parallel to $\boldsymbol{Q}$. In this situation, by symmetry the quasiparticle distribution is a function of the angle from the electric field θ alone, and we are able to perform the polar integrals in the numerator of equation (4.2.26) exactly. Letting $\Phi_{\boldsymbol{k}} = \Phi(\theta)$, the numerator can be written as

$$\begin{aligned} &\oint \frac{d\boldsymbol{k}}{v_{\boldsymbol{k}}} \frac{d\boldsymbol{k'}}{v_{\boldsymbol{k'}}} F_2(\boldsymbol{k}, \boldsymbol{k'}) \left(\Phi(\theta) - \Phi(\theta')\right)^2 \\ &\qquad = \int \frac{d\theta d\phi d\theta' d\phi'}{(2\pi)^6} \frac{k_F^4 \sin\theta \sin\theta'}{v_F^2} F_2(\theta, \phi; \theta', \phi') \left(\Phi(\theta) - \Phi(\theta')\right)^2, \end{aligned} \tag{4.2.33}$$

where k_F is the radius of the Fermi surface. Since F_2 only depends on $\phi - \phi'$ we may shift the ϕ integral and perform the ϕ' integral by multiplying by 2π. We must then investigate

$$\frac{m^4 v_F^2}{\hbar^4 (2\pi)^5} \int d\theta d\theta' d\phi \sin\theta \sin\theta' F_2(\theta, \theta', \phi) \left(\Phi(\theta) - \Phi(\theta')\right)^2, \tag{4.2.34}$$

where the only dependence on the angles in F_2 is through $(\boldsymbol{k'} - \boldsymbol{k} \pm \boldsymbol{Q})^2$. As Rosch [45] does,

we choose to parametrise $\boldsymbol{Q} = 2k_F \cos\theta_H \hat{\boldsymbol{z}}$ so that the hot lines are located at angles θ_H and $\pi - \theta_H$ around the Fermi surface. Using this we may write that

$$\begin{aligned}(\boldsymbol{q} \pm \boldsymbol{Q})^2 = 2k_F^2\Big(1 - \cos\theta\cos\theta' - \sin\theta\sin\theta'\cos\phi \\ + 2\cos\theta_H\left(\cos\theta_H \pm (\cos\theta - \cos\theta')\right)\Big),\end{aligned} \tag{4.2.35}$$

which means that we can write $R_2 = r_2(T) + c_2^2(\boldsymbol{q} \pm \boldsymbol{Q})^2 \equiv a - b\cos\phi$ where a and b depend on θ and θ'. We are now able to evaluate the polar integral exactly. We analyse

$$\int \frac{d\phi}{2\pi} F_2(\theta, \theta', \phi) = \frac{2g_A^2\pi^2\mathcal{T}_2^2}{3}\int_{-\pi}^{\pi}\frac{d\phi}{2\pi}\frac{1}{(a - b\cos\phi)\left(a - b\cos\phi + \frac{2\pi}{3}\mathcal{T}_2\right)}, \tag{4.2.36}$$

by changing variables to $z = e^{i\phi}$ so that $\cos\phi = (z + z^{-1})/2$, and performing the integral around the unit circle. This integral can be written as

$$F_2(\theta, \theta') = 2g_A^2\frac{4\pi^2\mathcal{T}_2^2}{3}\oint\frac{dz}{2\pi i}\frac{z}{\left(z^2 - 2\frac{a}{b}z + 1\right)\left(z^2 - 2\frac{a+\delta}{b}z + 1\right)}, \tag{4.2.37}$$

where $\delta \equiv \frac{2\pi}{3}\mathcal{T}_2$. The integrand has four poles on the real axis at $\frac{a}{b} \pm \sqrt{\left(\frac{a}{b}\right)^2 - 1}$ and $\frac{a+\delta}{b} \pm \sqrt{\left(\frac{a+\delta}{b}\right) - 1}$. Since $a > b$, the two poles with the negative roots are within the unit circle. Using the residue theorem we can evaluate this integral and after a significant amount of algebra we find it is equal to

$$F_2(\theta, \theta') = g_A^2\pi\mathcal{T}_2\left[\frac{1}{\sqrt{a^2 - b^2}} - \frac{1}{\sqrt{\left(a + \frac{2\pi}{3}\mathcal{T}_2\right)^2 - b^2}}\right], \tag{4.2.38}$$

where $a = r_2(T) + 2c_2^2k_F^2\left[1 - \cos\theta\cos\theta' + 2\cos\theta_H\left(\cos\theta_H \pm (\cos\theta - \cos\theta')\right)\right]$ and $b = 2c_2^2k_F^2\sin\theta\sin\theta'$. We also evaluate the denominator in equation (4.2.26) as

$$\oint\frac{d\boldsymbol{k}}{v_{\boldsymbol{k}}}\boldsymbol{v}_{\boldsymbol{k}}.\hat{\boldsymbol{n}}\Phi_{\boldsymbol{k}} = \int\frac{d\theta}{(2\pi)^2}\frac{m^2v_F^2}{\hbar^2}\sin\theta\cos\theta\Phi(\theta), \tag{4.2.39}$$

so that ultimately

$$\rho = \frac{1}{2e^2 v_F^2} \frac{\int d\theta d\theta' \sin\theta \sin\theta' F_2(\theta,\theta') \left(\Phi(\theta) - \Phi(\theta')\right)^2}{\left[\int d\theta \sin\theta \cos\theta \Phi(\theta)\right]^2}. \tag{4.2.40}$$

Impurities can be taken into account by adding scattering from impurities using the methods of Section 4.2.1. The resulting scattering matrix is taken to be the sum of the two individual scattering matrices. This leads to

$$\rho = \frac{1}{2e^2 v_F^2} \frac{\int d\theta d\theta' \sin\theta \sin\theta' \left[g_{\text{imp}}^2 + F_2(\theta,\theta')\right] \left(\Phi(\theta) - \Phi(\theta')\right)^2}{\left[\int d\theta \sin\theta \cos\theta \Phi(\theta)\right]^2}. \tag{4.2.41}$$

Rosch [45] numerically solved this equation by evaluating the full polar integral in equation (4.2.32) to find the quasiparticle distributions shown in Figure 4.1 and the effective resistivity exponent in Figure 4.2.

4.3 Multicritical Scattering

Now that we have reviewed the literature on the three individual scattering mechanisms, and written the resistivity associated with each mechanism in a form which we find simple to program numerically, we begin our original analysis of a quantum multicritical point. In this section we consider transport near a quantum multicritical point by considering the Boltzmann equation where electronic quasiparticles scatter from both ferromagnetic and antiferromagnetic spin fluctuations, and also scatter from impurities. We shall find the effective power law of the resistivity in a material with a quantum multicritical point.

With the results of the previous sections in mind, we may be able to predict the answers without performing any calculations. In the presence of multiple scattering mechanisms, the quasiparticle distribution rearranges itself to minimise the resistivity. Scattering from both ferromagnetic fluctuations and disorder favours the $\Phi(\theta) \sim \cos\theta$ distribution function, whereas scattering from antiferromagnetic fluctuations favours a distribution where the hot lines are

avoided. In the limit of strong disorder and low temperature, we expect $\Phi(\theta) \sim \cos\theta$ to minimise the resistivity associated with impurity scattering. In this limit, we expect the ferromagnetic scattering to give a contribution to the resistivity proportional to $T^{5/3}$, and the antiferromagnetic scattering to give a stronger contribution proportional to $T^{3/2}$. So, at the lowest temperatures we expect the antiferromagnetic scattering to dominate the effective power law of the resistivity. However, with just impurities and antiferromagnetism alone, there is a large region of crossover behaviour when the strength of the antiferromagnetic scattering becomes comparable to the disorder. In the presence of ferromagnetic scattering we expect this crossover behaviour to be even more rich.

To test these predictions and investigate the crossover behaviour, we now analyse the Boltzmann equation with these three scattering mechanisms.

4.3.1 The Model

In the presence of the three scattering terms, the Boltzmann equation becomes

$$e\frac{\partial f^0_{\boldsymbol{k}}}{\partial \epsilon_{\boldsymbol{k}}}\boldsymbol{v}_{\boldsymbol{k}}.\boldsymbol{E} = \frac{1}{k_B T}\int d\boldsymbol{k'}\left[\mathcal{P}^{\text{imp}}_{\boldsymbol{k},\boldsymbol{k'}} + \mathcal{P}^{\text{F}}_{\boldsymbol{k},\boldsymbol{k'}} + \mathcal{P}^{\text{A}}_{\boldsymbol{k},\boldsymbol{k'}}\right](\Phi_{\boldsymbol{k}} - \Phi_{\boldsymbol{k'}}), \tag{4.3.1}$$

with

$$\mathcal{P}^{\text{imp}}_{\boldsymbol{k},\boldsymbol{k'}} = f^0_{\boldsymbol{k'}}\left(1 - f^0_{\boldsymbol{k}}\right) g^2_{\text{imp}}\delta(\epsilon_{\boldsymbol{k}} - \epsilon_{\boldsymbol{k'}}), \tag{4.3.2}$$

$$\mathcal{P}^{\text{F}}_{\boldsymbol{k},\boldsymbol{k'}} = \frac{g^2_F}{\Gamma_3}\int_0^\infty d\omega\delta(\epsilon_{\boldsymbol{k}} + \omega - \epsilon_{\boldsymbol{k'}})\, n^0(\omega)\, f^0_{\boldsymbol{k}}\left(1 - f^0_{\boldsymbol{k'}}\right)\Im\chi_3(\boldsymbol{k'} - \boldsymbol{k}, \omega), \tag{4.3.3}$$

$$\mathcal{P}^{\text{A}}_{\boldsymbol{k},\boldsymbol{k'}} = \frac{g^2_A}{\Gamma_2}\int_0^\infty d\omega\delta(\epsilon_{\boldsymbol{k}} + \omega - \epsilon_{\boldsymbol{k'}})\, n^0(\omega)\, f^0_{\boldsymbol{k}}\left(1 - f^0_{\boldsymbol{k'}}\right)\Im\chi_2(\boldsymbol{k'} - \boldsymbol{k}, \omega). \tag{4.3.4}$$

Since the function $\frac{\partial f^0_{\boldsymbol{k}}}{\partial \epsilon_{\boldsymbol{k}}}$ is sharply peaked at the Fermi surface, we may integrate the Boltzmann equation over $\epsilon_{\boldsymbol{k}}$, and following the analysis of the previous section we find that

$$e\boldsymbol{v}_{\boldsymbol{k}}.\boldsymbol{E} = \oint \frac{d\boldsymbol{k'}}{\hbar v_{\boldsymbol{k'}}}(\Phi_{\boldsymbol{k}} - \Phi_{\boldsymbol{k'}})\left[g^2_{\text{imp}} + F_3(\boldsymbol{k}, \boldsymbol{k'}) + F_2(\boldsymbol{k}, \boldsymbol{k'})\right], \tag{4.3.5}$$

where F_2 and F_3 are defined in Sections 4.2.3 and 4.2.2, and $\boldsymbol{k}$ and $\boldsymbol{k'}$ are vectors on the Fermi surface. The difference between the F_2 and F_3 functions used in this model and the models in the previous section, is that the temperature dependences of r_2 and r_3 may be different. The ferromagnetic tuning parameter is unchanged, but when the ferromagnetic modes are quantum critical the temperature dependence of the antiferromagnetic tuning parameter must be $r_2(T) = r_2 + a_2' T^{4/3}$.

The resistivity can be calculated either directly from $\Phi_{\boldsymbol{k}}$ as in equation (4.1.12), or from the functional

$$\rho = \frac{1}{2e^2} \frac{\oint \frac{d\boldsymbol{k}}{v_{\boldsymbol{k}}} \oint \frac{d\boldsymbol{k'}}{v_{\boldsymbol{k'}}} \left[g_{\text{imp}}^2 + F_2\left(\boldsymbol{k}, \boldsymbol{k'}\right) + F_3\left(\boldsymbol{k}, \boldsymbol{k'}\right) \right] \left(\Phi_{\boldsymbol{k}} - \Phi_{\boldsymbol{k'}}\right)^2}{\left(\oint \frac{d\boldsymbol{k}}{v_{\boldsymbol{k}}} \boldsymbol{v}_{\boldsymbol{k}} . \hat{\boldsymbol{n}} \Phi_{\boldsymbol{k}} \right)^2}, \tag{4.3.6}$$

which $\Phi_{\boldsymbol{k}}$ minimises. We now analyse this model numerically.

4.3.2 Numerical Analysis

In order to calculate the temperature dependence of the resistivity, we numerically solve the Boltzmann equation to find $\Phi_{\boldsymbol{k}}$. We restrict ourselves to a spherical Fermi surface with quadratic dispersion $\epsilon_{\boldsymbol{k}} = \frac{\hbar^2 k^2}{2m}$, where m is the effective mass of the electronic quasiparticles at the Fermi surface. We also consider a uniform electric field parallel to the antiferromagnetic ordering wavevector $\boldsymbol{Q}$. In this case, $\Phi_{\boldsymbol{k}}$ only depends on the angle from the electric field (θ) and is independent of the polar angle (ϕ).

The general strategy is to calculate $\Phi(\theta)$ from the solution of the Boltzmann equation given by equation (4.3.1) and then calculate the resistivity from equation (4.3.6), noting that this depends only on the shape of $\Phi(\theta)$ and not the overall magnitude, and is thus more stable to numerical errors than if we use equation (4.1.12), where the result depends on the amplitude. We then calculate the resistivity at a series of points to find the effective temperature exponents.

We are able to write the Boltzmann equation for the model in Section 4.3.1 as

$$\alpha \cos\theta = \int_0^\pi d\theta' F(\theta,\theta') \left(\Phi(\theta) - \Phi(\theta')\right), \tag{4.3.7}$$

where $\alpha = (2\pi)^2 eE\hbar^3$, and $F(\theta,\theta') = g_{\text{imp}}^2 + F_2(\theta,\theta') + F_3(\theta,\theta')$. This can be rearranged into the form

$$\Phi(x) = f(x) + \int_0^\pi dt K(x,t)\,\Phi(t), \tag{4.3.8}$$

where $f(x) = \alpha\cos x/G(x)$, and $K(x,t) = F(x,t)/G(x)$ with $G(x) = \int_0^\pi dt F(x,t)$. This is a Fredholm equation of the second kind [50]. By substituting this equation into itself in an iterative manner, we find that

$$\begin{aligned}\Phi(x) = f(x) &+ \int_0^\pi dt_1 K(x,t_1) f(t_1) + \int_0^\pi \int_0^\pi dt_1 dt_2 K(x,t_1) K(t_1,t_2) f(t_2) \\ &+ \int_0^\pi \int_0^\pi \int_0^\pi dt_1 dt_2 dt_3 K(x,t_1) K(t_1,t_2) K(t_2,t_3) f(t_3) + ...,\end{aligned} \tag{4.3.9}$$

which can be written as

$$\Phi(x) = \sum_n f_n(x), \tag{4.3.10}$$

with $f_0(x) = f(x)$ and $f_{n+1}(x) = \int_0^\pi dt K(x,t) f_n(t)$.

This is the formula we use to find $\Phi(x)$ numerically. Calculating $K(x,t)$ is computationally very time-consuming, whereas calculating these integrals is relatively inexpensive. Numerically we find that the series converges relatively quickly and typically we only need to calculate approximately 10 terms before we conclude that the series has converged.

Our strategy once the quasiparticle distribution has been calculated is to evaluate the resistivity using equation (4.3.6), which is independent of the coefficient of $\Phi(\theta)$. Calculating the resistivity from equation (4.1.12) would be slightly more simple numerically, however we find that the coefficient of $\Phi(\theta)$ is very sensitive to the number of points we numerically calcu-

late the function at, but the overall shape is much less sensitive. This means that the results from calculating the resistivity from equation (4.3.6) are much more stable under changing the accuracy of the program.

We then calculate the resistivity at a variety of different temperatures, and attempt to find an effective exponent by fitting the results to $\rho(T) - \rho_0 \sim aT^{\alpha(T)}$, where ρ_0 is the zero-temperature resistivity, and the ultimate aim of the program is to find $\alpha(T)$ at various points on the phase diagram. The zero-temperature resistivity is given by the impurity scattering alone, and is

$$\rho_0 = \frac{g_{\text{imp}}^2}{2e^2 v_F^2} \frac{\int_0^\pi d\theta \int_0^\pi d\theta' \sin\theta \sin\theta' (\cos\theta - \cos\theta')^2}{\left(\int_0^\pi d\theta \sin\theta \cos^2\theta\right)^2} = \frac{3g_{\text{imp}}^2}{e^2 v_F^2}. \tag{4.3.11}$$

We give further details of the numerical methods in Appendix B.

4.4 Numerical Results

We now present the results of the numerical calculations. We begin with a discussion on the accuracy of our program and demonstrate that we can reproduce the known results associated with ferromagnetic and antiferromagnetic scattering in the relevant limits. Then we analyse the equations directly above the quantum multicritical point in Section 4.4.2.

4.4.1 Precautions and Accuracy

There are several parameters in the code which we set to one.

We set $\Gamma_3 = c_3 k_F = 1$. For a single quantum critical point this amounts to a rescaling of the units of momentum and temperature. We then set $c_2 k_F = 1$. This amounts to a rescaling of the tuning parameter $r_2(T)$, the constant Γ_2, and the antiferromagntic scattering strength g_A. We now set $\Gamma_2 = 1$, as we find it does not qualitatively affect the numeric results. Following Rosch [48] we set $a_2 = a_3 = 1$, with the understanding that for a single antiferromagnetic

quantum critical point this does not affect the low-temperature properties in zero magnetic field. We calculate the resistivity in units of $(2e^2 v_F^2)^{-1}$.

There are a large number of parameters we can vary to increase the accuracy of the computer program, but the computational time also increases. The accuracy of the final result is most sensitive to the size of the matrix $F(\theta, \theta')$. Increasing the size increases the accuracy of the program, but also drastically increases the computational time taken. A balance between time and accuracy must be struck.

We have decided to calculate the results with the following parameters: The matrix $F(\theta, \theta')$ is of size 6000 by 6000. Before calculating the matrix, we calculate the ω integral for 50000 different values of q, and calculate the integral in 5000 steps for each of these. Then we split each polar integral into 2000 steps. These integrals are explained in more detail in Appendix B.

We find that in the ferromagnetic case there are some incorrect aspects of our numerical results, specifically that the quasiparticle distribution looks like $\cos\theta$ with a couple of 'flicks' near $\theta = 0$ and $\theta = \pi$, as shown in Figure 4.3. We believe that these inaccuracies occur because of the low value of $\sin\theta$ at these angles. However, we find that while increasing the size of the matrix shrinks the size of these incorrect tails, it does not affect the resistivity very much at all. This is most likely because of the small value of $\sin\theta$ near these points, which suppresses their contribution in the calculation of the resistivity.

We now demonstrate that our program can reproduce the results of the literature discussed earlier. We are able to reproduce Rosch's results for the resistivity exponent of a dirty antiferromagnetic as shown in Figure 4.4a, and reproduce the quasiparticle distribution functions in Figure 4.5. In Figure 4.4c we calculate the resistivity exponent with only ferromagnetic scattering, and at low temperatures we find the $\rho \sim T^{5/3}$ power law as found analytically in Section 4.2.2. Numerically we find that the exponent at $T = 10^{-4}$ is 1.66 to three significant figures.

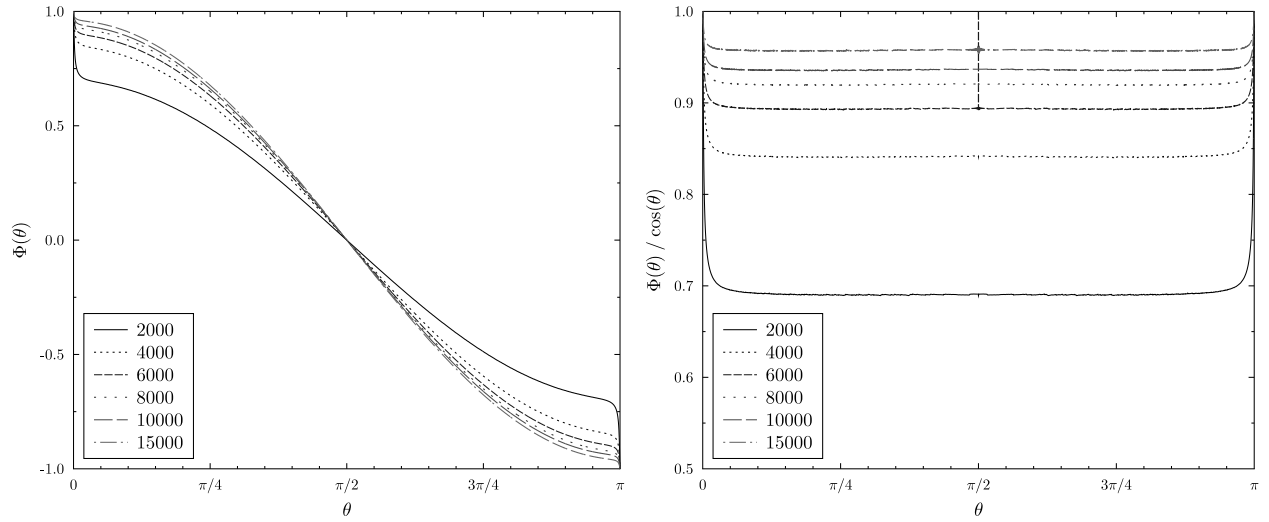

(a) $\Phi(\theta)$ (b) $\Phi(\theta) / \cos\theta$

Figure 4.3: The quasiparticle distribution $\Phi(\theta)$ calculated using different sizes of the matrix $F(\theta, \theta')$ as denoted by the key. The distribution is normalised to $\Phi(0) = 1$. The measurements are taken at $g_A^2 = 1$, $g_F^2 = 10$, $g_{\text{imp}} = 0$, and $T = 10^{-4}$.

4.4.2 Directly Above the QMCP

We now describe our original results and their interpretation. We investigate directly above the QMCP, where $r_2 = r_3 = 0$.

We calculate the effective resistivity exponent, the resistivity, and the quasiparticle distributions at various strengths of ferromagnetic scattering (g_F) and impurity scattering (g_{imp}) while keeping the antiferromagnetic scattering strength constant ($g_A = 1$). The resistivity exponents are shown in Figure 4.6, the resistivity in Figure 4.7, and the quasiparticle distributions in Figures 4.8, 4.9 and 4.10.

In clean systems, in the absence of ferromagnetic scattering the hot lines are avoided in the quasiparticle distribution at low temperatures. Figure 4.8 shows that in the presence of sufficiently strong ferromagnetic scattering the hot lines are no longer avoided and the quasiparticle distribution becomes proportional to $\cos\theta$. At low temperatures for $g_F^2 \sim 1$ this leads to a resistivity exponent of 3/2 as shown in Figure 4.6a. In this sense, ferromagnetic scattering plays the role of disorder and *stabilises* the $\rho \sim T^{3/2}$ power law usually associated with antiferromagnetic quantum criticality. At higher values of g_F, when $g_F \gg g_A$, the

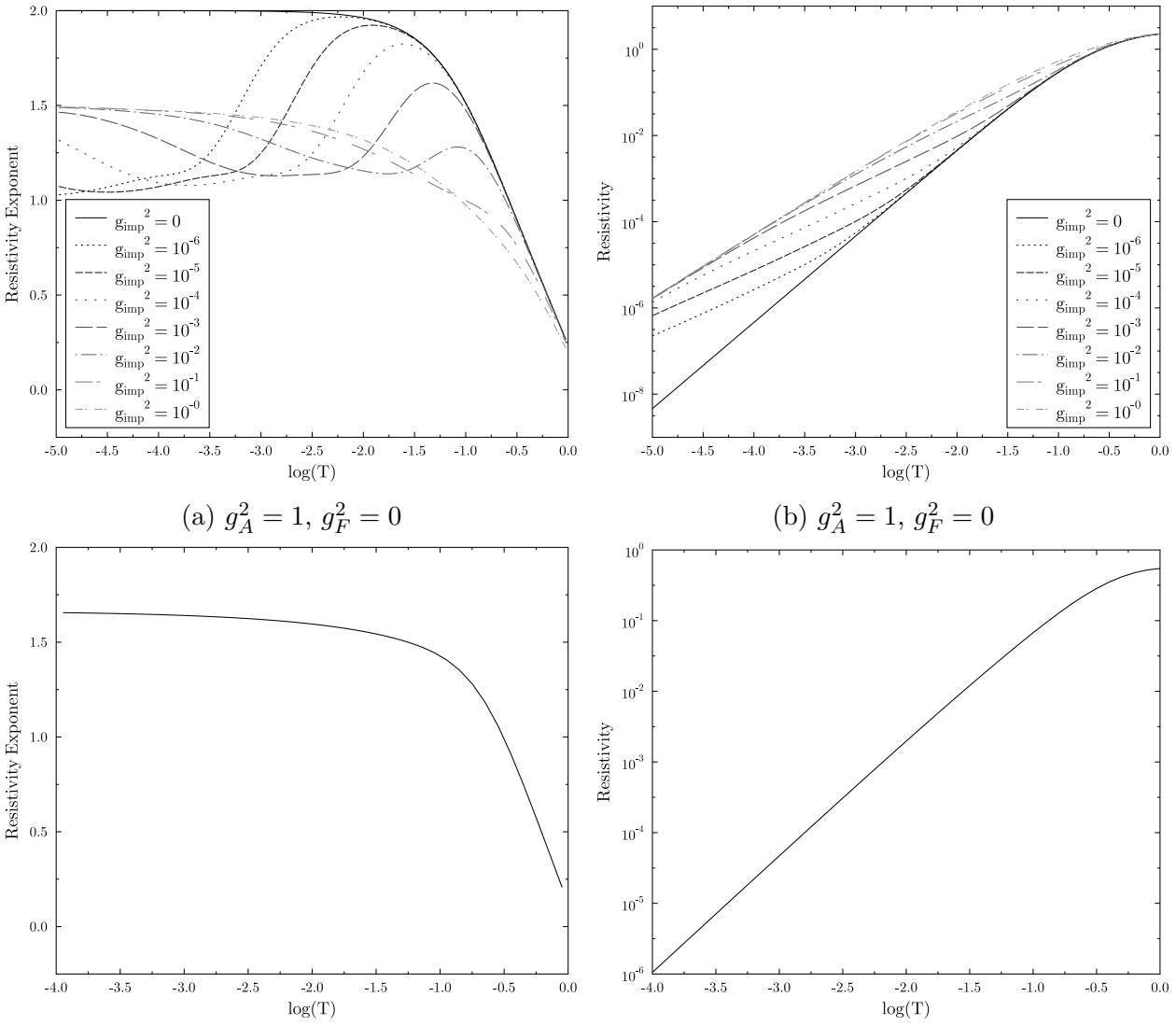

(a) $g_A^2 = 1$, $g_F^2 = 0$

(b) $g_A^2 = 1$, $g_F^2 = 0$

(c) $g_A^2 = 0$, $g_F^2 = 1$, $g_{\text{imp}}^2 = 0$

(d) $g_A^2 = 0$, $g_F^2 = 1$, $g_{\text{imp}}^2 = 0$

Figure 4.4: The temperature-dependent part of resistivity, and resistivity of systems previously investigated. (a) and (b) show a system with scattering from antiferromagnetic spin fluctuations and disorder, in the absence of ferromagnetic spin fluctuations. (c) and (d) show a system with scattering from ferromagnetic spin fluctuations, in the absence of antiferromagnetic spin fluctuations. The graphs (c) and (d) are independent of g_{imp}.

power law associated with ferromagnetic quantum criticality $\rho \sim T^{5/3}$ is observed at low temperatures. This is as expected when the effect of antiferromagnetic scattering is negligible in comparison to the ferromagnetic scattering. When the ferromagnetic scattering is very weak, the quasiparticle distribution is very similar to the quasiparticle distribution in slightly impure systems. The effective resistivity exponent, however, does not show the almost-linear

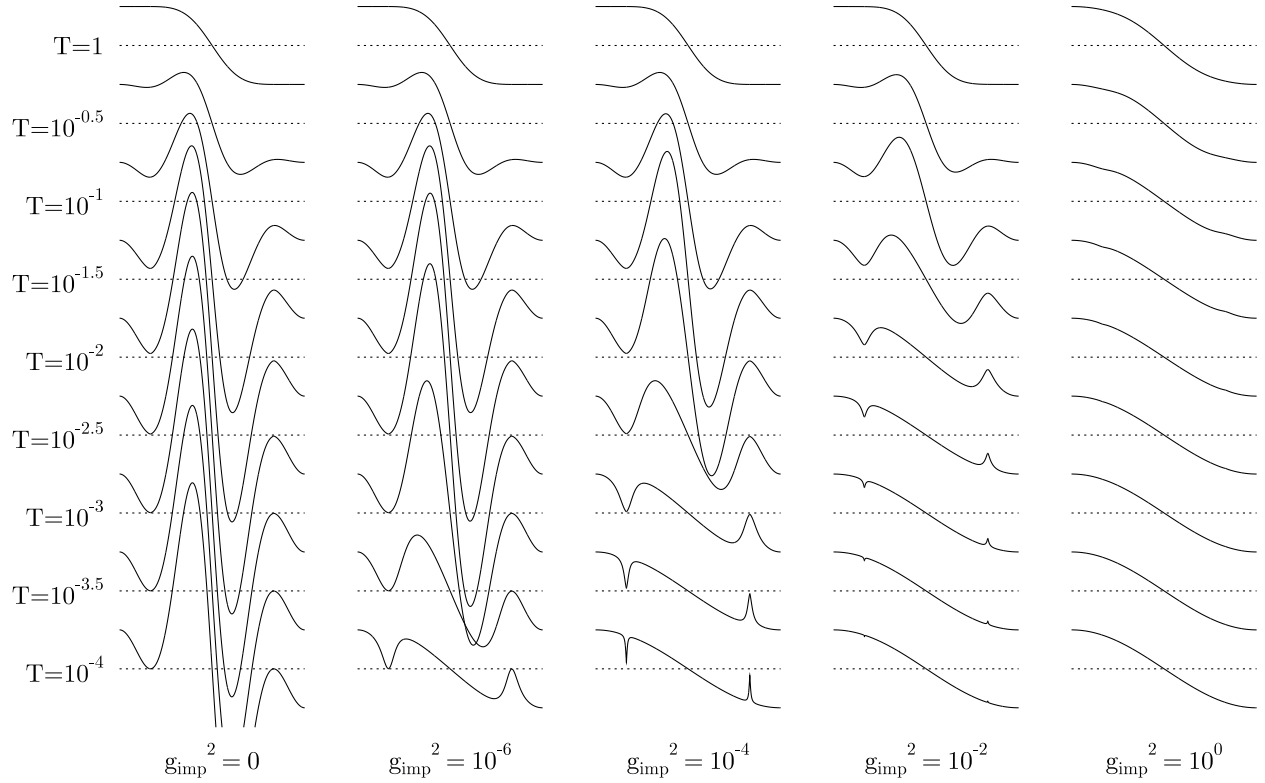

Figure 4.5: The quasiparticle distributions as functions of angle around the Fermi surface in the absence of ferromagnetic spin fluctuations at different temperatures and different impurities. Here, $g_A^2 = 1$.

crossover behaviour observed in impure antiferromagnetic systems.

In dirty systems, the story is very similar. Greater ferromagnetic scattering acts similarly to increased disorder in the sense that it favours the $\cos\theta$ form of the quasiparticle distribution. This can be seen from Figures 4.9 and 4.10, where increased ferromagnetic scattering causes the 'dips' in the quasiparticle distribution around the hot lines to become smaller. From Figure 4.6b we see that if both impurities and ferromagnetic scattering are weak, an almost-linear crossover can be observed. From Figures 4.6c and 4.6d however, we can see that if the disorder and ferromagnetic scattering are strong enough the linear crossover regime is not present.

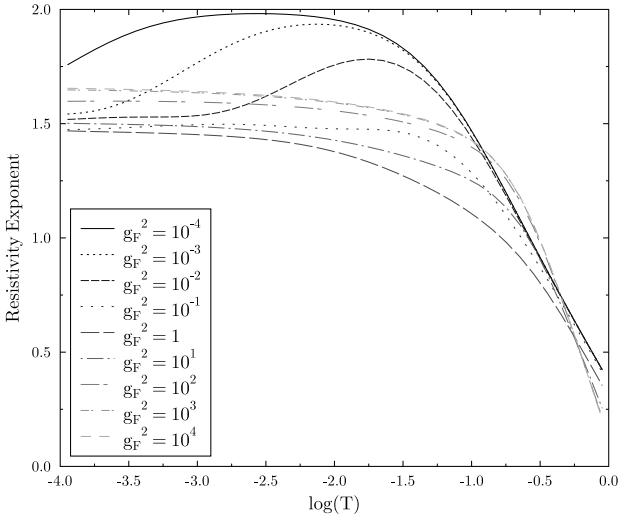

(a) Clean system $g^2_{\text{imp}} = 0$

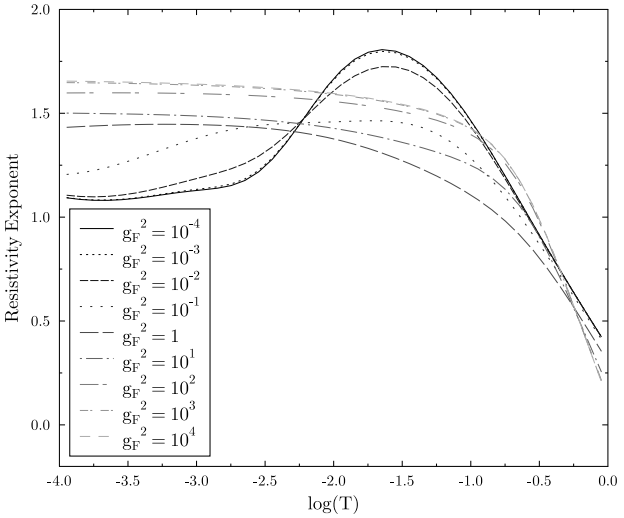

(b) Dirty system $g^2_{\text{imp}} = 10^{-4}$

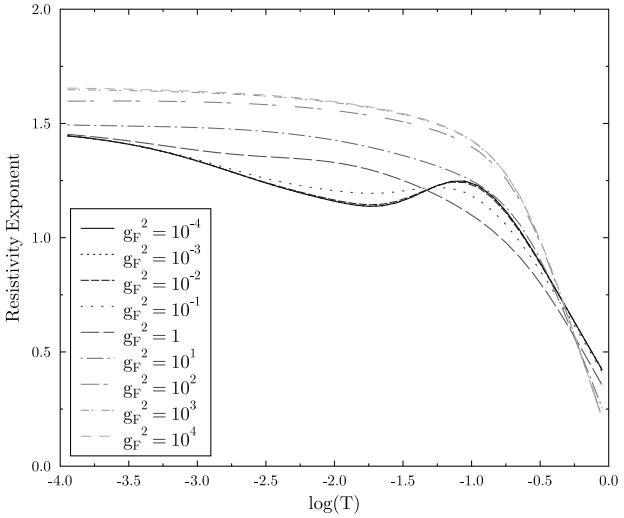

(c) Dirty system $g^2_{\text{imp}} = 10^{-2}$

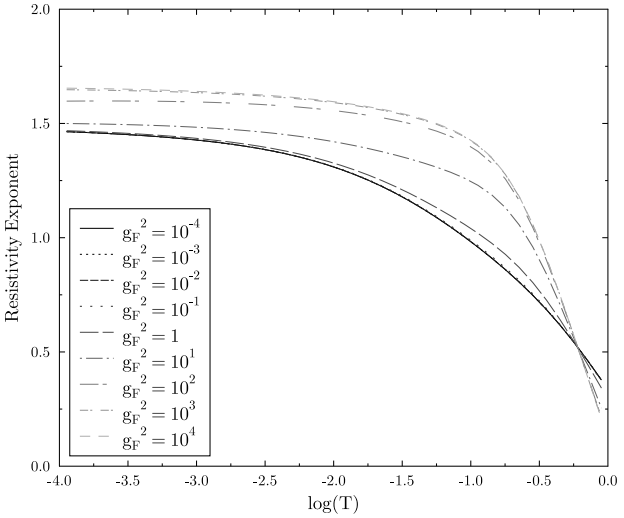

(d) Dirty system $g^2_{\text{imp}} = 1$

Figure 4.6: Resistivity exponent at different levels impurities and ferromagnetic scattering strengths

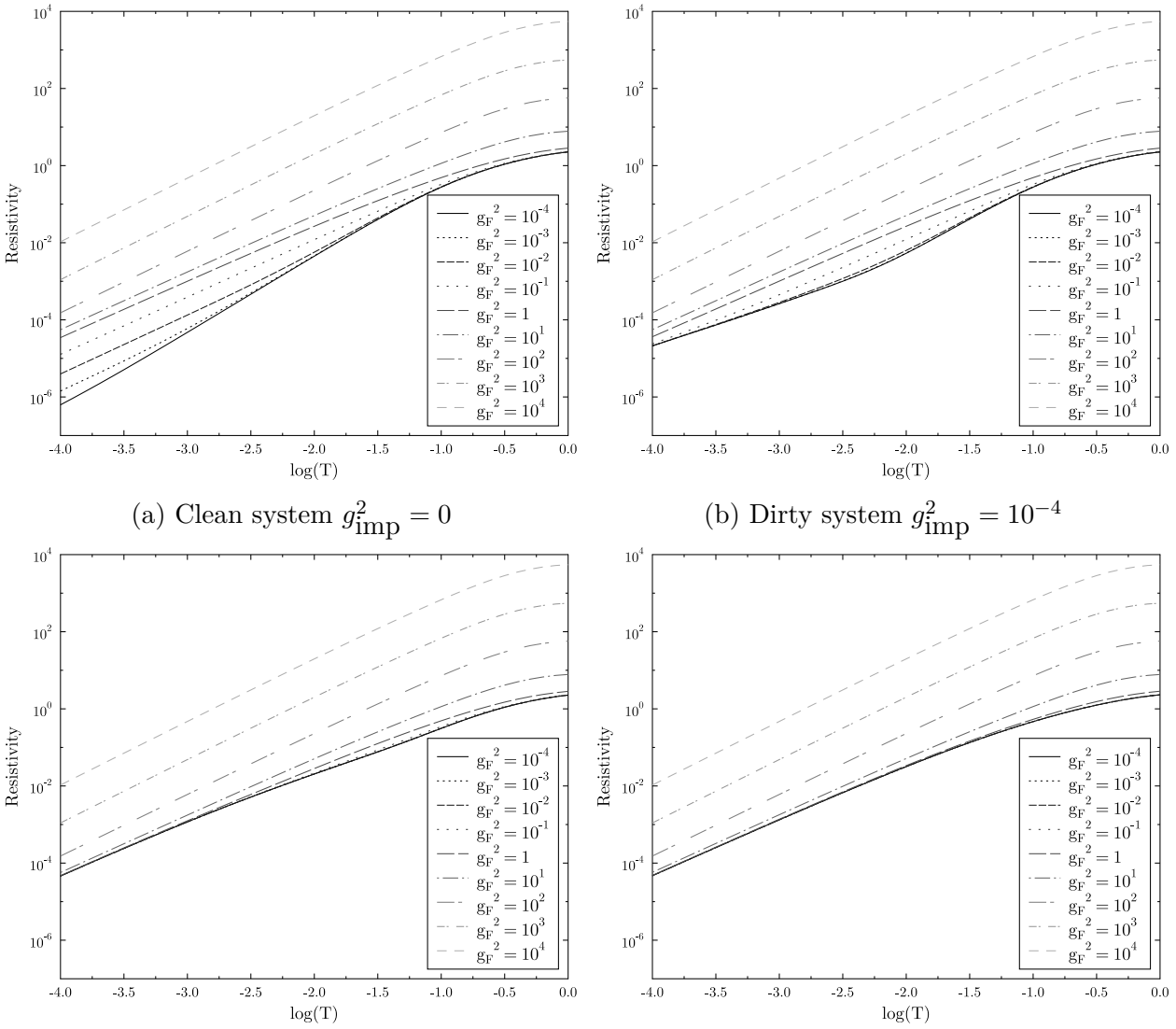

(a) Clean system $g^2_{\text{imp}} = 0$

(b) Dirty system $g^2_{\text{imp}} = 10^{-4}$

(c) Dirty system $g^2_{\text{imp}} = 10^{-2}$

(d) Dirty system $g^2_{\text{imp}} = 1$

Figure 4.7: Temperature-dependent part of the resistivity at different levels impurities and ferromagnetic scattering strengths

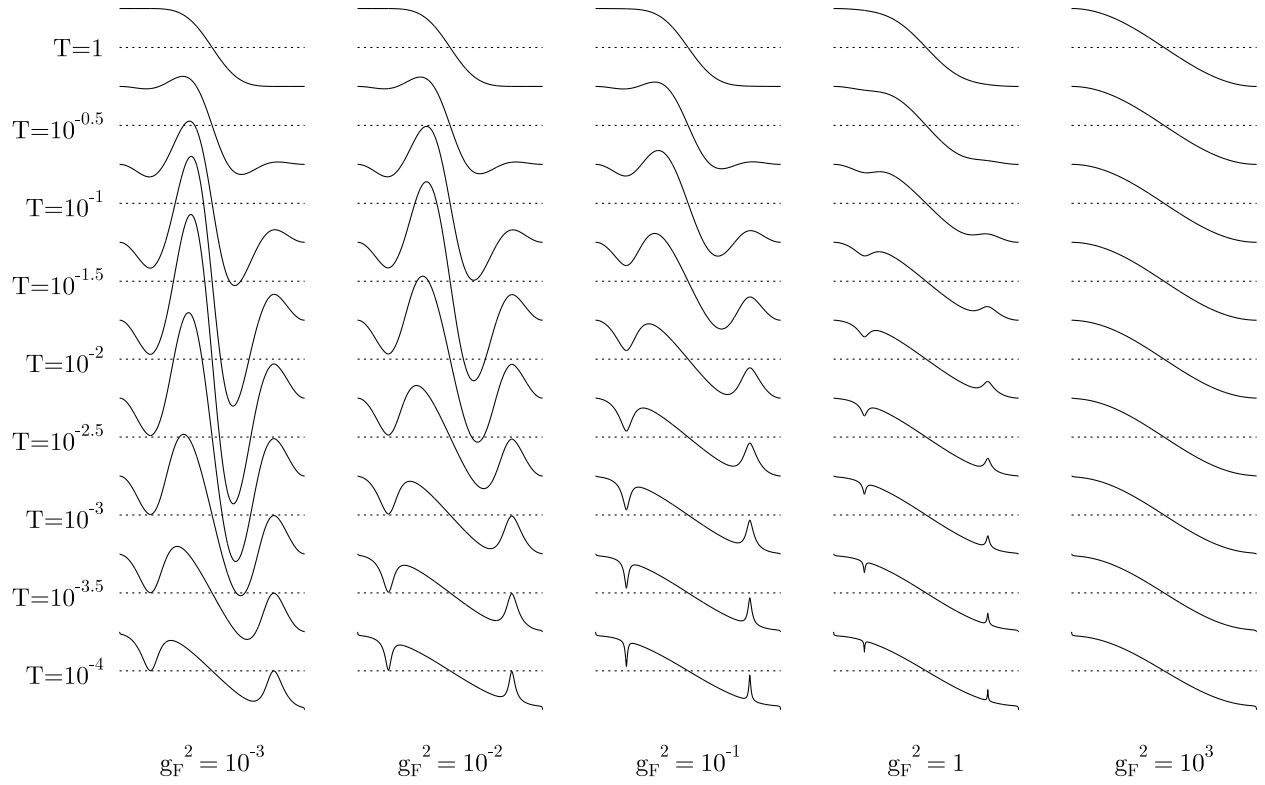

Figure 4.8: The quasiparticle distributions as functions of angle around the Fermi surface in clean systems ($g_{\rm imp} = 0$) at different temperatures and different strengths of the ferromagnetic scattering. Here $g_A^2 = 1$.

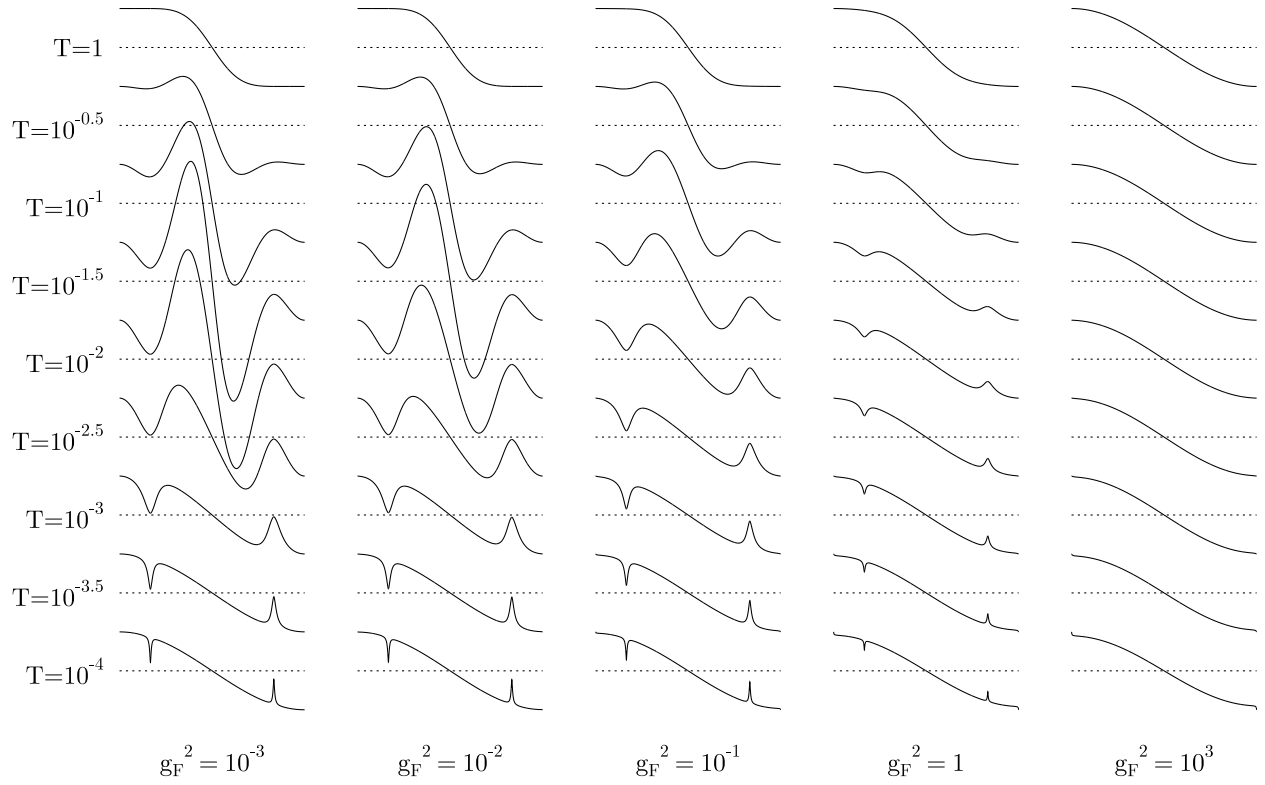

Figure 4.9: The quasiparticle distributions as functions of angle around the Fermi surface in dirty systems with $g^2_{\rm imp} = 10^{-4}$ at different temperatures and different strengths of the ferromagnetic scattering. Here $g_A^2 = 1$.

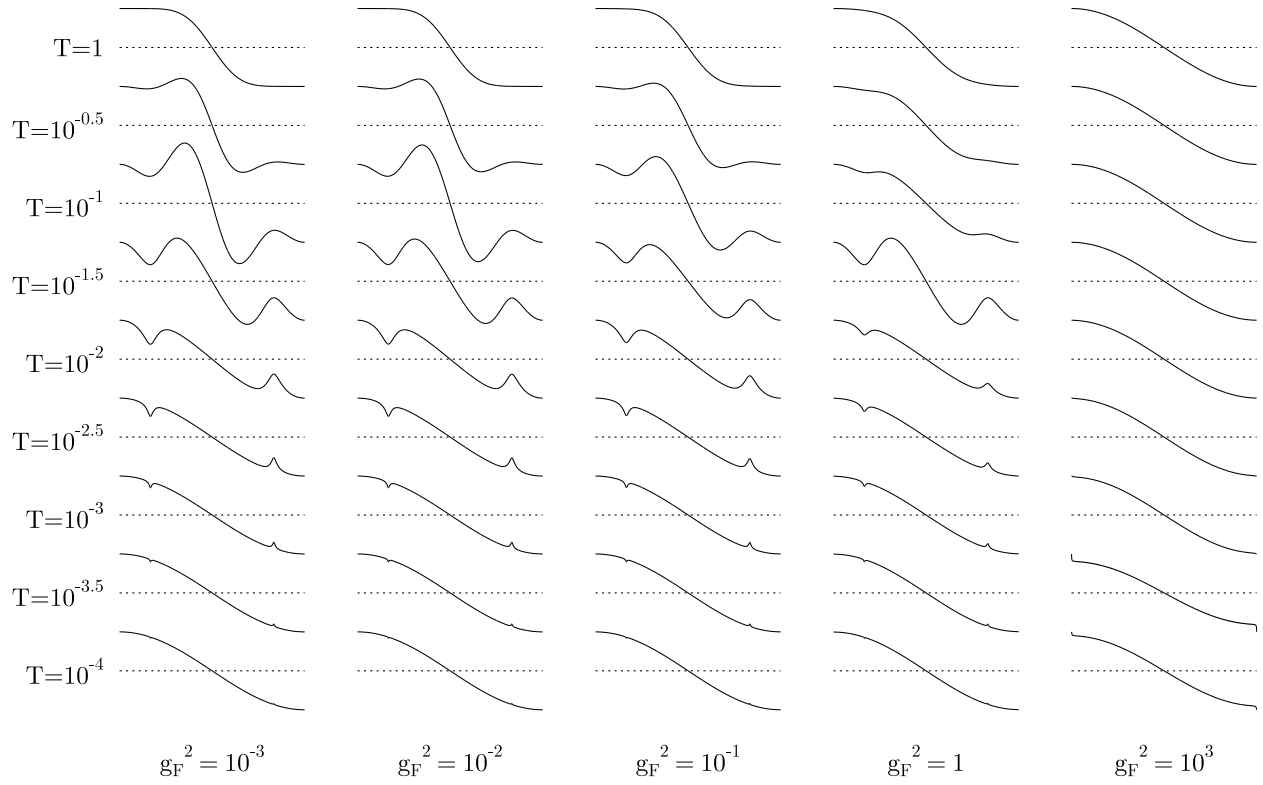

Figure 4.10: The quasiparticle distributions as functions of angle around the Fermi surface in dirty systems with $g^2_{\rm imp} = 10^{-2}$ at different temperatures and different strengths of the ferromagnetic scattering. Here $g_A^2 = 1$.

4.5 Conclusions

We have numerically solved the Boltzmann transport equation to find the quasiparticle distribution and resistivity exponent over a range of temperatures, at varying strengths of antiferromagnetic and ferromagnetic scattering, and scattering from disorder.

Our key conclusion is that in the presence of scattering from both ferromagnetic and antiferromagnetic spin-fluctuations of similar strengths, the resistivity is expected to obey a $T^{3/2}$ power law, usually associated with antiferromagnetism in disordered systems. This remains the case even in clean systems, and so the ferromagnetic fluctuations stabilise the antiferromagnetic $T^{3/2}$ power law.

The physical reason for this is that the quasiparticle distribution rearranges itself to minimise the resistivity. Since the scattering from ferromagnetic spin fluctuations and disorder only depends upon the angle between the two states, the resistivity is minimised by the familiar quasiparticle distribution $\Phi \sim \cos\theta$. When the quasiparticle distribution takes this form in the presence of antiferromagnetic spin-fluctuations, scattering is strong between the two hot lines on the Fermi surface and a $\rho \sim T^{3/2}$ power law is observed.

The resistivity from antiferromagnetic scattering alone is minimised by a quasiparticle distribution that looks like $\cos\theta$ but with 'dips' at the hot lines. This can be interpreted as the whole Fermi surface shifting, except around the hot-lines where the quasiparticle distribution is unchanged by the electric field. When the quasiparticle distribution takes this form, there is no scattering between the hot lines and so the resistivity has the exponent associated with the other scattering mechanisms in the problem. In the presence of ferromagnetic scattering we observe a $T^{5/3}$ power law, or in scenarios without ferromagnetic scattering we see a T^2 resistivity which is characteristic of a Fermi liquid.

The conclusion is that ferromagnetic spin fluctuations stabilise the $\Phi \sim \cos\theta$ form of the quasiparticle distribution, which in turn stabilises the $T^{3/2}$ behaviour of the resistivity.

This $T^{3/2}$ power law in the presence of both ferromagnetic and antiferromagnetic spin-fluctuations is precisely what is observed for $NbFe_2$ and $Ta(Fe_{1-x}V_x)_2$, as discussed in Chapter

3. We now believe we have a coherent theory for the mechanisms behind ferromagnetism dominating the specific heat in these systems, but antiferromagnetism dominating the resistivity.

We now turn our attention to another model of quantum criticality where $z = 3$ modes interact with $z = 2$ modes. In the next chapter we consider a metamagnetic quantum critical end-point interacting with an antiferromagnetic quantum critical point in the presence of a magnetic field. This is an example of a multicritical situation where the issues with Hertz-Millis theory discussed in Section 2.5 are not expected to arise.

Chapter 5

METAMAGNETISM AND ANTIFERROMAGNETISM

5.1 Introduction

In Chapters 3 and 4, we derived and analysed a model of a ferromagnetic ($z = 3$) QCP interacting with an antiferromagnetic ($z = 2$) QCP. The results of this model seemed to agree with certain experimental discoveries, and have made predictions about currently unmeasured quantities. Despite this, in Section 3.6.2 we questioned the applicability of the model which has the same failings as Hertz-Millis theory, described in Section 2.5. In this chapter we build a model of a different physical scenario, where these complications do not arise.

Up until now, in this thesis we have been considering quantum criticality occurring around a second order phase transition that has been suppressed to zero temperature. First order phase

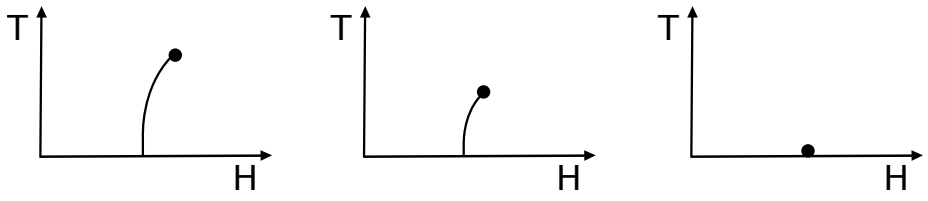

Figure 5.1: The critical end-point of a first order transition being suppressed to zero by tuning some non-thermal control parameter in successive graphs. This is adapted from Ref. [32]

.

transitions do not exhibit quantum criticality as there are no critical modes which become massless at the phase transition. However, massless excitations exist at the end-point of a line of first order transitions, and if this is suppressed to zero temperature quantum criticality is observed. The resulting point is termed a quantum critical endpoint (QCEP), and this is shown schematically in Figure 5.1.

An example of such a scenario is a metamagnetic transition, where as a magnetic field is increased through a critical value the magnetism of the sample has a discontinuous jump. If the end-point of the line of metamagnetic transitions is suppressed to zero temperature, it can be described by a quantum critical theory with dynamical exponent $z = 3$ [51, 52]. This has been proposed as an explanation for experimental data on $Sr_2Ru_2O_7$ [23] and $CeRu_2Si_2$ [53].

The reason we consider such a scenario is that while the non-analytic terms neglected by Hertz-Millis theory generically cause ferromagnetic transitions to become first order, under application of a magnetic field the end-point of this transition can be suppressed to absolute zero, leading to first order 'wings' on the phase diagram [54]. This is shown schematically in Figure 5.2.

At such a point, the finite magnetic field creates an energy gap in the fermionic modes, due to the energy difference between the spin-up and spin-down Fermi surfaces. There are no zero-energy fermionic modes at the transition, meaning that the non-analytic terms due to integrating them out do not arise [55].

If we take these non-analytic terms into account when considering a quantum multicritical point, we would expect the ferromagnetic transition to go first order, as in Figure 5.3a. We now consider applying a magnetic field to this phase diagram. As shown in Figure 5.3b, under a magnetic field there is no longer a symmetry-breaking phase transition, as $\langle \phi_3 \rangle$ is finite everywhere. The end-point of the line of first order transitions can be suppressed to $T = 0$, as shown in Figure 5.3c. As long as the antiferromagnetic state survives under the application of such a field, then we have a metamagnetic quantum critical end-point interacting with an antiferromagnetic quantum critical point. This is the scenario we analyse in this chapter. To

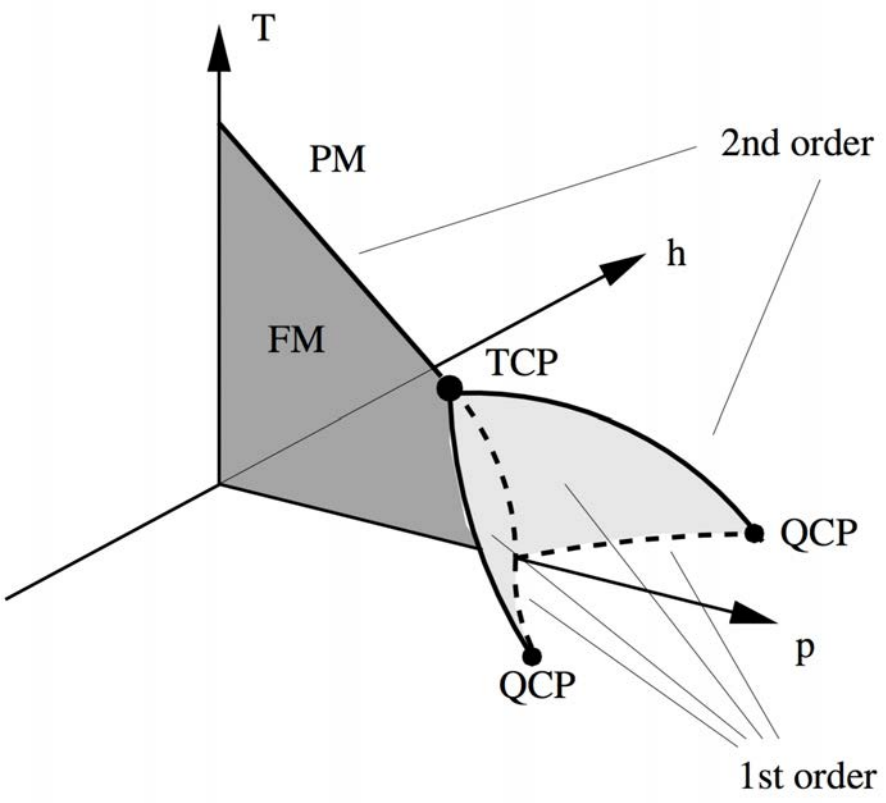

Figure 5.2: Phase diagram of a quantum critical ferromagnet in three dimensions, taken from Ref. [54]. Upon approaching the QCP the transition becomes first order, but the end-point of the first order transition can be suppressed to zero with a magnetic field. The point at which the first order line meets the second order line is called a tricritical point (TCP).

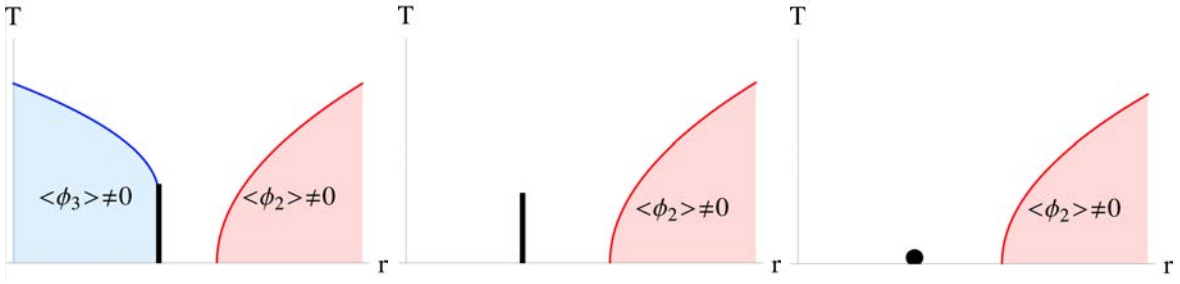

(a) Zero field (b) Finite field (c) Critical field

Figure 5.3: The phase diagram of a material featuring a first order ferromagnetic transition and an antiferromagnetic quantum critical point, at various amounts of magnetic field. The phase diagram in Figure 5.3a could be realised near a quantum multicritical point, by the electronic modes causing the ferromagnetic quantum critical point to go first order.

avoid complications arising from the marginal nature of the antiferromagnetic modes in $d = 2$, we only consider this in three dimensions.

We aim to find out to what extent the conclusions of Chapter 3 hold in this new scenario. We investigate whether the $z = 3$ QCEP still dominates over the $z = 2$ QCP when a magnetic field is applied, and whether the thermodynamic properties listed in Table 3.1 are changed by the presence of the field.

The metamagnetic quantum critical end-point is not the sole example of a $z = 3$ quantum critical end-point. The valence transition is a first order transition where the occupation number of f-electrons on certain atoms discontinuously changes. It is thought that in certain situations, the critical end-point of this situation also appears near zero temperature [56]. Moreover, in many systems argued to have a valence transition in them there is also an antiferromagnetic quantum critical point in the phase diagram. This is the case for $CeCu_2Si_2$ [57] and $CeRhIn_5$ [58]. While a phenomenological model for the valence QCEP does exist [56], in this chapter we restrict our attention to the more well-established theory of metamagnetic QCEPs.

The rest of the chapter is structured as follows. In Section 5.2 we review the literature on metamagnetic quantum critical end-points. In Section 5.3 we develop a model of an interacting antiferromagnetic QCP and a metamagnetic QCEP, by first reviewing the literature on anti-

ferromagnetic QCPs in magnetic fields, and then building a Landau theory for the transition. This model is analysed using the self-consistently renormalised (SCR) technique, which we describe and use in Section 5.4. By combining the SCR results with the results of Chapters 2 and 3, we derive the correlation lengths, phase diagram, and thermodynamic properties of this model. In Section 5.5 we analyse the model using the renormalisation group technique. In Section 5.6 we summarise our results and discuss their experimental relevance.

5.2 Metamagnetic Quantum Critical End-Points

Before building a model of an interacting metamagnetic QCEP and an antiferromagnetic QCP, we first review the literature on metamagnetic QCEPs. In Section 5.2.1 we analyse a Landau theory for the metamagnetic end-point at zero temperature, and in Section 5.2.2 we review the literature on the quantum critical theory.

5.2.1 Landau Theory

In this section we describe the zero-temperature Landau free energy which contains a quantum critical end-point at some value of magnetic field. Following the analysis of Ref. [32], we consider the Landau theory

$$F = R\Phi^2 - U\Phi^4 + V\Phi^6 - H\Phi, \tag{5.2.1}$$

where none of the parameters are temperature-dependent. H is the magnetic field and R is another non-thermal tuning parameter, for example pressure or chemical doping. We assume that U and V are constants, and are both positive so that the coefficient of the quartic term in the Landau theory is negative.

Our strategy to develop a quantum critical model of this transition is not to fully solve this model and find the value of Φ everywhere in the $R-H$ plane, but just to look at this theory in

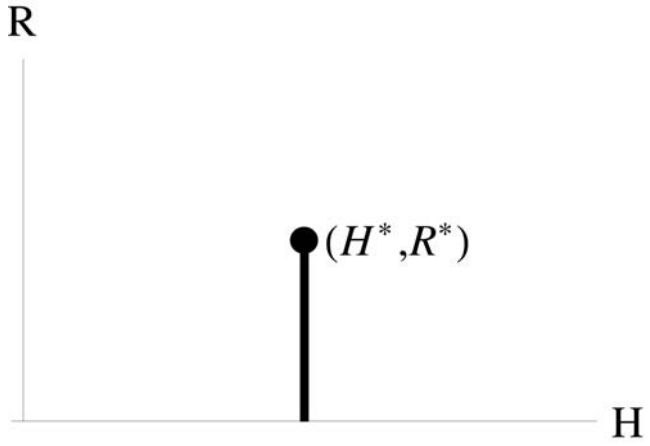

Figure 5.4: Phase diagram in the vicinity of the end-point of the metamagnetic transition in the $H - R$ plane

the vicinity of the quantum critical end-point. Unlike in the Landau theories investigated in Sections 1.3.2 and 1.5.2, we are not interested the behaviour of this model when the coefficient of the quadratic term is negative and only consider this model for $R > 0$.

This model has a critical end-point in the phase diagram at the point (H^*, R^*). In the vicinity of this point, for $R < R^*$ there is a first order transition as H is varied, where Φ discontinuously jumps. For $R > R^*$ the evolution of Φ is smooth, and there is no transition. This is shown schematically in Figure 5.4.

In order to find H^* and U^* in terms of U and V, we find the point where the first three derivatives of the free energy are equal to zero. We find that the value of Φ at (H^*, R^*) is $(\Phi^*)^2 = \frac{U}{5V}$. We then find that $R^* = \frac{3}{5}\frac{U^2}{V}$ and $H^*/\Phi^* = \frac{U^2}{V}\left[\frac{16}{25}\right]$.

We may look at the theory in the vicinity of this point by letting $R = R^* + \delta R$, $H = H^* + \delta H$ and $\Phi = \Phi^* + \phi$. The theory becomes

$$F(\phi) = F(\Phi^*) + \delta R(\Phi^*)^2 - \delta H \Phi^* + (2\Phi^* \delta R - \delta H)\phi + \delta R \phi^2 + 2U\phi^4, \tag{5.2.2}$$

and so if we consider the free energy in powers of ϕ alone, we find that

$$F(\phi) = -h\phi + r\phi^2 + u\phi^4. \tag{5.2.3}$$

Here, $r = \delta R$, $h = \delta H - 2\Phi^* \delta R$, and $u = 2U$. Since the coefficient of the quartic term is positive, we do not need to include the quintic and sextic terms as the quartic term controls the expansion. This is a typical ϕ^4 theory with a field h. At $h = 0$ there is a second order phase transition at $r = 0$, however we are not interested in this transition in this chapter and only consider $r \geq 0$.

In the next section we include temperature into this problem by allowing the order parameter to fluctuate in space and imaginary time. We are interested in the physical properties of the quantum critical system in the $h - T$ plane, at fixed $r \geq 0$.

5.2.2 Quantum Critical Theory

In this section we review the literature on metamagnetic quantum criticality. Metamagnetic transitions at zero temperature have been studied theoretically under the same assumptions behind the Hertz-Millis action [51, 32, 52]. The assumption is that the electronic degrees of freedom can be integrated out and the critical behaviour can be described in terms of overdamped spin-fluctuations alone. The resulting theory is similar to Hertz-Millis theory for a $z = 3$ order parameter, but with a magnetic field which couples linearly to the order parameter

$$\begin{aligned} S = & \frac{1}{\beta V} \sum_{\omega_n, \boldsymbol{q}} \chi^{-1}(\boldsymbol{q}, \omega_n) \phi(\boldsymbol{q}, \omega_n) \phi(-\boldsymbol{q}, -\omega_n) \\ & -h \int d\boldsymbol{x} d\tau \phi_3(\boldsymbol{x}, \tau) + u \int d\boldsymbol{x} d\tau \phi^4(\boldsymbol{x}, \tau), \end{aligned} \tag{5.2.4}$$

where

$$\chi^{-1}(\boldsymbol{q}, \omega_n) = r + q^2 + \frac{|\omega_n|}{q}. \tag{5.2.5}$$

As explained in Section 5.1, it is believed that we do not need to worry about the presence of non-analytic terms due to the finite magnetic field.

The most comprehensive study of this model has been performed by Zacharias and Garst

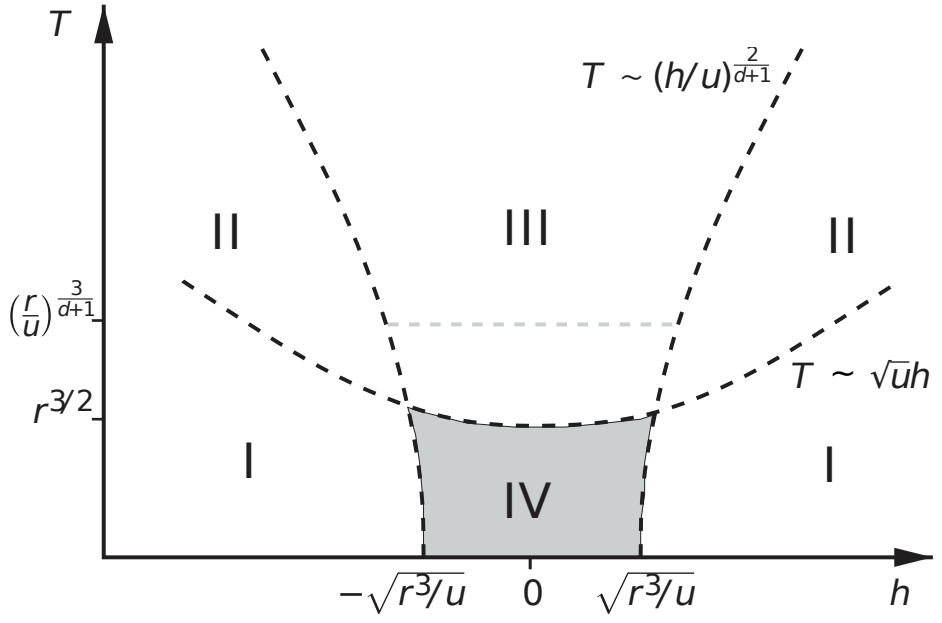

Figure 5.5: Regions in the phase diagram of a metamagnetic quantum critical end-point in the h-T plane at fixed r, taken from Ref. [52]. The regions are described in the main text.

[52] using a renormalisation group approach, from which the phase diagram and thermodynamic properties can be found. They find that just as for the ferromagnetic quantum critical point, the quartic and higher order terms are irrelevant in the renormalisation group sense. When the quintic and higher order terms are neglected, the action is symmetric under $h \to -h$ and so the free energy is an even function of h. In the rest of this section we summarise the key aspects of their results.

The critical part of the free energy has two components. One component comes from the optimal field configuration $\bar{\phi}$ which is non-zero at any non-zero h, and the other component comes from the Gaussian fluctuations of the field about this value.

There are two main crossovers in the h-T plane as shown in Figure 5.5. One crossover is $R^3 \sim uh^2$, which is the difference between low-field and high-field behaviour, which depends on the form of $\bar{\phi}$. Here, R is the renormalised tuning parameter r which has acquired some temperature-dependence. In the high-field region, $\bar{\phi} \approx \left|\frac{6h}{u}\right|^{1/3} \mathrm{sign}(h)$, and in the low-field region, $\bar{\phi} \approx \frac{h}{R}$. The other crossover is between the Fermi liquid-like and the quantum critical

regimes, which is determined by the properties of the Gaussian fluctuations. This is controlled by the curvature of the effective potential at $\bar{\phi}$. In the low-field region this leads to a crossover at $R^{3/2} \sim T$, which is the crossover between the Fermi-liquid and quantum critical regions for a single $z = 3$ quantum critical point. In the regime at temperatures above this, region III in Figure 5.5, there is an additional crossover associated with whether the correlation length is dominated by thermal contributions or not. This is the difference between the two distinct regions in the quantum critical regime for a single Hertz-Millis quantum critical point. In the high field regime this crossover is at $T \sim u^{1/2}h$. This leads to four distinct regions of the phase diagram in Figure 5.5. Regions I and II are in the non-linear regime, and regions III and IV are in the linear regime. Regions I and IV are in the Fermi liquid regime, and regions II and III are in the quantum critical regime. Region III is further subdivided depending on whether the correlation length is dominated by temperature or the parameter r.

In calculating the thermodynamic properties, h and r depend upon both the external magnetic field H and pressure p. Because of this, derivatives with respect to external field and pressure are related, as

$$\frac{\partial}{\partial H} = \frac{\partial r}{\partial H}\frac{\partial}{\partial r} + \frac{\partial h}{\partial H}\frac{\partial}{\partial h}, \tag{5.2.6}$$

and

$$\frac{\partial}{\partial p} = \frac{\partial r}{\partial p}\frac{\partial}{\partial r} + \frac{\partial h}{\partial p}\frac{\partial}{\partial h}. \tag{5.2.7}$$

The strategy of Zacharias and Garst [52] is to first examine the thermodynamic properties assuming that $h(H, p) = H - H^*(p)$ and treat r as a constant, and subsequently look at corrections to this. Under this approximation, derivatives with respect to H and p are directly proportional to each other. The relation $\mathcal{F}_{cr}\left(H - H^*(p), T\right) = \mathcal{F}_{cr}\left(H^*(p) - H, T\right)$ implies that the thermal expansion goes to zero at the critical field.

Under this assumption, the thermodynamic properties are shown in Figure 5.6. Note that

the temperature derivatives originate from $R(T) = r + uT^{4/3}$ in regions II and III. The $h = 0$ component of the specific heat coefficient in region III is $T^{(d-3)/3}$ which is the contribution from Gaussian fluctuations, and is the same as for a ferromagnetic quantum critical point.

While the thermal expansion is zero when $h = 0$ at zero temperature, corrections to the finite temperature thermal expansion arise for two reasons; the pressure-dependence of r, and the temperature dependence of the field h. Due to the pressure-dependence of r, the thermal expansion has an additive component proportional to $\delta\alpha \sim T^{(d+z-2)/z}$ in region III, which is the same for the quantum critical ferromagnetic transition. This effect is negligible compared to the contribution from the temperature-dependence of the field h. Since h does not acquire any temperature-dependent renormalisation from the spin-fluctuations, it has the standard Fermi liquid form of $h(T) = h + h_T T^2$. In region III of the phase diagram, when the correlation length is dominated by temperature, this correction becomes

$$\delta\alpha \sim \frac{h_T}{u} T^{-(d-2)/3} \tag{5.2.8}$$

for temperatures $T \gg (r/u)^{3/(d+1)}$. A physical consequence of this is that at finite temperatures, the field at which the thermal expansion is zero is shifted by a temperature-dependent amount

$$h|_{\alpha=0} \sim h_T T^2. \tag{5.2.9}$$

The contribution to the physical properties from $r(p, H)$ is subleading in all regions.

There are two Grüneisen parameters which can be measured in this system. The usual Grüneisen parameter Γ, and the magnetic analogue Γ_H, discussed in Section 2.2.1. When r is approximated as a constant, these two quantities are directly proportional to each other. When the effect of r changing is taken into account, these parameters are no longer directly proportional to each other due to the relations between the derivatives in equations (5.2.6) and (5.2.7). Both Γ and Γ_H are proportional to the sum of the same two terms, but the coefficients

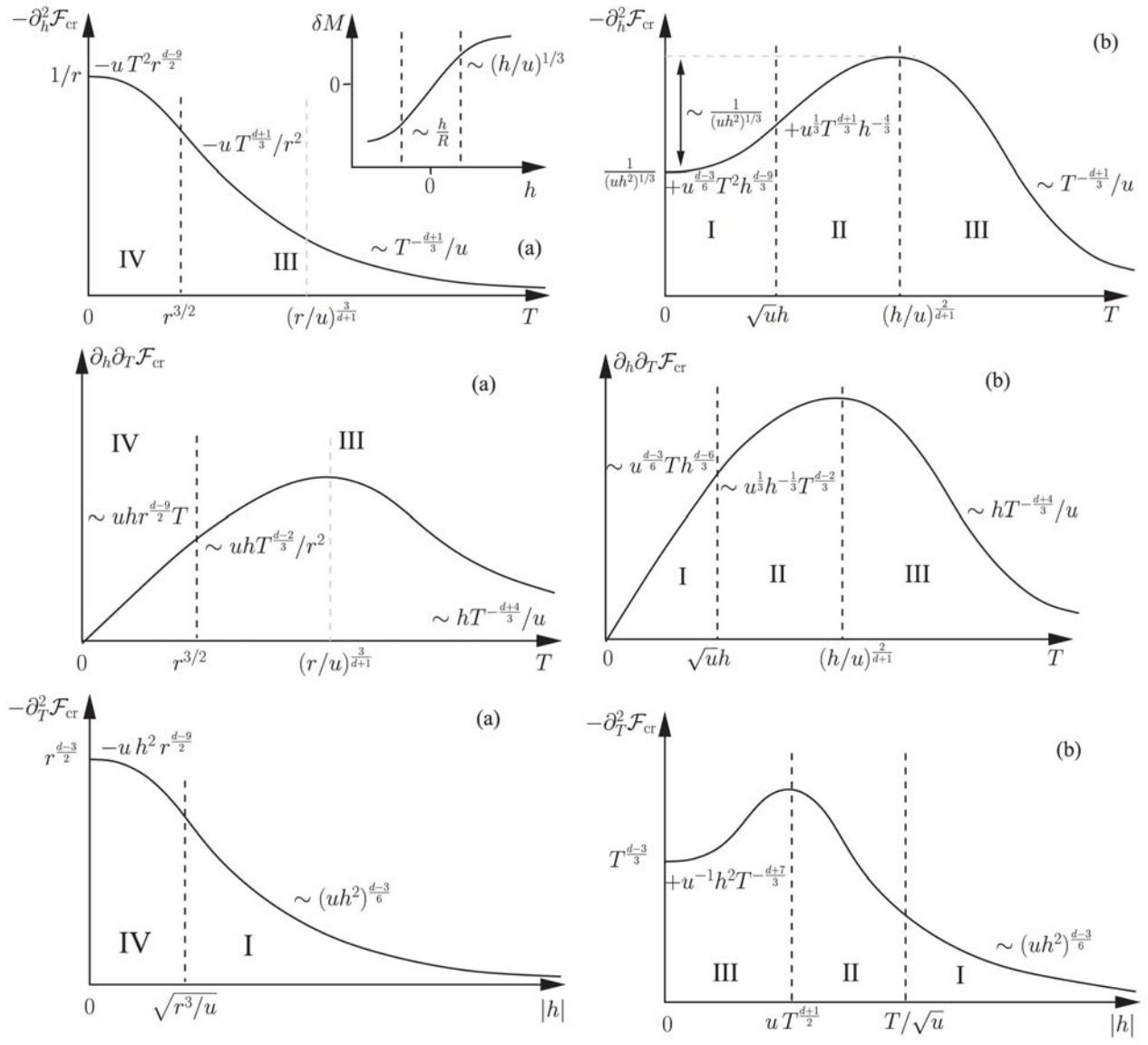

Figure 5.6: The compressibility, thermal expansion, and specific heat coefficient in the various regions of the phase diagram, taken from Ref. [52]. The regions of the phase diagram are described in the main text.

of each term are different in both cases.

The Grüneisen parameter and its magnetic analogue change sign at the critical field, when $h(T) = 0$. The leading order behaviour of the Grüneisen parameter in region I of the phase diagram is found to be $\Gamma_h \sim \frac{1}{h \ln\left(\frac{1}{h}\right)}$, and in region III it is found to be $\Gamma_H \sim h/\left(T^{10/3}\right)$ in three dimensions.

We now discuss a model of a metamagnetic quantum critical end-point and an antiferromagnetic quantum critical point in close proximity in the phase diagram.

5.3 Quantum Critical Metamagnetism and Antiferromagnetism

5.3.1 Generating the Situation

Now that we have reviewed the literature on metamagnetic quantum critical end-points, we discuss the possibility of a metamagnetic quantum critical end-point in proximity on the phase diagram to an antiferromagnetic quantum critical point. In Section 5.1 we discussed the possibility of realising this scenario by applying a magnetic field to the phase diagram of Figure 5.3a, to generate the phase diagram in Figure 5.3c.

In this section we generate an original model for this. Firstly, we review the literature on antiferromagnetism in magnetic fields. We then discuss a Landau theory for the interacting AFM QCP and metamagnetic QCEP, and make the model quantum critical by drawing inspiration from Chapters 2 and 3.

5.3.2 Antiferromagnetism in a Magnetic Field

Under the influence of a magnetic field, the antiferromagnetism precesses. This is another dynamical effect which must be accounted for when considering a quantum critical transition in a magnetic field. This scenario has been analysed by Fischer and Rosch [22], where they find

the precession term can also be characterised by the dynamical exponent $z = 2$. The key result is that the critical exponents associated with the transition are unchanged by this precession term, however the scaling functions are affected. If the precession terms are sufficiently strong, this can change the sign of the leading correction to the specific heat.

In the rest of this chapter, we assume that the precession terms are sufficiently weak compared to the damping terms so that we may effectively ignore their effects. We expect the critical exponents will not depend on this approximation.

5.3.3 Landau Theory

In this section we build a Landau theory for a metamagnetic quantum critical end-point and an antiferromagnetic QCP in close proximity on the phase diagram. By adapting the derivation of Section 5.2.1 we show that around this multicritical point the free energy does not look like that for a bicritical or tetracritical point with a field, but has an additional coupling term which is linear in the metamagnetic modes and quadratic in the antiferromagnetic modes.

To generate an action based around a quantum critical end-point, we first consider the Landau theory for a model with a quantum critical end-point in it, and a second order phase transition into antiferromagnetism. The Landau energy we start with is

$$F = R_3\Phi_3^2 - U_3\Phi_3^4 + V_3\Phi_3^6 - H\Phi_3 + R_2\phi_2^2 + U_2\phi_2^4 + U_{32}\phi_2^2\Phi_3^2, \tag{5.3.1}$$

where U_3, V_3, U_2 and U_{32} are all positive. Φ_3 represents metamagnetic modes, and ϕ_2 represents antiferromagnetic modes. When $\phi_2 = 0$, the model reduces to the model of a classical metamagnet, analysed in Section 5.2.1. With the understanding that eventually our quantum critical model in terms of spin-fluctuations will not be applicable in the antiferromagnetic ordered phase as explained in Chapter 2, we only analyse this model when $\langle\phi_2\rangle = 0$.

As for the model in Section 5.2.1, when the optimal value of $\phi_2 = 0$,the model has a quantum critical end-point at $R_3 = \frac{3}{5}\frac{U_3^2}{V_3}$, $\frac{H^*}{\Phi_3^*} = \frac{16}{25}\frac{U_3^2}{V_3}$, where $(\Phi_3^*)^2 = \frac{U_3}{5V_3}$. To find the effective

model in the vicinity of this point, we let $R_3 = R_3^* + \delta R_3$, $H = H^* + \delta H$, and $\Phi_3 = \Phi_3^* + \phi_3$. To quartic order in ϕ_3 we find that

$$\begin{aligned} F(\phi_3, \phi_2) = F(\Phi_3^*, 0) + \delta R_3 (\Phi_3^*)^2 - \delta H \Phi_3^* + (2\Phi_3^* \delta R_3 - \delta H)\phi_3 + \delta R_3 \phi_3^2 \\ + \left(R_2 + U_{32}(\Phi_3^*)^2\right)\phi_2^2 + 2U_{32}\Phi_3^* \phi_2^2 \phi_3 + 2U_3 \phi_3^4 + U_2 \phi_2^4 + U_{32}\phi_2^2 \phi_3^2, \end{aligned} \tag{5.3.2}$$

and so if we consider the free energy in powers of ϕ_3 and ϕ_2 alone, we find that

$$F(\phi_3, \phi_2) = -h\phi_3 + r_3\phi_3^2 + r_2\phi_2^2 + \gamma\phi_2^2\phi_3 + u_3\phi_3^4 + u_2\phi_2^4 + u_{32}\phi_2^2\phi_3^2. \tag{5.3.3}$$

Here, $h = \delta H - 2\Phi_3^* \delta R_3$, $r_3 = \delta R_3$, $r_2 = R_2 + U_{32}(\Phi_3^*)^2$, $\gamma = 2U_{32}\Phi_3^*$, $u_{32} = U_{32}$, $u_3 = 2U_3$, and $u_2 = U_2$. We note that all of the interaction terms, γ, u_2, u_3 and u_{32} are independent.

We only consider this model for $r_2 \geq 0$ so that $\langle \phi_2 \rangle = 0$, and only consider the model for $r_3 \geq 0$ as we are not interested in the second order phase transition at $r_3 = 0$ when $h = 0$. We are interested in the behaviour of this model as h changes.

If $r_3 \geq 0$ at the transition into the antiferromagnetic state (at $r_2 = 0$), then the antiferromagnetic transition is second order. This derivation has shown that a new term, quadratic in ϕ_2 and linear in ϕ_3 must appear in the Landau theory for this multicritical point. This simple argument based on the Landau free energy demonstrates that it is theoretically possible to have the end-point of a metamagnetic transition and a second order antiferromagnetic transition in the phase diagram, and has generated the effective model in the vicinity of such a point.

5.3.4 Making the Model Quantum Critical

We now attempt to build a quantum critical version of the Landau free energy of equation (5.3.3). Our technique in suggesting a model does not follow the analysis of Chapter 2 and Chapter 3, where the models were derived by integrating out the electrons, but instead to turn the Landau free energy in equation (5.3.3) into a quantum critical theory. We allow the

order parameter to fluctuate in both space and imaginary time, and use the damping terms that Hertz-Millis theory associates with each type of order.

Allowing the order parameters to fluctuate in space and imaginary time, the quantum critical model is

$$\begin{aligned} S = & -h\int d\boldsymbol{x}d\tau\phi_3(\boldsymbol{x},\tau) + \frac{1}{\beta V}\sum_{\omega_n,\boldsymbol{q}}\chi_3^{-1}(\boldsymbol{q},\omega_n)\,\phi_3(\boldsymbol{q},\omega_n)\phi_3(-\boldsymbol{q},-\omega_n) \\ & + \frac{1}{\beta V}\sum_{\omega_n,\boldsymbol{q}}\chi_2^{-1}(\boldsymbol{q},\omega_n)\,\phi_2(\boldsymbol{q},\omega_n)\phi_2(-\boldsymbol{q},-\omega_n) + \gamma\int d\boldsymbol{x}d\tau\phi_2^2(\boldsymbol{x},\tau)\phi_3(\boldsymbol{x},\tau) \\ & + \int d\boldsymbol{x}d\tau\left[u_3\phi_3^4(\boldsymbol{x},\tau) + u_2\phi_2^4(\boldsymbol{x},\tau) + u_{32}\phi_2^2(\boldsymbol{x},\tau)\phi_3^2(\boldsymbol{x},\tau)\right] \end{aligned} \tag{5.3.4}$$

where the two inverse susceptibilities are the same as for the model of a quantum multicritical point,

$$\chi_2^{-1}(\boldsymbol{q},\omega_n) = r_2 + q^2 + \eta_2\left|\omega_n\right|, \tag{5.3.5}$$

$$\chi_3^{-1}(\boldsymbol{q},\omega_n) = r_3 + q^2 + \eta_3\frac{|\omega_n|}{q}. \tag{5.3.6}$$

This action is the same as the action for a quantum multicritical point discussed in Chapter 3, but with two additional terms. The question we wish to address is how do the additional terms affect the model studied in Chapter 3? The magnetic field term has already been discussed in Section 5.2, however the term proportional to γ is new.

Qualitatively, the γ term acts like an effective field for the ϕ_3 modes, which depends on the fluctuating antiferromagnetism. When the expectation value of ϕ_3 is non-zero, it also acts as a shift in the antiferromagnetic tuning parameter. The γ term also affects the quartic interaction u_2. This can be seen as if both h and u_3 were zero, the ϕ_3 modes could be integrated out and the action could be written in terms of ϕ_2 alone. The new quartic coupling for ϕ_2 would be $u_2 - \frac{\gamma^2}{4r_3}$, which may become negative. This would mean that the sixth order term would need to be taken into account. Even in the presence of a finite u_3 there is the possibility that antiferromagnetism could be stabilised in the vicinity of the QCP.

This new term is difficult to deal with using the renormalisation group, as we shall see in Section 5.5, however we believe that the physics of this term can be captured by dealing with it in a self-consistently renormalised (SCR) approach.

5.4 Self-Consistently Renormalised Approach

In this section we analyse the model of a metamagnetic quantum critical end-point interacting with an antiferromagnetic quantum critical point, using a self-consistently renormalised (SCR) approach, which we believe captures the physics in the vicinity of the transition. To avoid complications arising from the marginal nature of the antiferromagnetic interactions, we restrict our attention to three dimensional systems. We defer a more detailed RG treatment to Section 5.5. We first define the SCR method and its historic use, before applying it to the model of Section 5.3. We use the SCR method to find the regions of the phase diagram, and in each region we find the thermal expansion, specific heat and Grüneisen parameter.

5.4.1 For General Quantum Critical Systems

Here we briefly summarise the SCR method, and its application to the Hertz-Millis action. The SCR method is an approximate method, pre-dating Hertz-Millis theory, which can be used to investigate physics near a quantum critical point [31]. The basic idea is to deal with fourth order terms in the action by the substitution

$$u \int d\boldsymbol{x} d\tau \phi^4 (\boldsymbol{x}, \tau) \rightarrow u \int d\boldsymbol{x} d\tau \left\langle \phi^2 (\boldsymbol{x}, \tau) \right\rangle \phi^2 (\boldsymbol{x}, \tau) , \tag{5.4.1}$$

to arrive at an effective Gaussian action in terms of averages of the field, which must be calculated self-consistently. In this case the effective inverse susceptibility $X^{-1} (\boldsymbol{q}, \omega_n)$ is written

in terms of the bare susceptibility $\chi^{-1}(\boldsymbol{q}, \omega_n)$ as

$$X^{-1}(\boldsymbol{q}, \omega_n) = \chi^{-1}(\boldsymbol{q}, \omega_n) + u \int d\boldsymbol{x} d\tau \left\langle \phi^2(\boldsymbol{x}, \tau) \right\rangle, \tag{5.4.2}$$

$$= \chi^{-1}(\boldsymbol{q}, \omega_n) + u \frac{1}{\beta} \sum_{\Omega_n} \int d\boldsymbol{p} X(\boldsymbol{p}, \Omega_n). \tag{5.4.3}$$

Here the averages have been performed with respect to the effective inverse susceptibility.

Using the bare susceptibilities in the Hertz-Millis action, in three dimensions the sum can be performed directly above the critical point, and the temperature-dependence can be found. The effective inverse susceptibility is found to be

$$X^{-1}(\boldsymbol{q}, \omega_n) = r + q^2 + \frac{|\omega_n|}{q^{z-2}} + cuT^{\frac{z+1}{z}}, \tag{5.4.4}$$

where r is the renormalised tuning parameter which is zero at the transition, and c is a constant [31]. This formula is valid for ferromagnetic ($z = 3$) and antiferromagnetic ($z = 2$) systems in three dimensions. The temperature-dependence of the susceptibility agrees with Hertz-Millis theory for $d = 3$, discussed in Section 2.4.2. The sum over the effective inverse susceptibility used to derive equation (5.4.4) was derived by performing the sum exactly at $r = 0$, however we know from the analysis on the Hertz-Millis model in Chapter 2 that the inverse susceptibility takes this form as long as $r < T^{2/z}$.

Prior to the Hertz-Millis formalism of quantum criticality, the SCR method was the standard approach to analyse spin fluctuations in itinerant magnets. Within this theory physical properties such as the specific heat can be calculated. The results of the SCR calculation can reproduce the $C \sim T \ln\left(\frac{1}{T}\right)$ specific heat, for example [31]. However, in the SCR method there is no systematic way, beyond comparing results with other methods, to determine the suitability of the substitution in equation (5.4.1). This is not an approximation based on the existence of a small parameter, which would be a reasonable assumption in a certain limit, but it is just an assumption made purely to simplify the algebra.

5.4.2 For the Quantum Critical Metamagnet and Antiferromagnet

We now extend the SCR method to the model of a quantum critical metamagnetic transition and an antiferromagnetic transition, defined by the model in equation (5.3.4). Here we restrict our attention to three dimensions to avoid complications arising from the marginal antiferromagnetic interactions. In this section we do not need the kinetic coefficients, so we let $\eta_2 = \eta_3 = 1$.

To proceed, we make the same substitution for the quartic terms in ϕ_2 and ϕ_3 as in equation (5.4.1), but the u_{32} and γ terms require more careful consideration. We approximate the $u_{32}\phi_2^2\phi_3^2$ term as

$$\begin{aligned} u_{32}\int d\boldsymbol{x}d\tau\phi_2^2\left(\boldsymbol{x},\tau\right)\phi_3^2\left(\boldsymbol{x},\tau\right) \rightarrow & \frac{u_{32}}{2}\int d\boldsymbol{x}d\tau\left\langle\phi_2^2\left(\boldsymbol{x},\tau\right)\right\rangle\phi_3^2\left(\boldsymbol{x},\tau\right) \\ & + \frac{u_{32}}{2}\int d\boldsymbol{x}d\tau\phi_2^2\left(\boldsymbol{x},\tau\right)\left\langle\phi_3^2\left(\boldsymbol{x},\tau\right)\right\rangle. \end{aligned} \tag{5.4.5}$$

We approximate the $\gamma\phi_3\phi_2^2$ term in a similar manner, letting

$$\begin{aligned} \gamma\int d\boldsymbol{x}d\tau\phi_3\left(\boldsymbol{x},\tau\right)\phi_2^2\left(\boldsymbol{x},\tau\right) \rightarrow & \frac{\gamma}{2}\int d\boldsymbol{x}d\tau\left\langle\phi_3\left(\boldsymbol{x},\tau\right)\right\rangle\phi_2^2\left(\boldsymbol{x},\tau\right) \\ & + \frac{\gamma}{2}\int d\boldsymbol{x}d\tau\left\langle\phi_2^2\left(\boldsymbol{x},\tau\right)\right\rangle\phi_3\left(\boldsymbol{x},\tau\right). \end{aligned} \tag{5.4.6}$$

These approximations capture the influences γ has as an effective field and a shift in the antiferromagnetic tuning parameter. However, they do not capture the possible effect on the quartic interaction u_2 mentioned in Section 5.3.4. Such approximations seem to be valid as long as the effective u_2 remains positive, which would require a sufficiently large u_3.

Under these approximations, we find that we can write down three SCR equations for the renormalised magnetic field H, and the renormalised inverse susceptibilities X_3^{-1} and X_2^{-1}. We find that

$$H = h - \frac{\gamma}{2}\int d\zeta X_2\left(\zeta\right), \tag{5.4.7}$$

$$X_3^{-1}\left(\zeta\right) = \chi_3^{-1}\left(\zeta\right) + u_3\left\langle\phi_3\right\rangle^2 + u_3\int d\zeta' X_3\left(\zeta'\right) + \frac{u_{32}}{2}\int d\zeta' X_2\left(\zeta'\right), \tag{5.4.8}$$

and

$$X_2^{-1}(\zeta) = \chi_2^{-1}(\zeta) + \frac{\gamma}{2}\langle\phi_3\rangle + \frac{u_{32}}{2}\langle\phi_3\rangle^2 + u_2\int d\zeta' X_2(\zeta') + \frac{u_{32}}{2}\int d\zeta' X_3(\zeta') \tag{5.4.9}$$

where $\zeta \equiv (\boldsymbol{q}, \omega)$ and $\langle\phi_3\rangle$ is the expectation value of ϕ_3, which is spatially uniform.

The result of these sums depends on whether the modes are in the quantum critical or Fermi liquid regimes, which depends on the uniform part of the inverse susceptibility, $X_i^{-1}(q=0,\omega=0)$. We use the notation that $X_i^{-1}(q=0,\omega=0) \equiv X_i^{-1}$. If $X_i^{-1} \gg T^{2/z_i}$ then the sum yields no interesting temperature dependence, and the renormalised tuning parameters are shifted by a constant, and an amount proportional to T^2. In the opposite case, the sum has a temperature-dependent contribution proportional to $T^{(1+z)/z}$.

We use the notation that $R_3(T) = \chi_3^{-1}(0) + u_3\int d\zeta' X_3(\zeta') + \frac{u_{32}}{2}\int d\zeta' X_2(\zeta')$ and $R_2(T) = \chi_2^{-1}(0) + u_2\int d\zeta' X_2(\zeta') + \frac{u_{32}}{2}\int d\zeta' X_3(\zeta')$, which are the magnetic field-independent parts of X_3^{-1} and X_2^{-1} respectively.

Just as for a single metamagnetic quantum critical point, there are two regimes for the expectation value of the field ϕ_3, which is calculated as $\langle\phi_3\rangle = H(T)X_3$. In the linear regime, $R_3^3(T) \gg uH^2(T)$, the inverse susceptibility X_3^{-1} is dominated by the renormalised tuning parameter $X_3^{-1} \approx R_3(T)$ leading to $\langle\phi_3\rangle = \frac{H(T)}{R_3(T)}$. In the non-linear regime, $R_3^3(T) \ll H^2(T)$, the susceptibility is dominated by the magnetic field-dependent contribution, leading to $X_3^{-1} \approx \frac{1}{u_3 H^2(T)}$ and so $\langle\phi_3\rangle = \left(\frac{H(T)}{u_3}\right)^{1/3}$.

Therefore in the linear regime

$$X_3^{-1}(q,\omega) = R_3(T) + q^2 + \frac{\omega}{q} \tag{5.4.10}$$

$$X_2^{-1}(q,\omega) = R_2(T) + \frac{\gamma}{2}\frac{H(T)}{R_3(T)} + q^2 + |\omega|. \tag{5.4.11}$$

In the non-linear regime

$$X_3^{-1}(q,\omega) = u_3^{1/3}H^{2/3}(T) + q^2 + \frac{\omega}{q}, \tag{5.4.12}$$

	$[R_3(T)]^3 \ll u_3 [H(T)]^2$	$X_3^{-1} \ll T^{2/3}$	$X_2^{-1} \ll T$
(a)	✓	✓	✓
(b)	✓	✓	
(c)	✓		✓
(d)	✓		
(A)		✓	✓
(B)		✓	
(C)			✓
(D)			

Table 5.1: Definitions of the regions of the phase diagram. If the column is ticked the inequality is obeyed, and if blank the inverse is true. Regions (a) and (b) should be further subdivided into a region where the correlation length is dominated by temperature ($X_3 < T^{4/3}$), and a region where the temperature-independent part dominates. Similarly, regions (a) and (c) should be further subdivided based upon whether the antiferromagnetic correlation length is dominated by temperature ($X_2 < T^{3/2}$) or a temperature-independent part.

and

$$X_2^{-1}(q,\omega) = R_2(T) + \frac{\gamma}{2}\left(\frac{H(T)}{u_3}\right)^{1/3} + q^2 + |\omega|\,. \tag{5.4.13}$$

This leads to eight distinct regions of the phase diagram where the inverse susceptibilities have different forms, separated by the linear to non-linear crossover, and the two quantum critical to Fermi liquid crossovers. The notation for these eight regions of the phase diagram is given in Table 5.1.

The temperature dependence of the magnetic field depends on the antiferromagnetic modes, and is given by

$$H(T) = \begin{cases} h - c_{2h}\gamma T^{3/2} & \text{in regions (a), (c), (A), (C),} \\ h + h_T T^2 & \text{in regions (b), (d), (B), (D),} \end{cases} \tag{5.4.14}$$

where the $T^{3/2}$ power law is due to the antiferromagnetic modes.

The expectation value of $\langle\phi_3\rangle$ is different in the linear and non-linear regimes, and is given

by

$$\langle \phi_3 \rangle = \begin{cases} \frac{H(T)}{R_3(T)} & \text{in regions (a), (b), (c), (d),} \\ \left(\frac{H(T)}{u_3}\right)^{1/3} & \text{in regions (A), (B), (C), (D).} \end{cases} \tag{5.4.15}$$

The renormalised metamagnetic tuning parameter is given by

$$R_3(T) = \begin{cases} r_3 + c_{33} u_3 T^{4/3} & \text{in regions (a), (b), (A), (B),} \\ r_3 + c_{32} u_{32} T^{3/2} & \text{in regions (c), (C),} \\ r_3 + c_{3F} T^2 & \text{in regions (d), (D).} \end{cases} \tag{5.4.16}$$

In regions (c) and (C) the temperature-dependent part is much smaller than r_3, and in regions (d) and (D) the leading temperature dependent correction is of order T^2. In regions (a), (b), (A) and (B), there is also a subleading additive correction of $c_{32} u_{32} T^{3/2}$.

The renormalised antiferromagnetic tuning parameter is given by

$$R_2(T) = \begin{cases} r_2 + c_{23} u_{32} T^{4/3} & \text{in regions (a), (b), (A), (B),} \\ r_2 + c_{22} u_2 T^{3/2} & \text{in regions (c), (C),} \\ r_2 + c_{2F} T^2 & \text{in regions (d), (D).} \end{cases} \tag{5.4.17}$$

In regions (d) and (D) the leading temperature dependent correction is of order T^2. In regions (a), (b), (A) and (B), there is also a subleading additive correction of $c_{22} u_2 T^{3/2}$.

5.4.3 Phase Diagram

Using the renormalised tuning parameters, we now find the various crossovers between the various regions of the phase diagram. We consider the phase diagram in the $h - T$ plane, at fixed r_2 and r_3. We first note that the crossovers associated with the metamagnetic modes only, shown in Figure 5.5, are unchanged by the presence of the antiferromagnetic modes. We consider how the crossovers and phase transitions associated with antiferromagnetism overlay

this figure and divide up the phase diagram.

Figure 5.7 shows examples of possible phase diagrams in the $h-T$ plane. In the following we shall describe the various crossovers in this phase diagram. In the $h-T$ plane there is a phase transition into the antiferromagnetic phase. At $T=0$ this occurs at $h^*=-r_2-\frac{\gamma}{2}\langle\phi_3\rangle$ which is in the linear regime if $r_2<\frac{\gamma}{2}\sqrt{r_3}u_3$ and in the non-linear regime if this inequality is reversed. This is the difference between Figures 5.7i and 5.7ii where the transition is in the linear regime, and Figures 5.7iii and 5.7iv where the transition is in the non-linear regime.

The crossovers between Fermi-liquid and quantum critical behaviour of the antiferromagnetic modes depends on whether the metamagnetic modes are Fermi-liquid like. In the linear regime, this is the line $r_3\sim T^{2/3}$. The crossover between regions (d) and (c) is $\Delta h/r_3=2T/\gamma$, where Δh is $h-h^*$. Depending on the gradients of the lines in the phase diagram, this line may or may not cross the line $r_3\sim T^{2/3}$ in the linear regime. This is the difference between Figures 5.7i and 5.7iii where the lines intersect in the linear regime, and Figures 5.7ii and 5.7iv where they do not. If they do intersect in the linear regime then there is a crossover between regions (a) and (b), which is $T\sim\left[\frac{\gamma}{2u_3}\Delta h\right]^{3/7}$. The exponent comes from the temperature-dependence of $R_3(T)$ dominating $\langle\phi_3\rangle$ in these regimes.

In the non-linear regime, the crossover between Fermi-liquid and quantum critical behaviour of the antiferromagnetic modes is $u_3\left(\frac{2}{\gamma}\right)^3(T-r_2)^3=h^*h_TT^2+\Delta h$. This describes either the crossover between (A) and (B), or (C) and (D). This crossover can be written as $T\sim\frac{1}{u_3}\left(\frac{\gamma}{2}\right)^3\frac{\Delta h}{r_2^2}$ if $T<r_2$, and as $\Delta h=-h_TT^2$ otherwise, with a T^3 correction. So for $T>r_2$ this is dominated by the temperature-dependence of the scaling field $H(T)$. If $h_T>0$ then this will mean that for $T>r_2$, the inequality $X_2^{-1}>T$ is always true, and regimes (A) and (C) do not exist above these temperatures. However, if h_T is negative, then it *is* possible that the inequality $X_2^{-1}>T$ can be violated, even at temperatures $T>r_2$. In this case, regions (A) and (C) may exist at such temperatures, with a quadratic crossover.

When $X_2^{-1}<0$, an antiferromagnetically ordered phase is entered. The critical temperature can be found by solving $X_2^{-1}=0$, and we find that in each region (a), (c), (A) and

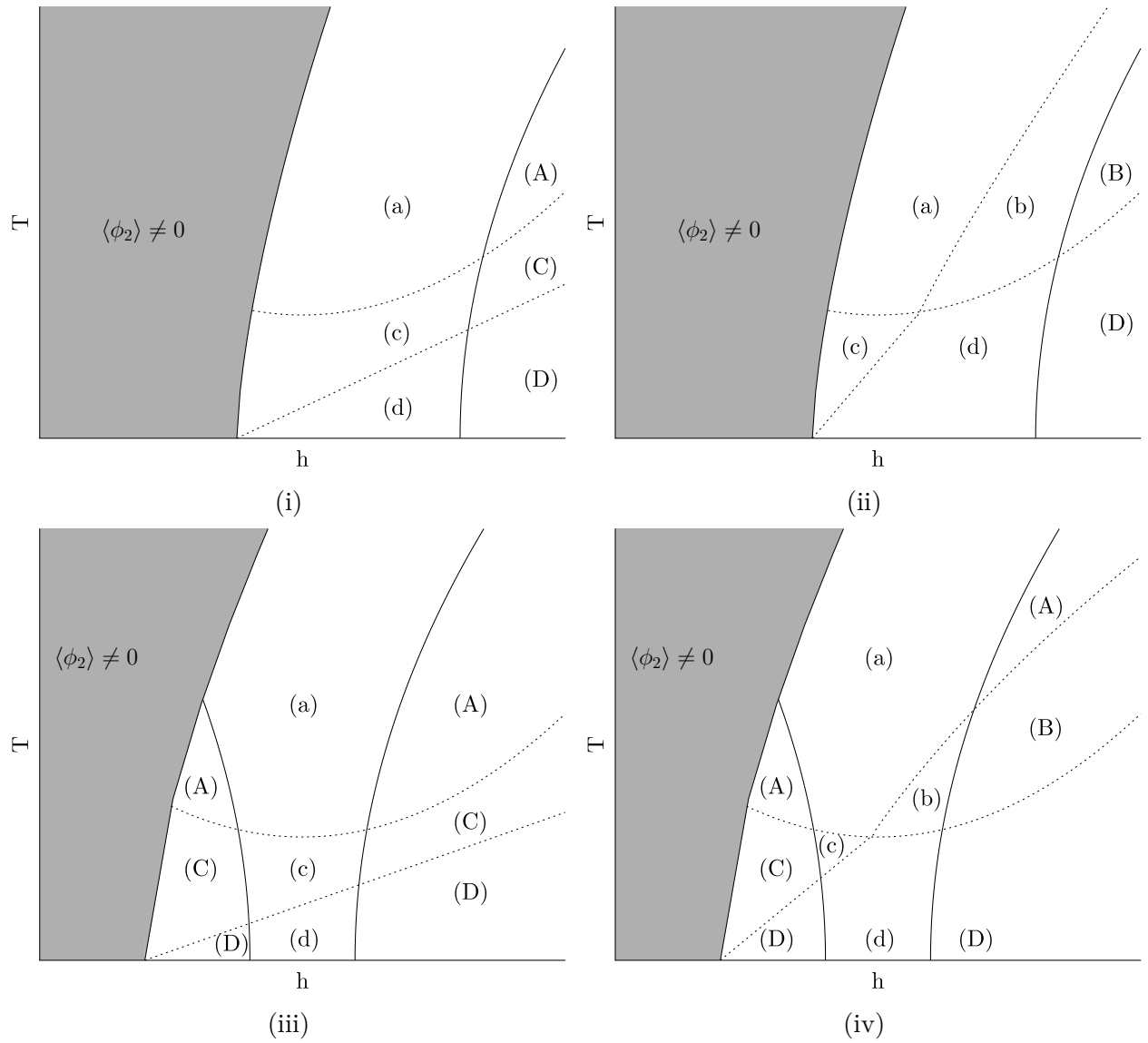

Figure 5.7: Examples of possible phase diagrams of a metamagnetic quantum critical endpoint and an antiferromagnetic quantum critical point, in the h-T plane at fixed r_2 and r_3. The regions of the phase diagram are described in the main text.

(C), the boundary of the ordered phase is dominated by the temperature dependence of the magnetic field $H(T) = h - c_{h2}\frac{\gamma}{2}T^{3/2}$. This leads to $T_c = \left(\frac{\gamma}{2}\Delta h\right)^{2/3}$ in all regimes. There are two exceptions. If $T < r_2^6$ in region (a), then the boundary is instead $\Delta h = -T_c^{4/3}c_{33}u_3 r^3$. If $T < r_2^3$ in region (A), then the ordered phase boundary is instead $\Delta h = -3c_{22}u_2u_3\left(\frac{2}{\gamma}\right)^3 r_2^2 T_c^{4/3}$. Since these are only relevant for very small temperatures, these regions are not shown in Figure 5.7.

5.4.4 Physical Properties

Using the SCR method, we have arrived at an effective Gaussian model for the situation of an antiferromagnetic quantum critical point interacting with a metamagnetic quantum critical end-point. We now use this to investigate the physical properties of the system.

There are three contributions to the critical part of the free energy, the component from the optimal value of $\langle\phi_3\rangle$, and the Gaussian fluctuations of both antiferromagnetic and metamagnetic modes. The contribution to the free energy from $\langle\phi_3\rangle \equiv \bar{\phi}_3$ is given by $\mathcal{F}_{\bar{\phi}_3} = -H(T)\bar{\phi}_3$. In the linear regime $\bar{\phi}_3 = \frac{H(T)}{R_3(T)}$ and in the non-linear regime $\bar{\phi}_3 = \frac{1}{u_3^{1/3}}H^{4/3}(T)$. These have different expansions in each regime.

Since we are left with a Gaussian model, we can evaluate the free energy and its derivatives using techniques already described. The free energy associated with the fluctuations could be calculated directly from Gaussian integration, as in equation (2.3.4). It is more simple to use equation (2.4.20), which was derived by successively integrating out the highest momentum modes. Since they have already been analysed in Sections 2.4.4 and 3.5, we may directly use the results of these calculations in this section.

We now consider the thermal expansion, specific heat and Grüneisen parameter in each regime.

	$\alpha_{\bar{\phi}_3}$	α_{fl3}	α_{fl2}
(a_+)	$\frac{h}{u_3}T^{-7/3}+\frac{\gamma}{u_3}T^{-5/6}$	$T^{1/3}$	$T^{1/2}+\frac{\gamma}{u_3}T^{-4/3}-\frac{\gamma h}{u_3^2}T^{-8/3}$
(a_-)	$\frac{hu_3T^{1/3}}{r_3^2}+\gamma\frac{T^{1/2}}{r_3}$	$T^{1/3}$	$T^{1/2}\left(1+\frac{\gamma}{2}\frac{1}{r_3}-\frac{\gamma}{2}\frac{h}{r_3^2}\right)$
(b_+)	$\frac{h}{u_3}T^{-7/3}-\frac{h_T}{u_3}T^{-1/3}$	$T^{1/3}$	$\frac{\left(T+\frac{\gamma}{2u_3}T^{-1/3}-\frac{\gamma h}{2u_3^2}T^{-5/3}\right)}{\left(r_2+\frac{\gamma}{2}\frac{h}{u_3}T^{-4/3}\right)^{1/2}}$
(b_-)	$\frac{hu_3T^{1/3}}{r_3^2}-h_T\frac{T}{r_3}$	$T^{1/3}$	$\frac{T}{\left(r_2+\frac{\gamma}{2}\frac{h}{r_3}\right)^{1/2}}\left(1+\frac{\gamma}{2r_3}-\frac{\gamma h}{2r_3^2}\right)$
(c)	$u_{32}\frac{hT^{1/2}}{r_3^2}+\gamma\frac{T^{1/2}}{r_3}$	$\frac{T}{r_3}$	$T^{1/2}\left(1+\frac{\gamma}{2}\frac{1}{r_3}-\frac{\gamma}{2}\frac{h}{r_3^2}\right)$
(d)	$\frac{hT}{r_3^2}-h_T\frac{T}{r_3}$	$\frac{T}{r_3}$	$\frac{T}{\left(r_2+\frac{\gamma}{2}\frac{h}{r_3}\right)^{1/2}}\left(1+\frac{\gamma}{2}\frac{1}{r_3}-\frac{\gamma}{2}\frac{h}{r_3^2}\right)$
(A)	$\frac{u_3^{-1/3}T^{1/2}}{\left(h-\frac{\gamma}{2}T^{3/2}\right)^{2/3}}$	$u_3^{1/3}\left(\frac{T}{h-\frac{\gamma}{2}T^{3/2}}\right)^{1/3}$	$T^{1/2}\left(1+\frac{\gamma}{6u_3^{1/3}}\left(h-\frac{\gamma}{2}T^{3/2}\right)^{-2/3}\right)$
(B)	$\frac{u_3^{-1/3}h_TT}{(h+h_TT^2)^{2/3}}$	$u_3^{1/3}\left(\frac{T}{h+h_TT^2}\right)^{1/3}$	$\frac{T\left(1+\frac{\gamma}{6u_3^{1/3}}\left(h+h_TT^2\right)^{-2/3}\right)}{\left(r_2+\frac{\gamma}{2u_3^{1/3}}(h+h_TT^2)^{1/3}\right)^{1/2}}$
(C)	$\frac{u_3^{-1/3}T^{1/2}}{\left(h-\frac{\gamma}{2}T^{3/2}\right)^{2/3}}$	$\frac{T}{h-\frac{\gamma}{2}T^{3/2}}$	$T^{1/2}\left(1+\frac{\gamma}{6u_3^{1/3}}\left(h-\frac{\gamma}{2}T^{3/2}\right)^{-2/3}\right)$
(D)	$\frac{u_3^{-1/3}h_TT}{(h+h_TT^2)^{2/3}}$	$\frac{T}{h+h_TT^2}$	$\frac{T\left(1+\frac{\gamma}{6u_3^{1/3}}\left(h+h_TT^2\right)^{-2/3}\right)}{\left(r_2+\frac{\gamma}{2u_3^{1/3}}(h+h_TT^2)^{1/3}\right)^{1/2}}$

Table 5.2: Leading order contributions to the thermal expansion in each region of the phase diagram. $\alpha_{\bar{\phi}_3}$ is the contribution from $\bar{\phi}_3$, α_{fl3} is the contribution from metamagnetic fluctuations, and α_{fl2} is the contribution from antiferromagnetic fluctuations. We have split regions (a) and (b) into (a_+) and (b_+) where $u_3T^{4/3} > r_3$, and (a_-) and (b_-) where this inequality is reversed.

Thermal Expansion

The thermal expansion is calculated as

$$\alpha = \frac{\partial^2 \mathcal{F}_{cr}}{\partial T \partial p}, \tag{5.4.18}$$

where $\mathcal{F}_{cr}$ is the critical part of the free energy, and p is the physical pressure. When changing the physical pressure, we expect the parameters r_2, r_3 and h to all change. We assume that the derivatives of these parameters with respect to pressure are constants. The contributions to the thermal expansion in each regime from each part of the free energy are listed in Table 5.2. We now discuss how these have been calculated.

The contribution to the thermal expansion from $\bar{\phi_3}$, which we denote as $\alpha_{\bar{\phi_3}}$, is dominated by $\frac{\partial^2 \mathcal{F}_{\bar{\phi_3}}}{\partial T \partial h}$ which is proportional to $\alpha_{\bar{\phi_3}} \sim -\frac{\partial}{\partial T}\frac{H(T)}{R_3(T)}$ in the linear regimes and $\alpha_{\bar{\phi_3}} \sim -\frac{4}{3}\frac{\partial}{\partial T}\frac{H^{1/3}(T)}{u_3^{1/3}}$ in the non-linear regimes.

There are also additive contributions arising from fluctuations of the ϕ_3 modes. There are two contributions to $\alpha_{fl3} = \frac{\partial \mathcal{F}_{fl3}}{\partial p}$, from $\frac{\partial \mathcal{F}_{fl3}}{\partial r_3}$ and $\frac{\partial \mathcal{F}_{fl3}}{\partial h}$. From Section 2.4.4 we find that

$$\alpha_{fl3} = \frac{\partial X_3^{-1}(T)}{\partial p} T^{1/3}, \tag{5.4.19}$$

in regions (a), (b), (A) and (B). In regions (c), (d), (C) and (D) it is

$$\alpha_{fl3} = \frac{T}{X_3^{-1}(T)} \frac{\partial X_3^{-1}(T)}{\partial p}. \tag{5.4.20}$$

We calculate this using the approximation that $X_3^{-1}(T) = R_3(T)$ in the linear regions, and $X_3^{-1} = u_3^{1/3} H^{2/3}(T)$ in the non-linear regions.

The component from the antiferromagnetic fluctuations, α_{fl2} is given by

$$\alpha_{fl2} = \frac{\partial X_2^{-1}(T)}{\partial p} T^{1/2}, \tag{5.4.21}$$

in regimes (a), (c), (A) and (C), and

$$\alpha_{fl2} = \frac{\partial X_2^{-1}(T)}{\partial p} \frac{T}{X_2^{-1/2}(T)}, \tag{5.4.22}$$

in regimes (b), (d), (B) and (D). X_2^{-1} is equal to $R_2(T) + \frac{h}{R_3(T)}$ in the linear regimes and $R_2(T) + \frac{\gamma}{2u_3^{1/3}} h^{1/3}$ in the non-linear regimes.

We now analyse the thermal expansion in Table 5.2. The contribution from $\bar{\phi}_3$ dominates in all linear regions as temperature is changed at fixed h, r_3 and r_2, but the form of the thermal expansion and the subleading corrections depend on the region. The thermal expansion takes different forms in two different limits of regions (a) and (b), which we call (a_+) and (b_+) (where $r_3 \ll u_3 T^{4/3}$) and (a_-) and (b_-) (where $r_3 \gg u_3 T^{4/3}$). In region (c) the thermal expansion is dominated by $\alpha_{\bar{\phi}_3} = u_{32} \frac{h T^{1/2}}{r_3}$ where the temperature-dependence originates from the $T^{3/2}$ renormalisation to $R_3(T)$ from the antiferromagnetic fluctuations, and is a result of multicriticality.

The effective Gaussian model is symmetric about $h \to -h$ at $T = 0$, which means that if the changes in r_3 and r_2 as pressure is changed are ignored, the thermal expansion becomes zero at $H = 0$. Table 5.2 includes all corrections to this, and as in the case of an isolated metamagnetic QCEP, the dominant correction is from the temperature-dependent part of $H(T)$, which shifts the zero of thermal expansion away from $h = 0$. This shift is proportional to $h_T T^2$ when the antiferromagnetic modes are Fermi-liquid like, in region (b) of the phase diagram, which is the same as for an isolated metamagnetic QCEP. However, when the antiferromagnetic modes are quantum critical, in region (a) of the phase diagram the shift is proportional to $\gamma T^{3/2}$ due to the field being renormalised by the antiferromagnetic fluctuations.

While in all linear regions the thermal expansion is dominated by $\alpha_{\bar{\phi}_3}$ at fixed r_2, r_3 and h, the other contributions are sometimes important. Specifically in all linear regions except (a_+) and (b_+), some terms in α_{fl2} are of the same order as the components in $\alpha_{\bar{\phi}_3}$. These terms arise from the pressure-derivative of $X_2^{-1}(T)$, and sometimes have the opposite sign from the

components of $\alpha_{\bar{\phi}_3}$. In region (d), α_{fl3} is on the same order as $\alpha_{\bar{\phi}_3}$.

In the non-linear regions (A) and (B) at fixed T, the strongest varying terms as h changes are $\alpha_{\bar{\phi}_3}$ and α_{fl2}. These are both proportional to $T^{1/2}\,(\Delta h)^{-2/3}$ in region (A) and $T\,(\Delta h)^{-2/3}$ in region (B), where Δh is the deviation from the line $H(T) = 0$. In regions (C) and (D) however, the strongest term is α_{fl3}, proportional to $T\,(\Delta h)^{-1}$.

Specific Heat

The specific heat is calculated from

$$\frac{C}{T} = -\frac{\partial^2 \mathcal{F}_{cr}}{\partial T^2}. \tag{5.4.23}$$

The contributions to the specific heat in each regime from each part of the free energy are listed in Table 5.3. We now discuss how these have been calculated.

The component from $\bar{\phi}_3$ in the linear regime is dominated by the temperature dependence of $R_3(T)$, as opposed to the temperature dependence of $H(T)$. This is true even in region (d), where the T^2 correction to $R_3(T)$ is important.

The contribution from metamagnetic fluctuations is given by $C_{fl3}/T \sim \ln(1/T)$ in regions (a), (b), (A) and (B), and is given by $C_{fl3}/T \sim \ln\left(1/X_3^{-1}(T)\right)$ in regions (c), (d), (C) and (D). The contributions from the antiferromagnetic fluctuations is given by $C_{fl2}/T \sim -T^{1/2}$ in regions (a), (c), (A) and (C), and is given by $C_{fl2}/T \sim -X_2^{1/2}(T)$ in regions (b), (d), (B) and (D). Here, X_2^{-1} is equal to $R_2(T) + \frac{h}{R_3(T)}$ in the linear regimes and $R_2(T) + \frac{\gamma}{2u_3^{1/3}} h^{1/3}$ in the non-linear regimes.

We now analyse the specific heat in each region, using Table 5.3. In all regimes the contribution from $\bar{\phi}_3$ dominates, with the other two contributions giving the $H(T) = 0$ contribution. The form of $C_{\bar{\phi}_3}$ in region (c) of the phase diagram is due to the temperature-dependence of $R_3(T)$, which is in the region is controlled by fluctuations of the antiferromagnetic mode. The $h^2 T^{-1/2}/r_3^2$ behaviour of the specific heat in this region is a consequence of multicriticality.

	$C_{\bar{\phi}_3}/T$	C_{fl3}/T	C_{fl2}/T
(a_+)	$\frac{h^2}{u_3}T^{-10/3}$	$\ln(1/T)$	$-T^{1/2}$
(a_-)	$u_3 h^2 \frac{T^{-2/3}}{r_3^2}$	$\ln(1/T)$	$-T^{1/2}$
(b_+)	$\frac{h^2}{u_3}T^{-10/3}$	$\ln(1/T)$	$-\left(r_2 + \frac{\gamma}{2}\frac{h}{u_3 T^{3/4}}\right)^{-1/2}$
(b_-)	$u_3 h^2 \frac{T^{-2/3}}{r_3^2}$	$\ln(1/T)$	$-\left(r_2 + \frac{\gamma}{2}\frac{h}{r_3}\right)^{-1/2}$
(c)	$-u_{32} h^2 \frac{T^{-1/2}}{r_3^2}$	$\ln(1/r_3)$	$-T^{1/2}$
(d)	$-\frac{h^2}{r_3^2}$	$\ln(1/r_3)$	$-\left(r_2 + \frac{\gamma}{2}\frac{h}{r_3}\right)^{-1/2}$
(A)	$-\gamma\frac{\left(h-\frac{\gamma}{2}T^{3/2}\right)^{1/3}}{T^{1/2}} + \frac{\gamma^2 T}{\left(h-\frac{\gamma}{2}T^{3/2}\right)^{2/3}}$	$\ln(1/T)$	$-T^{1/2}$
(B)	$h_T\left(h + h_T T^2\right)^{1/3} + \frac{h_T^2 T^2}{(h+h_T T^2)^{2/3}}$	$\ln(1/T)$	$-\left(r_2 + \frac{\gamma}{2u_3^{1/3}}\left(h + h_T T^2\right)^{1/3}\right)^{-1/2}$
(C)	$-\gamma\frac{\left(h-\frac{\gamma}{2}T^{3/2}\right)^{1/3}}{T^{1/2}} + \frac{\gamma^2 T}{\left(h-\frac{\gamma}{2}T^{3/2}\right)^{2/3}}$	$\ln\left(1/\left(h - \frac{\gamma}{2}T^{3/2}\right)^{1/3}\right)$	$-T^{1/2}$
(D)	$h_T\left(h + h_T T^2\right)^{1/3} + \frac{h_T^2 T^2}{(h+h_T T^2)^{2/3}}$	$\ln\left(1/\left(h + h_T T^2\right)^{1/3}\right)$	$-\left(r_2 + \frac{\gamma}{2u_3^{1/3}}\left(h + h_T T^2\right)^{1/3}\right)^{-1/2}$

Table 5.3: Contributions to the specific in each region of the phase diagram. $C_{\bar{\phi}_3}$ is the contribution from $\bar{\phi}_3$, C_{fl3} is the contribution from metamagnetic fluctuations, and C_{fl2} is the contribution from antiferromagnetic fluctuations. We have split regions (a) and (b) into (a_+) and (b_+) where $u_3 T^{4/3} > r_3$, and (a_-) and (b_-) where this inequality is reversed.

$C_{\bar{\phi}_3}$ has two components in the non-linear region, both originating from the temperature-dependence of $H(T)$. The dominant contribution depends on whether considering $T \to 0$ at fixed h or vice-versa. As for the thermal expansion, in regions (b), (d), (B) and (D), the contribution from antiferromagnetic fluctuations diverges as $X_2^{-1}(T) \to 0$.

Grüneisen Parameter

As explained in Section 5.2.2, there are two Grüneisen parameters; the usual Grüneisen parameter Γ, and its magnetic analogue Γ_H. Since r_2, r_3 and h all depend on both the physical pressure and the physical magnetic field, these parameters are related. As in Section 5.2.2 there are several contributions to each Grüneisen parameter, which should are multiplied by the derivatives $\frac{\partial r_2}{\partial p}$ or $\frac{\partial h}{\partial H}$, for example.

We calculate the Grüneisen parameter as $\Gamma_H = \frac{\alpha}{C}$. In all regions, the result is similar to the Grüneisen parameter for an isolated metamagnetic QCEP. In regions (a_+) and (b_+) the

Grüneisen parameter is proportional to $h/\left(u_3 T^{10/3}\right)$, and in regions (C) and (D) we find it is proportional to $\left[\Delta h \ln\left(\frac{1}{\Delta h}\right)\right]^{-1}$, where Δh is the deviation from the line $H(T) = 0$. Within the regions (b), (d), (B) and (D), when $R_2(T) \to 0$ the antiferromagnetic fluctuations dominate both α and C. In this case they also dominate Γ and we find $\Gamma \sim -\frac{\partial X_2^{-1}}{\partial p}$, which is proportional to $-\left[1 + \frac{\gamma}{2}\frac{1}{R_3(T)} - \frac{\gamma}{2}\frac{h}{R_3^2(T)}\right]$ in regions (b) and (d), and proportional to $-\left[1 + \frac{\gamma}{6u_3^{1/3}} H^{-2/3}(T)\right]$ in regions (B) and (D).

5.4.5 Summary of Results

Our key results are the phase diagrams in Figure 5.7, and the specific heat and thermal expansion which are listed in Table 5.3 and Table 5.2. In the plane $H(T) = 0$, the specific heat and thermal expansion are the same as in the model of a multicritical point in Chapter 3. Any slight deviation from the critical magnetic field induces a non-zero expectation value of the metamagnetic mode $\bar{\phi}_3$, which strongly influences the specific heat and thermal expansion. These terms tend to dominate the thermodynamic properties, but the contributions from fluctuations can sometimes be of the same order.

In general the magnetic field and temperature-dependence of the physical properties is complex, but there are some indicators of multicriticality in the phase diagram. The temperature-dependence of the renormalised magnetic field is significantly different from the temperature-dependence for the metamagnetic transition. While for a quantum critical metamagnetic transition, the temperature-dependence is the usual Fermi liquid $h_T T^2$, in the presence of quantum critical antiferromagnetic fluctuations the temperature-dependence is $-\gamma T^{3/2}$. This affects the location of the zero of the thermal expansion and the sign-change of the Grüneisen parameter at finite temperatures above the quantum critical point.

Another indicator of multicriticality can be seen in region (c) of the phase diagram, where the dominant contribution to the specific heat at finite field is $-u_{32} h^2 \frac{T^{-1/2}}{r_3^2}$. This temperature-dependence is due to the quantum critical antiferromagnetic fluctuations affecting the temperature-dependence of the metamagnetic tuning parameter $R_3(T)$.

We now discuss how the model can be analysed using the renormalisation group.

5.5 Renormalisation Group Analysis

In the previous section, using the SCR method we found the phase diagram, correlation lengths and thermodynamic properties of the model of an antiferromagnetic QCP interacting with a metamagnetic quantum critical end-point. As mentioned when introducing the model, the SCR method is a rather ad-hoc procedure and there is no systematic way of testing its validity. It is therefore desirable to have a more formal analysis of this model, based on the renormalisation group scheme implemented in Chapter 3, to test the validity of the conclusions of the SCR method. The goal of this section is to derive such a model.

Our strategy is to perform a renormalisation group analysis on the action of equation (5.3.4), in order to identify which terms are irrelevant in the RG sense. The goal is to find out in which numbers of dimensions enough interactions scale to zero such that the action becomes manageable, and physical properties could be calculated by treating the irrelevant interactions perturbatively.

As a first step towards this, we analyse the corresponding classical model of equation (5.3.4), where the fields do not depend on imaginary time and only fluctuate spatially. We find that the upper critical dimension of this model is 6, and discuss the fixed point structure of the model in the vicinity of the upper critical dimension. In Section 5.5.2 we derive the RG equations for the quantum mechanical model and discuss the fixed point structure, and the differences between the quantum critical model and the corresponding classical model.

5.5.1 Corresponding Classical Model

Before analysing the full model in equation (5.3.4), we find it helpful to analyse the corresponding classical model, given by

$$\begin{aligned} F = &\int d\boldsymbol{q} \left(r_3 + q^2\right) \phi_3^2(q) + \int d\boldsymbol{q} \left(r_2 + q^2\right) \phi_2^2(q) - h \int d\boldsymbol{x} \phi_3(x) \\ &+ \gamma \int d\boldsymbol{x} \phi_3(x) \phi_2^2(x) + \int d\boldsymbol{x} \left[u_3 \phi_3^4(x) + u_2 \phi_2^4(x) + u_{32} \phi_3^2(x) \phi_2^2(x)\right]. \end{aligned} \tag{5.5.1}$$

In this equation, as an argument of ϕ_2, q measures the deviation from the antiferromagnetic ordering wavevector $\boldsymbol{Q}$. The momentum integrals are up to high momentum cut-offs Λ_2 and Λ_3 for the ϕ_2 and ϕ_3 modes respectively.

Cubic Terms in the Literature

Before embarking on a study of this model, we first discuss similar models which have been discussed in the literature. The difference between the model in equation (5.5.1) and the other models we have studied in this thesis is the presence of the cubic term, γ. Models with cubic terms have been studied in the literature, in a variety of contexts.

The most basic model one could write down with cubic terms is ϕ^3 theory, where the action has only quadratic and cubic terms. This model has attracted attention from field theorists due to the presence of cubic terms in the standard model [59]. The upper critical dimension of such a theory is found to be equal to 6. The scalar ϕ^3 model has been analysed using the ϵ expansion, which we discussed in Section 1.4.4, however there are no real fixed points below the upper critical dimension. Instead, interacting fixed points have been found to order ϵ *above* the upper critical dimension [60].

In n-component vector models, interacting fixed points are sometimes found below the upper critical dimension. However in such models, the coefficient of the cubic interaction is no longer a constant, but a tensor. The presence of stable fixed points below the upper critical dimension depends upon the number of field components, and crucially, on the symmetries of

the cubic tensor [61]. This stability of the fixed points with respect to quartic interactions has also been analysed in this model, and they are found to be irrelevant for $d - \epsilon > 4$ [62].

In the next section we analyse the model in equation (5.5.1) using the momentum-shell renormalisation group, and the ϵ expansion. This model does not have such luxurious symmetries, and we find that real, interacting fixed points only exist above the upper critical dimension.

Analysis of the Model

We now perform renormalisation on the free energy given in equation (5.5.1). To analyse this energy we employ the momentum-shell renormalisation group procedure described in Section 1.4.3, by successively integrating out high momenta modes. We simultaneously reduce both cut-offs by a factor b, and integrate out the modes above the cut-off. We calculate the renormalisation group equations to one-loop order, by analysing the diagrams shown in Appendix C. We find that

$$\frac{dh}{d\ln b} = \left(1 + \frac{d}{2}\right) h + n_2 \frac{\gamma}{1 + r_2}, \tag{5.5.2a}$$

$$\frac{dr_2}{d\ln b} = 2r_2 + 2\left(n_2 + 2\right) \frac{u_2}{1 + r_2} + n_3 \frac{u_{32}}{1 + r_3} - 2c_{32} \frac{\gamma^2}{\left(1 + r_2\right)\left(1 + r_3\right)}, \tag{5.5.2b}$$

$$\frac{dr_3}{d\ln b} = 2r_3 + 2\left(n_3 + 2\right) \frac{u_3}{1 + r_3} + n_2 \frac{u_{32}}{1 + r_2} - n_2 \frac{\gamma^2}{\left(1 + r_2\right)^2}, \tag{5.5.2c}$$

$$\frac{d\gamma}{d\ln b} = \left(3 - \frac{d}{2}\right) \gamma - 4\left(n_2 + 2\right) \frac{\gamma u_2}{\left(1 + r_2\right)^2} + 4c_{322} \frac{\gamma^3}{\left(1 + r_3\right)\left(1 + r_2\right)^2}, \tag{5.5.2d}$$

$$\frac{du_2}{d\ln b} = \left(4 - d\right) u_2 - 4\left(n_2 + 8\right) \frac{u_2^2}{\left(1 + r_2\right)^2} - n_3 \frac{u_{32}^2}{\left(1 + r_3\right)^2} - 4c_{3322} \frac{\gamma^4}{\left(1 + r_2\right)^2 \left(1 + r_3\right)^2}, \tag{5.5.2e}$$

$$\frac{du_3}{d\ln b} = \left(4 - d\right) u_3 - 4\left(n_3 + 8\right) \frac{u_3^2}{\left(1 + r_3\right)^2} - n_2 \frac{u_{32}^2}{\left(1 + r_2\right)^2} - 4n_2 \frac{\gamma^4}{\left(1 + r_2\right)^4}, \tag{5.5.2f}$$

$$\begin{aligned} \frac{du_{32}}{d\ln b} = {} & \left(4 - d\right) u_{32} - 8c'_{32} \frac{u_{32}^2}{\left(1 + r_2\right)\left(1 + r_3\right)} - 4\left(n_2 + 2\right) \frac{u_{32} u_2}{\left(1 + r_2\right)^2} \\ & - 4\left(n_3 + 2\right) \frac{u_{32} u_3}{\left(1 + r_3\right)^2} - 2c_{3222} \frac{\gamma^4}{\left(1 + r_3\right)\left(1 + r_2\right)^3}, \end{aligned} \tag{5.5.2g}$$

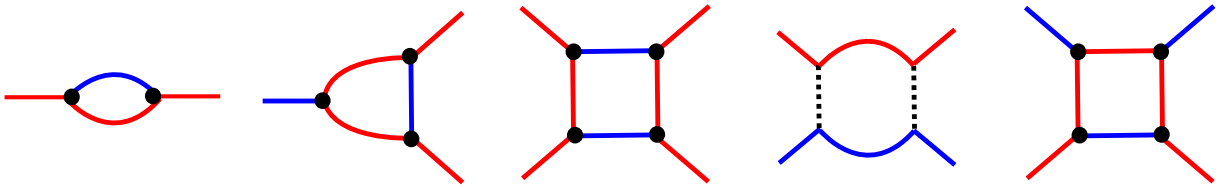

(a) $\frac{dr_2}{\delta \ln b} \sim c_{32}\gamma^2$ (b) $\frac{d\gamma}{\delta \ln b} \sim c_{322}\gamma^3$ (c) $\frac{du_2}{\delta \ln b} \sim c_{3322}\gamma^4$ (d) $\frac{du_{32}}{\delta \ln b} \sim c'_{32}u_{32}^2$ (e) $\frac{du_{32}}{\delta \ln b} \sim c_{3222}\gamma^4$

Figure 5.8: One-loop diagrams with both ϕ_2 (red) modes and ϕ_3 (blue) modes above the cut-off. The dotted line represents the interactions u_{32}, and the black dot represents the interaction γ.

where c_{322}, c_{3322}, c_{32} and c_{3222} are constants. These constants come from diagrams where both ϕ_2 and ϕ_3 modes are above the cut-off, which are shown in Figure 5.8.

These constants arise if Λ_2 and Λ_3 are not the same. In the normal momentum-shell RG approach, we neglect the momentum-dependence of the one-loop diagrams by only evaluating them when no momentum in transferred across the loop. In the diagrams of Figure 5.8, we have both ϕ_2 and ϕ_3 modes above the momentum cut-offs within the loop, so if Λ_2 and Λ_3 are different a momentum of at least $|\Lambda_2 - \Lambda_3|$ must travel through the loop. We assume that we may simply calculate these diagrams as if the ϕ_3 modes carry momentum Λ_3 and the ϕ_2 modes carry momentum Λ_2, and multiply by a constant to take account of this approximation. Another justification for this is that Λ_3 and Λ_2 are just high momentum cut-offs imposed on our calculations, and the physical properties should not depend on their choice. If we set $\Lambda_3 = \Lambda_2$, these constants would reduce to unity. We believe we are entitled to do this, as if we neglected these diagrams we would be ignoring possible physical processes in the RG flow.

Before we analyse these equations, we note that the one-loop corrections are actually $1/(r_i + \Lambda_i^2)$ for $i = 3, 2$, but in the RG equations we have set $\Lambda_2 = \Lambda_3 = 1$. We have also neglected coefficients of K_d. We suppose that if these factors were included, they would slightly change the location of the fixed points, and change the coefficients of the order ϵ corrections to the RG eigenvalues we find. However, they would not change the fixed point structure of the theory and not change the conclusions we draw from this analysis.

We now analyse these equations. We can immediate see that there is a Gaussian fixed point where u_2, u_3, u_{32} and γ are zero, however in dimensions less than 4 this fixed point is unstable with respect to the quartic couplings, and is unstable with respect to the cubic term γ in dimensions less than 6.

Since the γ term contains no powers of either mode greater than the quadratic, if we had no quartic interactions we would be able to integrate out either of the modes using Gaussian integration to find the free energy. However the resultant model for the other mode is not a Gaussian model, and so we conclude that the upper critical dimension of this model is 6. When we form a quantum critical version of this action in Section 5.5.2, we expect the two effective dimensions $d + z_3$ and $d + z_2$ to play a role in renormalisation, and in three spatial dimensions these are the effective dimensions 5 and 6. We therefore need to analyse this model below its upper critical dimension.

One method of investigating models below their upper critical dimension is the ϵ-expansion described in Section 1.4.4. If applied in the standard way to this model, we find there are no interacting fixed points below the upper critical dimension with real values of the parameters. However in dimensions $d = 6 + \epsilon$ we find there are two interacting fixed points at

$$\gamma^* = \pm \frac{1}{2}\sqrt{\frac{\epsilon}{2c_{322}}}, \tag{5.5.3a}$$

$$r_2^* = \frac{\epsilon}{8}\frac{c_{32}}{c_{322}}, \tag{5.5.3b}$$

$$r_3^* = \frac{n_2\epsilon}{16}\frac{1}{c_{322}}, \tag{5.5.3c}$$

$$h^* = -\operatorname{sign}(\gamma^*)\frac{n_2}{8}\sqrt{\frac{\epsilon}{2c_{322}}}, \tag{5.5.3d}$$

$$u_3^* = u_2^* = u_{32}^* = 0, \tag{5.5.3e}$$

which we now look at the physical properties in the vicinity of. The critical properties around each fixed point are the same, as the two fixed points are just related by $\phi_3 \to -\phi_3$. We now investigate theory in the vicinity of the positive root.

We linearise the RG equations around this fixed point, keeping terms to order ϵ. We write the RG equations in matrix form, as

$$\begin{pmatrix} \frac{d\delta h}{d\ln b} \\ \frac{d\delta r_2}{d\ln b} \\ \frac{d\delta r_3}{d\ln b} \\ \frac{d\delta \gamma}{d\ln b} \\ \frac{d\delta u_2}{d\ln b} \\ \frac{d\delta u_3}{d\ln b} \\ \frac{d\delta u_{32}}{d\ln b} \end{pmatrix} = \mathcal{R}_G \begin{pmatrix} \delta h \\ \delta r_2 \\ \delta r_3 \\ \delta \gamma \\ \delta u_2 \\ \delta u_3 \\ \delta u_{32} \end{pmatrix}, \tag{5.5.4}$$

where the matrix $\mathcal{R}_G$ is given by

$$\mathcal{R}_G = \begin{pmatrix} 4+\frac{\epsilon}{2} & -\frac{n_2}{2\sqrt{2c_{322}}}\epsilon^{1/2} & 0 & n_2\left(1-\frac{c_{32}}{8c_{322}}\epsilon\right) & 0 & 0 & 0 \\ 0 & 2+\frac{c_{32}}{4c_{322}}\epsilon & \frac{c_{32}}{4c_{322}}\epsilon & -\sqrt{2c_{322}}\epsilon^{1/2} & 2\left(n_2+2\right)\left(1-\frac{\epsilon}{8}\right) & 0 & n_3\left(1-\frac{n_2}{16c_{322}}\epsilon\right) \\ 0 & \frac{n_2}{4_{32}}\epsilon & 2+\frac{n_2}{4c_{322}}\epsilon & -\frac{n_2}{\sqrt{2c_{322}}}\epsilon^{1/2} & 0 & 2\left(n_3+2\right)\left(1-\frac{n_2}{16c_{322}}\epsilon\right) & n_2\left(1-\frac{c_{32}}{8c_{322}}\epsilon\right) \\ 0 & 0 & 0 & \frac{\epsilon}{2} & -\frac{2(n_2+2)}{\sqrt{2c_{322}}}\epsilon^{1/2} & 0 & 0 \\ 0 & 0 & 0 & 0 & -2-\epsilon & 0 & 0 \\ 0 & 0 & 0 & 0 & 0 & -2-\epsilon & 0 \\ 0 & 0 & 0 & 0 & 0 & 0 & -2-\epsilon \end{pmatrix}. \quad (5.5.5)$$

The eigenvalues of this matrix associated with the quartic interactions and the magnetic field are unchanged from the values about the Gaussian fixed point, however this point is unstable with respect to the cubic interaction. The two eigenvalues related to the renormalised tuning parameters (and therefore the correlation lengths) are $\lambda_a = 2$ and $\lambda_b = 2 + \frac{\epsilon}{4}\left(\frac{c_{32}}{c_{322}} + \frac{n_2}{c_{322}}\right)$. λ_b becomes 2 in the limit $\epsilon \to 0$, as one would expect. The RG eigenvectors are complicated combinations of all variables.

The analysis presented in this section shows that the term proportional to γ is relevant in less than 6 dimensions, so in the full quantum critical theory careful analysis of this term is required.

5.5.2 The Quantum Critical Model

We now turn our attention to the full quantum critical model described by equation (5.3.4). We derive the one-loop RG equations for all parameters and investigate the fixed point structure in the vicinity of the upper critical dimension of the system.

We derive the RG equations for this model in a slightly different way to that of the Hertz-Millis case, and the model of a multicritical point of Chapter 3. As noted in Section 2.3.1, the reason for deriving the RG equations from the linked cluster expansion was because of concerns as to how to continually reduce a cut-off of a discontinuous Matsubara sum. We noted that the derived RG equations could be derived by analogy with the usual momentum-shell RG by calculating diagrams with external vertices, as long as we used the correct expressions for the one-loop integrals.

Since we have already derived the integrals of modes above the cut-off in a situation with multiple dynamical exponents, we write down the RG equations by analogy with the diagrammatic expansion of Section 5.5.1 and the analysis of a quantum multicritical point in Chapter 3. Again, we find that we can write the RG equations in terms of previously analysed functions if we absorb factors of η_2 and η_3 into the definition of certain variables. The magnetic field enters the RG equations only in terms of $\tilde{h_2} = \eta_2^{1/2} h$, and the cubic term

enters as $\tilde{\gamma}_i = \gamma_i/\eta_i^{1/2}$ for $i = 2, 3$. The RG equations are

$$\frac{d\tilde{h}_2}{d\ln b} = \left[1 + \frac{D_2}{2}\right]\tilde{h}_2 + n_2\tilde{\gamma}_2 f_2^{(2)}, \tag{5.5.6a}$$

$$\frac{dr_2}{d\ln b} = 2r_2 + 2\left(n_2+2\right)\tilde{u}_2 f_2^{(2)} + n_3\tilde{w}_3 f_3^{(2)} - 2\tilde{\gamma}_3^2 f_{32}^{(4)}, \tag{5.5.6b}$$

$$\frac{dr_3}{d\ln b} = 2r_3 + 2\left(n_3+2\right)\tilde{u}_3 f_3^{(2)} + n_2\tilde{w}_2 f_2^{(2)} - n_2\tilde{\gamma}_2^2 f_2^{(4)}, \tag{5.5.6c}$$

$$\frac{d\tilde{\gamma}_2}{d\ln b} = \left[3 - \frac{D_2}{2}\right]\tilde{\gamma}_2 - 4\left(n_2+2\right)\tilde{\gamma}_2\tilde{u}_2 f_2^{(4)} + 4\tilde{\gamma}_2\tilde{\gamma}_3^2 f_{32}^{(4)}, \tag{5.5.6d}$$

$$\frac{d\tilde{\gamma}_3}{d\ln b} = \left[3 - \frac{D_3}{2}\right]\tilde{\gamma}_3 - 4\left(n_2+2\right)\tilde{\gamma}_3\tilde{u}_2 f_2^{(4)} + 4\tilde{\gamma}_3^3 f_{32}^{(4)}, \tag{5.5.6e}$$

$$\frac{d\tilde{u}_2}{d\ln b} = \left[4 - D_2\right]\tilde{u}_2 - 4\left(n_2+8\right)\tilde{u}_2^2 f_2^{(4)} - n_3\tilde{w}_2\tilde{w}_3 f_3^{(4)} - 4\tilde{\gamma}_2^2\tilde{\gamma}_3^2 f_{3322}, \tag{5.5.6f}$$

$$\frac{\tilde{u}_3}{d\ln b} = \left[4 - D_3\right]\tilde{u}_3 - 4\left(n_3+8\right)\tilde{u}_3^2 f_3^{(4)} - n_2\tilde{w}_2\tilde{w}_3 f_2^{(4)} - 4n_2\tilde{\gamma}_2^2\tilde{\gamma}_3^2 f_2^{(8)}, \tag{5.5.6g}$$

$$\frac{d\tilde{w}_2}{d\ln b} = \left[4 - D_2\right]\tilde{w}_2 - 8\tilde{w}_2\tilde{w}_3 f_{32}^{(4)} - 4\left(n_2+2\right)\tilde{u}_2\tilde{w}_2 f_2^{(4)} - 4\left(n_3+2\right)\tilde{w}_2\tilde{u}_3 f_3^{(4)} - 2\tilde{\gamma}_2^2\tilde{\gamma}_3^2 f_{3222}, \tag{5.5.6h}$$

$$\frac{d\tilde{w}_3}{d\ln b} = \left[4 - D_3\right]\tilde{w}_3 - 8\tilde{w}_3^2\frac{K_{32}f_3^{(2)}}{r_2+\Lambda_2^2} - 4\left(n_2+2\right)\tilde{u}_2\tilde{w}_3 f_2^{(4)} - 4\left(n_3+2\right)\tilde{u}_3\tilde{w}_3 f_3^{(4)} - 2\tilde{\gamma}_3^4 f_{3222}, \tag{5.5.6i}$$

where $D_i = d + z_i$. The function $f_2^{(8)}$, comes from diagrams with four ϕ_2 modes above the cut-off, and is

$$\begin{aligned} f_2^{(8)} = \Lambda_2^{d-1}K_d\int_0^{\Omega_2}\frac{d\omega}{\pi}\coth\left(\frac{\omega}{2\mathcal{T}_2}\right)\frac{4\omega\left(\delta_2+\Lambda_2^2\right)\left[\left(\delta_2+\Lambda_2^2\right)^2-\omega^2\right]}{\left[\left(\delta_2+\Lambda_2^2\right)^2+\omega^2\right]^4} \\ +\frac{1}{\pi}\int_0^{\Lambda_2}\frac{d^dq}{\left(2\pi\right)^d}\coth\left(\frac{\Omega}{2\mathcal{T}_2}\right)\frac{4\Omega\left(\delta_2+q^2\right)\left[\left(\delta_2+q^2\right)^2-\omega^2\right]}{\left[\left(\delta_2+q^2\right)^2+\omega^2\right]^4}. \end{aligned} \tag{5.5.7}$$

The function f_{3222} comes from diagrams with three ϕ_2 modes and one ϕ_3 mode above the

cut-off as in Figure 5.8e, and is given by

$$f_{3222} = \frac{1}{\left(\delta_2 + \Lambda_<^2\right)^3} \Lambda_<^{d-1} K_d \int_0^{\Omega_3 \Lambda_<} \frac{d\omega}{\pi} \coth\left(\frac{\omega}{2\mathcal{T}_3}\right) \frac{\omega/\Lambda_<}{\left(\delta_3 + \Lambda_<^2\right)^2 + \left(\omega/\Lambda_<\right)^2} + \frac{1}{\pi} \int^{\Lambda_<} \frac{d^d q}{(2\pi)^d} \coth\left(\frac{\Omega_3 q}{2\mathcal{T}_3}\right) \frac{1}{\left(\delta_2 + q^2\right)^3} \frac{\Omega_3}{\left(\delta_3 + q^2\right)^2 + \left(\Omega_3\right)^2}. \tag{5.5.8}$$

The function f_{3322} comes from diagrams with two ϕ_2 modes and two ϕ_3 modes above the cut-off as in Figure 5.8c, and is given by

$$f_{3322} = \frac{1}{\left(\delta_2 + \Lambda_<^2\right)^2} \Lambda_<^{d-1} K_d \int_0^{\Omega_3 \Lambda_<} \frac{d\omega}{\pi} \coth\left(\frac{\omega}{2\mathcal{T}_3}\right) \frac{2\left(\delta_3 + \Lambda_<^2\right)\omega/\Lambda_<}{\left[\left(\delta_3 + \Lambda_<^2\right)^2 + \left(\omega/\Lambda\right)^2\right]^2} + \frac{2}{\pi} \int^{\Lambda_<} \frac{d^d q}{(2\pi)^d} \coth\left(\frac{\Omega_3 q}{2\mathcal{T}_3}\right) \frac{1}{\left(\delta_2 + q^2\right)^2} \frac{\Omega_3\left(\delta_3 + q^2\right)}{\left[\left(\delta_3 + q^2\right)^2 + \Omega_3^2\right]^2}, \tag{5.5.9}$$

and all other functions are previously defined. The functions defined in equations (5.5.8) and (5.5.9) are derived by adapting the methods of deriving $f_{32}^{(4)}$ in Section 3.3.3. In writing these down, we have made the same approximation as in equation (3.3.31), and neglected terms in the integrands proportional to $\eta_2(b)/\eta_3(b)$.

We now analyse the RG equations. The quartic couplings are irrelevant in spatial dimensions greater than 2, and in the case of $d = 2$ the terms $\tilde{u_2}$ and $\tilde{w_2}$ are marginal. In two spatial dimensions, the cubic interactions $\tilde{\gamma_2}$ and $\tilde{\gamma_3}$ are both relevant, and in three spatial dimensions $\tilde{\gamma_2}$ is relevant while $\tilde{\gamma_3}$ is marginal.

To one-loop order, the only fixed point of the RG flow is the fixed point where all the terms in the RG equations are zero, which is unstable with respect to perturbations of γ, r and h. If we approximate the coefficient of ${\tilde{\gamma_3}}^3$ in equation (5.5.6e) as a constant K, then there is another fixed point of the RG flow in dimensions $d = 3 + \epsilon$ at

$$\left(\tilde{\gamma_3^*}\right)^2 = \frac{\epsilon}{2K}. \tag{5.5.10}$$

However, since $\tilde{\gamma_2}(b) = b^{1/2}\tilde{\gamma_3}(b)$, under RG $\tilde{\gamma_2}$ still grows, and this fixed point is of limited use

in calculating physical properties.

We have demonstrated that the presence of the cubic γ term complicates the RG calculation, and means that quantum critical RG equations do not have simple solutions below 4 spatial dimensions. How the renormalisation group analysis of this model should proceed remains an open question.

5.6 Conclusion

In this section we derived and analysed a model of a quantum critical end-point in proximity to an antiferromagnetic QCP in the phase diagram. Like the model examined in Chapter 3, this is another example of a quantum critical theory featuring the two dynamical exponents $z = 2$ and $z = 3$. However the model of this chapter differs because the symmetry-breaking field causes other terms to be present in the action.

The new terms turn out to be relevant in a renormalisation group sense, and any physical systems in a realistic number of spatial dimensions are below the upper critical dimension of the new theory, meaning that the interactions are important. How a full renormalisation group analysis of this model should be performed remains an open question. Despite this we have analysed the model using the self-consistently renormalised approach, and found the phase diagram and thermodynamic properties in each region.

The original goal was to see if the conclusions about the thermodynamic properties of a multicritical point survived under the application of a magnetic field to generate the phase diagram shown in Figure 5.3c, and we are able to answer this question within the SCR approximation. The key results are that the physical properties to leading order tend to be the same as in the metamagnetic transition, with corrections as discussed in Section 5.4.5. The largest effect of multicriticality is the temperature-dependence of the magnetic field, which acquires a renormalisation proportional to $T^{3/2}$ due to interactions with the antiferromagnetic modes. This is in contrast to the T^2 correction for a metamagnetic QCEP. This strong

temperature-dependence shifts the location of the sign change of the Grüneisen parameter at finite temperatures.

Our results may have some application to the compound YbAgGe, which was mentioned in Section 3.1.1. This material has a bicritical point at $T \approx 0.3K$ at $\mu_0 H \approx 4.5T$ between two distinct magnetically ordered phases, and exhibits quantum critical scaling at temperatures above this point [10]. One notable feature of the material is that the temperature dependence of the critical field is much stronger than in other quantum critical metamagnets, such as $CeRu_2Si_2$ [53] and $Sr_3Ru_2O_7$ [63]. We believe this stronger temperature dependence can be attributed to the strong renomalisation effects of antiferromagnetic fluctuations, which we have found from the SCR method. However, we note that this material is not expected to be explained by a $d = 3$ theory. Hints of a low effective dimensionality are seen in the quantum critical scaling relations [10], and the magnetic fluctuations in zero field seem to have a quasi-one-dimensional nature [64]. Nevertheless, even in a lower effective dimensionality we would expect the antiferromagnetic fluctuations to provide the field with a stronger temperature dependence than the Fermi liquid.

Chapter 6

CONCLUSIONS

In this thesis we have developed a model of a quantum multicritical point in a material unstable towards both ferromagnetic and antiferromagnetic order. Our model is based upon the Hertz-Millis theory detailed in Chapter 2, and in Chapter 3 we performed an analysis of the model using the techniques of the renormalisation group. We identified the distinct regions of the phase diagram, and the thermal expansion, specific heat and Grüneisen parameter in each region. We found these results to be consistent with the experimental data which motivated our investigation, and make predictions about currently unmeasured quantities. In Chapter 4 we investigated another aspect of the model that could not be captured from the renormalisation group analysis, which is the resistivity near a quantum multicritical point. Again, we found our results to be consistent with experimental data. In Chapter 5 we extended our model to consider a metamagnetic quantum critical end-point and an antiferromagnetic quantum critical point, under the influence of a magnetic field. Using the self-consistently renormalised approach we were able to find the regions of the phase diagram and the specific heat, thermal expansion and Grüneisen parameter in each region. We found that the presence of a magnetic field changes many of the properties of the multicritical model developed in Chapter 3, but we have predicted some indicators of multicriticality in the presence of a magnetic field.

We now summarise our key results. The phase diagram for a quantum multicritical point between a ferromagnetic phase and an antiferromagnetic phase is shown in Figure 3.5 in three

dimensions, and Figure 3.6 in two dimensions. We find it helpful to interpret the results as two interacting quantum critical points. The ferromagnetic QCP is unaffected by the antiferromagnetism, but the antiferromagnetic correlation length (and hence the boundary of the antiferromagnetically ordered phase) acquires the temperature-dependence usually associated with ferromagnetic correlations. Thermodynamic properties in three dimensions are detailed in Table 3.1, and properties in two dimensons are detailed in Table 3.2. The contribution from quantum critical ferromagnetism tends to dominate these properties. In Section 3.5 we found that in the presence of both ferromagnetic fluctuations and antiferromagnetic fluctuations, the resistivity obeys the power law usually associated with antiferromagnetism in disordered systems. Moreover, we found that the ferromagnetic fluctuations actually stabilise this power law, and we would expect to find it even in clean systems.

These results appear to match up with experimentally available data on both $NbFe_2$ and $Ta(Fe_{1-x}V_x)_2$, which both display specific heat obeying the ferromagnet $C \sim T \ln\left(\frac{1}{T}\right)$ power law and resistivities obeying the antiferromagnetic $\rho \sim \rho_0 + AT^{3/2}$ power law. Our prediction that the thermal expansion and Grüneisen parameter should also obey the power laws usually associated with ferromagnetism has not yet been tested. The boundaries of the ordered phases have not yet been measured in sufficient detail to allow comparison with the phase diagrams that we have derived.

In Chapter 5 we explained how we expect this model to develop under the influence of a magnetic field, and looked at a model of a metamagnetic quantum critical end-point interacting with an antiferromagnetic quantum critical point in three dimensions. The phase diagram in the $h - T$ plane is shown in Figure 5.7, and in Tables 5.2 and 5.3 we list the thermodynamic properties expected in each region of this phase diagram. While the thermodynamic properties are in general very complicated, we find that they tend to be dominated by the contribution from the metamagnetic modes, which is associated with the $z = 3$ theory. The main result of multicriticality is the temperature-dependent renormalisation of the magnetic field, which acquires a much stronger renormalisation in the presence of antiferromagnetic fluctuations

than the typical Fermi liquid corrections. In Section 5.6 we were able to identify the case of YbAgGe in the literature, which is a material which has a bicritical point in the phase diagram, where the magnetic field acquires a stronger temperature-dependent renormalisation than in other quantum critical metamagnets.

Within the context of the types of multiple dynamic scaling described in Section 2.6, the model of multicriticality we have analysed in Chapters 3 and 4 falls under the classification of decoupled multiple dynamic scaling. This is because the critical part of the free energy is the sum of two distinct contributions, associated with the fluctuations of each mode. Because we have analysed the model in Chapter 3 at or above its upper critical dimension the only option is to flow to the non-interacting fixed point. Nevertheless, the dangerously irrelevant interaction terms are what give the renormalised tuning parameters their temperature-dependence and hence shape the phase diagram. These are the effects of multicriticality not captured by the scaling analysis in Section 3.2. The simple scaling analysis also fails to capture the behaviour of the resistivity in such systems, which is dominated by multicritical behaviour.

This thesis raises some theoretical and experimental questions, and several avenues of research are now opened. One main question is how should the renormalisation group procedure be employed in the model of a metamagnetic QCEP interacting with an antiferromagnetic QCP? As the interaction term γ in equation (5.3.4) appears to be relevant in 3 spatial dimensions, there is the possibility that this model could exhibit stronger signatures of multicriticality that those predicted by the SCR theory we presented. Another possible avenue of research is how the resistivity behaves under a magnetic field. Rosch [48] predicted that the magnetoresistivity near an antiferromagnetic QCP depends on the temperature-dependence of the antiferromagnetic correlation length. In our analysis this has been shown to be changed by quantum critical ferromagnetic fluctuations, and thus magnetotransport near a QMCP could be significantly affected by multicriticality. Another avenue of possible further research is to see how the model of an interacting QCEP and an antiferromagnetic QCP could be extended or adapted to the situation of a quantum critical valence transition and an antiferromagnetic

QCP in close proximity on the phase diagram.

In summary, in this thesis we have developed and analysed a model of quantum multicriticality which we believe successfully explains the specific heat and resistivity measurements of the quantum critical compounds $NbFe_2$ and $Ta(Fe_{1-x}V_x)_2$. We have predicted the power-law behaviour of the thermal expansion and Grüneisen parameter, which to our knowledge are currently unmeasured. We have extended the model for finite magnetic fields and made physical predictions about scenarios where a metamagnetic QCEP interacts with an antiferromagnetic QCP. We hope that the experimental and theoretical questions raised by this thesis stimulate further research into quantum multicritical points.

Quantum Multicriticality

arXiv:1506.03021

Quantum Multicriticality

G.T. Oliver and A.J. Schofield
School of Physics and Astronomy, University of Birmingham, Edgbaston, Birmingham, B15 2TT, United Kingdom.
(Dated: June 10, 2015)

Several quantum critical compounds have been argued to have multiple instabilities towards orders with distinct dynamical exponents. We present an analysis of a quantum multicritical point in an itinerant magnet with competition between ferro- and antiferromagnetic order, modelled using Hertz-Millis theory. We perform a one-loop renormalization group treatment of this action in the presence of two dynamical exponents. In two and in three dimensions, when both incipient orders are quantum critical, we find that the specific heat, thermal expansion and Grüneisen parameter obey the same power laws as those expected for a single ferromagnetic quantum critical point. The antiferromagnetic correlation length and boundary of the antiferromagnetic ordered phase are suppressed by the dangerously irrelevant interactions with quantum critical ferromagnetic fluctuations. We find no difference between a quantum bicritical point and a quantum tetracritical point. Our results are compared with experiments on $NbFe_2$.

PACS numbers: 73.43.Nq, 71.10.Hf, 64.40.Kw

Quantum criticality is characterised by universal divergences of thermodynamic quantities at a continuous zero-temperature phase-transition as some non-thermal control parameter (e.g. pressure, doping or magnetic field) is changed. The much-studied power laws associated with the quantum phase transition depend on the universality class, which in contrast to the classical case depends on the dynamics of the order parameter fluctuations in imaginary time. The dynamic effects are characterized by a dynamical exponent, z, which, in addition to controlling the power-law divergences, defines the boundaries of distinct regions in the phase diagram [1–4].

In recent years quantum critical behaviour has been observed in systems that do not seem to conform to the standard theoretical picture of fluctuations of an order parameter with a unique dynamical exponent. For example the specific heat in $NbFe_2$ displays a $C \sim -T \ln T$ relation as would be expected for three dimensional itinerant ferromagnetic quantum criticality which is described with $z = 3$. In contrast the resistivity displays $\rho \sim T^{3/2}$ as expected for a dirty three dimensional antiferromagnet, usually described with $z = 2$ [5, 6].

In this Letter we report results of a study into quantum criticality where an itinerant material is unstable to both ferro- and antiferromagnetic order. Materials with a multicritical point in the phase diagram [as shown in Figs. 1(a) and 1(b)] show a competition between two distinct types of order. Here we assume that if we had control over another tuning parameter we could suppress this multicritical point to zero temperature, to form a quantum multicritical point [as shown in Fig. 1(c)]. This type of phase diagram has been considered before [7], but in the presence of a symmetry-breaking field, which we do not treat here. To model quantum multicriticality we construct an effective action in terms of spin-fluctuations by adapting Hertz-Millis theory [3, 4, 8]. This neglects important non-analytic terms which sometimes arise from integrating out the fermionic degrees of freedom [2]. Ignoring such terms seems valid slightly away from the critical point [9]. Nevertheless their inclusion could stabilize a finite-momentum spin-density wave near the ferromagnetic quantum critical point [10] to generate the scenario considered here. We extend Millis' calculation [4] to treat the quantum multicritical point by following the renormalization group (RG) procedure. This enables us to map out the rich phase diagram and calculate the leading order critical parts of the specific heat, thermal expansion and Grüneisen parameter.

Our main result is that, since we are at or above the upper critical dimension of our model ($d_c^+ = 2$), we can essentially treat the fluctuations of each type of order independently, and the critical part of the free energy and therefore its derivatives simply become the sum of the contributions associated with each individual order parameter. The caveat is that whenever the *dangerously irrelevant* interactions affect the RG flow, due to the multiple dynamics they can produce novel temperature dependences. This allows the dangerously irrelevant interactions to shape the phase diagram. We also discuss the resistivity in relation to experiments, though do not offer an explicit calculation here.

Our analysis is formulated in terms of an order parameter field $\phi(\boldsymbol{q}, \omega_n)$ which describes the magnetization of the system. In a system unstable towards both ferro- and antiferromagnetic order, the susceptibility will be large near zero momentum and near the antiferromagnetic wavevector $\boldsymbol{Q}$. We split the magnetization field into two parts to represent these different regimes. We denote the small momentum part of the field as $\phi_3(\boldsymbol{q}, \omega_n)$ for $|\boldsymbol{q}| < \Lambda_3$ where the subscript 3 refers to the fact that this field is usually described by a dynamical exponent $z = 3$. To denote the field near momentum $\boldsymbol{Q}$ we use the notation $\phi_2(\boldsymbol{q}, \omega_n)$ where here $\boldsymbol{q}$ (which we restrict such that $|\boldsymbol{q}| < \Lambda_2$) measures the deviation from $\boldsymbol{Q}$. Here the subscript 2 refers to the dynamical exponent $z = 2$ usually associated with antiferromagnetic order. We allow

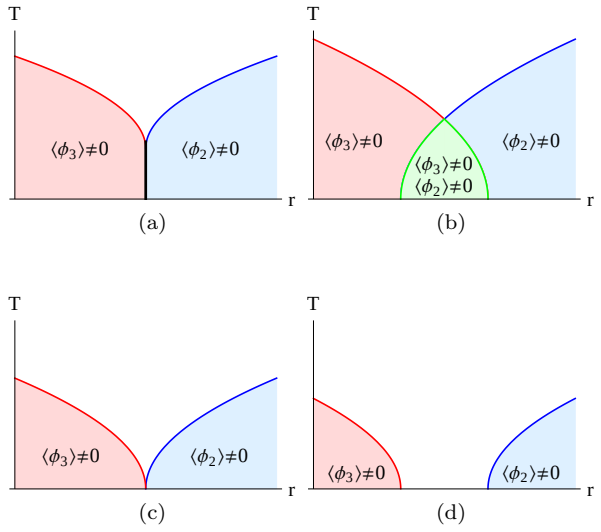

FIG. 1: Suppressing a multicritical point to zero temperature. (a) and (b) show bicritical and tetracritical points respectively. By invoking another non-thermal control parameter g, these multicritical points can be tuned to zero temperature, as shown in (c). (d) shows the expected phase diagram when two quantum critical points arise for increasing g.

for ϕ_3 and ϕ_2 to have n_3 and n_2 components respectively.

The action we use to describe a quantum multicritical point is the sum of the actions of a ferromagnetic and an antiferromagnetic quantum critical point (QCP),

$$S\left[\phi_3,\phi_2\right] = \sum_{i=3,2}\sum_{\omega_n}\sum_{q}\chi_i^{-1}\left(\boldsymbol{q},\omega_n\right)\phi_i^2\left(\boldsymbol{q},\omega_n\right) + \int d\boldsymbol{x}d\tau\left[u_3\phi_3^4(\boldsymbol{x},\tau)+u_2\phi_2^4(\boldsymbol{x},\tau) + u_{32}\phi_3^2(\boldsymbol{x},\tau)\phi_2^2(\boldsymbol{x},\tau)\right], \quad (1)$$

where the two QCPs are coupled together by a mode-mode coupling term u_{32}. The bare inverse spin susceptibilities are given by

$$\chi_i^{-1}(\boldsymbol{q},\omega_n) = \delta_i + q^2 + \eta_i\frac{|\omega_n|}{q^{z_i-2}}, \quad (2)$$

where z_3 is the dynamical exponent associated with ferromagnetic order, $z=3$, and z_2 is the dynamical exponent associated with antiferromagnetic order, $z=2$. We have added 'kinetic coefficients' η_3 and η_2 which allow us to renormalize in the imaginary time direction [11, 12]. The classical analogue of the action describes a multicritical point in the δ_3-δ_2 plane. The model shows bicriticality if $u_{32}^2 > 4u_3u_2$ and tetracriticality if this is inequality is reversed [13, 14].

In order to map out the phase diagram and predict thermodynamic quantities, we perform an RG analysis by simultaneously integrating out the ϕ_3 modes in a small shell with momenta between Λ_3/b and Λ_3, and the ϕ_2 modes with momenta between Λ_2/b and Λ_2. We then rescale such that the original cut-offs are restored and calculate how the other parameters in the model must rescale. The presence of multiple dynamical exponents means there is no unique way to rescale frequency. We choose to rescale it as b^z where z is a fictitious dynamical exponent which we leave unspecific (see Ref. [11] and [12]). This enables renormalization but will drop out of our calculations so that no physical properties depend on it. The RG equations can either be derived directly from the action or by calculating a physical property (such as the free energy) and ensuring it does not change under renormalization. We have done both, and find that the one-loop RG equations for the tuning parameters and interactions are

$$\frac{d\delta_i}{d\ln b} = 2\delta_i(b) + \tilde{u}_i(b)4(n_i+2)f_i^{(2)}\left(\delta_i(b),\mathcal{T}_i(b)\right) + \tilde{w}_{\bar{\imath}}(b)4n_{\bar{\imath}}f_{\bar{\imath}}^{(2)}\left(\delta_{\bar{\imath}}(b),\mathcal{T}_{\bar{\imath}}(b)\right), \quad (3a)$$

$$\frac{d\tilde{u}_i}{d\ln b} = \left[4-(d+z_i)\right]\tilde{u}_i(b) - 4(n_i+8)f_i^{(4)}(\delta_i(b),\mathcal{T}_i(b))\tilde{u}_i^2 - 4n_{\bar{\imath}}f_{\bar{\imath}}^{(4)}(\delta_{\bar{\imath}}(b),\mathcal{T}_{\bar{\imath}}(b))\tilde{w}_i(b)\tilde{w}_{\bar{\imath}}(b), \quad (3b)$$

$$\frac{d\tilde{w}_i}{d\ln b} = \left[4-(d+z_i)\right]\tilde{w}_i(b) - \sum_{j=3,2}4\left(n_j+2\right)f_j^{(4)}(\delta_j(b),\mathcal{T}_j(b))\tilde{u}_j(b)\tilde{w}_i(b), \quad (3c)$$

where i is either 3 or 2 and $\bar{\imath}$ is correspondingly either 2 or 3. We have defined $\tilde{u}_i \equiv u_i/\eta_i$ and $\tilde{w}_i \equiv u_{32}/\eta_i$, as we find that the only way the interactions enter the RG equations is in these combinations. For the rest of this Letter, when a parameter is written without explicit scale-dependence we are referring to the bare, unrenormalized value. We find that the temperature scales as $T(b) = b^zT$ and the kinetic coefficients are $\eta_i(b) = b^{z_i-z}\eta_i$. The RG equations can be written in terms of two temperature fields $\mathcal{T}_i(b) = \eta_i(b)T(b) = \mathcal{T}_ib^{z_i}$ which represent the effective temperature felt by the ϕ_i modes. The $f_i^{(2)}$ and $f_i^{(4)}$ functions are the one-loop integrals shown in Fig. 2, which arise in the RG procedure due to interactions with modes above the cut-off. They are exactly the same functions which appear in Hertz-Millis theory, defined in Ref. [4]. The scaling of the interaction terms can be calculated from Eqs. (3b) and (3c), which can be analysed under the usual approximation that the $f^{(4)}$ functions are constant [4]. In $d=3$ we find all interaction terms decay as some power of b, whereas in $d=2$, $\tilde{u}_2$ and $\tilde{w}_2$ decay logarithmically. We find that at large values of b, $\tilde{u}_2(b) \sim (\ln b)^{-1}$ just as in the $d=z=2$ Hertz-Millis case, and $\tilde{w}_2(b) \sim (\ln b)^{-(n_2+2)/(n_2+8)}$, which is a very slow decay unique to the multicritical case. Because the free energy can be written as a power series in these interaction terms, we conclude that the upper critical dimension is $d_c^+ = 2$, just as for an antiferromagnetic QCP.

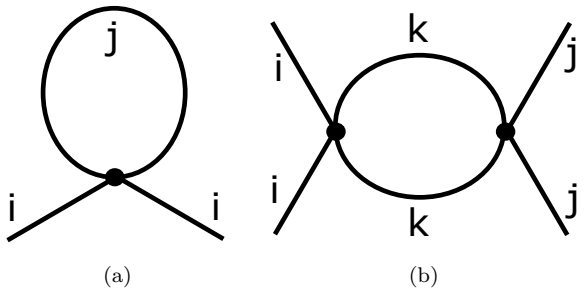

FIG. 2: One-loop diagrams that contribute to the RG flow and Eqs. (3a), (3b) and (3b). Lines with free (connected) ends represent modes below (above) the cut-off. The symbols $i, j, k = 3, 2$ label which modes the lines represent. (a) shows a contribution to the renormalization of δ_i from interaction with ϕ_j modes above the cut-off, and is proportional to $f_j^{(2)}(\delta_j, \mathcal{T}_j)$. (b) shows a contribution to the renormalization of u_i if $j = i$ and u_{32} if $j \neq i$, due to interactions with k modes above the cut-off, and is proportional to $f_k^{(4)}(\delta_k, \mathcal{T}_k)$.

In the cases of two and three dimensions considered here, we are at or above the upper critical dimension and so are controlled by the Gaussian fixed point where all interactions flow to zero.

The distinct regions of the phase diagrams and the correlation lengths in each regime can be calculated from Eq. 3(a). In our calculation we use Millis' approximation for the integral of the $f^{(2)}(\delta, \mathcal{T})$ function, which is different in the quantum critical and quantum disordered regimes [4], defined by $R \ll \mathcal{T}^{2/z}$ and $R \gg \mathcal{T}^{2/z}$ for a single QCP. Here R is the renormalized tuning parameter or quasiparticle mass, which may acquire some temperature dependence. In the multicritical case, we conclude that both the ferro- and antiferromagnetic modes can independently be quantum critical or quantum disordered, splitting the phase diagram into four regions separated by the two lines $R_i \sim \mathcal{T}_i^{2/z_i}$. The solution of Eq. 3(a) at large values of b yields a tuning parameter becomes $\delta_i(b) = b^2 R_i$ where R_i is renormalized by interactions with both modes independently. This can be related to the correlation length of the corresponding order parameter by $R_i = \xi_i^{-2}$. We denote the zero temperature part of R_i by r_i, and it is this which tunes to the QCP at $r_i = 0$.

It is the dangerously irrelevant interaction terms which give the renormalized tuning parameters their temperature dependence, which in turn control the correlation lengths and the boundaries of the ordered phases. In three dimensions the boundaries of the ordered phases can be calculated from the lines $T(r_i)$ where the corresponding correlation length diverges. While no true order can exist in 2D, we adopt the usual convention and use the point that the Ginzburg criterion of the classical theory breaks down to identify the 'phase boundary'.

The generic phase diagram for a quantum multicritical point is shown in Fig. 3, which is qualitatively the same in both two and three dimensions. We find it most revealing to interpret the results as the sum of two quantum critical points. In both two and three dimensions, we find that to leading order the ferromagnetic $z = 3$ QCP is qualitatively unaffected by the antiferromagnetic $z = 2$ QCP. However the antiferromagnetic QCP is strongly affected by the proximity to a ferromagnetic QCP. When the ferromagnetic modes are quantum critical, the antiferromagnetic correlation length acquires the temperature dependence of the ferromagnetic correlation $\xi_2^{-2} \sim r_2 + AT^{4/3}$ instead of the usual $\xi_2^{-2} \sim r_2 + BT^{3/2}$ in three dimensions, and $\xi_2^{-2} \sim r_2 + CT \ln(1/T)$ instead of the usual $\xi_2^{-2} = r_2 + D \ln(\ln(1/T)) / \ln(1/T)$ in two dimensions. This temperature dependence dominates the antiferromagnetic correlation length in region I of the phase diagram in Fig. 3. Interactions with quantum critical ferromagnetic fluctuations therefore reduce the antiferromagnetic correlation length, which in turn suppresses the boundary of the antiferromagnetic phase. If the ferromagnetic fluctuations are Fermi liquid-like then the antiferromagnetic QCP is qualitatively unaffected.

Since the interactions are irrelevant, thermodynamic properties in the disordered region of the phase diagram can be obtained from the Gaussian part of the free energy, which can be calculated directly from the action. This is just the sum of the contributions from both individual QCPs weighted by η_i^{-1}, $F_G(T, \delta_3, \delta_2) = \frac{1}{\eta_3} F_G^{(3)}(\delta_3, \mathcal{T}_3) + \frac{1}{\eta_2} F_G^{(2)}(\delta_2, \mathcal{T}_2)$, where $F_G^{(i)}(\delta_i, \mathcal{T}_i)$ is the Hertz-Millis free energy for order with dynamical exponent z_i defined explicitly in Ref [4]. While the free energy is described by the Gaussian part, the effect of the interactions is seen in the rescaling of the Gaussian parameters.

For a single QCP, the specific heat and thermal expansion behave differently in the quantum critical and Fermi liquid regimes, as tabulated in Ref. [15]. In the multicritical case, in each of the four distinct regions of the paramagnetic phase in Fig. 3 the specific heat and thermal expansion are just the sum of the contributions from each individual QCP, which we find to leading order are unchanged by the interactions. In both two and three dimensions, in region I of the phase diagram in Fig. 3, where both ferro- and antiferromagnetic modes would expected be to quantum critical, then the strong temperature dependence of the ferromagnetic contribution dominates, and the presence of antiferromagnetic quantum criticality is subleading. In the other regions of the disordered phase, the observed quantities are the sum of the two terms. When the QCPs are separated, sufficiently close to each QCP the effects of the other QCP are not measurable and the thermodynamics is as would be expected from a single QCP.

The exception to this is in two dimensions in region I of the phase diagram in Fig. 3. In this case the temperature dependent renormalization of the antiferromagnetic tuning parameter is strong enough to push the antiferromagnetic mode out of the quantum critical regime, as the

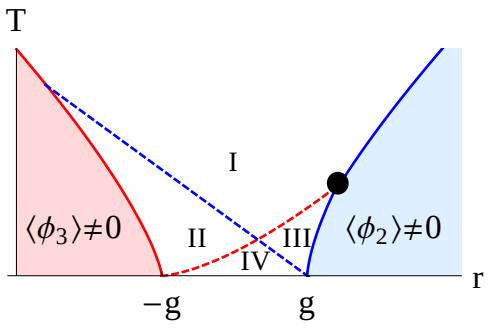

FIG. 3: Generic phase diagram of a quantum multicritical point, derived by setting $r_3 = g + r$ and $r_2 = g - r$. The regions in the paramagnetic regime have been identified. I and II are quantum critical regions where the ferromagnetic contributions dominate specific heat and thermal expansion. In I the ferromagnetic fluctuations control the antiferromagnetic correlation length and the boundary of the antiferromagnetic ordered phase. In II the antiferromagnetic correlation length is dominated by the tuning parameter. III is an antiferromagnetic quantum critical region, where the antiferromagnetic correlation length and boundary of the ordered phase are dominated by the antiferromagnetic fluctuations, and the ferromagnetic correlation length is dominated by the tuning parameter. IV is a Fermi liquid. The black dot indicates approximately where the antiferromagnetic phase boundary undergoes a crossover from a power law associated with antiferromagnetism to one normally associated with ferromagnetism. The subleading contributions depend on the dimensionality of space, as explained in the main text.

condition $R_2 < T$ will never be satisfied. This means we must use the Fermi liquid approximation ($R_2 > T$) in calculations of the antiferromagnetic contribution to physical quantities, but the correlation length is still dominated by temperature. However in this regime the ferromagnetic contributions dominate specific heat and thermal expansion and this effect is subleading.

We now compare our theory with the existing experimental results in $Nb_{1-y}Fe_{2+y}$. Near $y = 0$ this material shows both ferro- and antiferromagnetic quantum critical points [16, 17]. There the measured specific heat shows a $-T \ln T$ dependence consistent with the dominance of ferromagnetic fluctuations as we have shown above. The thermal exapansion has not been measured but we predict it to show a $T^{1/3}$ dependence at low temperatures. In this work we have not calculated the resistivity because of the complex interplay we anticipate between hotspot/line scattering of the antiferomagnet [18] and the small angle scattering for the ferromagnetic fluctuations. The measured resistivity is $\Delta\rho \sim T^{3/2}$ which is consistent with a naive extension of our theory with the antiferromagnetic fluctuations dominating [2] because of their increased effectiveness in momentum relaxation when compared to small q scattering. A detailed analysis is left for future work. Similarly a more detailed doping-dependent study of the Neél phase boundary $T_N(y)$ is necessary to compare with our predictions of a cross-over in power law.

$NbFe_2$ is not unique in showing quantum multicriticality. $YbRh_2Si_2$ orders antiferromagnetically at low temperatures but the specific heat and Grüneisen parameter at low temperatures obey power laws as would be expected of a ferromagnet [2]. This could be the result of the presence of both ferro- and antiferromagnetic fluctuations [19, 20]. However, this material is usually thought to lie outside the Hertz-Millis scenario for quantum criticality because of Kondo breakdown effects [21].

In summary we have analysed the interplay of two quantum critical points in an itinerant magnet in both two and three dimensions. Our main prediction is that if quantum critical fluctuations of both ferro- and antiferromagnetic order are present then the specific heat, thermal expansion and Grüneisen parameter will have the temperature dependence associated with just the ferromagnetic modes. In addition, the correlation length of antiferromagnetic order will acquire the temperature dependence of the ferromagnetic correlation length, and this suppresses the boundary of the ordered phase (or region of applicability in two dimensions). We find that the boundary of the antiferromagnetic phase can undergo a crossover from its usual Hertz-Millis power law at low temperatures to the power law usually associated with a *ferromagnetic* instability at higher temperatures. We find no difference between a quantum bicritical and a quantum tetracritical point, as under renormalization the system always flows to the Gaussian fixed point where the interactions are zero.

Acknowledgments

We would like to thank Sven Friedemann and Manuel Brando for sharing experimental data, and John Cleave for useful discussions. We acknowledge the funding support of EPSRC and grant EP/J016888/1. This research was also supported in part by the National Science Foundation under Grant No. NSF PHY11-25915.

[1] S. Sachdev, *Quantum Phase Transitions* (Cambridge University Press, 2011), 2nd ed.
[2] H. v. Löhneysen, A. Rosch, M. Vojta, and P. Wölfle, Rev. Mod. Phys. **79**, 1015 (2007).
[3] J. A. Hertz, Phys. Rev. B **14**, 1165 (1976).
[4] A. J. Millis, Phys. Rev. B **48**, 7183 (1993).
[5] D. Moroni-Klementowicz, M. Brando, C. Albrecht, W. J. Duncan, F. M. Grosche, D. Grüner, and G. Kreiner, Phys. Rev. B **79**, 224410 (2009).
[6] M. Brando, W. J. Duncan, D. Moroni-Klementowicz,

C. Albrecht, D. Grüner, R. Ballou, and F. M. Grosche, Phys. Rev. Lett. **101**, 026401 (2008).
[7] Y. Tokiwa, M. Garst, P. Gegenwart, S. L. Bud'ko, and P. C. Canfield, Phys. Rev. Lett. **111**, 116401 (2013).
[8] M. Garst, Ph.D. thesis, University of Karlsruhe (2003).
[9] R. P. Smith, M. Sutherland, G. G. Lonzarich, S. S. Saxena, N. Kimura, S. Takashima, M. Nohara, and H. Takagi, Nature **455**, 1220 (2008).
[10] G. J. Conduit, A. G. Green, and B. D. Simons, Phys. Rev. Lett. **103**, 207201 (2009).
[11] M. Zacharias, P. Wölfle, and M. Garst, Phys. Rev. B **80**, 165116 (2009).
[12] T. Meng, A. Rosch, and M. Garst, Phys. Rev. B **86**, 125107 (2012).
[13] J. M. Kosterlitz, D. R. Nelson, and M. E. Fisher, Phys. Rev. B **13**, 412 (1976).
[14] P. Chaikin and T. Lubensky, *Principles of Condensed Matter Physics* (Cambridge University Press, 1995).
[15] M. Garst and A. Rosch, Phys. Rev. B **72**, 205129 (2005).
[16] D. A. Tompsett, R. J. Needs, F. M. Grosche, and G. G. Lonzarich, Phys. Rev. B **82**, 155137 (2010).
[17] T. D. Haynes, I. Maskery, M. W. Butchers, J. A. Duffy, J. W. Taylor, S. R. Giblin, C. Utfeld, J. Laverock, S. B. Dugdale, Y. Sakurai, et al., Phys. Rev. B **85**, 115137 (2012).
[18] R. Hlubina and T. M. Rice, Phys. Rev. B **51**, 9253 (1995).
[19] D. M. Klementowicz, R. Burrell, D. Fort, and M. Grosche, Physica B: Condensed Matter **359361**, 80 (2005), ISSN 0921-4526, proceedings of the International Conference on Strongly Correlated Electron Systems.
[20] E. C. Andrade, M. Brando, C. Geibel, and M. Vojta, Phys. Rev. B **90**, 075138 (2014).
[21] S. Nair, S. Wirth, S. Friedemann, F. Steglich, Q. Si, and A. J. Schofield, Adv. Phys. **61**, 583 (2012).

Appendix A

DIAGRAMS FOR A QUANTUM MULTICRITICAL POINT

In this appendix we list the diagrams contributing to the linked cluster expansion for a quantum multicritical point. We represent ϕ_3 modes by blue lines, and ϕ_2 modes by red lines. We represent the interactions u_3, u_2 and u_{32} by black dashed lines. The captions of each diagram indicate which interactions and integrals contribute to the diagram. We group the diagrams by comparing them to the diagrams which contribute to the linked cluster expansion for a single quantum critical point, described in Section 2.3.1. Diagrams which look like those contributing to I^2 for a single QCP (in Figure 2.4) are shown in Figure A.1. Those which look similar to those proportional to I^2J for a single QCP (in Figure 2.5) are shown in Figure A.2. Those which look similar to those proportional to K for a single QCP (in Figure 2.6) are shown in Figure A.3.

(a) $u_2 I_2^2$ (b) $u_3 I_3^2$ (c) $u_{32} I_3 I_2$

(d) $u_2 I_2^2$ (e) $u_3 I_3^2$

Figure A.1: Diagrams of type I^2

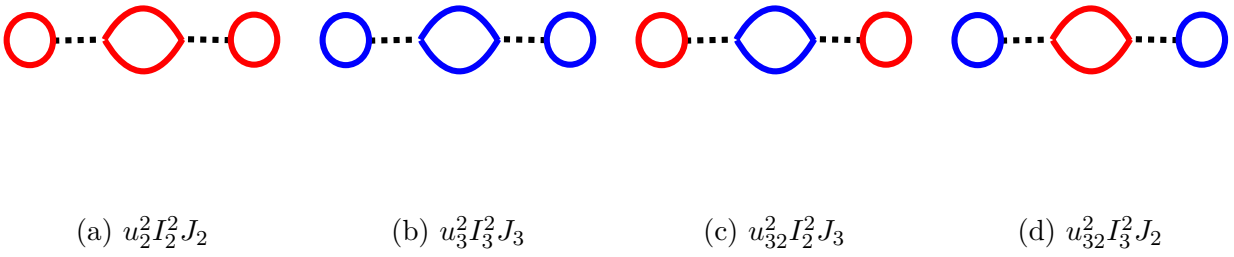

(a) $u_2^2 I_2^2 J_2$ (b) $u_3^2 I_3^2 J_3$ (c) $u_{32}^2 I_2^2 J_3$ (d) $u_{32}^2 I_3^2 J_2$

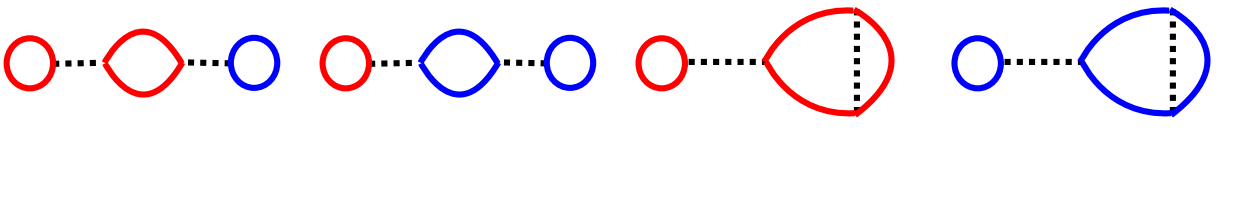

(e) $u_2 u_{32} I_3 I_2 J_2$ (f) $u_3 u_{32} I_3 I_2 J_3$ (g) $u_2^2 I_2^2 J_2$ (h) $u_3^2 I_3 J_3$

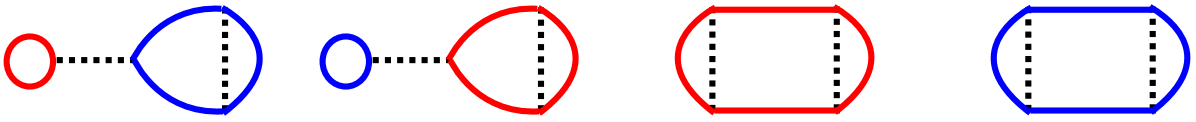

(i) $u_3 u_{32} I_3 I_2 J_3$ (j) $u_2 u_{32} I_3 I_2 J_2$ (k) $u_2^2 I_2^2 J_2$ (l) $u_3^2 I_3^2 J_3$

Figure A.2: Diagrams of type $I^2 J$

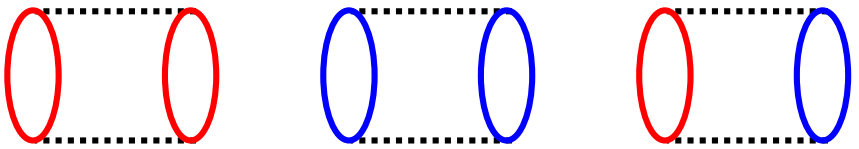

(a) $u_2^2 K_2$ (b) $u_3^2 K_3$ (c) $u_{32}^2 K_{32}$

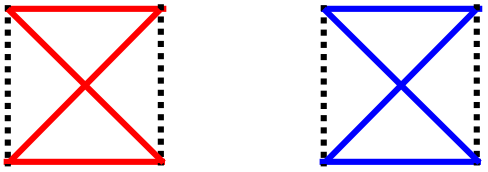

(d) $u_2^2 K_2$ (e) $u_3^2 K_3$

Figure A.3: Diagrams of type K

Appendix B

DETAILS OF THE NUMERICAL RESISTIVITY CALCULATION

In this appendix we discuss the program we use to generate the results of Chapter 5 in more detail. The flow of the program is, for each temperature point:

- Calculate the temperature-dependent tuning parameters.
- Calculate a look-up table for $F_3(\boldsymbol{k}, \boldsymbol{k'})$ for different values of $|\boldsymbol{k'} - \boldsymbol{k}|$, where the ω has been integrated over.
- Calculate the total $F(\theta, \theta')$ matrix, where the polar integral for the ferromagnetic matrix elements is done using the look-up table.
- Calculate the quasiparticle distribution $\Phi(\theta)$ from equation (4.3.1) by repeated application of the matrix.
- Calculate the resistivity from equation (4.3.6).

These steps are then repeated for all temperature values required. We now describe each step in more detail.

Step 1: The first step is calculating $r_2(T)$ and $r_3(T)$, which are interpreted as the square of

the inverse correlation lengths of each type of order. If r_2 and r_3 are the bare zero temperature tuning parameters (which are inputs of the program), then we calculate the temperature dependent component using the results of Chapter 3.

In the presence of multicritical scaling, both $r_2(T)$ and $r_3(T)$ are proportional to $T^{4/3}$. The constant of proportionality is chosen to be equal to one.

Step 2: In order to calculate the matrix $F_3(\theta, \theta')$ from $F_3(\boldsymbol{k}, \boldsymbol{k'})$ given in equation (4.2.24), integrals over both the polar angle ϕ' and ω must be calculated. Since $F_3(\boldsymbol{k}, \boldsymbol{k'})$ only depends on $|\boldsymbol{k'} - \boldsymbol{k}|$, when we calculate the polar integral over ϕ' at different values of θ and θ', we shall need to access the function multiple times for each value of $|\boldsymbol{k'} - \boldsymbol{k}|$. By creating a look-up table for this function at different values of $|\boldsymbol{k'} - \boldsymbol{k}|$, we are able to perform the ω integral only once for each value of $|\boldsymbol{k'} - \boldsymbol{k}|$. The integral is (after a rescaling of variables)

$$F_3(\boldsymbol{q}) = \frac{2g_F^2}{k_B(T/\Gamma_3)} \int_0^1 dw \frac{c_3^2 q^2 w^2 n^0(c_3 q \Gamma_3 w)(n^0(c_3 q \Gamma_3 w) + 1)}{(r_3(T) + c_3^2 q^2)^2 + w^2}, \tag{B.0.1}$$

which decays rapidly with w. In our program we make a further change of variables in the integral to $u = w^7$ so that the integrand is much smoother. We make this polynomial substitution so that the limits of the integral are still 0 and 1, and choose w^7 as this sufficiently increases the accuracy of numerical integration. The integral is evaluated using Simpson's rule.

Step 3: Calculating the matrix elements $F(\theta, \theta')$ is the most computationally expensive part of the code, however increasing the size of the matrix (the number of points we split the interval 0 to π into) increases the accuracy of the results, and allows us to access lower temperatures. In order to speed up computation, we use the symmetries of the matrix. Because the only way $F(\theta, \theta')$ depends on θ and θ' is through $|q|$ and $|\boldsymbol{q} \pm \boldsymbol{Q}|^2$, we are able to show that $F(\theta, \theta') = F(\theta', \theta)$ and $F(\theta, \theta') = F(\pi - \theta, \pi - \theta')$. This means we only need to calculate a quarter of the elements of the matrix, and the rest follow from symmetry. The

ferromagnetic scattering matrix element is calculated by evaluating the polar integral numerically, by calculating an equivalent q for each point in the polar integral, and looking up the closest equivalent $F(\boldsymbol{q})$ from the look-up table created earlier. The antiferromagnetic matrix element is calculated directly from equation (4.2.38).

Step 4: The next step is to calculate the quasiparticle distribution. By integrating over θ' in the $F(\theta,\theta')$ matrix found in the previous step, we can find the matrix $F(\theta,\theta')/G(\theta)$ where $G(\theta) = \int_0^\pi d\theta'' \sin\theta'' F(\theta,\theta'')$, which generates the quasiparticle distribution if repeatedly applied to $\cos\theta/G(\theta)$. At low temperatures, the function $F(\theta,\theta')$ is very sharply peaked as a function of θ', making the numerical integration in finding $G(\theta)$ difficult. In order to get accurate results at lower temperatures, we must have a larger matrix in order to sample the peak at more points. However, this drastically affects the time the program takes to run. When attempting to numerically calculate these integrals using Simpson's rule, we encounter difficulties when the matrix is not big enough to sample the peak sufficiently many times. We find we obtain a more realistic $\Phi(\theta)$ when performing this integral using the trapezium rule as opposed to Simpson's rule. This is because in Simpson's rule the integrand at some points is multiplied by 4/3, and 2/3 at others. If the integrand is sharply peaked such that one point is significantly larger than the others, then the answer depends on whether this value is multiplied by 4/3 and 2/3. In our analysis this error carries through to the shape of $\Phi(\theta)$. We thus use the trapezium rule to calculate $G(\theta)$.

We calculate $\Phi(\theta)$ as in equation (4.3.10). To test if the series has converged when adding $f_{n+1}(\theta)$, we calculate the largest value of $|f_{n+1}(\theta)/\sum_{i=1}^{n} f_i(\theta)|$, and if this is less than 10^{-8}, we conclude that $\Phi(\theta)$ has converged.

Step 5: We then calculate the resistivity from (4.3.6) using Simpson's rule to evaluate the integrals. Once we have calculated the resistivity at different points we calculate the effective power law by modelling the function as $\rho(T) - \rho_0 = aT^{\alpha(T)}$, to find $\alpha(T)$ at different

points on the phase diagram. We do this by calculating

$$\alpha(T+\frac{\delta}{2}) = \frac{\ln\left[f\left(T+\delta\right)\right] - \ln\left[f\left(T\right)\right]}{\ln\left[T+\delta\right] - \ln\left[T\right]} \tag{B.0.2}$$

where $f(T) = \rho(T) - \rho_0$. The results we expect are $f(T) = aT^n + bT^m$, which will give

$$\alpha(T) \approx m\left[\frac{1+\frac{n}{m}\frac{a}{b}T^{n/m}}{1+\frac{a}{b}T^{n/m}}\right] \tag{B.0.3}$$

as $\delta \to 0$. If $n > m$, we expect m to dominate at low temperatures, but see a crossover to n as temperature is increased. The details of the crossover depend both on the exponents and their coefficients, which we do not expect to be universal.

Appendix C

DIAGRAMS FOR A METAMAGNETIC QUANTUM CRITICAL END-POINT AND AN ANTIFERROMAGNETIC QUANTUM CRITICAL POINT

In this appendix we list the one-loop diagrams contributing to the RG equations for a metamagnetic quantum critical end-point interacting with an antiferromagneitc quantum critical point. The same diagrams contribute to both the RG equations of the corresponding classical model in equations (5.5.2) and the quantum critical model in equations (5.5.6). The blue lines represent ϕ_3 modes and the red lines represent ϕ_2 modes. The internal lines represent modes above the cut-off and are integrated over, and the external legs represent modes below the cut-off. The interactions u_3, u_2 and u_{32} are all denoted by black dashed lines. The interaction γ is denoted by a black dot. The captions of each diagram indicate which interactions contribute to the diagram.

The diagram contributing to the renormalisation of h is shown in Figure C.1. The diagrams contributing to the renormalisation of r_3 are shown in Figure C.2. The diagrams contributing to the renormalisation of r_2 are shown in Figure C.3. The diagrams contributing to the renormalisation of γ are shown in Figure C.4. The diagrams contributing to the renormalisation of u_3 are shown in Figure C.5. The diagrams contributing to the renormalisation of u_2 are shown

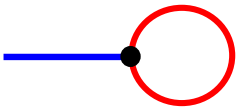

(a) γ

Figure C.1: Diagram contributing to h

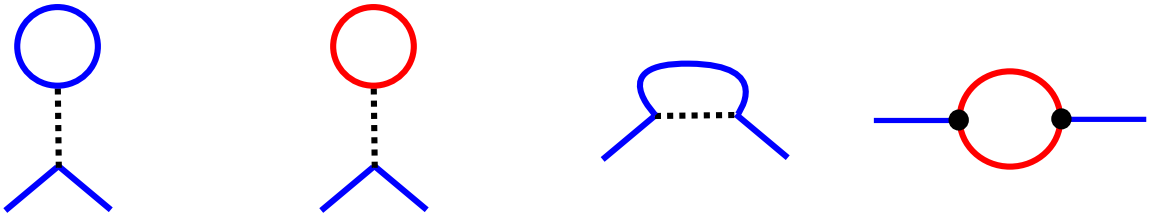

(a) u_3 (b) u_{32} (c) u_3 (d) γ^2

Figure C.2: Diagrams contributing to r_3

in Figure C.6. The diagrams contributing to the renormalisation of u_{32} are shown in Figure C.7.

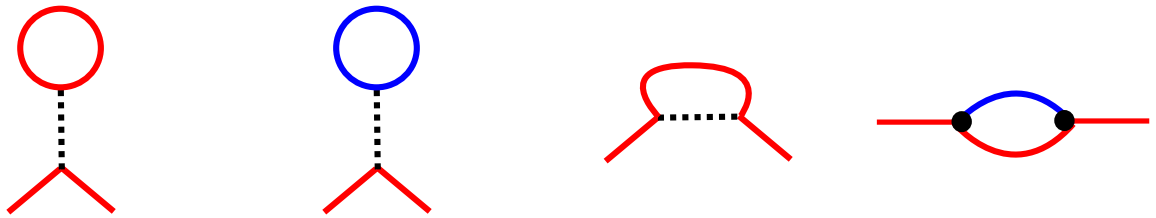

(a) u_2 (b) u_{32} (c) u_2 (d) γ^2

Figure C.3: Diagrams contributing to r_2

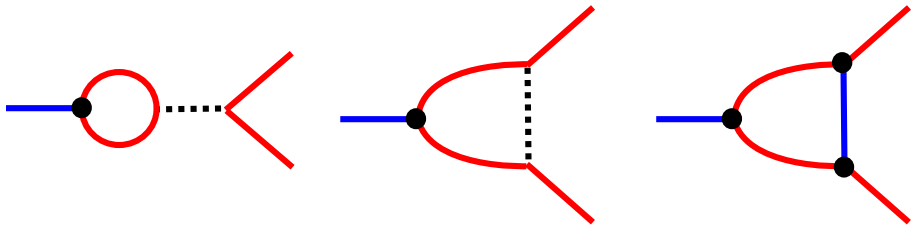

(a) $u_3\gamma$ (b) $u_3\gamma$ (c) γ^3

Figure C.4: Diagrams contributing to γ

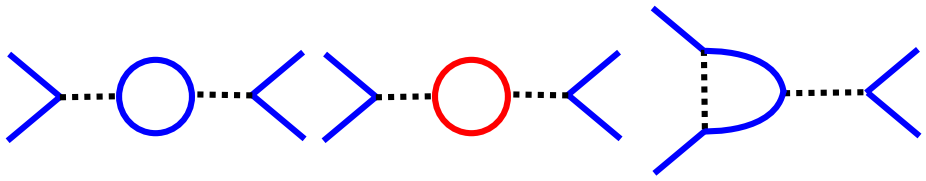

(a) u_3^2 (b) u_{32}^2 (c) u_3^2

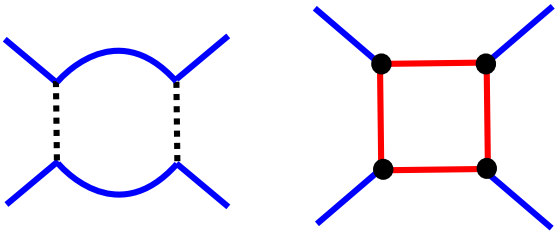

(d) u_3^2 (e) γ^4

Figure C.5: Diagrams contributing to u_3

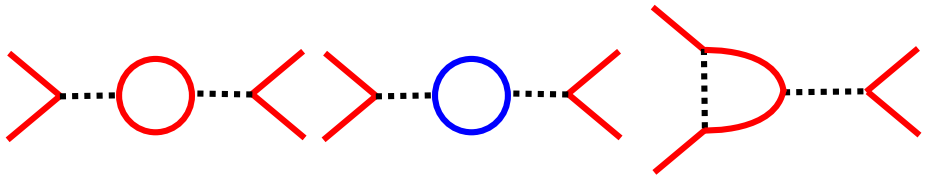

(a) u_2^2 (b) u_{32}^2 (c) u_2^2

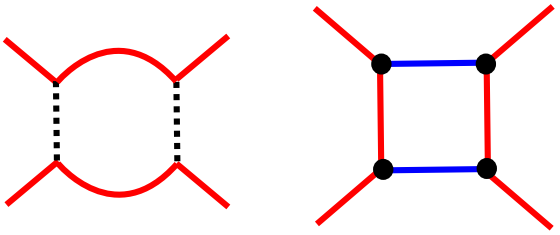

(d) u_2^2 (e) γ^4

Figure C.6: Diagrams contributing to u_2

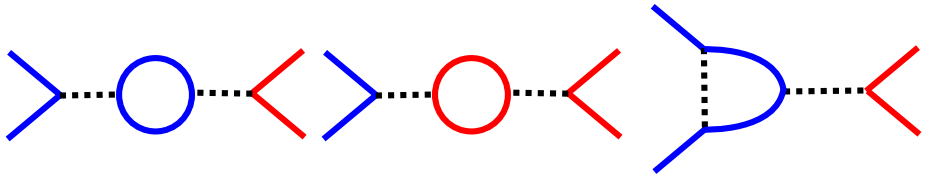

(a) $u_3 u_{32}$ (b) $u_2 u_{32}$ (c) $u_3 u_{32}$

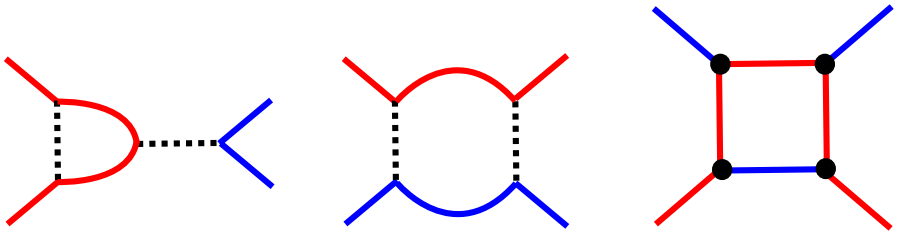

(d) $u_2 u_{32}$ (e) u_{32}^2 (f) γ^4

Figure C.7: Diagrams contributing to u_{32}

List of references

[1] Hilbert v. Löhneysen, Achim Rosch, Matthias Vojta, and Peter Wölfle. Fermi-liquid instabilities at magnetic quantum phase transitions. *Rev. Mod. Phys.*, 79:1015–1075, Aug 2007.

[2] Subir Sachdev. *Quantum Phase Transitions*. Cambridge University Press, 2 edition, 2011.

[3] P Chaikin and T Lubensky. *Principles of Condensed Matter*. Cambridge University Press, 1995.

[4] D. A. Tompsett, R. J. Needs, F. M. Grosche, and G. G. Lonzarich. Doping-driven magnetic instabilities and quantum criticality of $NbFe_2$. *Phys. Rev. B*, 82:155137, Oct 2010.

[5] T. D. Haynes, I. Maskery, M. W. Butchers, J. A. Duffy, J. W. Taylor, S. R. Giblin, C. Utfeld, J. Laverock, S. B. Dugdale, Y. Sakurai, M. Itou, C. Pfleiderer, M. Hirschberger, A. Neubauer, W. Duncan, and F. M. Grosche. Ferrimagnetism in Fe-rich $NbFe_2$. *Phys. Rev. B*, 85:115137, Mar 2012.

[6] M. Brando, W. J. Duncan, D. Moroni-Klementowicz, C. Albrecht, D. Grüner, R. Ballou, and F. M. Grosche. Logarithmic fermi-liquid breakdown in $NbFe_2$. *Phys. Rev. Lett.*, 101:026401, Jul 2008.

[7] D. Moroni-Klementowicz, M. Brando, C. Albrecht, W. J. Duncan, F. M. Grosche, D. Grüner, and G. Kreiner. Magnetism in $Nb_{1-y}Fe_{2+y}$: Composition and magnetic field dependence. *Phys. Rev. B*, 79:224410, Jun 2009.

[8] M. Brando, A. Kerkau, A. Todorova, Y. Yamada, P. Khuntia, T. Förster, U. Burkhard, M. Baenitz, and G. Kreiner. Quantum Phase Transitions and Multicriticality in $Ta(Fe_{1-x}V_x)_2$. *Journal of the Physical Society of Japan*, 85(8):084707, August 2016.

[9] Eric C. Andrade, Manuel Brando, Christoph Geibel, and Matthias Vojta. Competing orders, competing anisotropies, and multicriticality: The case of co-doped $YbRh_2Si_2$. *Phys. Rev. B*, 90:075138, Aug 2014.

[10] Y. Tokiwa, M. Garst, P. Gegenwart, S. L. Bud'ko, and P. C. Canfield. Quantum bicriticality in the heavy-fermion metamagnet YbAgGe. *Phys. Rev. Lett.*, 111:116401, Sep 2013.

[11] Alexander Altland and Ben Simons. *Condensed Matter Field Theory*. Cambridge University Press, 2006.

[12] John Cardy. *Scaling and Renormalization in Statistical Physics.* Cambridge University Press, 1996.

[13] Roger Bowley and Mariana Sánchez. *Introductory Statistical Mechanics.* Oxford Science Publications, 2 edition, 1999.

[14] Naoto Nagaosa. *Quantum Field Theory in Condensed Matter Physics.* Springer, 1999.

[15] Lifshitz E.M. Landau L.D. *Course of Theoretical Physics Volume 5: Statistical Physics Vol 1.* Pergamon Press, 3 edition, 1980.

[16] J. Zinn-Justin. *Quantum Field Theory and Critical Phenomena.* Oxford Science Publications, 2 edition, 1993.

[17] Kenneth G. Wilson and Michael E. Fisher. Critical exponents in 3.99 dimensions. *Phys. Rev. Lett.*, 28:240–243, Jan 1972.

[18] J. M. Kosterlitz, David R. Nelson, and Michael E. Fisher. Bicritical and tetracritical points in anisotropic antiferromagnetic systems. *Phys. Rev. B*, 13:412–432, Jan 1976.

[19] L.D. Landau. The theory of a fermi liquid. *Sov. Phys. JETP*, 3:920, 1957.

[20] Lifshitz E.M. Landau L.D. *Course of Theoretical Physics Volume 5: Statistical Physics Vol 2.* Pergamon Press, 3 edition, 1980.

[21] Neil W. Ashcroft and N. David Mermin. *Solid State Physcs.* Holt, Rinehart and Winston, 3 edition, 1976.

[22] I. Fischer and A. Rosch. Field-tuned quantum critical point of antiferromagnetic metals. *Phys. Rev. B*, 71:184429, May 2005.

[23] S. A. Grigera, R. S. Perry, A. J. Schofield, M. Chiao, S. R. Julian, G. G. Lonzarich, S. I. Ikeda, Y. Maeno, A. J. Millis, and A. P. Mackenzie. Magnetic field-tuned quantum criticality in the metallic ruthenate $Sr_3Ru_2O_7$. *Science*, 294(5541):329–332, 2001.

[24] A. J. Millis. Effect of a nonzero temperature on quantum critical points in itinerant fermion systems. *Phys. Rev. B*, 48:7183–7196, Sep 1993.

[25] U. Zülicke and A. J. Millis. Specific heat of a three-dimensional metal near a zero-temperature magnetic phase transition with dynamic exponent z =2, 3, or 4. *Phys. Rev. B*, 51:8996–9004, Apr 1995.

[26] John A. Hertz. Quantum critical phenomena. *Phys. Rev. B*, 14:1165–1184, Aug 1976.

[27] N. D. Mathur, F. M. Grosche, S. R. Julian, I. R. Walker, D. M. Freye, R. K. W. Haselwimmer, and G. G. Lonzarich. Magnetically mediated superconductivity in heavy fermion compounds. *Nature*, 394(6688):39–43, 1998.

[28] Sunil Nair, S. Wirth, S. Friedemann, F. Steglich, Q. Si, and A. J. Schofield. Hall effect in heavy fermion metals. *Adv. Phys.*, 61(5):583–664, 2012.

[29] Lijun Zhu, Markus Garst, Achim Rosch, and Qimiao Si. Universally diverging grüneisen parameter and the magnetocaloric effect close to quantum critical points. *Phys. Rev. Lett.*, 91:066404, Aug 2003.

[30] Markus Garst and Achim Rosch. Sign change of the grüneisen parameter and magnetocaloric effect near quantum critical points. *Phys. Rev. B*, 72:205129, Nov 2005.

[31] Tôru Moriya. *Spin Fluctuations in Itinerant Electron Magnetism*. Springer-Verlag, 1985.

[32] A. J. Schofield, A. J. Millis, S. A. Grigera, and G. G. Lonzarich. *Metamagnetic Quantum Criticality in $Sr_3Ru_2O_7$*, pages 271–289. Springer Berlin Heidelberg, Berlin, Heidelberg, 2002.

[33] Markus Garst. *Quantum Phase Transitions: Grüneisen Parameter, Dimensional Crossover and Coupled Impurities*. PhD thesis, University of Karlsruhe, 2003.

[34] Gerald D. Mahan. *Many-Particle Physics*. Kluwer Academic / Plenum Publishers, 3 edition, 2000.

[35] N. D. Mermin and H. Wagner. Absence of ferromagnetism or antiferromagnetism in one- or two-dimensional isotropic heisenberg models. *Phys. Rev. Lett.*, 17:1133–1136, Nov 1966.

[36] D. Belitz, T. R. Kirkpatrick, and Thomas Vojta. Nonanalytic behavior of the spin susceptibility in clean fermi systems. *Phys. Rev. B*, 55:9452–9462, Apr 1997.

[37] T. R. Kirkpatrick and D. Belitz. Quantum critical behavior of disordered itinerant ferromagnets. *Phys. Rev. B*, 53:14364–14376, Jun 1996.

[38] D. Belitz, T. R. Kirkpatrick, and Thomas Vojta. First order transitions and multicritical points in weak itinerant ferromagnets. *Phys. Rev. Lett.*, 82:4707–4710, Jun 1999.

[39] D. Belitz, T. R. Kirkpatrick, and Jörg Rollbühler. Breakdown of the perturbative renormalization group at certain quantum critical points. *Phys. Rev. Lett.*, 93:155701, Oct 2004.

[40] Ar. Abanov and A. Chubukov. Anomalous scaling at the quantum critical point in itinerant antiferromagnets. *Phys. Rev. Lett.*, 93:255702, Dec 2004.

[41] Tobias Meng, Achim Rosch, and Markus Garst. Quantum criticality with multiple dynamics. *Phys. Rev. B*, 86:125107, Sep 2012.

[42] I. Ia. Pomeranchuk. On the stability of a fermi liquid. *Sov. Phys. JETP*, 8:361, 1959.

[43] Mario Zacharias, Peter Wölfle, and Markus Garst. Multiscale quantum criticality: Pomeranchuk instability in isotropic metals. *Phys. Rev. B*, 80:165116, Oct 2009.

[44] J. Mathon. Magnetic and electrical properties of ferromagnetic alloys near the critical concentration. *Proc. Roy. Soc. A*, 306:355–368, 1968.

[45] A. Rosch. Interplay of disorder and spin fluctuations in the resistivity near a quantum critical point. *Phys. Rev. Lett.*, 82:4280–4283, May 1999.

[46] J.M. Ziman. *Electrons and Phonons*. Oxford University Press, 1960.

[47] J.M. Ziman. *Theory of Solids*. Cambridge University Press, 2 edition, 1972.

[48] A. Rosch. Magnetotransport in nearly antiferromagnetic metals. *Phys. Rev. B*, 62:4945–4962, Aug 2000.

[49] R. Hlubina and T. M. Rice. Resistivity as a function of temperature for models with hot spots on the fermi surface. *Phys. Rev. B*, 51:9253–9260, Apr 1995.

[50] Eric W. Weisstein. Fredholm integral equation of the second kind. Available from URL: http://mathworld.wolfram.com/FredholmIntegralEquationoftheSecondKind.html, Visited on 19.09.16.

[51] A. J. Millis, A. J. Schofield, G. G. Lonzarich, and S. A. Grigera. Metamagnetic quantum criticality in metals. *Phys. Rev. Lett.*, 88:217204, May 2002.

[52] Mario Zacharias and Markus Garst. Quantum criticality in itinerant metamagnets. *Phys. Rev. B*, 87:075119, Feb 2013.

[53] Franziska Weickert, Manuel Brando, Frank Steglich, Philipp Gegenwart, and Markus Garst. Universal signatures of the metamagnetic quantum critical endpoint: Application to $CeRu_2Si_2$. *Phys. Rev. B*, 81:134438, Apr 2010.

[54] D. Belitz, T. R. Kirkpatrick, and Jörg Rollbühler. Tricritical behavior in itinerant quantum ferromagnets. *Phys. Rev. Lett.*, 94:247205, Jun 2005.

[55] D. Belitz, T. R. Kirkpatrick, and Thomas Vojta. Local versus nonlocal order-parameter field theories for quantum phase transitions. *Phys. Rev. B*, 65:165112, Apr 2002.

[56] Kazumasa Miyake and Shinji Watanabe. Unconventional quantum criticality due to critical valence transition. *Journal of the Physical Society of Japan*, 83(6):061006, 2014.

[57] H. Q. Yuan, F. M. Grosche, M. Deppe, C. Geibel, G. Sparn, and F. Steglich. Observation of two distinct superconducting phases in $CeCu_2Si_2$. *Science*, 302(5653):2104–2107, 2003.

[58] Georg Knebel, Dai Aoki, Jean-Pascal Brison, and Jacques Flouquet. The quantum critical point in cerhin$_5$: A resistivity study. *Journal of the Physical Society of Japan*, 77(11):114704, 2008.

[59] George Sterman. *An Introduction to Quantum Field Theory*. Cambridge University Press, 1993.

[60] Gregory Dee and Siddhartha Sen. Calculating anomalous dimensions in a ϕ^3 field theory in $6 + \epsilon$ dimensions using the methods of statistical mechanics. *Annals of Physics*, 107(1):188 – 200, 1977.

[61] D J Amit. Renormalization of the potts model. *Journal of Physics A: Mathematical and General*, 9(9):1441, 1976.

[62] D. J. Amit, D. J. Wallace, and R. K. P. Zia. Universality in the percolation problem—anomalous dimensions of φ^4 operators. *Phys. Rev. B*, 15:4657–4666, May 1977.

[63] P. Gegenwart, F. Weickert, M. Garst, R. S. Perry, and Y. Maeno. Metamagnetic quantum criticality in $Sr_3Ru_2O_7$ studied by thermal expansion. *Phys. Rev. Lett.*, 96:136402, Apr 2006.

[64] B Fak, D F McMorrow, P G Niklowitz, S Raymond, E Ressouche, J Flouquet, P C Canfield, S L Bud'ko, Y Janssen, and M J Gutmann. An inelastic neutron scattering study of single-crystal heavy-fermion YbAgGe. *Journal of Physics: Condensed Matter*, 17(2):301–311, 1 2005.